THE CHARACTERIZATION OF THE EFFECTS OF STRESS CONCENTRATIONS ON THE MECHANICAL BEHAVIOR OF A MICRONIC WOVEN WIRE MESH

by

STEVEN MICHAEL KRAFT
B.S.M.E University of Central Florida, 2010

A thesis submitted in partial fulfillment of the requirements
for the degree of Master of Science
in the Department of Mechanical and Aerospace Engineering
in the College of Engineering and Computer Science
at the University of Central Florida
Orlando, Florida

Spring Term
2013

ABSTRACT

Woven structures are steadily emerging as excellent reinforcing components in dual-phase composite materials subjected to multiaxial loads, thermal shock, and aggressive reactants in the environment. Metallic woven wire mesh materials display good ductility and relatively high specific strength and specific resilience. While use of this class of materials is rapidly expanding, significant gaps in mechanical behavior classification remain. This thesis works to address the mechanics of material knowledge gap that exists for characterizing the behavior of a metallic woven structure, composed of stainless steel wires on the order of 25 microns in diameter, and subjected to various loading conditions and stress risers. Uniaxial and biaxial tensile experiments, employing Digital Image Correlation (DIC) as a strain measurement tool, are conducted on woven wire mesh specimens incised in various material orientations, and with various notch geometries. Experimental results, supported by an ample analytic modeling effort, indicate that an orthotropic elastic constitutive model is reasonably capable of governing the macro-scale elasticity of the subject material. Also, the Stress Concentration Factor (SCF) associated with various notch geometries is documented experimentally and analytically, and it is shown that the degree of stress concentration is dependent on both notch and material orientation. The Finite Element Method (FEM) is employed on the macro-scale to expand the experimental test matrix, and to judge the effects of a homogenization assumption when modeling metallic woven structures. Additionally, plasticity of the stainless steel woven wire mesh is considered through experimental determination of the yield surface, and a thorough analytic modeling effort resulting in a modified form of the Hill yield criterion. Finally, meso-scale plasticity of the woven structure is considered, and the form of a multi-scale failure criterion is proposed and exercised numerically.

This work is dedicated to my parents, whose unyielding support and love has been the catalyst for my success, and to Denise, who always provided support and encouragement despite being forced to bear the brunt of my neglect during the composition of this thesis.

ACKNOWLEDGEMENTS

The author is grateful to Dr. Ali P. Gordon for his guidance and expertise, which was critical to the success of this thesis. The author is also grateful to the other committee members, Dr. Yuanli Bai and Dr. Jan Gou, for their time, guidance, and the for use of their equipment. Special acknowledgment must be given to Mr. Michael Gapuz for his assistance in development of the biaxial load frame, and to Mr. Yueqian Jia for his assistance with the DIC equipment. Thanks is also owed to the many members of The Mechanics of Materials Research Group, all of whom have contributed to this thesis in some way. The research presented in this thesis was funded by the Federal Aviation Administration.

If I have seen further, it is by standing on the shoulders of giants.

-Sir Isaac Newton

TABLE OF CONTENTS

LIST OF FIGURES

LIST OF TABLES

CHAPTER 1: INTRODUCTION

As composite materials continue to become more prominent in taxing engineering applications, woven fiber geometries are emerging as ideal reinforcement materials. While woven materials show great potential in composites and other applications, a thorough understanding of their governing mechanics is still evolving. In recent years, industry has expressed a need for high performance woven structures for applications such as hydrogen fuel cells and high temperature petroleum refinement [Zhang et al., 2010; Juan et al., 2009]. This need has led to renewed interest in a class of woven materials referred to as micronic woven wire mesh, which in general can refer to a wide range of products manufactured from various base wire materials and taking on numerous different weave structures. For applications involving filtration of fine particles from high pressure fluids, particularly those were corrosion or thermal shock may impact material integrity, industry often turns to the stainless steel 316L (SS316L) twill dutch woven wire mesh. This mesh material allows for extremely fine particle retention rates while maintaining high mass flow, and displaying excellent specific resilience and specific strength. While use of this class of material is widespread in the filtration industry, expanded use of stainless steel woven wire mesh products into other engineering applications where it may be ideally suited has been hampered by a lack of scientific material characterization. Ultimately, identification of new applications for woven wire mesh materials will rely upon the acquisition of material property data, the identification of viable constitutive models, and an understanding of material failure characteristics under torturous boundary conditions. The purpose of this thesis is to provide a foundation for the development of mechanical behavior characterization in this

class of materials, particularly when they are subjected to adverse stress concentrations in both uniaxial and multiaxial loading. The subject material is a finely woven 325x2300 SS316L micronic wire mesh, often used in air, water, and oil filtration applications. The relevance of continuum theory to model the notched mechanical behavior of this class of materials is investigated via a rigorous experimental and numerical test sequence, in which loading mode, material orientation, notch geometry, and notch orientation are considered as variables. The final result is a collection of stress concentration factor (SCF) curves documenting the effects of notch parameters and material orientation on stress amplification in the notched region, as well as a complete fractographic analysis documenting the various fracture mechanisms. Full field Digital Image Correlation (DIC) is used as a means for experimental strain measurement, allowing for the comparison of experimental, analytical, and numerical results to assess the ability of classical continuum approaches to model the subject material.

1.1 Literature Review

1.1.1 Previous Efforts in Woven Material Modeling

Pierce first addressed the modeling of woven textiles in 1936 [Pierce, 1936] by proposing a simple geometric model for a plain weave fabric that formed the basis of several mechanical models in future works. The geometry consisted of round weft wires, orthogonal to the round warp wires and tangential at the interface. The weft wires were assumed to always be in plane, and were linear between the warps. These assumptions prove somewhat simplistic, not allowing for any crimping of the weft wires out of plane. The geometry of Pierce has been used in several cases to develop numerical models for the study of fabric behavior, most notably in the case of Tarfaoui and co-authors [Tarfaoui et al., 2001]. Their work employed the Pierce geometric

model in a 'fundamental cell' Finite Element Model (FEM). This model was used to facilitate damage prediction in the form of yarn breakage. Similar to the Pierce model, Kawabata [Kawabata, et al., 1964] proposed a meso-scale model in 1964 that made use of a simplified geometry to study the biaxial deformation of plain weave fabrics. He treated the fabric yarns as simple beam like structures, imparting loads on each other at a single cross over point in the plane of the weave. This work was extended as King and co-workers [King et al., 2005] made use of the Kawabata geometric model to formulate a continuum constitutive model for woven fabrics which considerably simplified the load paths in the meso-structure. The continuum approach, while an idealization, still proved very accurate for modeling in-plane loading. King and co-authors utilized a modified Kawabata geometry, adding axial and rotational springs at the contact points to simulate wire interaction. This model presents a means to predict macro-scale behavior based on the weave geometry and yarn (or wire) materials through a simplification that treats the weave as a homogenized anisotropic body. Such simplification of fabric geometry is common throughout the literature [Kraft and Gordon, 2011; Chen et al., 2007; King et al., 2005], but is typically made after significant numerical modeling or mechanical testing has been performed to formulate the material response. Recent work by the author [Kraft and Gordon, 2011] has shown that a plane stress orthotropic assumption models the behavior of the subject material very accurately, and this conclusion will be drawn upon extensively in this thesis as the foundation for analytical and numerical modeling of notched geometries.

1.1.2 Experimental Methods Common to Woven Materials

Several mechanical testing methods for fabrics are present in the literature. The ASTM standard D4964 (2008) gives guidelines for the tension testing of elastic fabrics, and forms the

basis for the uniaxial testing regimen performed in this study. These tests are performed in the main weave directions and at intermediate orientations using a Constant Rate of Extension (CRE) type control. Off-axis tensile testing subjects the woven material to bi-axial plus shear type conditions, enabling the characterization of the yield surface [Chen et al., 2007, Kraft and Gordon, 2011], and estimation of shear properties [Chen et al., 2007, Saliklis and Falk, 2000]. While off-axis tensile testing is not a standard test method, several researchers have leveraged the off-axis uniaxial tensile test to estimate yield and shear properties. Chen and co-workers [Chen et al., 2007] used this test method to successfully characterize the anisotropic tensile behavior of a flexible polyvinyl chloride coated fabric. By using tensile tests in the principle material axes, and at intermediate orientations in intervals of 15º, Chen was able to develop an exceptional estimation for the Tsai-Hill yield surface, and demonstrated that the shear modulus could be related to the elastic properties of the material in the bias (45º) orientation. Saliklis and co-author [Saliklis and Falk, 2000] performed extensive research on the subject of relating the off-axis tensile properties of thin orthotropic plates to their shear properties. In their work on wood-based panels, Saliklis and Falk were able to identify a relationship for the shear modulus of orthotropic plates that is independent of the difficult to measure Poisson's ratio. The proposed relationship is based on a curve fit of the elastic modulus as a function of material orientation, and proved quite accurate in estimation of the shear modulus. As an extension of the research conducted by Chen and Saliklis, the author and co-workers [Kraft et al., Pending] have shown that uniaxial tensile tests performed only in the principle material orientations can produce in full the independent material properties associated with a plane-stress orthotropic constitutive model of the subject material.

Another common form of mechanical testing found in the literature is the biaxial tension test. In a thorough review of mechanical testing methods for woven fabrics, Bassett and co-workers [Bassett et al., 1999] list the cruciform biaxial test as the most common and accepted biaxial method for woven geometries. Indeed, the use of cruciform (e.g. t-shaped) test specimens for biaxial testing of fabrics is fairly common in the literature, being utilized by noted researchers in the field such as Kawabata [Kawabata et al., 1964], among others. This method of testing is ideal in that the results are not adversely affected by shear coupling [Gibson, 2007], and it reduces clamping difficulties associated with large transverse strains encountered in bias (45º) uniaxial tensile tests [Basset et al., 1999]; however, difficulties arise in the form of cruciform specimen limitations stemming from adverse stress concentrations [Smits et al., 2006], non-uniform biaxial stress fields [Basset et al., 1999], and the need for more sophisticated testing devices [Makinde et al., 1992, Cavallaro et al., 2007]. Much work has been done in the development and optimization of cruciform tensile specimens and biaxial load frames. Hannon and Tiernan [Hannon and Tiernan, 2008] present a review of in-plane biaxial tensile test methods, in which they identify two basic types of biaxial frames: standalone biaxial machines, and link mechanism biaxial machines. Representative standalone devices have been developed by several researchers, most notably Makinde and co-workers [Makinde et al., 1992]. Makinde makes use of four independent linear hydraulic actuators; two per axis, with each axis independently controlled using two closed-loop channels, as illustrated in Fig. 1.1. The displacement of each actuator is measured using a Linear Variable Displacement Transformer (LVDT), and load is monitored on each axis using independent load cells. Benefits of such a device include virtually unlimited possible strain paths, dynamic test capabilities, and a high level of control of biaxial stress ratios. Makinde notes, however, that the high loads generated by

the hydraulic actuators create the need for a very robust load frame, which ultimately reduces flexibility and portability of such a device.

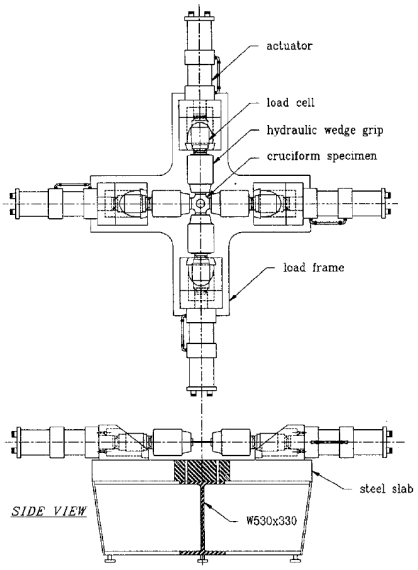

Figure 1.1: Servo-hydraulic biaxial load frame proposed by Makinde [Makinde et al., 1992].

Several researches have proposed designs for linkage-based biaxial test machines, including Cavallaro and co-workers [Cavallaro et al., 2007], and Bhatnagar and co-authors [Bhatnagar et al, 2007]. These devices overcome the need for complicated control systems required by standalone hydraulic actuator frames, and are generally very portable. Linkage based devices are typically designed to integrate into the very common uniaxial load frame, giving them tremendous flexibility and cost effectiveness. Linkage based biaxial load frames make use of pivoting joints and two-force members to transfer the uniaxial motion of a universal load frame into biaxial motion, and can be either vertically or horizontally aligned. These machines tend to have limited available stress ratios, defined as the ratio of the magnitudes of the orthogonally applied stresses, and rely heavily on precise machining to achieve an equibiaxial loading. Bhatnagar designed a vertically aligned load frame, shown in Figure 1.2(a) which is

adjustable to many different biaxial stress ratios, and relies on only a single load cell for force measurement. Such a vertical design is advantageous to optical strain measurement techniques, as the plane of the specimen is held constant throughout the test. While the design proposed by Bhatnagar is sufficient for pure biaxial tension, it may be desirable to achieve a more generalized state of stress in a biaxial cruciform specimen. The design proposed by Cavallaro and co-workers, as shown in Fig. 1.2(b), is perhaps the most sophisticated linkage based biaxial load frame present in the literature, possessing the ability to provide stiffness results both in shear and in multi-axial tension tests. The design of Cavallaro has been adopted, and improved upon, in this work to facilitate the biaxial testing of the subject material.

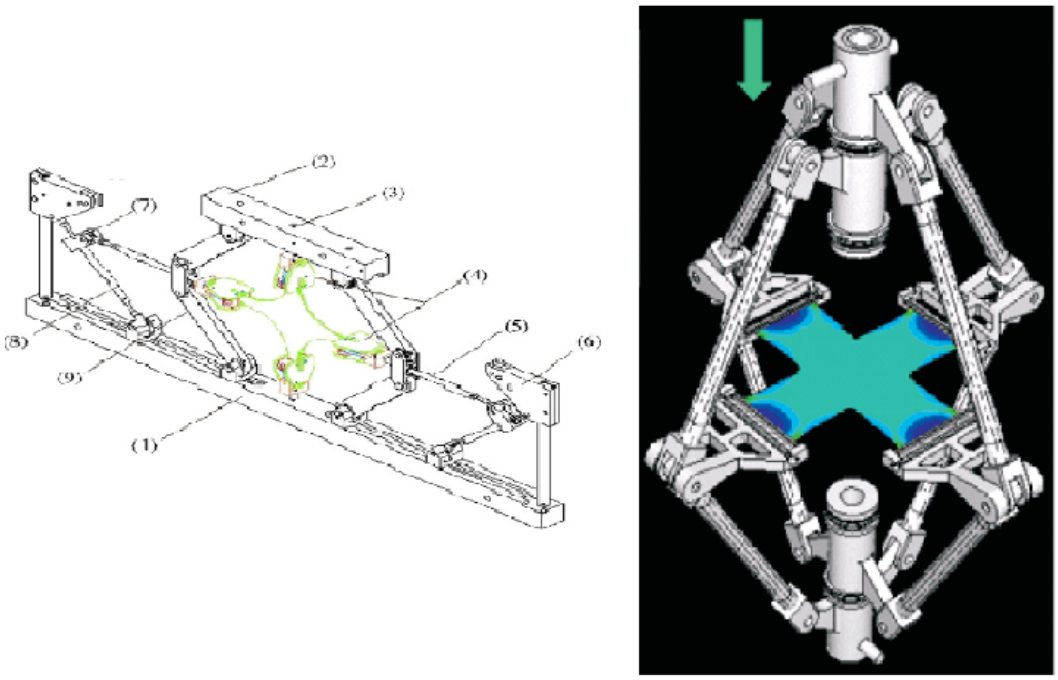

Figure 1.2: Linkage based biaxial load frame as proposed by (a) Bhatnagar, and (b) Cavallaro [Bhatnagar et al., 2007; Cavallaro et al., 2007].

In addition to the development of biaxial testing devices, much work is present in the literature concerning the design of an optimal biaxial specimen. While much of this previous

work has been focused on the development of specimens for polymer and composite testing, and so is not directly applicable to testing of un-impregnated woven structures, there is still much to be gained from the results of these studies. Perhaps the most in-depth study of biaxial specimen optimization is presented by Smits and co-workers [Smits et al., 2006], in which they employ a combination of Finite Element Modeling (FEM), and Digital Image Correlation (DIC) driven experiments to investigate local strain fields in a number of candidate biaxial geometries. In their work, Smits and co-authors identify several criterions by which to optimize a cruciform specimen, all of which have been adopted in this thesis. These criteria include (i) maximization of the region of uniform biaxial strain, (ii) minimization of shear strains in the gage section, (iii) reduction of stress concentration at the fillets, (iv) specimen failure in the gage section, and (v) repeatability of the experiments. Smits evaluated parameters such as relative thickness of the gage section, radius of the corner fillets, and gage section shape for four different cruciform specimens of an epoxy-glass fiber composite. Ultimately, Smits and co-authors recommend a biaxial geometry with small-radius circular corner fillets and a milled biaxial gage section, as shown in Fig. 1.3.

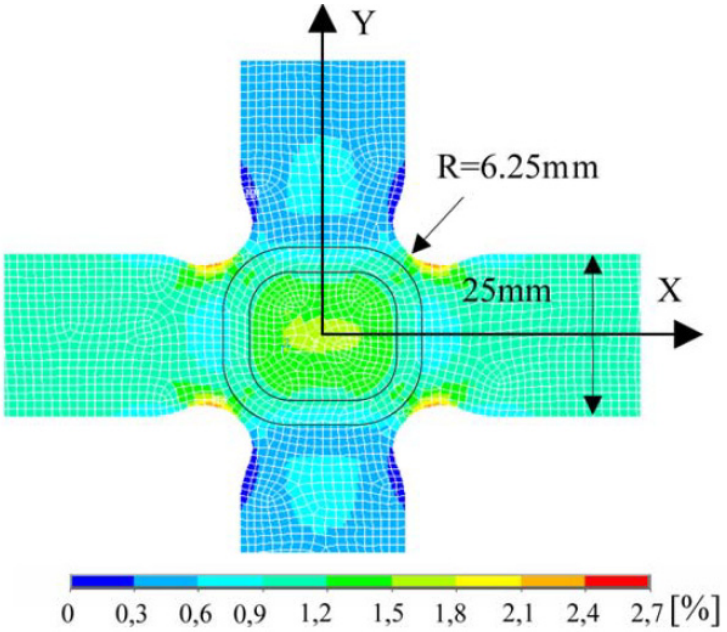

Figure 1.3: Finite Element Model of optimal cruciform specimen geometry as proposed by Smits. The contours show the predicted distribution of the first principle strain upon unequal-biaxial loading [Smits et al, 2006].

Smits notes the inability to achieve initial failure away from the corner fillets in any of the proposed geometries, and states that a reduced cross-section in the gage region is ultimately necessary to consistently propagate the crack into the biaxial region upon fracture. While this research provides valuable experimental and numerical results for various cruciform specimens, it does not provide any parametric data showing trends in fillet SCFs, nor does it provide any means of addressing problematic failure at the fillets. This thesis intends to address this by providing numerically derived SCF curves for various cruciform geometries that will provide future researchers with a systematic path towards optimized cruciform specimen design.

1.2 The Woven Wire Mesh

1.2.1 Wire Material and Weave Geometry

The material of interest in this study is a 325x2300 micronic twill-dutch woven wire mesh. This material is frequently used in fine filtration applications where it is exposed to biaxial

loads in the form of hydrodynamic pressure, as well as temperature gradients and particle deposition. Recently, this material has been employed in explosive trace detection (ETD) applications in which it is simultaneously exposed to extreme temperature gradients and hydrodynamic forces. The mesh is woven from austenitic Cr-Ni-Mo stainless steel 316L (SS316L) wires, conferring superior tolerance to thermal shock and repeated loading cycles. The material properties of AISI for bulk SS316L are provided in Table 1.1 [Blandford et al., 2007]. It is noted, however, that material strength in stainless steel wires tends to increase with decreasing diameter, i.e.,

$$S_{ut} = Ad^{-m} \tag{1.2.1}$$

where A and m are material properties, and d is the wire diameter. Figure 1.4 shows experimental results documenting the trend in strength with wire diameter [ASM, 2000], along with a regression fit of Eq. (1.2.1). In the case of room temperature SS316 wires, A is given as 145.43 ksi-in^m (1623.7MPa-mm^m), while m is 0.149. Austenitic stainless steel wires on the order of 0.010 inches (0.254mm) in diameter have tensile strengths as high as 275ksi (1896MPa). The wires making up the woven mesh in question are of the order of one thousandth of an inch (25.4 microns) in diameter, resulting in wire strengths significantly higher than listed in Table 1.1. An exhaustive literature review yielded no similar models for yield strength of wires drawn from ferrous metals, and it is not customary for wire manufacturers to specify yield strength explicitly. Harvesting a single wire from the mesh material is possible, and mechanical characterization of single wires could be valuable for future work. Investigation of the wire grain structure is also possible, and could provide insight into the strengthening mechanisms predicted by Eq. (1.2.1).

Table 1.1: Material properties of bulk stainless steel 316L at room temperature [Blandford et al., 2007]

Units	Elastic Modulus, E	Yield Strength, σ_y	Ultimate Tensile Strength, S_{ut}	Density, ρ	Elongation, ε_f (%)	Poisson's Ratio, ν	Shear Modulus, G
SI	193 *GPa*	205 *MPa*	520 *MPa*	0.008 g/mm^3	40	0.28	75.4 *GPa*
English	28.0 *Msi*	29.7 *ksi*	75.4 *ksi*	0.289 lbf/in^3	40	0.28	10.94 *Msi*

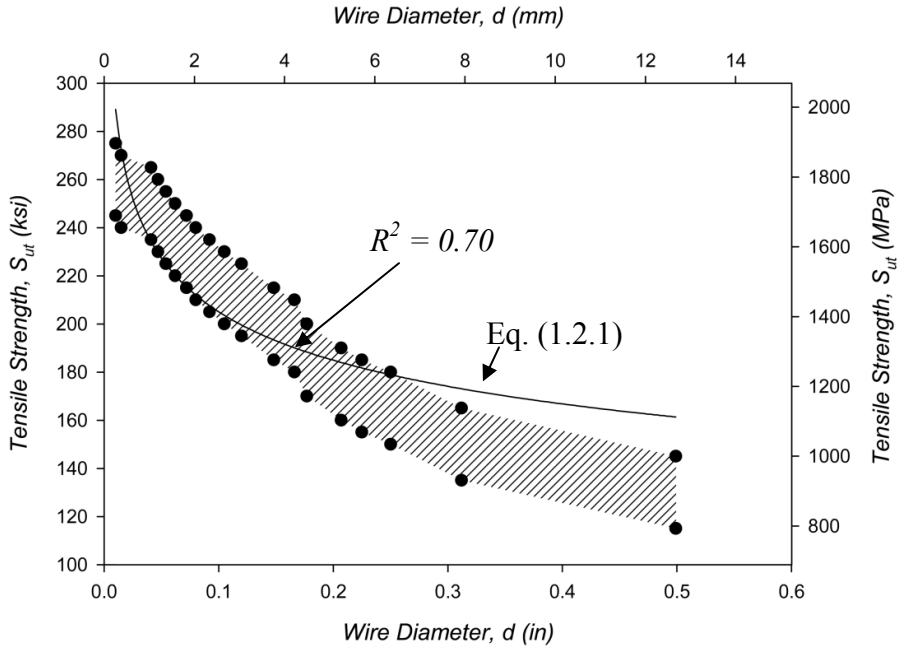

Figure 1.4: Experimental and modeled tensile strength of SS316 based on wire size, and a regression fit by means of Eq. 1 used to produce the supplied constants *A* and *m* [modified from ASM, 2000].

The SS316L wires are woven into the mesh in a twill-dutch pattern. This weave pattern produces an extremely dense mesh, with nominal and absolute pore sizes of 2 and 7 microns, respectively. It is assumed that the warp (toe) wires are initially un-crimped, and that all wires are in a damage free state prior to loading. The warp wire weave direction is referenced as the 0° material direction in this study, while the weft (shute) wire weave direction is referred to as the 90° orientation. Figure 1.5 illustrates the woven wire mesh in both micro [Fig. 1.5(c)], and macroscopic perspectives [Fig. 1.5(d)], and all key dimensions are summarized in detail in Table

1.2. The ASTM standard E2016 [ASTM, 2006] provides the equations used to arrive at the reported weight values for the mesh, and the reported thickness is based on manufacturer specifications of the material.

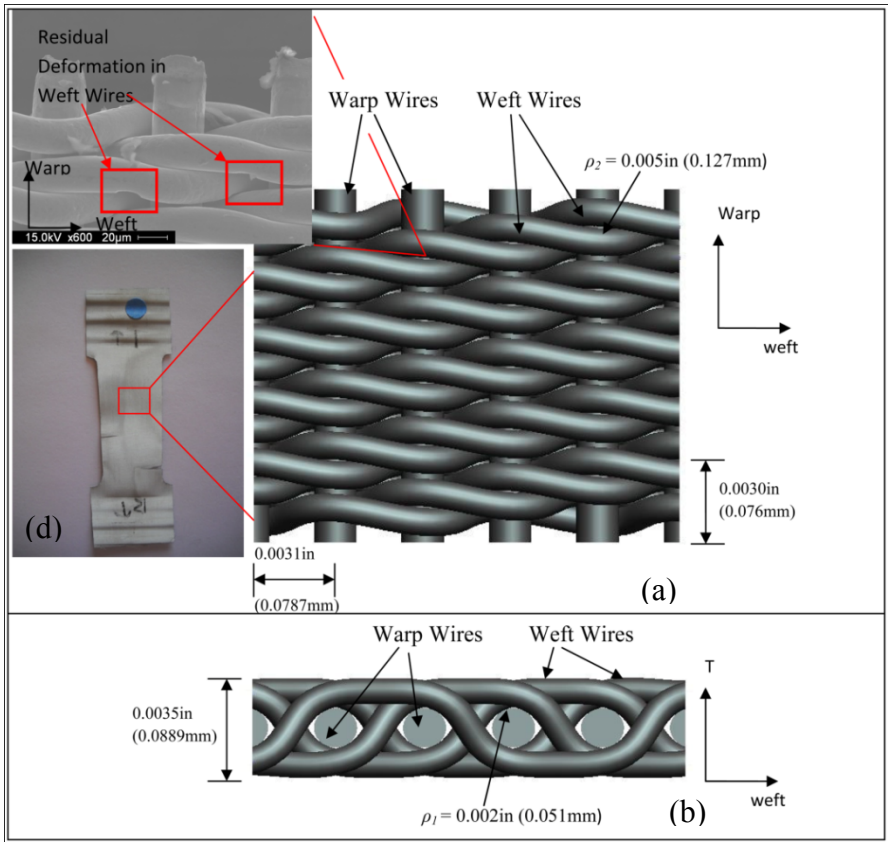

Figure 1.5: Images and rendering of the 325x2300 SS316L twill dutch woven wire mesh specimen and weave geometry outlining key dimensions, and the principle material orientations referred to as the warp (*w*) and weft (*s*) directions.

Table 1.2: 325x2300 316L SS Woven Wire Mesh Specifications

Units	Warp Wire Count, N_s	Weft Wire Count, N_w	Warp Wire Diameter, D_s	Weft Wire Diameter, D_w	Mesh Thickness, T	Mesh Weight, W
SI	127 *wires/cm*	905 *wires/cm*	0.0381 *mm*	0.0254 *mm*	0.0889 *mm*	483.4 g/m^2
English	325 *wires/in.*	2300 *wires/in.*	0.0015 *in.*	0.0010 *in.*	0.0035 *in.*	0.099 lb/ft^2

1.2.2 The Orthotropic Thin Sheet Assumption

The mechanical response of a woven wire mesh at the meso-scale is multifaceted and complex, with factors such as crimp interchange, wire sliding, wire binding, and wire tensioning all occurring simultaneously and dependently. Comprehensive mechanical analysis at the wire level quickly becomes unwieldy, and so an assumption that allows for the analysis of the material at the macro level is ideal. The assumption of homogeneity enables these materials to be modeled with a simplified orthotropic constitutive model. An orthotropic material may be defined as any material that possesses three mutually orthogonal planes of symmetry, which in general allows for the number of independent elastic coefficients to be reduced to nine. Most in-plane woven wire mesh materials possess two distinct and perpendicular weaving directions, referred to as the warp and the weft. The respective wire directions often possess their own distinct material properties due to differences in wire arrangement, size, density, processing, etc. Taking advantage of this wire configuration allows for the assumption that in-plane woven geometries behave as thin orthotropic sheets under plane stress. The assumption of plane stress allows for further reduction of the independent elastic constants from nine to four, resulting in the simple in-plane orthotropic compliance relationship given as,

$$\begin{bmatrix} \varepsilon_w \\ \varepsilon_s \\ \gamma_{ws} \end{bmatrix} = \begin{bmatrix} \frac{1}{E_w} & \frac{-\nu_{sw}}{E_s} & 0 \\ \frac{-\nu_{ws}}{E_w} & \frac{1}{E_s} & 0 \\ 0 & 0 & \frac{1}{G_{ws}} \end{bmatrix} \begin{bmatrix} \sigma_w \\ \sigma_s \\ \tau_{ws} \end{bmatrix} \tag{1.2.2}$$

where, E_w and E_s are the elastic moduli in the warp and weft (shute) directions respectively, and G_{ws} is the in-plane shear modulus. Of the two Poisson's ratios, v_{sw} and v_{ws}, only one is independent due to symmetry. Poisson's ratio is a fundamental elastic material property that describes the ratio of transverse contraction to axial dilatation as given by,

$$\begin{aligned} \nu_{ws} &= -\frac{\varepsilon_s}{\varepsilon_w} \\ \nu_{sw} &= -\frac{\varepsilon_w}{\varepsilon_s} \end{aligned} \tag{1.2.3}$$

Here, the first subscript is understood to indicate the loading axis, so for the case of ν_{ws}, ε_w is the axial strain in the warp (0º) orientation, while ε_s is the transverse strain exhibited by the material in the weft (90º) direction upon uniaxial loading in the warp (0º) direction. Any out-of-plane deformation in the thickness (*T*) direction is ignored in this work.

1.3 The Stress Concentration Factor

1.3.1 Definition and Background Theory

In the design and analysis of structural components, the engineer is often forced to deal with discontinuous geometries associated with bearing races, keyways, pin-joints, and even potential in-service damage from corrosion, erosion, or fatigue cracking. Such geometrical discontinuities alter the local stress fields in loaded components, and can result in very high stresses in the vicinity of the discontinuity. To reduce the impact of stress risers on potential component safety and cost, it is incumbent upon the engineer to accurately predict maximum stresses in notched geometries, and to exercise a systematic approach in minimization of stress concentrations. A failure to understand the degree of stress amplification present in a notched component under a given loading mode could result in localized yielding, and even catastrophic

failure of a component in service. As such, geometrical discontinuities in engineering components, referred to formally as stress concentrations, are often the critical point in a design, and it is vital that the engineer possess effective tools for dealing with such design problems. The classical design approach to handling stress concentrations is to linearly scale the elastic stresses by some stress concentration factor (SCF), typically represented as K_t, as shown in Eq. (1.3.1).

$$\sigma_{\max} = K_t \sigma_{nom} \tag{1.3.1}$$

For isotropic materials, the SCF is a dimensionless parameter dependent only on geometry and loading conditions, and completely independent of material properties. Such a definition allows for convenient graphical representations of the SCF, such as those presented by Pilkey in the classical reference Peterson's Stress Concentration Factors [Pilkey, 1997]. Even in the modern design environment, which is largely dominated by numerical methods, stress concentration factor curves allow for quick first-level approximations of the maximum component stress based solely on the specified geometry and loading condition, and are widely employed by design engineers. The key assumption when applying this metric to a component is that elastic conditions dominate, even if small scale yielding accompanies the mechanical loading.

The independence of the SCF on material properties stems from the theory of elasticity of a continuous isotropic body. In general, the strain-displacement compatibility equations can be written in tensor and index form, respectively, as the following,

$$\begin{aligned} &\nabla \times \left(\nabla \times \underset{\sim}{\varepsilon} \right)^{\mathrm{T}} = 0 \\ &e_{ikr} e_{jls} \varepsilon_{ij,kl} = 0 \end{aligned} \tag{1.3.2}$$

Where ∇ is the gradient operator, $\underset{\sim}{\varepsilon}$ is the engineering strain tensor, and e_{ijk} is the standard permutation symbol. For a state of three dimensional stress Eq. (1.3.2) results in six equations which specify the necessary and sufficient conditions to assure that a given strain field will produce a continuous displacement field in a simply connected domain. While this relationship is powerful, it is not immediately useful in determining the stress field of an elastic body, and so a constitutive equation must be introduced to relate the strain state in a body to the corresponding stress state. For an isotropic elastic body, the six equations that form the generalized Hooke's Law in three dimensions can be written compactly in index notation as,

$$\varepsilon_{ij} = \frac{1}{E}\left[\left(1+\nu\right)\sigma_{ij} - \nu\sigma_{kk}\delta_{ij}\right] \tag{1.3.3}$$

Here ν is the Poisson's ratio, E is the elastic modulus, and δ_{ij} is the Kronecker delta operator. Substitution of Eq. (1.3.3) into the strain compatibility relationship results in expressions for the condition of stress compatibility, known commonly as the Beltrami Equations, which can be written in index notation as [Reddy, 2008],

$$\sigma_{ij,kk} + \frac{1}{1+\nu}\sigma_{kk,ij} = 0 \tag{1.3.4}$$

Thus, it is seen that the stress compatibility condition is independent of the elastic modulus, and only dependent on the Poisson's ratio, which remains fairly constant in most engineering materials. Furthermore, if the assumption of plane stress is invoked, it can be shown that the stress compatibility equations reduce to the form of the Laplacian, i.e.,

$$\nabla^2 \underset{\sim}{\sigma} = 0 \tag{1.3.5}$$

which is completely independent of material properties. The consequence of Eq. (1.3.5) is quite useful, as it lays the foundation for experimental techniques such as photoelasticity, numerical techniques such as the Finite Element Method (FEM), and more pertinently, makes the application of geometrical SCFs practical for most common engineering materials.

While a stress field independent of material properties is certainly convenient for solving engineering problems, it must be noted that this assumption is only valid for the case of isotropic materials. To demonstrate this, we can consider the case of an orthotropic thin plate under the condition of plane stress, where the generalized Hooke's law has been previously given in matrix form as Eq. (1.2.2). In the case of plane stress, the condition for compatibility of deformation can be expressed as,

$$\frac{\partial^2 \varepsilon_x}{\partial y^2} + \frac{\partial^2 \varepsilon_y}{\partial x^2} - \frac{\partial^2 \gamma_{xy}}{\partial x \partial y} = 0 \tag{1.3.6}$$

where γ_{xy} is defined as the engineering shear strain, which equates to double that of the tensorial shear strain. In solving elasticity problems, it is often convenient to define a stress function, $\phi(x,y)$ under the assumption that,

$$\begin{aligned} \sigma_x &= \frac{\partial^2 \phi}{\partial y^2} \\ \sigma_y &= \frac{\partial^2 \phi}{\partial x^2} \\ \tau_{xy} &= -\frac{\partial^2 \phi}{\partial x \partial y} \end{aligned} \tag{1.3.7}$$

Then, by substituting Eq. (1.3.7) and Eq. (1.2.2) into Eq. (1.3.6), we can obtain the following expression of the stress field in a thin orthotropic body as,

$$\frac{1}{E_y}\frac{\partial^4\phi}{\partial x^4}+\left(\frac{1}{G}-\frac{2\nu_{xy}}{E_x}\right)\frac{\partial^4\phi}{\partial x^2\partial y^2}+\frac{1}{E_x}\frac{\partial^4\phi}{\partial y^4}=0 \tag{1.3.8}$$

Clearly Eq. (1.3.8) includes the orthotropic material properties, and so it can be concluded that the stress state of an anisotropic body must depend on material properties. As such, there is no purely geometric SCF available for anisotropic materials, and factors such as material orientation become important in documenting the effects of geometrical discontinuities on the stress field of a loaded body.

1.3.2 Application to Notched Thin Sheets

Several researchers in the past [Whitney and Nuismer, 1974; Probedrya and Gorbachev, 1983; Amer and Schadler, 1997; Chiang, 1999] have investigated stress distributions and SCFs in notched thin plates under a variety of loading modes. Generally, these solutions are derived using potential functions that are identified to satisfy the governing differential equation, i.e., Eq. (1.3.8), and the boundary conditions of the problem. The most classical and fundamental solution of this kind is the circular notch in an infinite isotropic continua under uniaxial tension. The solution in polar coordinates, as presented by Timoshenko and Goodier [Timoshenko and Goodier, 1969], is given as,

$$\begin{aligned}
\sigma_r &= \frac{1}{2}\sigma\left(1-\frac{a}{r^2}\right)+\frac{1}{2}\sigma\left(1-\frac{4a^2}{r^2}+\frac{3a^4}{r^4}\right)\cos 2\theta \\
\sigma_\theta &= \frac{1}{2}\sigma\left(1+\frac{a}{r^2}\right)-\frac{1}{2}\sigma\left(1+\frac{3a^4}{r^4}\right)\cos 2\theta \\
\tau_{r\theta} &= -\frac{1}{2}\sigma\left(1+\frac{2a^2}{r^2}-\frac{3a^4}{r^4}\right)\sin 2\theta
\end{aligned} \tag{1.3.9}$$

Where a is the radius of the circular opening, σ is the remotely applied tensile stress, r is the distance from the center of the circular opening to the point of interest and θ is the angular position of the point of interest wither respect to the axis of applied load. This solution, formulated by means of an Airy stress function, is independent of material properties as expected, and can be shown to produce the classical maximum SCF of 3.0 when $r = a$ and $\theta = 90^{o}$. This classical solution was extended to anisotropic materials by Lekhnitskii in the classical text, Anisotropic Plates [Lekhnitskii, 1968]. Lekhnitskii made use of a complex stress function to derive the expression for the stress on the edge of a circular opening ($r = a$) in an infinite orthotropic plate under uniaxial tension at some angle, φ, to the principle direction as,

$$\sigma_\theta = p\frac{E_\theta}{E_1}\left\{\begin{array}{l}\left[-\cos^2\varphi+\left(\sqrt{\frac{E_1}{E_2}}+\sqrt{2\left(\frac{E_1}{E_2}-\nu_1\right)+\frac{E_1}{G}}\right)\sin^2\varphi\right]\sqrt{\frac{E_1}{E_2}}\cos^2\theta \\ +\left[\left(1+\sqrt{2\left(\frac{E_1}{E_2}-\nu_1\right)+\frac{E_1}{G}}\right)\cos^2\varphi-\sqrt{\frac{E_1}{E_2}}\sin^2\varphi\right]\sin^2\theta- \\ \sqrt{2\left(\frac{E_1}{E_2}-\nu_1\right)+\frac{E_1}{G}}\left(1+\sqrt{\frac{E_1}{E_2}}+\sqrt{2\left(\frac{E_1}{E_2}-\nu_1\right)+\frac{E_1}{G}}\right)\sin\varphi\cos\varphi\sin\theta\cos\theta\end{array}\right\} \quad (1.3.10)$$

Where p is the applied uniaxial tensile stress. The derivation of Eq. (1.3.10) is provided in detail in Appendix A. Lekhnitskii goes on to derive solutions for infinite orthotropic plates with elliptical openings under various boundary conditions, including shear and off-axis uniaxial tension. These solutions are of great value to this current work, and are presented in Chapter 3.2.

Several methods have been proposed to estimate the SCF for a finite body using modifications to the infinite elasticity solution, the most common of which is referred to as the

Finite Width Correction (FWC) Factor. Tan [Tan, 1988] developed a highly used expression for the FWC of an anisotropic plate containing a central opening, based on the definition,

$$\frac{K_T}{K_T^{\infty}}\sigma_y^{\infty}(x,0) = \sigma_y(x.0) \tag{1.3.11}$$

Where the superscript ∞ represents the infinite plate solution, σ_y is the y-component of normal stress in a finite width plate, the ratio K_T / K_T^{∞} is the FWC factor, and K_T and K_T^{∞} denote the stress concentration factor at a point on the edge of the notch whose tangent line is parallel to the loading axis. Tan has shown that the stress field tends to follow this assumption under the conditions that, $a/b \geq 1$, and $2a/W < 0.5$. Tan goes on to provide an explicit relationship for the FWC, provided in Chapter 3, based on the complex form of the solution for the stress field of an infinite anisotropic plate with an elliptical notch derived by Lekhnitskii [Lekhnitskii, 1968].

1.4 Research Approach

1.4.1 Stress Concentration in Inhomogeneous Materials

It is clear that the topic of stress concentrations in homogenous isotropic continua has been thoroughly investigated by previous researches, and as a result, dealing with such a design challenge is largely a matter of protocol, with stress equations and scale factors readily available. Even in cases of complex geometry or anisotropic materials, modern numerical techniques allow for easy and accurate determination of the elastic and plastic stress field, and high confidence failure prediction. As the condition of material homogeneity and continuity is relaxed, however, the problem of mechanical behavior characterization becomes less straightforward, and meso-scale geometric considerations become increasingly important. In the case of woven geometries, meso-scale material interactions such as wire contact, wire crimp interchange, and relative wire

translations and rotations affect how the material responds to the presence of stress concentrations. In homogenous materials, strain energy is transmitted throughout the microstructure by intergranular bonding forces which are relatively strong. These intergranular forces allow for smooth strain distributions throughout the material, and an even distribution of load from remote displacements. In the case of woven wire materials, load is transmitted throughout the structure by discrete wires, and inter-wire forces consist only of relatively weak frictional and contact forces. It is postulated that the strength of the inter-wire forces, i.e., frictional forces, directly influences how well the information of a stress concentration is transmitted throughout the meso-structure, such that if the meso-scale forces are weak, only a very localized zone should be affected by a stress riser. The strength of the inter-wire forces can be treated as coupling between adjacent wires, and as such will be referred to as Meso-Scale Geometric Coupling (MSGC) in the remainder of this thesis. It is theorized that MSGC can have a range from 1.0, which would represent a behavior identical to a homogenous continuum, to zero, signifying no energy transference between adjacent contacting wires. The task of developing a quantitative analytic expression for this factor is beyond the scope of this work, however, and so the MSGC factor is left as a qualitative parameter in this thesis. It is noted that the mechanism by which strain energy is transferred between wires, i.e., wire bending and straitening, frictional sliding, crimp interchange, etc., is not accounted for in such an idealization, but these mechanisms can readily be identified post-failure, as is intended in this work. It is hypothesized that factors such as material orientation, notch orientation with respect to the loading direction, and notch aspect ratio will affect the MSCG factor, resulting in failure behaviors ranging from yield dominant, with large plastic zones and high ductility, to fracture dominant, with small process zones and brittle-type failure.

In addition to fracture mechanisms, it is also of great interest to quantify the degree to which a stress concentration negatively impacts the macro-scale mechanical performance of a structure. A classical metric typically reserved for fatigue characterization, the notch sensitivity factor, q, can be leveraged to explore the effect a stress riser has on the ultimate tensile strength, S_{ut}, of a material. To understand the notch sensitivity factor, it necessary to first define an effective SCF, K_e, as the ratio of nominal (un-notched) ultimate tensile load, P_{ut}, to the notched ultimate tensile load, P_{ut}', i.e. [Pilkey, 1997],

$$K_e = \frac{P_{ut}}{P_{ut}'} \tag{1.4.1}$$

The notch sensitivity factor can then be defined as [Pilkey, 1997],

$$q = \frac{K_e - 1}{K_t - 1} \tag{1.4.2}$$

Where K_t is as defined in Eq. (1.3.1). Both the effective and actual SCF, which are theorized to be dependent on notch aspect ratio and material orientation, determine the sensitivity of the ultimate tensile strength of the subject material to a given notch. As such, it is vital that SCF curves be developed for this material in a variety of orientations and geometrical configurations, and that a series of un-notched nominal cross-section tensile tests be carried out in all considered orientations.

1.4.2 Experimental and Numerical Methods

The goal of this thesis is to characterize the effect of stress concentrations on the mechanical behavior of a micronic woven wire mesh by testing the hypotheses presented above. This characterization is facilitated by means of a thorough experimental and numerical treatment

of notched SS316L 325x2300 twill dutch woven wire mesh. Uniaxial tensile experiments are conducted on notched strip specimens varying in material orientation from the warp (0º) material direction to the weft (90º) material direction in intervals of 45º. In addition to the parameter of material orientation, notch aspect ratio and notch orientation are parametrically varied in the uniaxial tensile experiments. These tests are conducted using Digital Image Correlation (DIC) as a full field strain measurement tool, allowing for experimental determination of the various SCFs, while facilitating comparisons to FEM and elasticity solutions. As DIC strain measurements are not restricted to small strains, this tool provides the capability for detailed investigation of the plastic zone, and can be leveraged to produce full-field shear strain, principle strain, and von-misses strain results in the vicinity of a developing crack. This allows for the experimental characterization of dominate rupture mechanisms, which in conjunction with post-failure analysis of the process zone, is vital in the development of failure models for notched micronic woven wire materials. In addition to the regimen of uniaxial tensile tests, a linkage-based biaxial load frame, also making use of a DIC strain measurement system, is employed to impart a state of biaxial tension onto notched and un-notched cruciform specimens. Such testing extends the definition of SCF curves into the biaxial domain, while imparting a loading mode more true to the in-service conditions often experienced by the subject material. Tests are conducted in various ratios of biaxial tension, and at various notch orientations, producing data relevant to determining the dominant weave orientation (warp or weft wires) contributing to mesh failure. Additionally, biaxial experiments can be leveraged to investigate the effects of shear coupling on the yielding behavior of the subject material, ultimately resulting in a proposed modification to the classical Hill yield criterion.

While experimental results provide data valuable to exploring the notched response of the subject material, it is advantageous to make use of the Finite Element Method (FEM) to both support and supplement the experimental data. Good correlations between the experimental DIC strain contours and the simulated macro-scale, i.e., specimen sized model, FEM strain contours suggest that a continuum based model is sufficient to capture the notched behavior of the subject material. Such findings work to both bolster the experimental results and justify the use of macro-scale FEM simulations to explore material orientations and notch configurations outside of the test regime. Parametric analysis of the test parameters can be quickly and efficiently carried out using FEM techniques, resulting in significantly more data than could be obtained from experiments alone. In addition, macro-scale FEM allows for the testing and optimization of failure models, which can be used to simulate failure propagation characteristics in non-experimentally treated domains.

In the current study, FEM simulations are performed on both the macro-scale, and meso-scale, where modeling is done using a Representative Volume Element (RVE) of the subject material which explicitly contains all of the detailed weave geometry. The meso-scale model is used in conjunction with the macro-scale FEM results to facilitate a multi-scale modeling effort aimed at discerning wire level behavior near the notch process zone. This modeling will reveal information such as wire level plasticity and stress distribution, such that dominant wire interactions and failure mechanisms can be identified. Together, the meso and macro-scale modeling, along with the uniaxial and biaxial experimental techniques provide ample data to fully characterize the effect of notches on the mechanical behavior of a woven wire mesh material, and will provide future researchers with a well established experimental and model foundation to continue application development for this class of materials.

CHAPTER 2: EXPERIMENTAL METHODS

A systematic characterization of the notched tensile behavior of 325x2300 SS316L twill dutch woven wire mesh requires the implementation of the scientific method to test proposed hypothesis, acquire pertinent data and results, and draw conclusions; therefore, before an experimental methodology can be derived, it is necessary and prudent to define the thesis of this work, and to outline the hypotheses to be tested.

As described in Section 1.4, the primary goal of this work is to characterize the effects of stress concentrations, i.e., notches of various aspect ratio, on the mechanical behavior of a thin, inhomogeneous orthotropic sheet. A metallic woven textile, such as the subject material, is an excellent representative of this class of materials, which posses desirable engineering properties for many possible applications. It has been demonstrated in previous sections that the effects of stress concentrations on continuous bodies are well understood, and it is well known that a host of analytic and numeric elasto-plastic modeling tools are available to the engineer to handle such cases. It is the role of the engineer in society to solve technical problems with maximal accuracy and minimal cost, and so it is advantageous to begin the characterization of stress concentrations in metallic woven structures by testing the validity of such existing models for this class of materials. In general, the behaviors of interest in this study are i) elastic response in the presence of a notch, ii) yielding in nominal geometries, and iii) the nature of material rupture in notched geometries, either being yield or brittle fracture dominant.

The elasticity of stress concentrations in continuous bodies has been introduced in Section 1.3, with the definition of the SCF and its dependence, in the case of orthotropic bodies, on material orientation and geometry. Section 1.4 has outlined the hypotheses pertinent to elastic

response of the subject material in the presence of a notch, namely the need to develop experimentally and numerically derived SCF curves for multiple material and notch orientations. In the process of developing these curves, DIC strain measurement will allow for full field analysis of the total strain in the region of the notch. Such data will make possible direct comparison to fields obtained from both analytical and numerical elasticity solutions based on continuum mechanics, allowing conclusions to be drawn regarding the applicability of a Hookean model to predict the elastic response of the subject material in the presence of a notch.

While the development of elastic SCF curves and the identification of appropriate elastic constitutive models represent useful contributions to the understanding of metallic woven material mechanics, the study of notched mechanical behavior in this class of materials demands that significant attention be paid to the elasto-plastic response. It is vital that design engineers be able to predict the boundary conditions that may cause yielding in the 325x2300 SS316L woven wire mesh, and have an understanding of how the material behaves plastically. To this end, an anisotropic yield criterion capable of modeling the subject material must be identified, and the model parameters defined. From previous work conducted by the author [Kraft and Gordon, 2011], the Hill Criterion, given in Eq. (2.1.1) for plane stress [Hill, 1956], has been identified as a viable, yet imperfect, model for the yield behavior of this class of materials.

$$\left(H+F\right)\sigma_y^2+\left(H+G\right)\sigma_x^2-2H\sigma_x\sigma_y+2N\tau_{xy}^2=1 \tag{2.1.1}$$

In previous work, the author utilized off-axis tensile test data to formulate the Hill parameters, *N*, *H*, *F*, and *G*, through a curve fit optimization. The Hill model was found to be highly un-conservative in many material orientations, particularly in orientations where axial and shearing strains are coupled. It is postulated that the inability of the Hill model to accurately fit yield

strength data for the subject material is a result of shear-normal stress coupling that is not directly accounted for in the Hill parameters. To test this hypothesis, a series of uniaxial and biaxial tensile tests, varying by stress ratio, must be performed to define the first quadrant yield surface. In addition to plotting the yield surface, the equibiaxial yield stress, in conjunction with yield stress data from uniaxial tensile tests in the principle material orientations, and on the bias (45º) orientation, provide sufficient data to derive the plane stress Hill parameters for the subject material directly from their definitions, i.e.,

$$\begin{aligned} H + F &= \frac{1}{\sigma_y^2} \\ H + G &= \frac{1}{\sigma_x^2} \\ F + G &= \frac{1}{\sigma_{BA}^2} \\ N &= \frac{1}{2\tau_{xy}^2} \end{aligned} \tag{2.1.2}$$

where σ_y is the yield stress determined from a uniaxial tensile test in the y-direction, σ_x is the yield tress determined from a uniaxial tensile test in the x-direction, σ_{BA} is the yield stress under equibiaxial tension, and τ_{xy} is the yield strength under pure shear. It has been shown in the literature [Chen et al., 2007] that the parameter *N* can be accurately estimated by obtaining the tensile yield stress in the bias (45º) orientation. With the Hill parameters determined from the relationships in Eq. (2.1.2), comparison to the yield surface can easily be accomplished, allowing for modifications to Eq. (2.1.1) that will result in an improved model for the orientation dependence of yield strength in this class of materials.

In general, failure of a component can be classified as either yield dominant or fracture dominant, and the identification of the failure mode can provide insight into the mechanics of the failure. A yielding dominant failure indicates general plasticity, and signifies that the macro-scale notch defect is not the dominant failure driving mechanism. A fracture dominant failure, indicated by highly localized yielding, communicates that the macro-scale notch defect dominants the mechanical response of the sample. It is theorized that the degree of meso-scale wire level coupling is dependent on the orientation of the material reference frame with respect to the loading axis, and so it follows that the dominant failure behavior is likely not only dependent on the notch geometry, but also on the material orientation. Such information is vital to system engineers who are tasked with component assessment after a notch or rip has been discovered, as fracture type failure is often sudden, and could potentially lead to loss of hardware or life. As such, it is essential the uniaxial and biaxial tensile experiments not only provide information on elastic and elasto-plastic material response, but also that the mesh rupture occurs in the gage section and at the notch location. Failure mechanism data can then be inferred from the tensile response and local strain distribution (measured with DIC), and also documented via post-mortem fractography.

2.1 Uniaxial Tensile Testing

2.1.1 Specimen Design and Fabrication

Several uniaxial tensile tests are necessary to define tensile material properties and to characterize the mechanical behavior of uniaxially loaded twill dutch SS316L woven wire mesh in the presence of a stress concentration. A uniaxial test specimen must be designed that facilitates both tensile property and notched behavior characterization. To this end, two different

uniaxial specimens have been designed: a flat tensile specimen for testing nominal geometries and a strip uniaxial specimen for testing notched geometries. The woven wire mesh specimens are incised by hand from larger material sheets [144.0in^2 (0.092m^2)] supplied by TWP Inc., into either the standard flat tensile specimen shape as per ASTM Standard E8 (2004), or a strip shape with identical gage dimensions. The flat tensile specimens have been iteratively designed to ensure optimal failure in the gauge section of the specimen, and this is the case in the majority of the experiments. The optimal flat tensile test specimen geometry is provided as Fig. 2.1(a), with a gauge width of 0.75in. (19.05mm.) and a gauge length of 1.25in. (31.75mm.). The gage section geometry produces an active (load bearing) wire count of 243 warp wires in the warp (0°) orientation, and 1725 weft wires in the weft (90°) orientation. Flat tensile (un-notched) specimens are incised in both the warp (0°) and weft (90°) material orientations, and at off-axis angles in 15° intervals, as illustrated by Fig. 2.1. This approach produces detailed information on the orientation dependence of the load versus deflection response of the subject material, which can be used to calculate material properties such as yield strength and elastic modulus, and allows for the application of classical mechanical models to the material through regression analysis or other means [Chen et al., 2007; and Gordon, 2011]. As the specimen orientation diverges from the main weave axes, edge effects due to wire cut-off are unavoidable. This problem is most pronounced in the 45° orientation, where a typical aspect-ratio flat tensile specimen could potentially have no wires that run the entire gauge length. The author has given much attention to the effects of widening the sample specimen to reduce edge effects in a previous work [Kraft and Gordon, 2011], with particular focus on how the elastic modulus and yield strength vary with orientation. From this work, it has been shown that widening the sample by a factor of two does not greatly improve material response. In fact, adverse boundary

conditions that arise in clamped off-axis specimens due to shear coupling [Gibson, 2007] are exasperated by reducing the aspect ratio of the specimens, causing failures near the specimen grips, and specimen twisting during the experiments.

The strip specimens as shown in Fig. 2.1(b), do not have corner fillets as they contain notches where failure is expected to occur. The notches are imparted onto the specimens by means of a light duty metal punch (Roper Whitney No. 5) using custom fabricated elliptical and circular punches and dies. The notches are aligned and oriented with the specimens via pre-fabricated aluminum punch stencils laid over the incised strip specimens. This process ensures accurate and precise generation of both circular and elliptical notches of various aspect ratios. Slit type notches were also cut by hand into several incised strip specimens via a sharp razor blade, with the slits being aligned via stencil

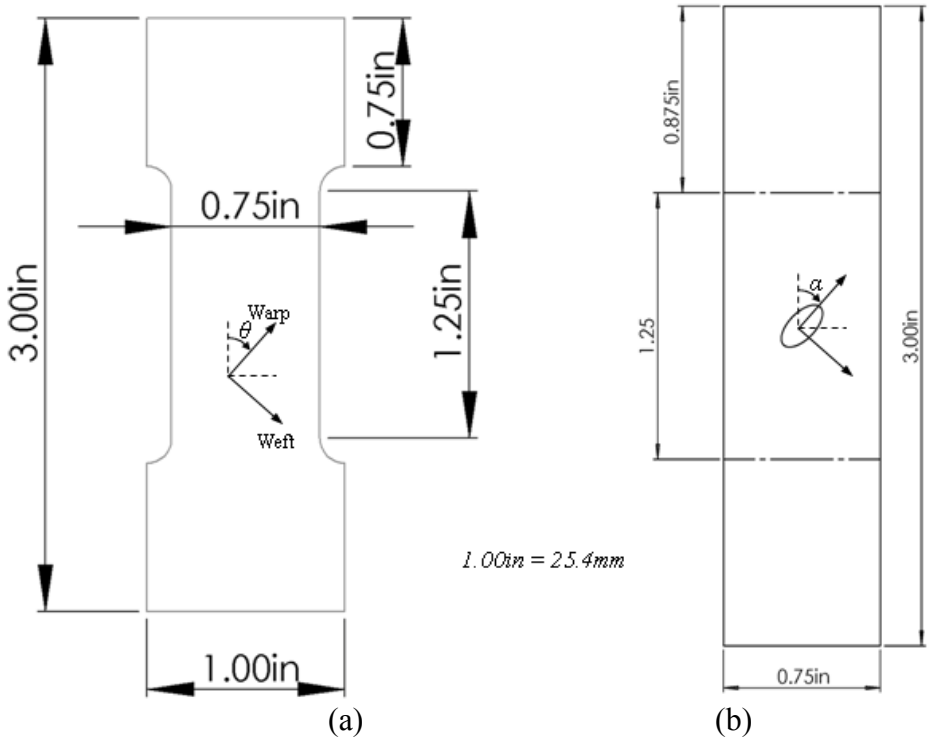

Figure 2.1: Smooth flat tensile and notched strip specimens used in uniaxial tensile experiments conducted in the 325x2300 SS316L twill dutch woven wire mesh.

Incision of the test samples by hand inherently introduces variability into the specimen geometry that could ultimately influence test results. To gauge the level of variability in these experiments arising from, amongst other possible factors, sample geometry, a series of ten tensile tests were initially run to fracture on un-notched flat tensile warp (0°) specimens. The results of this specimen variability testing are provided in Table 2.1 [Kraft and Gordon, 2011], where the values have been normalized such that A_0 = 0.00248in^2 (1.60mm^2), k_0 = 6.48kip/in (1134.8kN/m), S_{y0} = 11.4ksi (78.6MPa), UTS_0 = 12.7ksi (87.6MPa), S_{f0} = 11.9ksi (82.0MPa), and ε_{f0} = 0.084in (2.13mm). Note that the cross-sectional area, A_0, represents the cross section of the material as if it were a homogenous body. The highest degree of standard deviation observed in the normalized data was in the elongation to failure, with an acceptable value of 0.12. Yield strength and stiffness also show notable normalized standard deviations, with values of 0.04, and 0.10 respectively. These values are considered within statistical error limits for mechanical testing of this class of materials, and so it was justified to proceed with further testing of the material without multiple test duplications

Table 2.1: Normalized Mechanical properties of 316L SS Woven Wire Mesh in Warp (0°) direction [Kraft and Gordon, 2011]

Specimen ID	Cross-Sectional Area, A/A_0	Stiffness, k/k_o	Yield Strength, S_y/S_{yo}	Ultimate Strength, UTS/UTS_o	Fracture Stress, S_f/S_{fo}	Elongation, ϵ_f/ϵ_{fo}
AR-001	1.00	1.00	0.95	1.00	1.00	1.00
AR-002	1.01	0.96	0.89	0.97	1.00	0.92
AR-003	1.01	1.08	0.98	0.98	1.00	1.04
AR-004	0.99	1.17	1.00	1.03	1.00	1.13
AR-005	0.99	1.25	0.96	1.01	1.01	0.83
AR-006	0.99	1.05	0.96	1.03	0.98	1.13
AR-007	0.99	1.24	0.97	1.01	0.98	1.04
AR-008	1.00	0.99	1.01	1.01	0.99	1.11
AR-009	0.99	1.17	0.98	1.04	1.00	1.08
AR-010	1.00	1.05	1.02	1.03	0.98	1.25

2.1.2 The Uniaxial Test Setup - Load Frame and Specimen Grips

Tensile experiments were conducted on smooth flat tensile and notched strip specimens of the 325x2300 SS316L woven wire mesh in the main wire orientations, hereby referred to as the warp (0°) and the weft (90°) directions, and at several orientations in between. These tests were carried out using an MTS Insight 5 electromechanical uniaxial testing machine, as shown in Fig. 2.2(b). A constant rate of extension (CRE) test method was employed at a rate of 0.10 *in/min* (2.54 *mm/min*), as specified by ASTM Standard D4964 (2008). The device allowed for the acquisition of the load versus cross-head displacement response of each specimen, which could then be used to ascertain numerous material properties such as stiffness, yield strength, ultimate strength, toughness, elongation to failure, etc. Specimens were held by wave-shaped grips (Test Resources Model No.G86G) suitable for gripping the very thin material samples, as shown in Fig. 2.2(a).

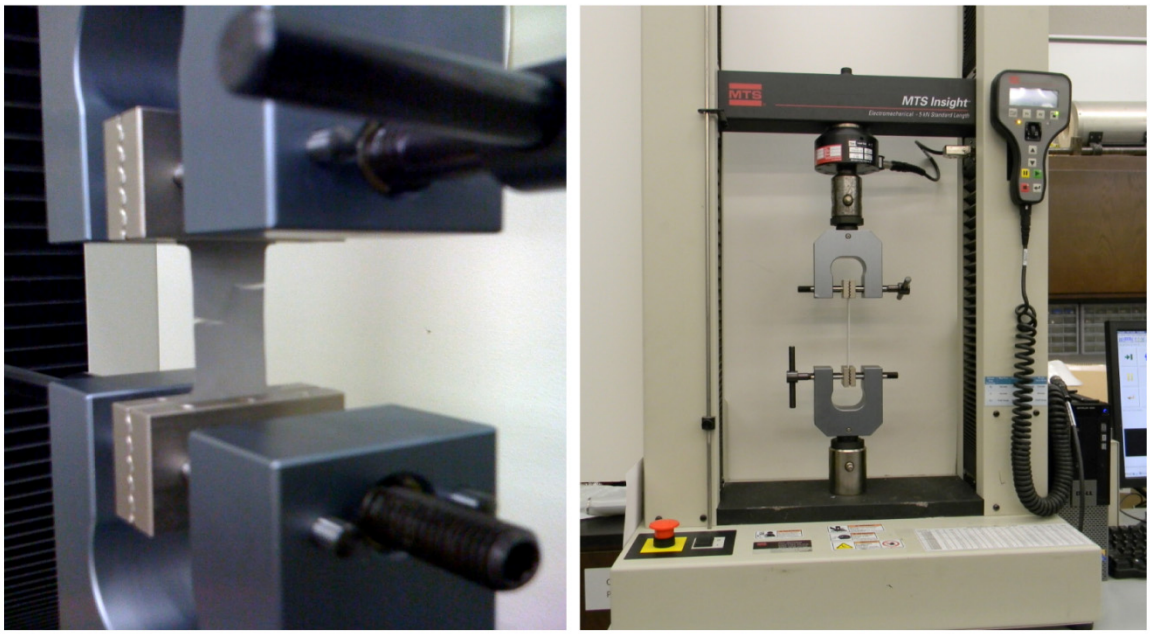

(a) (b)

Figure 2.2: (a) Wave grips used for uniaxial tensile testing on the 325x2300 SS316L twill dutch woven wire mesh, (b) MTS Insight 5kN load frame fitted with the screw action wave grips.

2.1.3 Digital Image Correlation for Strain Measurement

As is often the case with composite materials, fabrics pose a challenge in the definition of mechanical properties due to their inhomogeneous structure. Optical strain measurement techniques, including DIC, have emerged as the optimal solution to the problem of strain measurement in reinforced composites, and recent research by the author has formally validated the DIC method for un-impregnated fabrics [Kraft et al., Pending]. Digital Image Correlation (DIC) is a variant of the classical laser speckle approaches, which allows for the substitution of a painted speckle pattern and Charge-Coupled Device (CCD) camera in place of the more complex optical setup required for speckle interferometry. A series of images is captured in succession, starting with the un-deformed image and proceeding until the test is completed. As the specimen is deformed, the painted speckle pattern deforms with it, and this information is captured on the CCD in the form of pixel position and respective light intensity. In raw form, this generates a matrix of gray-scale values corresponding to the random speckle pattern on the specimen. As the target feature (speckle) moves in the frame onto new pixels, gray-scale values shift with it in the matrix, and this information is recorded. Digital Image Correlation has been shown to be an effective method for obtaining full-field strain measurements in woven composite materials [Lomov et al., 2006], and was used successfully by Hursa and co-workers to identify the Poisson's ratio of plane and twill woven cotton fabrics of significantly less mesh density than the subject material of the current study [Hursa et al., 2009].

Digital Image Correlation (DIC) is a widely used optical strain measurement technique first developed by Peters and Ranson in the early 1980's [Peters and Ranson, 1982]. The method is far less optically demanding than other experimental techniques such as laser speckle

photography, and does not require an isolation table. White light is sufficient to illuminate the specimen, and there is little restriction to specimen size or total specimen deformation. A sketch of the DIC setup used in the uniaxial portion of this investigation is illustrated in Fig. 2.3. In general, DIC requires the generation of a random speckle pattern directly on the surface of the test sample. The speckle pattern must be of sufficient contrast to the surface of the specimen to generate detectable gray scale value gradients across the specimen, and the speckle size must be sufficiently small as to obtain a reasonable resolution.

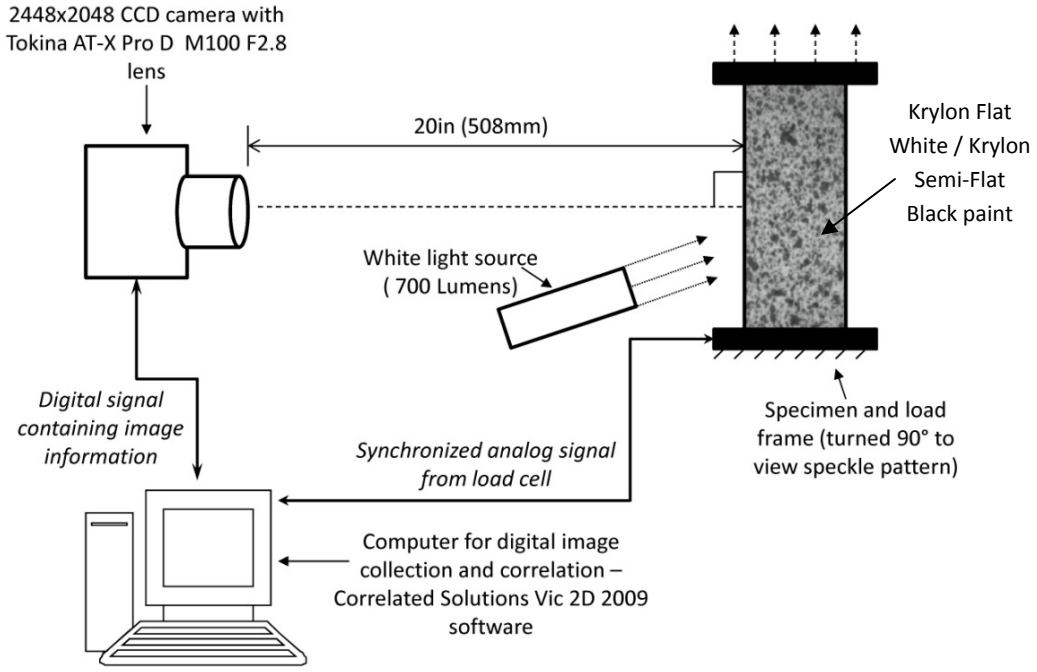

Figure 2.3: Diagram of experimental setup used for Digital Image Correlation of the woven wire mesh specimens

A digital image of the speckle pattern is then captured on a CCD camera before and after deformation, such that gray scale image intensity values can be recorded with respect to pixel

position in the un-deformed and deformed bodies. A correlation algorithm is then employed to systematically determine the most likely mapped position of a subset of pixels based on minimization of a correlation coefficient, which may be defined as [Shukla, 2010],

$$C = 1 - \frac{\sum_{S_p \in S} g(S_p) h(S_p, P)}{\left[\sum_{S_p \in S} g^2 \left(S_p \right) \sum_{S_p \in S} h^2 (S_p, P) \right]^{1/2}} \tag{2.1.3}$$

where g and h are bi-cubic spline interpolation functions of the reference and deformed images, respectively. The variable S represents a subset of points surrounding a single point in the subset, S_p, and P is a vector whose components are the mapping parameters used to relate the deformed and un-deformed geometries. The displacement mapping parameters, including the displacement components and the displacement gradients, can be determined via a second order Taylor series expansion of the mapping function about some point S, i.e.,

$$\begin{aligned} \tilde{x} &= x + u(x, y) \\ \tilde{y} &= y + v(x, y) \end{aligned} \tag{2.1.4}$$

$$\begin{aligned} \tilde{x} &= x_0 + u_0 + \frac{\partial u}{\partial y}\Delta x + \frac{\partial u}{\partial x}\Delta y + \frac{1}{2}\frac{\partial^2 u}{\partial x^2}\Delta x^2 + \frac{1}{2}\frac{\partial^2 u}{\partial y^2}\Delta y^2 + \frac{1}{2}\frac{\partial^2 u}{\partial x \partial y}\Delta x \Delta y \\ \tilde{y} &= y_0 + v_0 + \frac{\partial v}{\partial x}\Delta x + \frac{\partial v}{\partial y}\Delta y + \frac{1}{2}\frac{\partial^2 v}{\partial x^2}\Delta x^2 + \frac{1}{2}\frac{\partial^2 v}{\partial y^2}\Delta y^2 + \frac{1}{2}\frac{\partial^2 v}{\partial x \partial y}\Delta x \Delta y \end{aligned} \tag{2.1.5}$$

where the subscripts s and w refer to the weft (shute) and warp directions, respectively. Chu and co-workers [Chu et al., 1985] have shown that further manipulation of this relation, along with the definition of engineering strain, can be employed to develop accurate approximations for the

in-plane finite strain tensor. The result is a full-field optical strain measurement capable of determining the displacement gradients to within ± 0.0002 in/in (mm/mm) [Shukla, 2010].

To capture the images for correlation, a high-resolution (2448x2048) CCD camera with a Tokina AT-X Pro D M100 F2.8 lens was placed on a fully leveled Velbon GEO N840 tripod centered in front of the uniaxial specimen. The camera recorded images at a rate of 0.5 Hz throughout the duration of the test. Correlation of the DIC images was accomplished via a commercially available algorithm, Vic - 2D version 2009, with care being taken to assure the system was properly calibrated.

2.1.4 Uniaxial Tensile Testing Matrix of Experiments

A battery of uniaxial tensile tests on the subject material have been identified to address the hypothesis outlined in Sections 1.4 and 2.1 of this work. The uniaxial tensile experiments must facilitate both the experimental aspects of this work, such as development of the SCF curves and characterization of notch sensitivity, and the numerical simulations planned to validate the proposed orthotropic constitutive model and extend the experimental regime. As such, the uniaxial test matrix must extend beyond parametrically varied notched geometries and material orientations to incorporate testing aimed at elastic-plastic material property classification. Two experiments, labeled ARDIC-00-1 and ARDIC-90-1, conducted on smooth flat tensile specimens as shown in Fig. 2.1(a) in the warp (0º) and weft (90º) material orientations, respectively, are sufficient to characterize all four independent elastic constants in Eq. (1.2.2). These tests are necessary to facilitate elasto-plasitc macro scale FEM, and to allow analytic comparison to experimentally obtained stress fields via Eq. (1.3.9) and Eq. (1.3.10). In addition to these main material axis experiments, intermediate orientation tensile experiments

have been conducted on smooth flat tensile specimens to facilitate orientation modeling of the elastic properties and yield strength. These experiments were conducted in 15º intervals, and are again labeled as ARDIC specimens.

Uniaxial tensile testing of notched geometries will proceed in a parametric fashion with respect to material orientation, referred to by the angle θ with respect to the principle material orientation, notch orientation, referred to as the angle α with respect to the loading axis, and notch aspect ratio, λ, i.e.,

$$\lambda = \frac{a}{b} \tag{2.1.6}$$

where a is the minor elliptical radius, and b is the major elliptical radius, as illustrated in Fig. 2.4. In all cases, the major radius, b, is set to 0.125 in (3.175mm), and the minor radius, a, can be determined based on the specified value of λ. The λ ratio will be varied from a value of 1.0, corresponding to a circular notch, to a value approaching zero, representing a slit. For each case of λ, both the material orientation, θ, and the notch orientation, α, will be varied from 0º to 90º in intervals of 45º, totaling nine experiments per λ ratio, as shown in Table 2.2. Note that the 0.0º material orientation is referred to as the warp direction, while the 90.0º material orientation is referred to as the weft orientation. The λ ratios of interest have been chosen to provide for maximum change in SCF between the various levels, while allowing for easy and repeatable notch fabrication via the punch method. Testing in the bias (45º) orientation will provide experimental data on the effects of notches in this class of material when subjected to shear loading, providing valuable information for failure model calibration. Mapping of the degree of dependence observed in the SCF with changes in the angle α and the ratio λ will provide future

researchers with data pertinent to the determination of the MSGC coefficient, with strong dependence expected in material orientations exhibiting high inter-wire coupling.

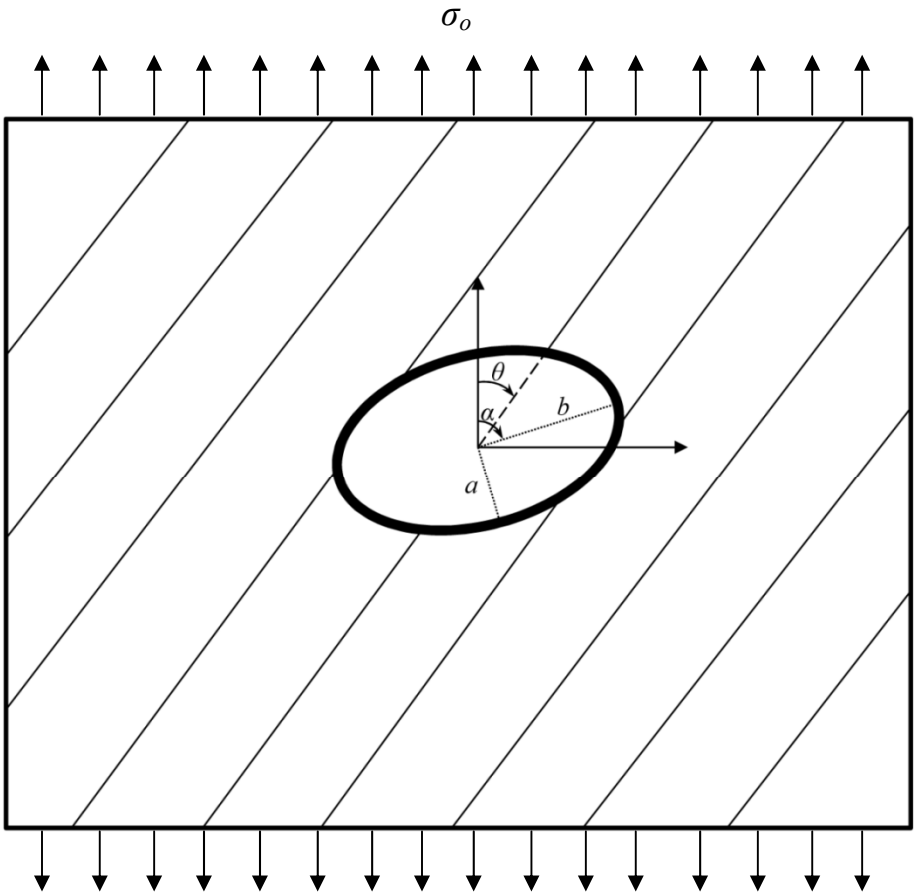

Figure 2.4: Illustration of the parameters to be varied in the sequence of uniaxial tensile experiments on the 325x2300 SS316L twill dutch woven wire mesh

In addition to the above uniaxial tensile tests performed on specimens conforming to Fig. 2.1, nominal width specimens have been incised to investigate the effects of the parameters λ, α, and θ in the reduction in fracture strength of the subject material. This investigation is meant to produce data relevant to determining the notch sensitivity of this material, q, as defined in Eq. (1.4.2), as a function of the experimental parameters.

Table 2.2: Matrix of Uniaxial Tensile Tests on 325x2300 SS316L Woven Wire Mesh

Test Number	Test ID #	Material Orientation, θ (°)	λ	Notch Orientation, α (°)
1	ARDIC-00-1	0.0	N/A	N/A
2	ARDIC-90-1	90.0	N/A	N/A
3	ARDIC-15-1	15.0	N/A	N/A
4	ARDIC-30-1	30.0	N/A	N/A
5	ARDIC-45-1	45.0	N/A	N/A
6	ARDIC-60-1	60.0	N/A	N/A
7	ARDIC-75-1	75.0	N/A	N/A
8	UA-C-00-00	0.0	1.0	N/A
9	UA-C-45-00	45.0	1.0	N/A
10	UA-C-90-00	90.0	1.0	N/A
11	UA-E05-00-00	0.0	0.5	0.0
12	UA-E05-45-00	45.0	0.5	0.0
13	UA-E05-90-00	90.0	0.5	0.0
14	UA-E05-00-45	0.0	0.5	45.0
15	UA-E05-45-45	45.0	0.5	45.0
16	UA-E05-90-45	90.0	0.5	45.0
17	UA-E05-00-90	0.0	0.5	90.0
18	UA-E05-45-90	45.0	0.5	90.0
19	UA-E05-90-90	90.0	0.5	90.0
29	UA-S-00-00	0.0	0.0	0.0
30	UA-S-45-00	45.0	0.0	0.0
31	UA-S-90-00	90.0	0.0	0.0
32	UA-S-00-45	0.0	0.0	45.0
33	UA-S-45-45	45.0	0.0	45.0
34	UA-S-90-45	90.0	0.0	45.0
35	UA-S-00-90	0.0	0.0	90.0
36	UA-S-45-90	45.0	0.0	90.0
37	UA-S-90-90	90.0	0.0	90.0

The nominal width of each respective specimen is determined based on the projected width of the notch on the axis perpendicular to the loading axis. A total of nine nominal width tensile experiments have been conducted, corresponding to the three experimentally treated notch

orientations, α = 0º, 45º, 90º, in all three tested material orientations, θ = 0º (warp), 45º, 90º (weft).

2.2 Biaxial Tensile Testing

A biaxial testing regimen has been designed to extend the study of the effects of stress concentrations on 325x2300 twill dutch woven wire mesh into the loading mode most common to this class of materials. When used in filtration and particle trace detection applications, hydrodynamic forces cause biaxial stresses to develop, and so it is necessary to investigate how such components behave, and ultimately fail, in the presence of a notch or tear. To this end, a linkage based biaxial load frame, inspired by the design proposed by Cavallaro and co-workers [Cavallaro et al., 2007], has been constructed to impart loads of varying biaxiality onto both notched and un-notched cruciform specimens. Digital Image Correlation will be used to provide full field tensorial and equivalent strain data, and a DAQ circuit has been developed to process and record remote load and displacement data from each axis. In addition to the remote and local response of notched specimens, the biaxial setup has been leveraged on smooth specimens to facilitate an investigation of potential modifications to the classical Hill yield criterion.

2.2.1 Specimen Design from Finite Element Optimization

As outlined in Section 1.1.2, design of a viable biaxial cruciform specimen is a challenging prospect, with difficulties arising from inherently non-uniform stress distributions caused by fillet stress concentrations. Such stress concentrations can cause failure outside of the gage section of the specimen, possibly even in notched geometries, rendering yield and rupture results invalid. To minimize the negative effects of the cruciform arm fillets on the stress distribution in the biaxial specimens, parametric FEM simulations were carried out using

ANSYS Mechanical APDL on three candidate geometries, shown in Fig. 2.5 below. The parameters of interest for each respective geometry are the radius of the fillet region, r_c, the length of the uniaxial cruciform arms, l_c, and the width of the biaxial gage section, d_c. Biaxial specimen A is characterized by a smooth circular arc fillet whose end points are tangent to the uniaxial arms. Specimen B also makes use of a smooth circular arc fillet, however the center of the arc fillet is defined as the point of intersection of the two axial arms, such that the defined arc forms three quadrants of a circle centered at the intersection point. Specimen C has a fillet radius described identically to specimen A, but incorporates tapered uniaxial arm sections. Note from Fig. 2.5 that the initial width of the uniaxial cruciform arm in specimen C is given as D_c, while the tapered width is assigned the parameter d_c.

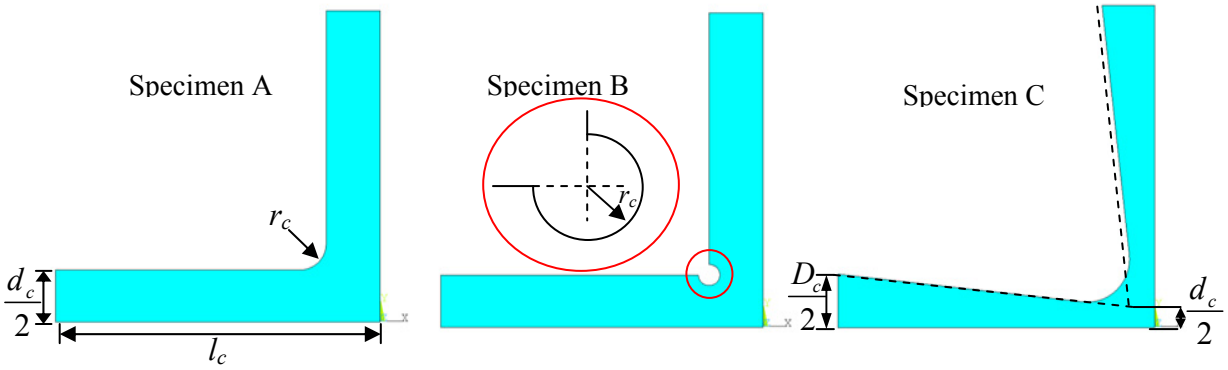

Figure 2.5: Candidate biaxial specimen geometries parametrically investigated using ANSYS. Note that geometric symmetry is taken advantage of in this modeling effort, such that only one quadrant of the biaxial specimen is modeled.

Each specimen is assigned isotropic elastic material properties, and meshed using 6-node isoparametric plane stress triangular elements (PLANE82), with increased mesh density in the region of the fillets, as shown in Fig. 2.6. Symmetry boundary conditions were employed, and an equibiaxial stress applied to the cruciform arms. Appendix B contains the ANSYS APDL codes used to model the biaxial cruciform specimens. For each specimen geometry, the

parameters of interest were parametrically varied to investigate their affect on the magnitude of the SCF for the fillet region of the specimen. Post-processing of the finite element model is facilitated by exporting the Von Mises stresses in the region of the fillet, and the Von Mises stress at the center of the gage section.

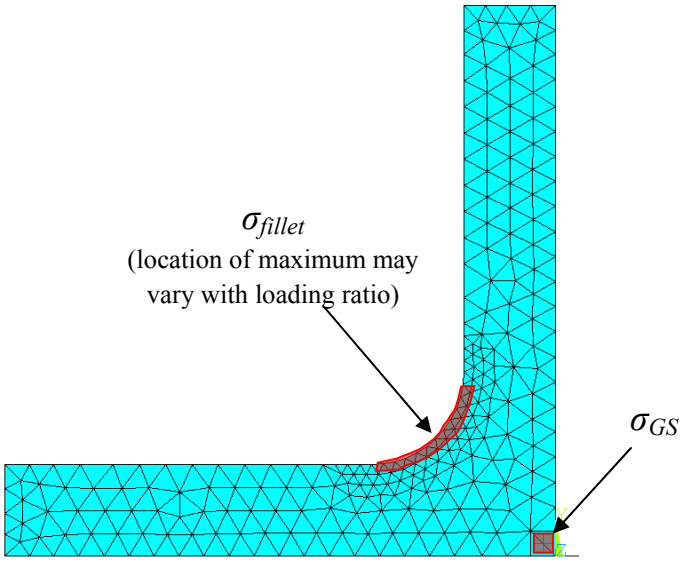

Figure 2.6: Finite element mesh of biaxial specimen A used to numerically optimize the cruciform specimen for the biaxial testing regimen.

The stress concentration factor (SCF) of the fillet region for each prospective biaxial geometry can then be defined as,

$$K_c = \frac{\sigma_{fillet,vm}}{\sigma_{GS,vm}} \tag{2.2.1}$$

Where $\sigma_{fillet,vm}$ is the maximum Von Mises stress in the region of the fillet, $\sigma_{GS,vm}$ is the Von Mises stress in the center of the gage section, and K_c is the resulting SCF. The SCF values as defined by Eq. (2.2.1) were then plotted for each specimen as a function of the geometry, with the goal being to identify the combination of geometrical parameters which reduce the fillet SCF

to a minimum. These results are provided in Fig. 2.7, where the parameter definitions for each specimen are as described in the inset. Inspection of Fig. 2.7 reveals no clear advantage for any of the proposed specimen designs in terms of minimal SCF, with all geometries producing a minimum value of approximately 2.3 at some respective geometric parameter combination. To facilitate a selection, the other important aspects of cruciform specimen design; repeatability and ease of fabrication, relative continuity of stress in the uniaxial cruciform arms, and a biaxial stress state in the gage section, must be considered. With regards to specimen fabrication, both specimens A and C contain high tolerance circular arc fillets, and specimen C entails the additional difficulty of tapered cruciform arms. Precise fabrication of these specimen designs would demand expensive procedures such as die fabrication or water jet cutting. Conversely, specimen B can easily be fabricated using a drill template along with stencil-assisted straight razor cuts. Specimen B can be produced at a high level of precision at low cost, and so is an ideal choice provided the other two conditions are satisfied. To investigate the continuity of the stress in the uniaxial cruciform arms of specimen B, and to assess the biaxiliaty in the gage section, ANSYS is again employed to generate the equivalent and directional stress contours for specimen B given the application of an equibiaxial tensile load. Figure 2.8 shows the stress contours developed in specimen B, using the same mesh parameters and boundary conditions as described in Appendix B for SCF determination. Inspection of the contours provided in Fig. 2.8 reveals that the Von Mises stress distribution (Fig. 2.8(d)) in the uniaxial cruciform arms of specimen B is uniform, and that the *x*-component (Fig. 2.8(a)) and *y*-component (Fig. 2.8(b)) of the applied stress proceeds into the specimen gage section with minimal disruption from the stress concentration at the fillet. The magnitudes of the axial stress components (σ_x and σ_y) in the gage section are nearly equal to each other, and are an order of magnitude higher the shear (τ_{xy})

in the gage section. It is also noted that the magnitude of the Von Vises stress in the gage section of specimen B is considerably higher than the Von Mises stress present in the uniaxial cruciform arms, suggesting that failure in the gage section is possible with this design.

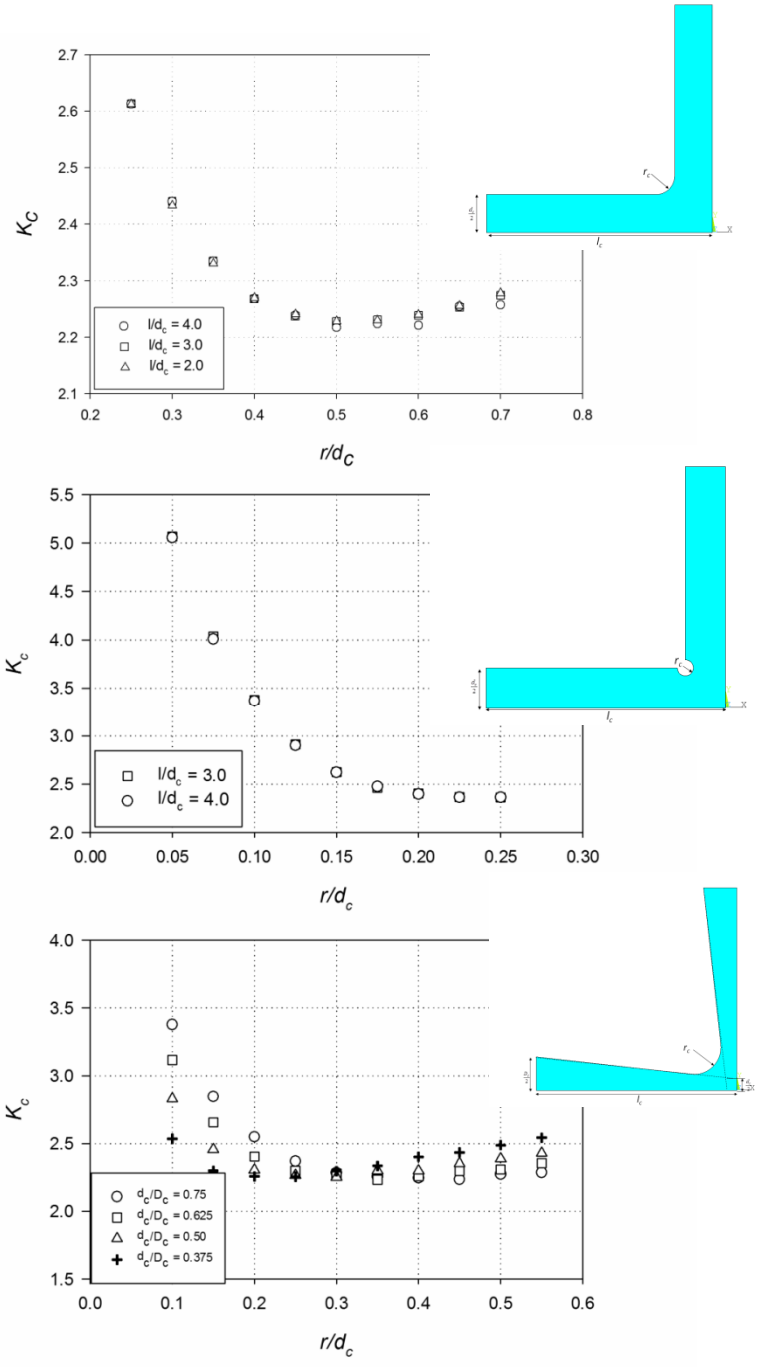

Figure 2.7: SCF curves for the various proposed cruciform specimen geometries under equibiaxial loading.

Given the favorable stress contours shown in Fig. 2.8, along with the repeatability and low cost of specimen fabrication, specimen B represents the optimal geometry for the biaxial testing to be carried out in this thesis.

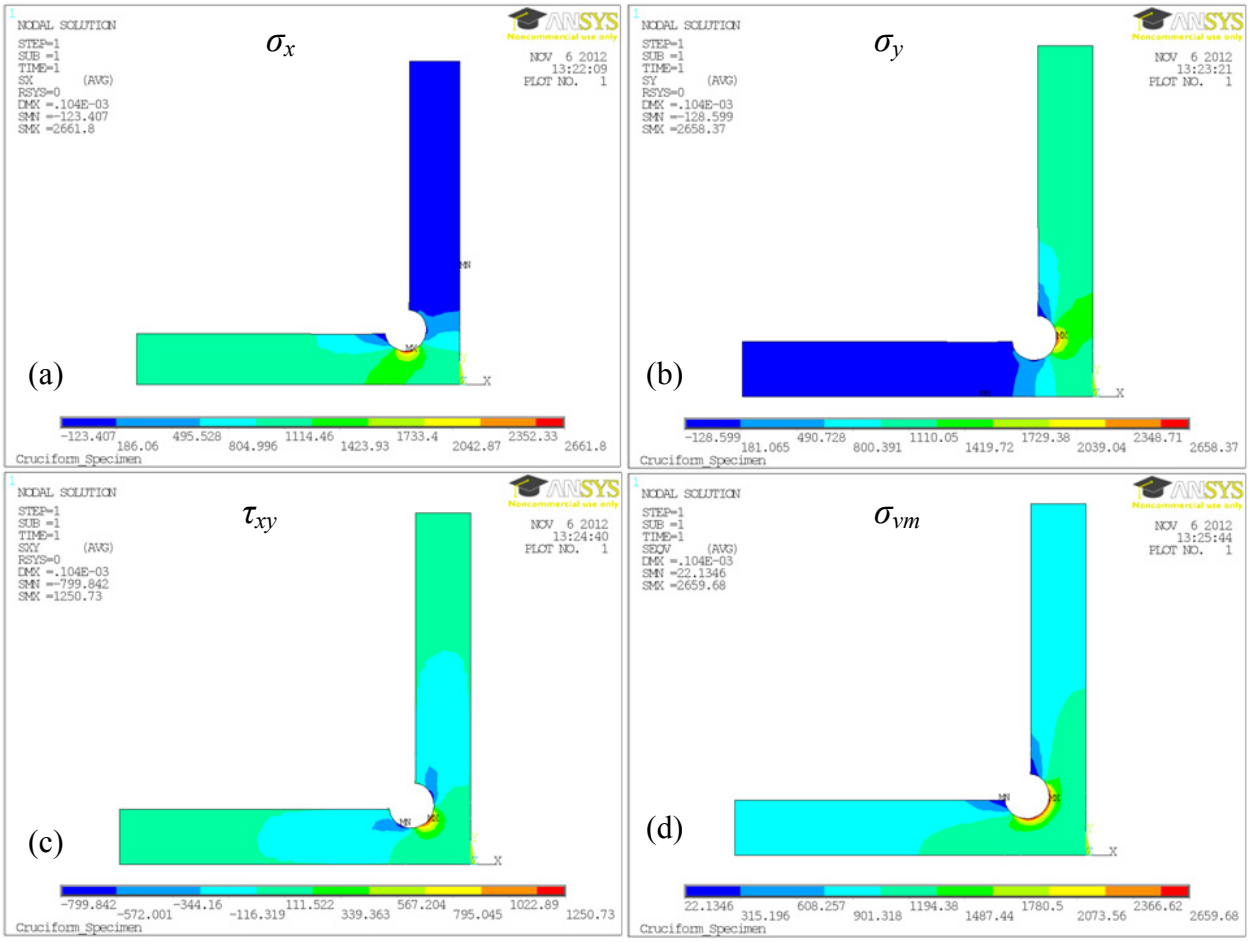

Figure 2.8: Contour plots of the axial stress distribution in the *x*-direction (a), and the *y*-direction (b), the shear stress distribution (c), and the von-mises stress distribution (d) in cruciform specimen B under equibiaxial tension.

Furthermore, Fig. 2.7 can be referenced to choose the optimal specimen geometry ratio for minimal stress concentration in specimen B, which corresponds to a r/d_c ratio of 0.225. Ultimately, the driving dimensions for the cruciform specimen are the length and width of the cruciform specimen arms, which are limited by the available space in the biaxial test frame. The

final geometry of the cruciform specimens employed in the biaxial testing regimen is provided in Fig. 2.9. Note that the notch angle parameter, α, is measured with respect to the weft (90º) material orientation for the biaxial experiments.

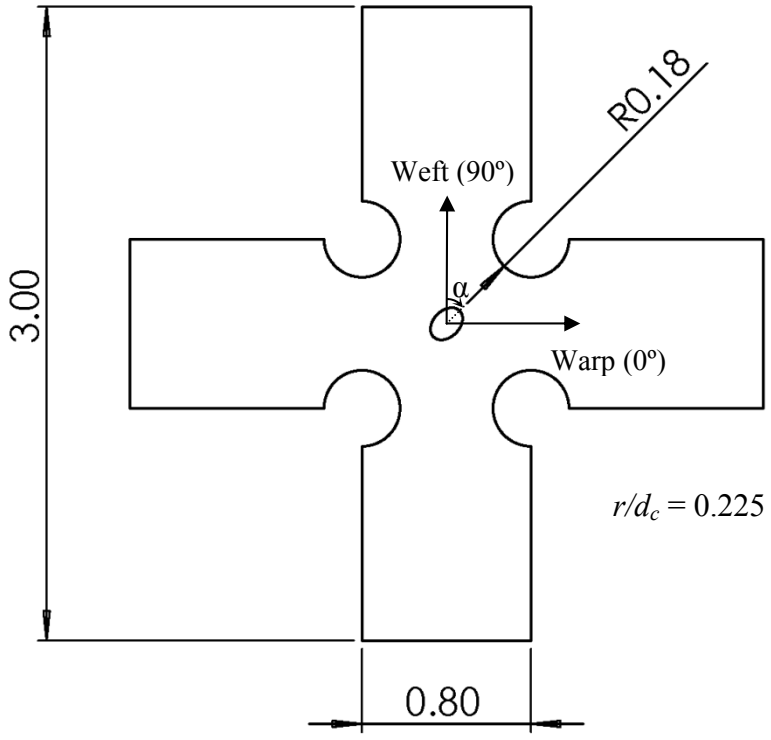

Figure 2.9: Optimized cruciform specimen used to investigate the effects of notches on biaxially loaded 325x2300 SS316L twill dutch woven wire mesh.

2.2.2 Cruciform Specimen Fabrication

The design of the biaxial cruciform specimen selected for this experimental work is conducive to simple and inexpensive specimen fabrication. The specimens are to be incised from 3.00in (7.62cm) square segments of 325x2300 SS316L twill dutch woven wire mesh, with the edges of the square aligned with the principle material orientations. All of the specimens are to receive the four circular fillets shown in Fig. 2.9 by means of a template-assisted milling

process. Once segmented from the main material sheet into carefully aligned squares, the individual specimen sheets are to be stacked and aligned in a fixture made from two 3.00in (7.62cm) square Lexan sheets which have been pre-milled with the fillet holes. The Lexan plates can then be clamped together and a precision end-mill employed to cut all of the circular fillets in a one step process. Once all of the holes have been drilled, the individual specimen sheets can be separated, and the uniaxial cruciform arm sections can be cut using a sharp razor, producing the final specimen shape as shown in Fig. 2.10. Measurements of the critical specimen dimensions show a specimen arm width of $0.80 \pm .01 in$ have been achieved using this fabrication method, which is considered an acceptable degree of variation.

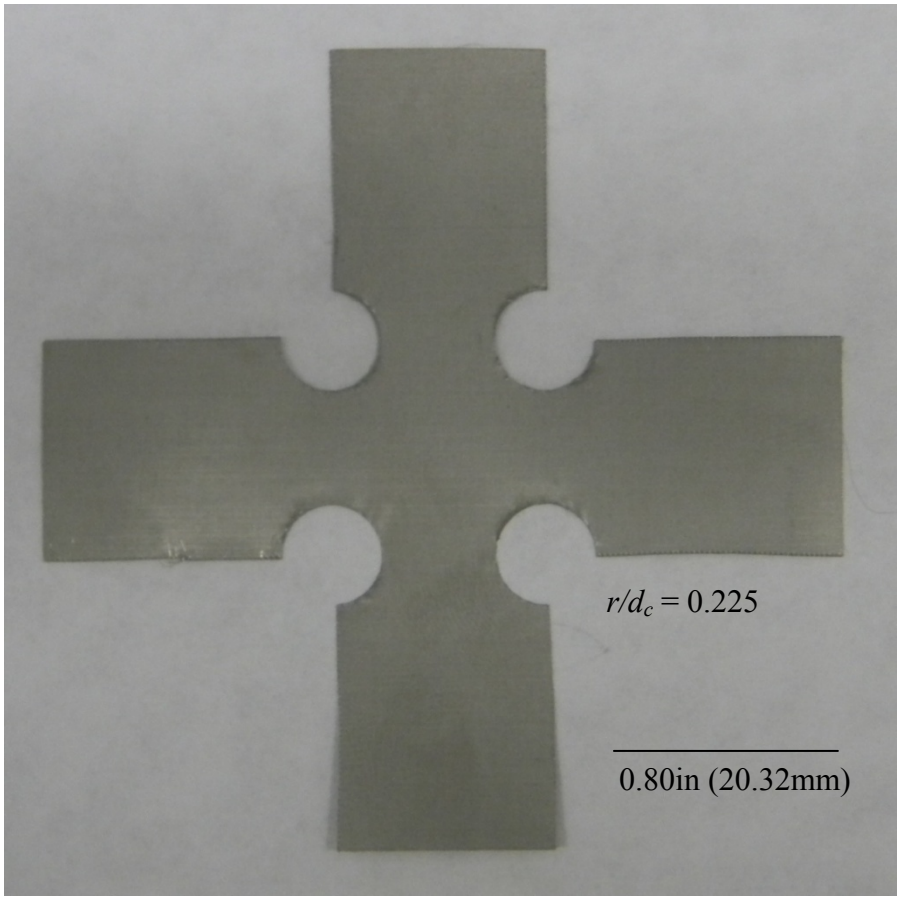

Figure 2.10: Biaxial cruciform specimen incised via the clamping and drilling process.

2.2.3 The Linkage Based Biaxial Load Frame

A linkage based biaxial load frame has been designed and fabricated to facilitate biaxial testing of the 325x2300 SS316L twill dutch woven wire mesh at various stretch ratios. The stretch ratio, γ, outlined in detail by Bhatnagar and others [Bhatnagar et al., 2007], is defined as the ratio of the grip displacements in each orientation. Stretch ratio is useful for linkage based biaxial load frames, which tend to be displacement controlled by design, in lieu of a stress ratio which can only be measured during the experiment. The device has been designed to interface with the aforementioned MTS Insight 5kN load frame, transferring the uniaxial crosshead displacement into biaxial tension or compression (or a combination of the two) through a series of two force members and pin connections. The biaxial loading axes are aligned on the horizontal, and their relative rate of displacement, i.e., the stretch ratio, γ, is controlled via positioning holes in the main load plates and grips, as shown in Fig. 2.11(b). As such, the biaxial axes can be displacement controlled relative to each other and relative to the displacement rate set at the MTS crosshead. The pin joints are outfitted with oil impregnated brass bushings (plane bearings), which allow for inexpensive friction reduction and high load capacity in comparison with instrumentation roller bearings. All of the load bearing components, including the linkage structure, the pin connectors, and the grips, are precision machined from low carbon tool steel (AISI 1020), and have been painted to reduce corrosion. The frame has been designed for testing of thin metallic and composite materials, and the rigidity provided by this material selection and geometry is more than sufficient for accurate testing of the subject material. Non-structural components, such as the LVDT rails and camera mounting fixture (Figs. 11(a) and 11(b)), are precision machined from Al-6061 for ease of machining and reasonable durability. Loads are

measured independently in each axis using two Fluke model LCM300 tension-compression load cells (Fig. 11(c)) with a maximum capacity of 250.0lb. (1112.5N). Grip displacement measurements for each axis are also available via two carefully aligned LVDT's (Omega model number LD621-15), which are positioned onto the guide rails after the specimen has been loaded into the frame, much like a clip gage.

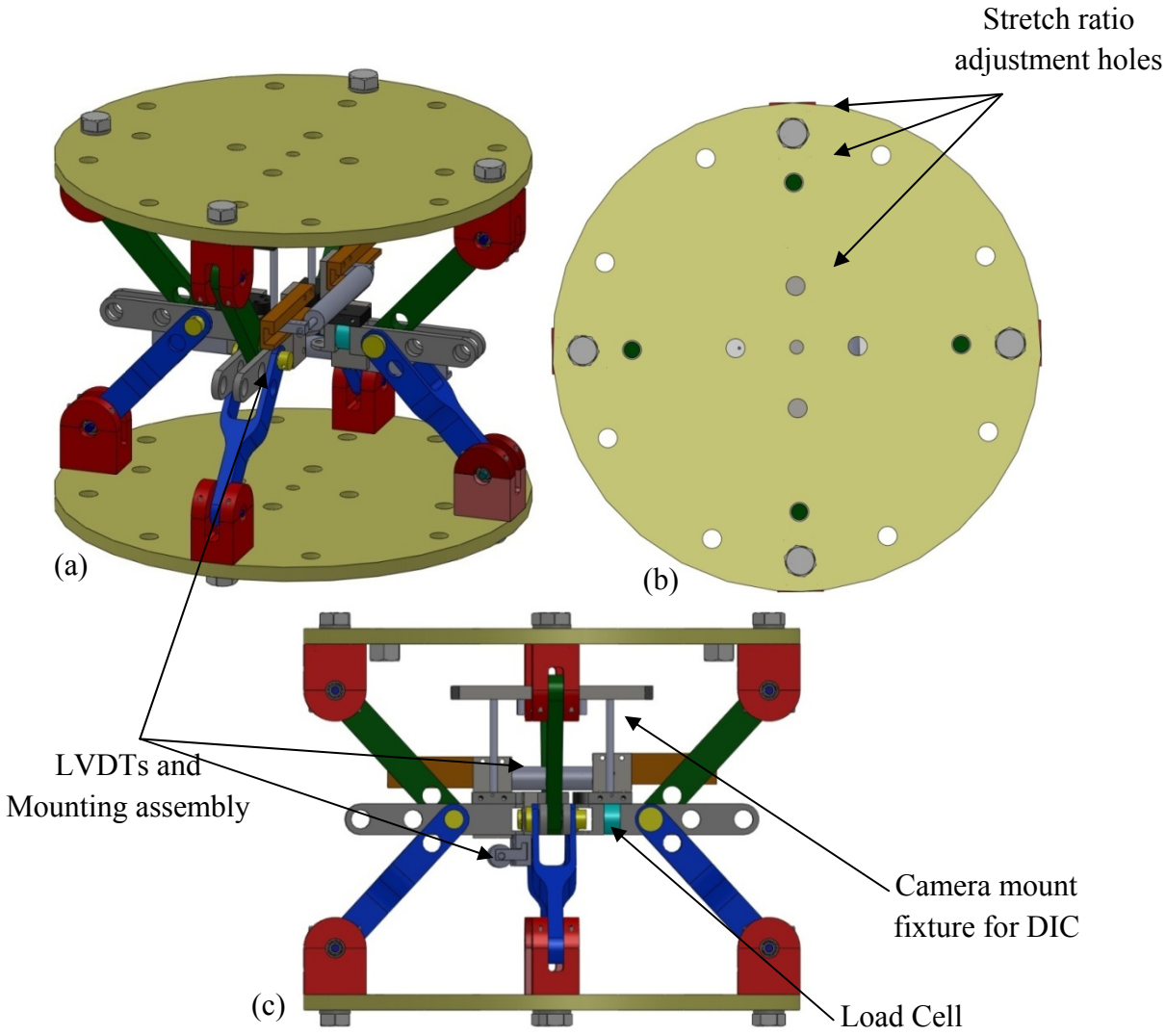

Figure 2.11: Computer rendering of the (a) isometric view, (b) top view, and (c) side view, of the biaxial linkage based load frame used to test the cruciform biaxial specimens of 325X2300 twill dutch woven wire mesh.

The four analog data channels are processed and recorded using a custom designed amplification circuit and a Lego Mindstorm NXT 2.0 control module which digitizes and stores all four channels at a sampling rate of 10Hz. The load cell analog data acquisition circuit design for the linkage based biaxial test frame is illustrated in Fig. 2.12 below. The power for the amplification circuit is provided by two AC-DC converter supplies providing 15VDC with a maximum output of 12W. The supplies are connected to the circuit with their polarity reversed, facilitating the dual supply op-amp design seen in Fig. 2.12. As the load cell selected for the biaxial load frame can output compression loads, i.e., can produce a negative output voltage, it is essential that the data processing circuit (DPC) be designed to facilitate recording by the 0-5VDC NXT logic controller. To accommodate this, the load cell output must not only be amplified, but also shifted such that a maximum negative reading [-250lb_f (-1112.5N)] produces an input of zero volts to the controller. This is solved by designing the DPC with two instrumentation amplifier stages, with the amplification being provided in the first stage by a Texas Instruments (TI) INA125, while a TI INA118 provides the necessary voltage addition and division operations in the second stage. The gain of the INA125 was chosen such that the load cell signal output would have a range of -5VDC to +5VDC. The INA125 instrumentation amplifier was chosen as the stage one amplifier because it provides a precision 5VDC reference, which can be added to the output signal in the INA118, hence providing the 5VDC offset required. All that remains is division of the voltage signal by two, which can be accomplished by again leveraging the INA118 instrumentation amplifier in a series operation. Appendix C provides the individual Op-Amp circuit designs used to for the DPC, which can also be found in several Op-Amp handbooks [Brown and Carter, 2001]. The LVDT signal, which ranges from 0VDC – 10VDC was simply divided in half using a resistive voltage dividing circuit, which is picture in detail in Appendix C.

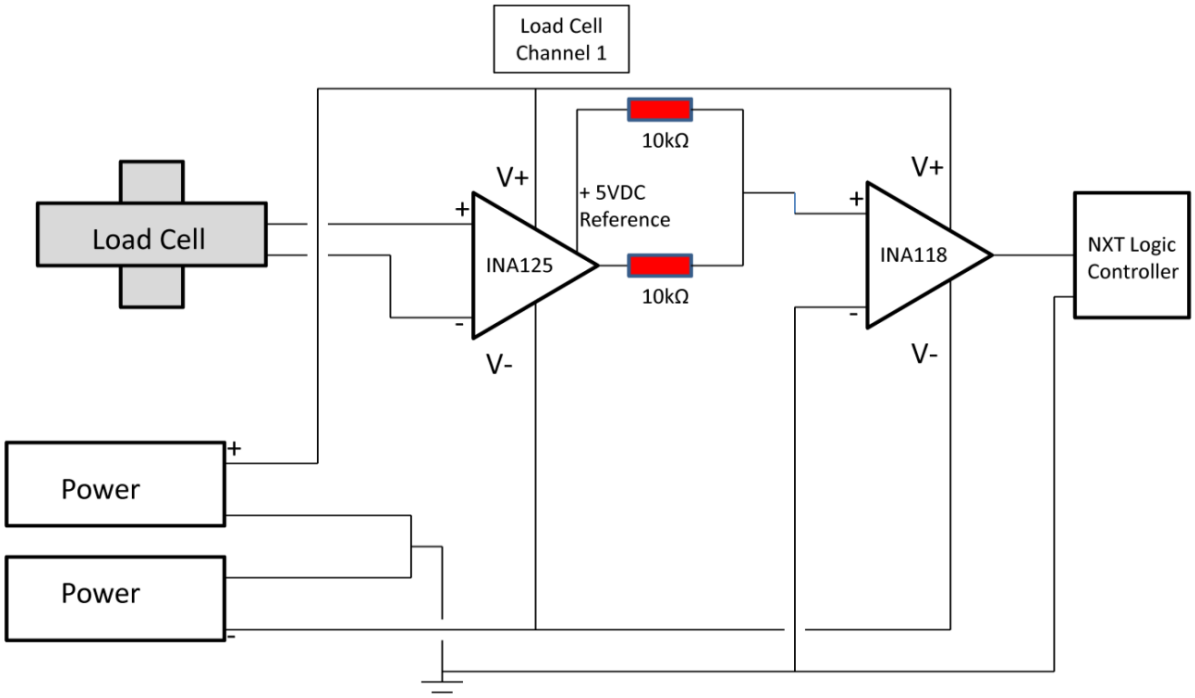

Figure 2.12: Schematic of the Data Processing Circuit (DPC) used to amplify and shift the load cell signal for recording by the NXT logic controller.

The camera mounting fixture, shown in Fig. 2.11(c) and Fig. 2.13 below, has been added to the biaxial load frame to support DIC strain analysis of the cruciform specimens. The need for such a fixture stems from the horizontal alignment of the loading axis of the biaxial frame. It can be shown that the plane of the specimen moves relative to the crosshead of the actuating frame at a rate of 1:2, rendering it impractical to mount a camera onto the main load plates of the biaxial structure for 2D-DIC purposes, as out of plane motion of the specimen relative to the camera would be recorded as strain. A solution is to mount the camera directly to the grips as shown, while providing for lateral movement and alignment with a track and spring system. This design ensures that the camera will always be at a constant distance from the plane of the specimen, and will not move laterally with respect to the gage section.

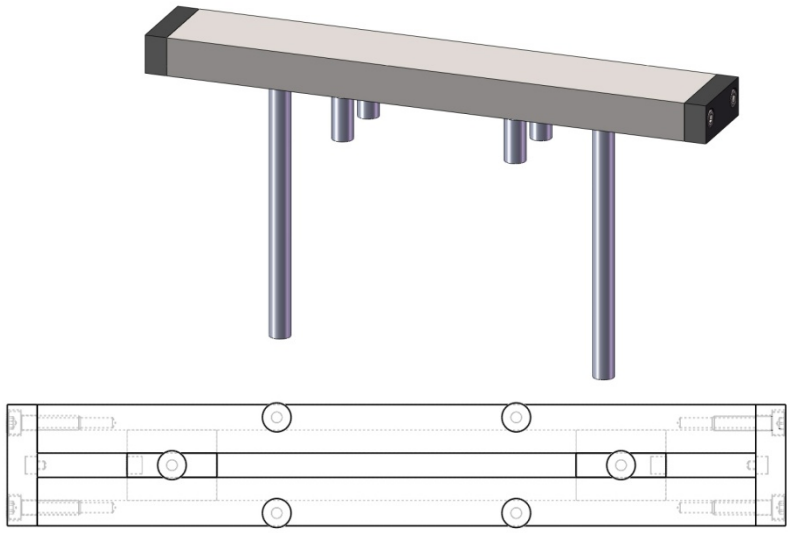

Figure 2.13: Rendering of the camera mounting assembly in the (a) diametric view, and (b) bottom view, for the biaxial load frame to facilitate DIC strain measurements in the plane of the specimen.

As this design requires the placement of a camera in the load path of the actuating frame, it is not ideal to use the expensive CCD camera and telephoto lens setup employed in the uniaxial test sequence. As such, a relatively inexpensive high definition web camera (Logitech 920) is employed to collect the necessary frames. This camera provides reasonable resolution (1.4 megapixels), does not auto focus, and provides output in uncompressed video format. The video data is extracted into individual frames at a known frame rate for correlation using the VLC Media Player software. As the sensor in this camera is color CMOS, the collected frames must be post-processed in a professional image processing software (Adobe Photoshop) for integration of the color information into grey scale pixel data for correlation by VIC-2D. The test frame and the camera are started simultaneously, thus allowing for the first data containing frame to be easily identified from the sequence of recorded images. The video data is then synced with the load cell data by noting the frame collection rate (2Hz) and the data recording rate (10Hz).

Figure 2.14 shows the assembled biaxial load frame and camera assembly, along with a speckle coated cruciform biaxial test specimen.

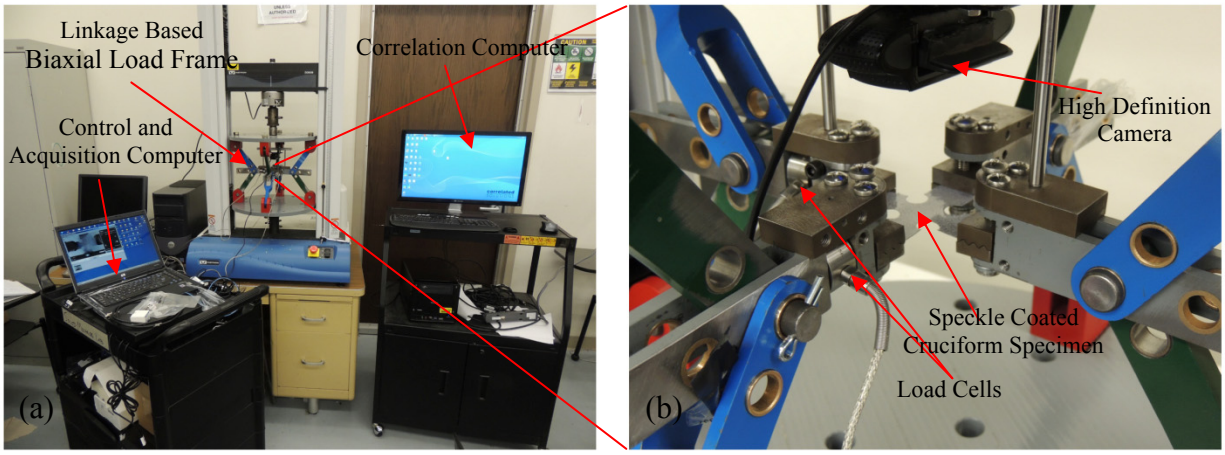

Figure 2.14: (a) The biaxial linkage based load frame installed on a uniaxial test machine, and (b) the DIC camera and grip system used to collect full field strain data from the speckle coated cruciform specimens.

2.2.4 Biaxial Tensile Testing Matrix of Experiments

The biaxial tensile testing matrix incorporates a series of experiments that vary parametrically by biaxial stretch ratio, γ, the notch aspect ratio, λ, and the notch orientation α. Un-notched biaxial tests are also prescribed to facilitate the modification of the Hill Criterion as described in Section 2.0. The notch aspect ratio and notch orientation are as defined for uniaxial tensile testing. Again, it is postulated that increasing notch sharpness will change the failure characteristic of the subject material in a manner that is dependent on both biaxial loading ratio and notch orientation, providing information regarding notch sensitivity, and failure mechanisms. The material orientation with respect to the loading axes, θ, is not varied as a parameter for the biaxial tests, and loading is in the principle material axes in all experiments. The matrix of biaxial experiments performed in this work is provided in Table 2.3. Again, the value $\lambda = 0$ represents a slit or crack type stress concentration, and all slit stress risers are varied

by orientation in intervals of 45º measured with respect to the warp (0º) material orientation. It should be noted that a stretch ratio, γ, of 1.0 does not imply an equibiaxial stress ratio.

Table 2.3: Matrix of Biaxial Tensile Tests on 325x2300 SS316L Woven Wire Mesh

Test Number	Test ID #	λ	Stretch Ratio, γ ($\varepsilon_w/\varepsilon_s$)	Notch Orientation, ϕ (°) *(WRT Warp Axis)*
1	BA-N-1.0	N/A	1.00	N/A
2	BA-N-1.2	N/A	1.20	N/A
3	BA-C-1.0	1.00	1.00	N/A
4	BA-C-1.2	1.00	1.20	N/A
5	BA-S-0-1.0	0	1.00	0
6	BA-S-45-45	0	1.00	45
7	BA-S-90-1.0	0	1.00	90
8	BA-S-0-1.2	0	1.20	0
9	BA-S-45-1.2	0	1.20	45
10	BA-S-90-1.2	0	1.20	90

CHAPTER 3: UNIAXIAL TENSILE EXPERIMENTS

3.1 Material Properties of the Un-Notched Wire Mesh

3.1.1 Uniaxial Tensile Test Results

Uniaxial tensile tests were run on un-notched woven wire mesh specimens with the goal of establishing base line elasto-plastic properties to facilitate modeling efforts and comparison to notched geometries. Experimental specimens were incised as per Fig. 2.1 (a) in the main material orientations, and in off-axis orientations in intervals of 15º. All tests incorporated DIC strain measurements for accurate measurement of axial and transverse specimen strain. This approach produces detailed information on the orientation-dependence of material properties such as yield strength and elastic modulus, allowing for the application of classical mechanical models to the material via regression analysis or other means [Chen et al., 2007; Kraft and Gordon, 2011].

The tensile response of the 325x2300 SS316L woven wire mesh in various material orientations is provided in Fig. 3.1. Several material properties for the as-received woven wire mesh have been established from the experimental data, and these properties are defined in Table 3.1. Note that properties presented here are normalized as in Table 2.1. It is noted that maximum stiffness is observed in the warp (0º) orientation at 6.48kip/in (1134.8kN/m). Maximum yield strength and ultimate strength are observed in the weft (90°) direction at 23.0ksi (158.6MPa) and 27.3ksi (188.2MPa) respectively. The weft (90°) orientation also shows the least elongation to fracture, and the warp (0º) orientation shows very little potential for work hardening. The elastic modulus of the subject material in the various material orientations can be obtained directly from the tensile response shown in Fig. 3.1. The values of E_w (warp) and E_s (weft) are concluded to be 3.09Msi (21.3GPa) and 2.88Msi (19.9GPa), respectively. Clearly, these values are significantly

less than bulk SS316L, which is reported in Table 1.1 as 28.0Msi (193.0GPa). If we define density of the subject material in terms of area, as provided in Table 1.2, the specific modulus is unitless, and takes values of 4.495×10^9 and 4.189×10^9 for the warp (0º) and weft (90º) orientations, respectively. This is compared to a specific modulus value for planar SS316L of 2.769×10^{10}, calculated using the density provided in Table 1.1.

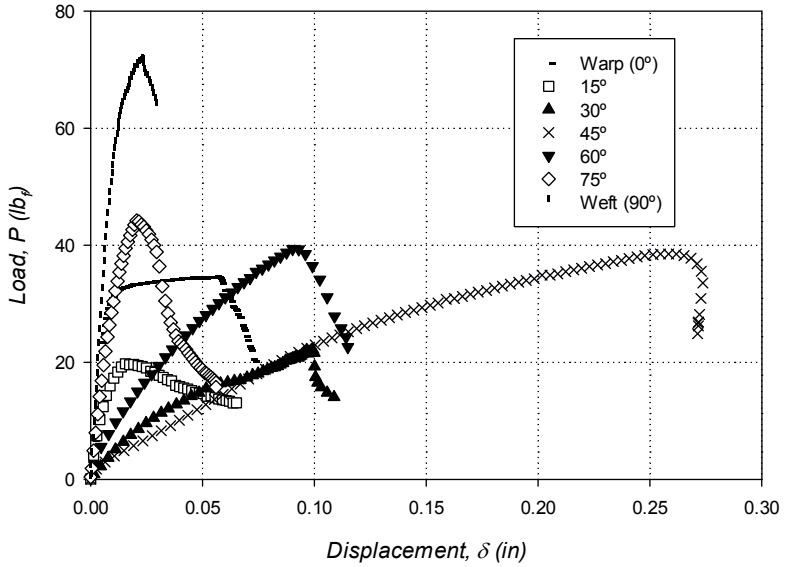

Figure 3.1: Load displacement response of the 325x2300 twill dutch woven wire mesh under uniaxial tension in various material orientations.

Table 3.1: Normalized tensile properties of 316L woven wire mesh at various material orientations

Orientation, θ (°)	Stiffness, K/K_w	Yield Strength, $S_y/S_{y,w}$	Ultimate Tensile Strength, $S_{ut}/S_{ut,w}$	Fracture Strength, $S_f/S_{f,w}$	Elongation, $\varepsilon_f/\varepsilon_{f,w}$
0° (Warp)	1.000	1.000	1.000	1.000	1.000
15°	0.37	0.53	0.59	0.40	0.63
30°	0.07	0.33	0.67	0.44	1.06
45° (Bias)	0.04	0.44	1.16	1.23	2.60
60°	0.18	0.75	1.19	1.27	1.10
75°	0.54	1.22	1.37	1.42	0.53
90° (Weft)	0.92	2.00	2.15	2.3	0.41

To facilitate the DIC measurements, a speckle pattern was placed on the gage section of each specimen via black spray paint as shown in Fig. 3.2(a), with speckle diameter on the order of 0.20mm. The application of the paint coating for DIC strain measurement resulted in only a

minimal increase in specimen thickness, measured at $1.00x10^{-4}$in (2.54microns). It is necessary, however, to insure that the application of paint to the woven mesh specimens does not alter their mechanical stiffness. Figure 3.3 shows comparisons of the mechanical response of the coated and un-coated specimens in both the warp (0º) and weft (90º) orientations. It is noted that similar observations can be made for the bias (45º) oriented specimens.

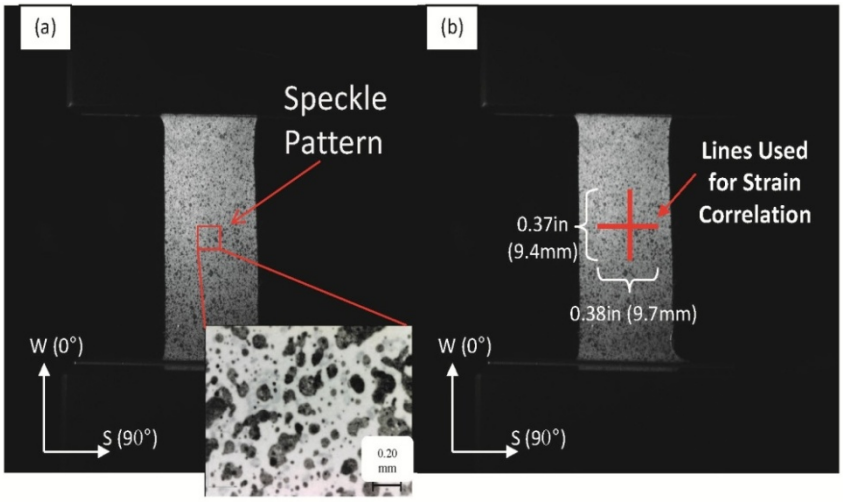

Figure 3.2: Image of the painted speckle pattern used for correlations (b) Illustration of the linear region used to correlate the specimen displacements and calculate the axial and transverse strains.

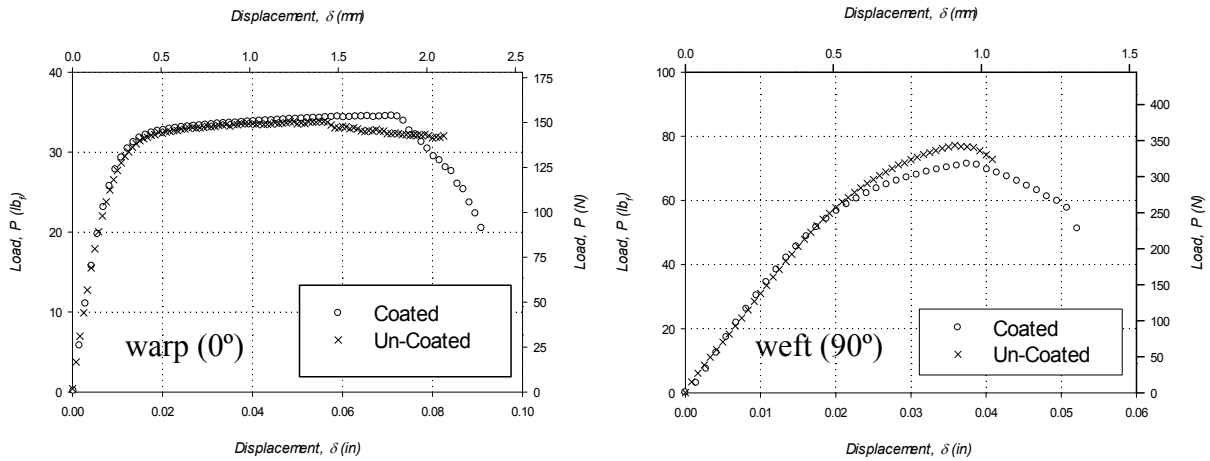

Figure 3.3: Comparison of the tensile response of SS316L 325x2300 twill dutch woven wire mesh in both as received and speckle coated states.

Inspection of Fig. 3.3 reveals that the application of the speckle coating has no significant effect on the elastic response of the woven wire mesh material, and only slightly decreases the ultimate tensile strength in the weft (90º) orientation. The proportional limit and elastic stiffness are unaffected by the paint coating, and thus it is concluded that DIC strain measurements can be performed on this class of materials without significant alteration of their tensile response.

As this material is being treated as a thin orthotropic sheet, it is necessary to analyze the strain developed upon loading in both the warp (0°) and weft (90°) orientations. This information was extracted from the DIC data via line correlation of the displacement, as illustrated in Fig. 3.2(b). The length of the lines used for these correlations are 0.380in (9.7mm) in the transverse direction, and 0.370in (9.4mm) in the axial direction. The results of this analysis are presented in Fig. 3.4, where strain is plotted with respect to the applied crosshead displacement. Analysis of Fig. 3.4 reveals excellent linear strain correlations in both of the axially measured directions, but considerable noise in the transverse strain correlations. It is postulated that this noise is due to the inhomogeneous structure of the material. In homogenous materials, strain energy is transmitted throughout the microstructure by intergranular bonding forces which are relatively strong. These intergranular forces allow for smooth strain distributions throughout the material, and even distribution of load from remote displacements. In the case of woven wire materials, load is transmitted throughout the structure via its wires, and inter-wire forces consist only of relatively weak frictional forces. As such, the transverse strain is theorized to be strongly influenced by Poisson's effect at the wire locations, but only weakly governed by Poisson's effect at intermediate locations between wires. This discretized material response is transmitted through the speckle coating placed on the surface of the wires, resulting in the erratic transverse strain

progression with time. This phenomenon is dealt with in this study through an effective averaging of the transverse strain, accomplished via a linear regression fit through the data.

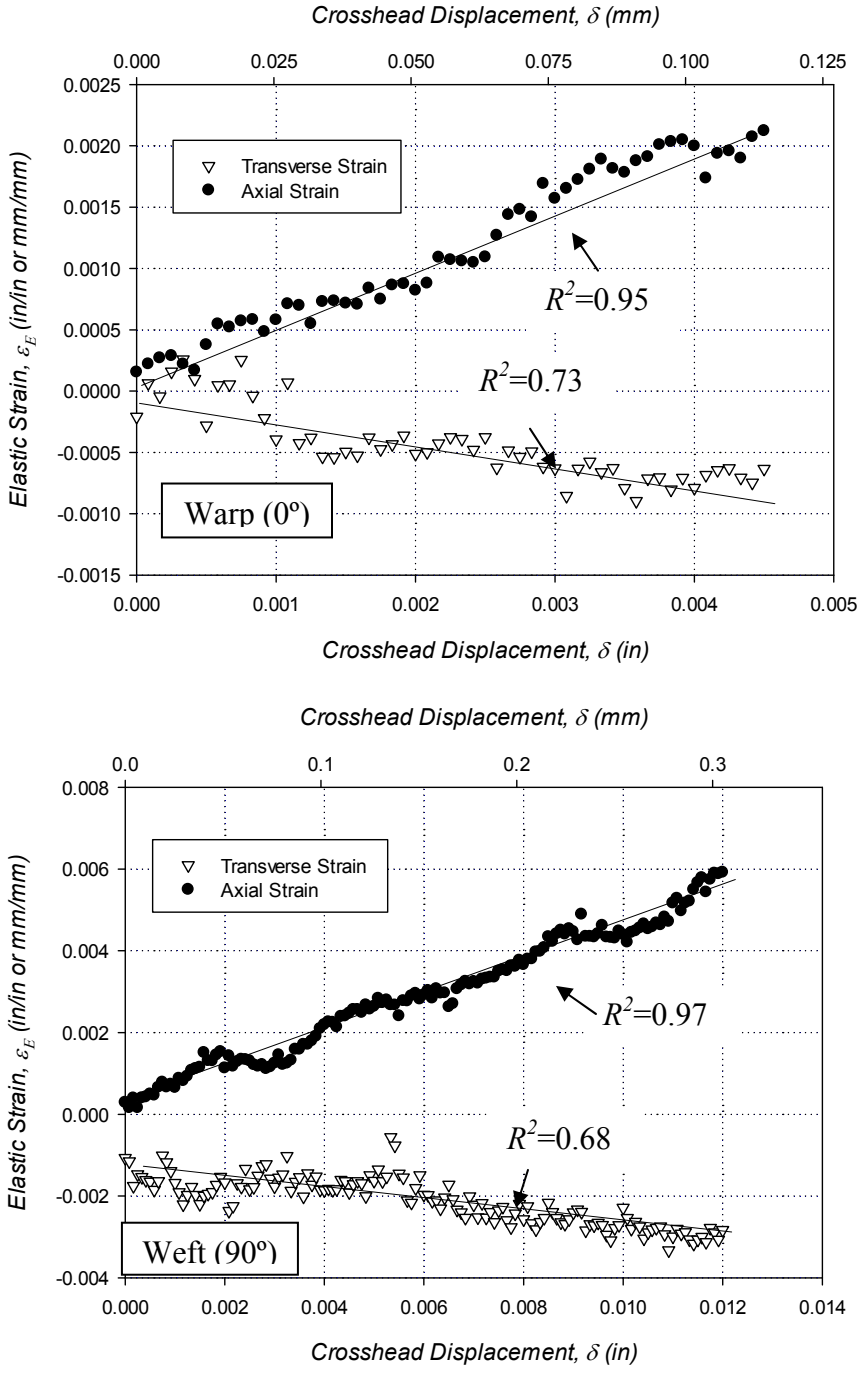

Figure 3.4: Digital Image Correlation measurements of transverse and axial elastic strain in the warp (0º) and weft (90º) material orientations.

Figure 3.4 shows that the linear regression coefficients for the axial strain measurements are nearly 1.0, while the regression coefficients in the transverse directions are reasonable enough to proceed with the classification of Poisson's ratio. Also, it is noted that the weft (90º) orientation transverse strain measurements appear to not pass through the origin as would be expected. This is due to a post-processing procedure necessary to correct for the presence of a non-linear strain region in the early stages of elastic loading caused by wire crimp interchange and relative sliding [Cavallaro et al, 2007]. To account for this, the linear transverse strain values have been shifted to the vertical axis, and the slope of this curve is taken as the value to calculate Poisson's ratio.

The Poisson's ratio of the twill dutch woven wire mesh in the warp (0º) direction, ν_{ws}, is found to be 0.398, while the value in the weft (90º) orientation, ν_{sw}, is 0.312. These values are within the range predicated by Hooke's law, and are consistent with values reported in the literature for woven materials [Hursa et al., 2009]. From these strain measurements, and the associated material stiffness values, the in-plane orthotropic elastic stiffness matrix can be populated. As a means to test the assumption that this material is orthotropic, the symmetry condition of in-plane orthotropic materials must be confirmed within the margin of experimental error. In this case, the experimentally-determined Poisson's ratio and elastic moduli values can be used to show that the symmetry condition is met only to within 18.0%, which draws into question the assumption of orthotropic behavior for this material. It is clear that further experiments are required to confirm the structural symmetry of this material, and to justify the use of an orthotropic constitutive assumption to model the SS316L woven wire mesh on a macro-scale. The dependence of the fifth elastic constant for the in-plane orthotropic constitutive model employed in this work can be established via Eq. (3.1.1)

$$\frac{\nu_{ws}}{E_w} = \frac{\nu_{sw}}{E_s} \tag{3.1.1}$$

In an effort to investigate the orthotropy of the subject material, two verification DIC experiments were conducted. These experiments were carried out on uniaxial specimens incised at 45º, and at the supplementary angle, 135º, to the specifications outlined in Fig. 2.1(a). It is assumed that any mechanical asymmetry present in the SS316L woven wire mesh will be clearly distinguishable through a comparison of the stiffness and elasto-plastic hardening response of these two orientations. The DIC results from the two bias experiments have been leveraged to construct the load-displacement response of the subject material in the 45º and 135º degree orientations. Figure 3.5 shows these results graphically. Emphasis should be placed on the similarity of the stiffness and the elasto-plastic response of the two orientations, suggesting that the material is in fact symmetric in-plane. This ultimately leads to the conclusion that the 325x2300 twill dutch woven wire mesh is mechanically symmetric, and thus by definition is orthotropic in-plane. The lack of dependence of the fifth in-plane orthotropic elastic constant is then deemed to be a result of error stemming from the assumption of continuity inherent to Hooke's law in general.

In addition to the tensile response obtained from DIC testing, further correlations were carried out to measure the axial and transverse strains in the 45º material orientation. It is noted that all experimental conditions and correlation procedures used for the 45º case are identical to those used for the principle material orientations. Figure 3.6 shows the elastic strain measurements in the 45º-oriented 325x2300 twill dutch woven wire mesh as they evolved with respect to crosshead displacement. Analysis of Fig. 3.6 reveals that the measured transverse strain is nearly equal to the axial strain, resulting in a Poisson's ratio of 1.09 for the 45º

orientation. While this value appears high, it is not unreasonable based on modeled and experimental data for woven fabrics available in literature [Sun et al., 2004; Boubaker et al., 2010], with Poisson's ratio values being observed well above 0.50.

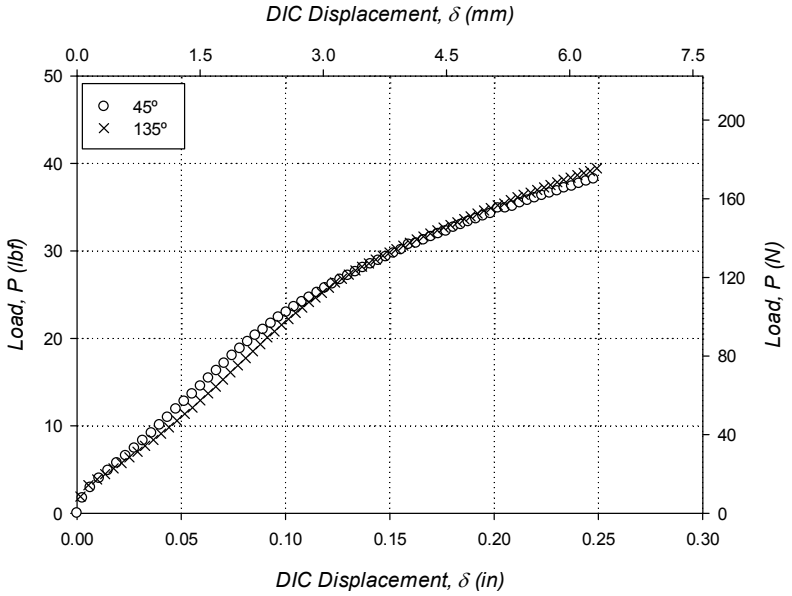

Figure 3.5: The tensile response of 325x2300 twill dutch woven wire mesh in the supplementary bias orientations.

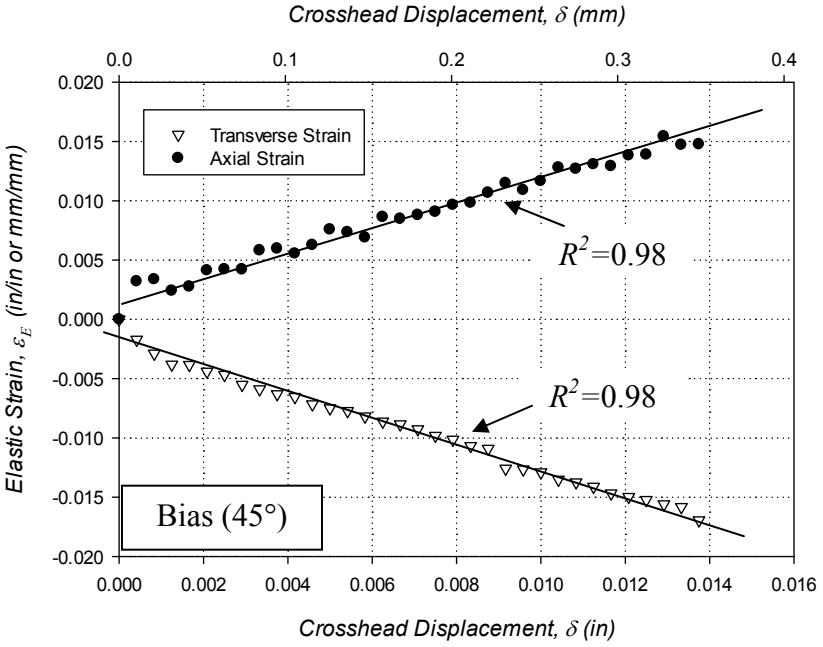

Figure 3.6:Digital Image Correlation measurements of the transverse and axial elastic strain in the bias (45º) material orientation.

Strain measurement using the optical extensometery technique employed in this section is of great value to elastic property determination for the 316L twill dutch woven wire mesh; however, the accuracy of the reported results is dependent on the uniformity of the strain distribution in the gage area. To investigate the uniformity of the strain fields in the gage section, the full-field features of DIC can be leveraged to plot the strain distributions. Figures 3.7 and 3.8 show the DIC measured strain fields in the *x* and *y* camera axes (not to be confused with the material axes), respectively, for all experimentally treated material orientations. Note that the strain distributions in both the *x* and *y* camera axes are relatively uniform, particularly in the areas of interest outlined in Fig. 3.2(b). The anisotropy of the material becomes clear upon inspection of both Fig. 3.7 and Fig. 3.8, where clearly defined strain contours develop along the main load bearing material axis. The material clearly exhibits a Poisson's effect, with areas of maximum negative transverse strain coinciding with areas of maximum axial strain. It is noted that the principal material orientations, warp (0º) and weft (90º), display more variability in strain distribution than the other orientations, but this is attributed to the fact that all of the wires are active in these material orientations, i.e., the gradient across the specimen width is not as severe. As such, the intricacies of the meso-scale material behavior dominant the variance in the DIC measurements, and the result is an image that appears non-uniform when scaled over the full range (as is the case in all images). The effects of load-bearing wire cut-off are made clear in Fig. 3.8, where the 30º and 60º DIC *y-camera* axis strain contours show narrow bands of loaded material, corresponding to the section of wires in the specimen running the full gage length. Overall, the conclusion drawn from Fig. 3.7 and 3.8 is that proceeding with strain measurements averaged over the region outlined in Fig. 3.2(b) is reasonable for the purpose of elastic constant calibration.

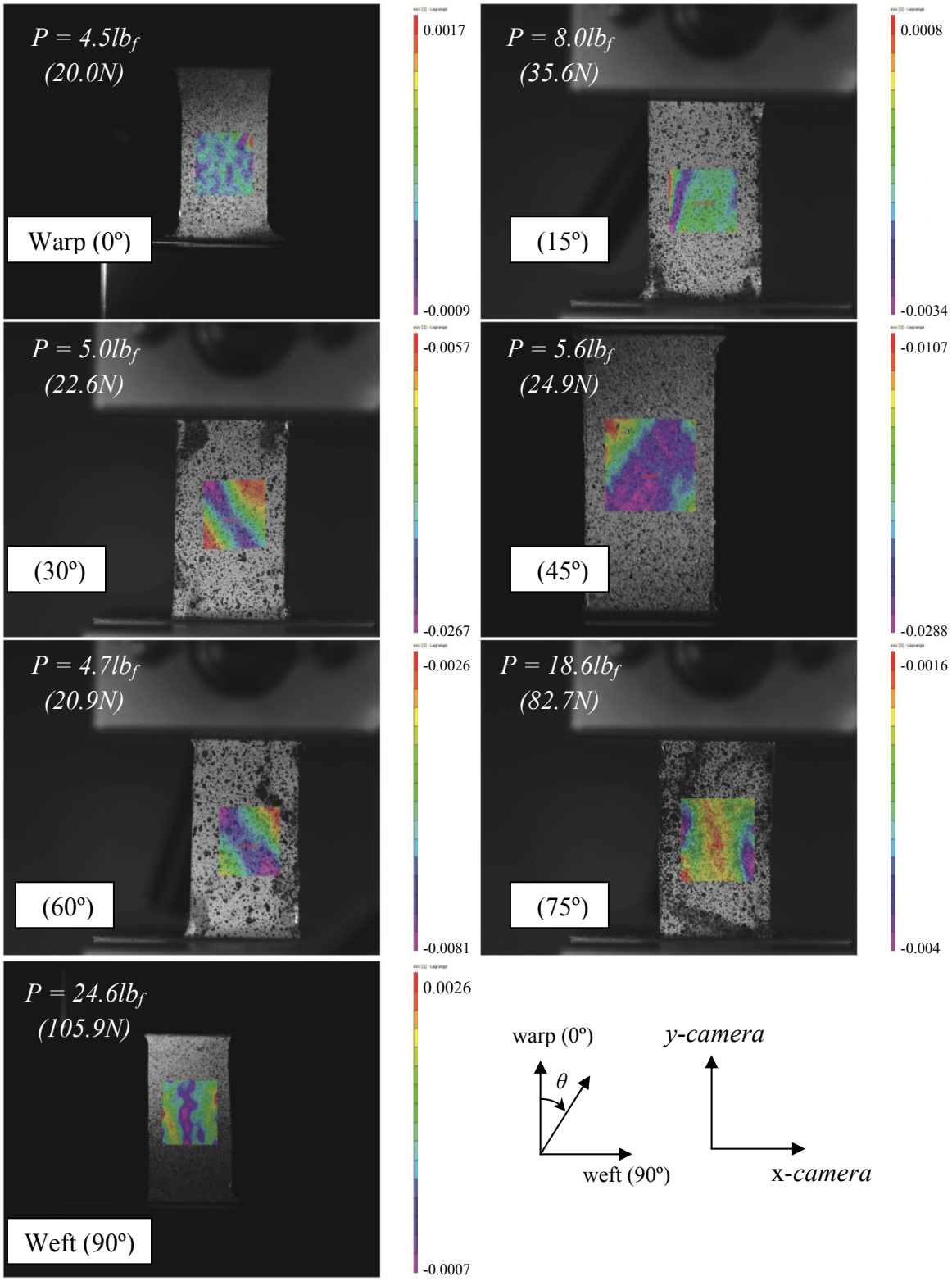

Figure 3.7: Strain contours in the *x-camera* axis from testing on the woven wire mesh in various material orientations.

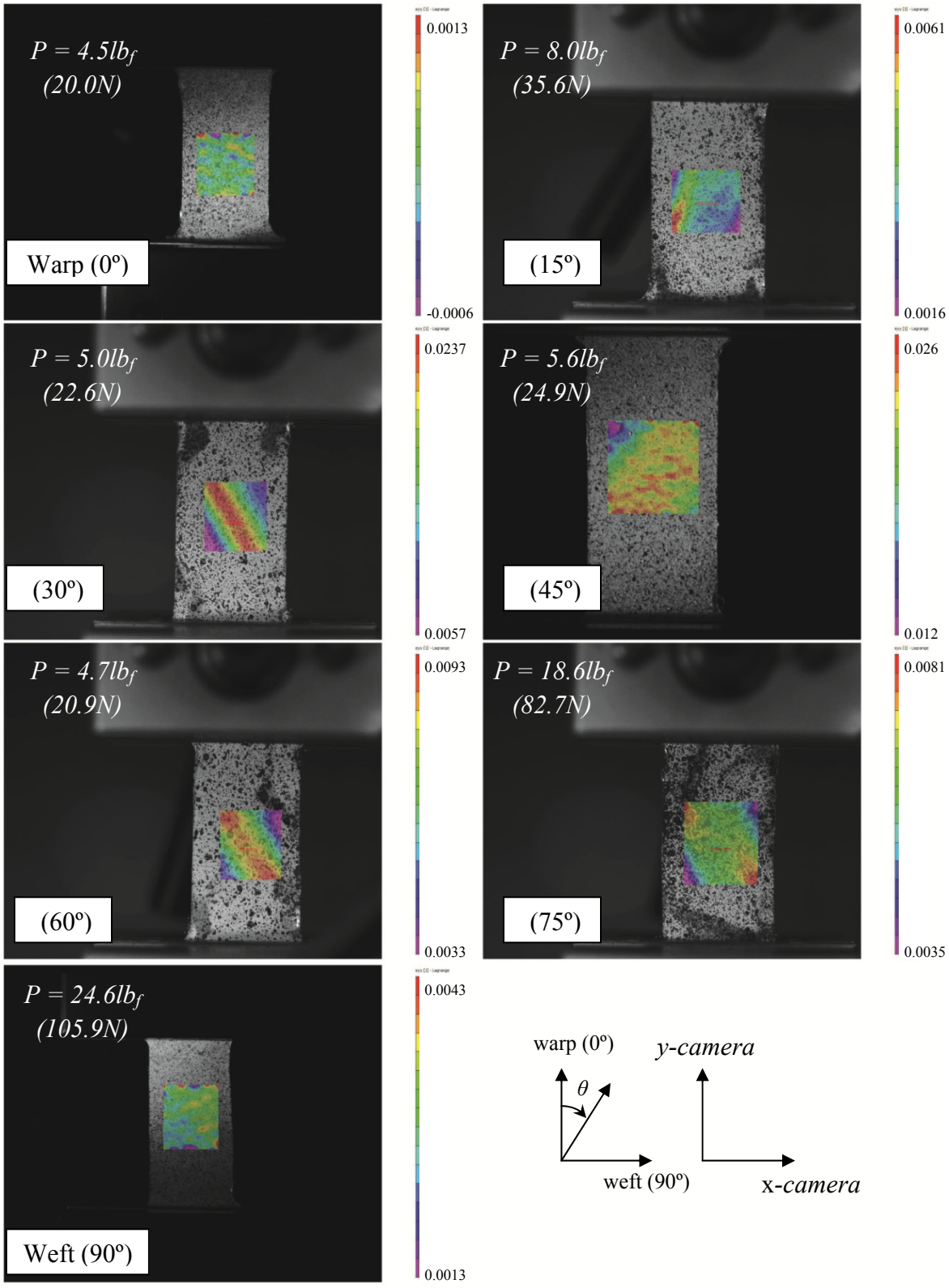

Figure 3.8: Strain contours in the *y-camera* axis from testing on the woven wire mesh in various material orientations.

3.1.2 Analytical Modeling Using the In-Plane Orthotropic Assumption

As there is currently no standard governing the use of DIC methods to characterize the mechanical properties of micronic metallic woven structures, particularly via off-axis uniaxial tensile tests, it is necessary to build confidence in the experimental results through either analytical or numerical modeling. In order to give credence to the experimental results, and to further strengthen the assumption of orthotropy, an effort has been made to model the elastic properties with respect to material orientation. Such modeling can be facilitated analytically by considering a transformation through θ of the compliance matrix of a generally orthotropic lamina under conditions of uniaxial stress [Gibson, 2007], i.e.,

$$E_\theta = \left[\frac{1}{E_w}\cos^4\theta + \left(\frac{1}{G_{ws}} - \frac{2\nu_{ws}}{E_w} \right)\sin^2\theta\cos^2\theta + \frac{1}{E_s}\sin^4\theta \right]^{-1} \tag{3.1.2}$$

$$\nu_{w's'} = E_\theta \left[\frac{\nu_{ws}}{E_w}\left(\sin^4\theta + \cos^4\theta\right) - \left(\frac{1}{E_w} + \frac{1}{E_s} - \frac{1}{G_{ws}} \right)\sin^2\theta\cos^2\theta \right] \tag{3.1.3}$$

Here, the subscripts w and s refer to the warp (0º) and weft (90º) principle material orientations, respectively, and the subscript θ is in reference to the loading direction relative to the warp (0º) axis. It is noted that similar equations exist for the other two independent elastic properties; the shear modulus and the transverse elastic modulus. It is clear from inspection of Eq. (3.1.2) that the bias (θ = 45º) elastic modulus, obtained from Table 3.1 as 122.9ksi (847.37MPa), along with the already determined elastic properties from the principle material axes, can be used to solve for the shear modulus, G_{ws}, of the woven wire mesh. Manipulation of Eq. (3.1.2), and substitution of the necessary material property values, results in a value for G_{ws} of 31.12ksi

(214.56MPa). Furthermore, the value for G_{ws} can be used in conjunction with the other determined elastic properties in Eq. (3.1.3) to model the off-axis Poisson's ratio of this material. Inspection of Fig 3.9 reveals that the model predicts a value of 0.975 for Poisson's ratio in the 45º orientation, which represents a percent difference of 11.4% from the experimentally measured value of 1.09. Table 3.2 provides the experimentally determined elastic modulus and Poisson's ratio values for the SS316L woven wire mesh material, along with the shear modulus derived from Eq. (3.1.2). It is noted that the principal shear modulus is approximately 1.0% of the principal tensile moduli, considerably lower than the ratio in bulk SS316L of 39.0%.

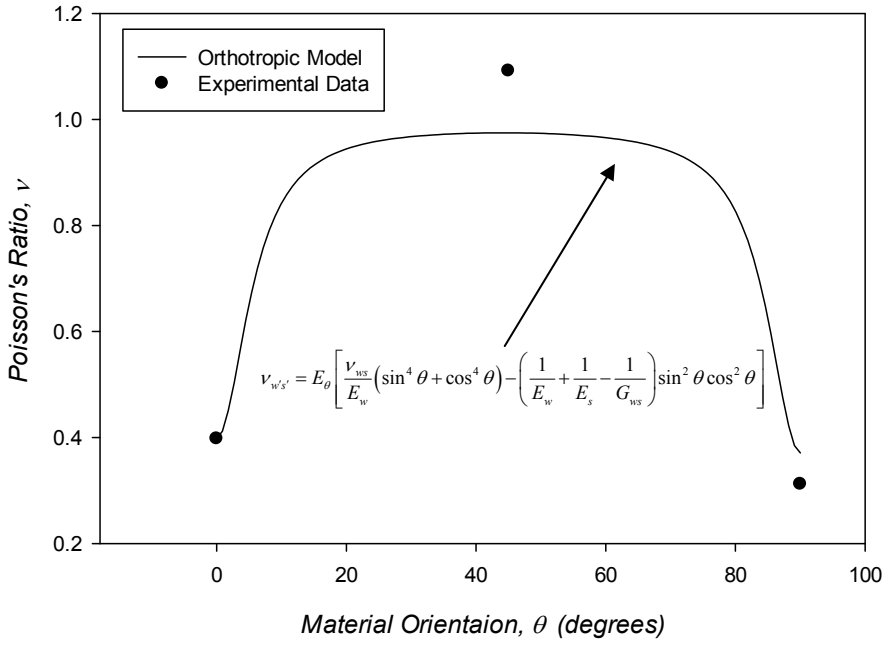

Figure 3.9: Model of the orientation dependence of the Poisons Ratio of the subject material in conjunction with the experimental results

Table 3.2: In-plane orthotropic elastic constants for SS316L 325x2300 woven wire mesh

Material Orientation, θ (°)	Elastic Modulus, E	Poisson's Ratio, ν	Shear Modulus, G
Warp (0°)	3.09Msi (21.3GPa)	0.398 (ν_{ws})	0.031Msi (0.214GPa)
Weft (90°)	2.88Msi (19.9GPa)	0.312 (ν_{sw})	0.031Msi (0.214GPa)
Bias (45º)	0.123Msi (0.848GPa)	1.09 ($\nu_{w's'}$)	1.08Msi (7.44GPa)

It is also of interest to utilize Eq. (3.1.2), referred to hereafter as the Elastic Modulus Orientation Function (EMOF), to model the off-axis elastic moduli of the woven wire mesh material. Figure 3.10 shows the variation in the elastic modulus with material orientation, along with the EMOF calibrated with the constants from Table 3.2. Note that the elastic moduli values reported in Fig. 3.10 are normalized by the value in the warp (0º) material orientation, E_w, 3.09Msi (21.3GPa). Investigation of Figure 3.10 reveals that the EMOF fits the off-axis elastic modulus data well, with an R^2 value of 0.95. Thus, it is concluded that the experimental and modeling efforts employed in this study have produced good results, and that use of a plane orthotropic constitutive model is within reason.

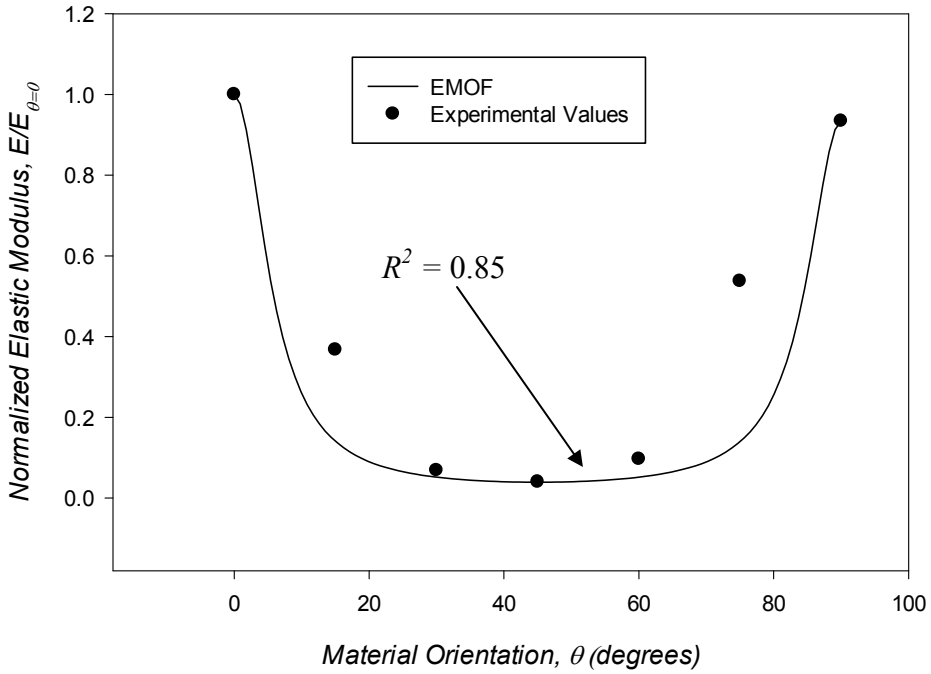

Figure 3.10: The elastic modulus of the 325x2300 twill dutch woven wire mesh as a function of material orientation, along with the EMOF calibrated from DIC experimental results

3.1.3 Yield Behavior of SS316L Twill Dutch Woven Wire Mesh: The Hill Criterion

It has been previously stated that this research has resulted in the optimized Hill criterion parameters [Eq. (2.1.1)] for the subject material in previous work from analysis of tensile test data in various material orientations [Kraft and Gordon, 2011]. It is necessary to present this work here, as the Hill criterion is used as a means to determine elasticity at the notch root point of interest, which is essential for valid SCF determination from experimental results presented in the subsequent sections. The Hill failure criterion is widely used for anisotropic (orthotropic, cubic, etc.) solids. The model is based on Distortion Energy Theory, and can be shown to simplify to the Von Mises criterion in the special case of isotropy. The criterion relates the directional yield strength of the material to the principal directions through the use of several curve-fitting parameters, resulting in a second order polynomial as shown in Eq. (2.1.1). The necessary constants may be ascertained either from Eq. (2.1.2), or from a regression analysis with the yield strengths of the material in the principle material orientations, and at several intermediate orientations.

The dependence of the normalized yield strength of the 316L SS woven wire mesh on material orientation, with σ_o equals 22.8ksi (157.2MPa), is presented graphically in Fig. 3.11, along with the Hill Analogy model calibrated with the constants presented in Table 3.3. Note that the values of the Hill constants presented in Table 3.3 are calibrated to normalized data, and so they are unitless. The Hill criterion proves serviceable for the prediction of the yield stress dependence on material orientation for the subject material, particularly at the principle and bias (45º) material orientation considered in SCF analysis. Thus, the Hill criterion may be used to determine the status of stress, either elastic or plastic, at the notch root to facilitate accurate

modeling of the SCF, which is by definition an elastic parameter. It should be noted that the Hill analogy, in the form presented in Eq. (2.1.1), does not account for the shear coupling exhibited by the subject material. It is postulated that improved fit to the orientation-dependence of the yield strength of this material can be achieved by modifying Eq. (2.1.1) to include interaction between the shear and normal stresses., and this is explored in detail in the subsequent chapter. Nevertheless, Fig. 3.11 shows the Hill Criterion provides very good fit at the material orientations considered in this work, and so can be used to establish the elasticity at the notch.

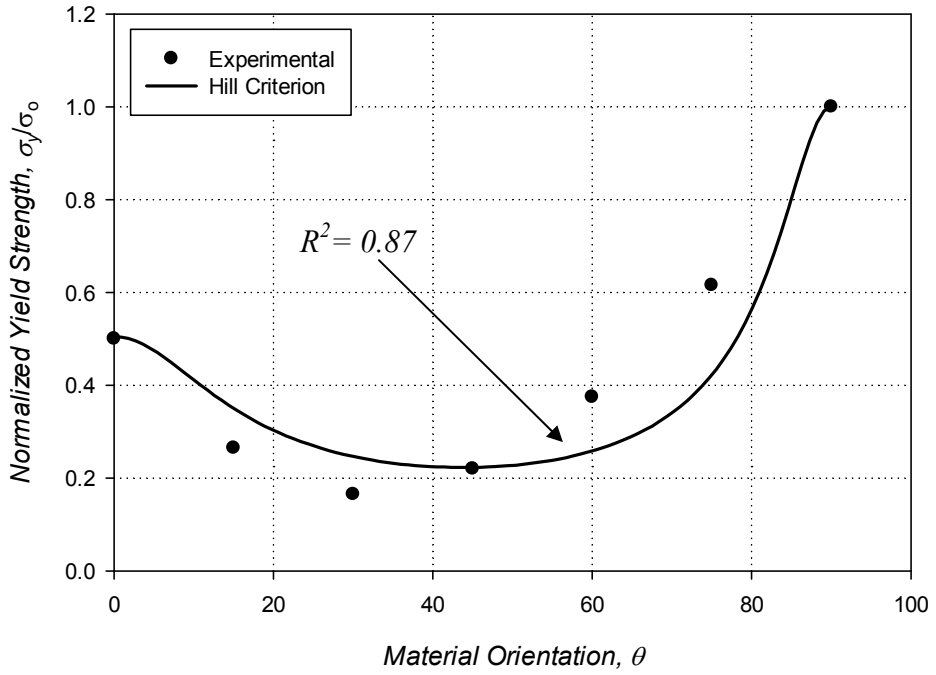

Figure 3.11: Orientation dependence of the yield strength of 325x2300 SS316L woven wire mesh.

Table 3.3: Plane stress Hill parameter values calibrated to the normalized experimental yield strength of the subject material.

Hill Parameter	F	G	H	N
Normalized Value	0.25	3.17	0.75	38.5

3.2 The Notched Mechanical Behavior under Uniaxial Tension

The effect of stress risers on the uniaxial mechanical behavior of the 325x2300 micronic wire mesh material has been investigated via a tension test sequence as outlined in Section 2.1. The goal of this testing is to develop both elastic stress concentration factors (SCFs) for the various specimen geometries investigated, and to investigate notch affects on material failure behavior as a function of orientation and notch aspect ratio. Failure mechanisms are inferred using a combination of strain field analysis from DIC measurements, and post-mortem fractography. Ultimately, the results presented in this section include various SCF curves based on material orientation and specimen geometry, a comprehensive analysis of rupture behavior via post-mortem fractography, comparisons to well established analytic solutions based on continuum theory, and a subsequent discussion and analysis regarding the sensitivity of the ultimate strength of the subject material to the presence of a stress riser.

3.2.1 Experimental SCF Curves for Circular Notched Strip Specimen under Uniaxial Tension

Experimental investigation of the effect of stress concentration on the mechanical responses of the subject material under uniaxial tension has been undertaken using the center notched uniaxial strip specimen shown in Fig. 2.1(b). In an effort to gauge the relevance of the solutions proposed by Lekhnitskii [Lekhnitskii, 1968] and others for the stress fields in notched orthotropic plates, the notches in this work have been formed as ellipses of varying aspect ratio, λ, ranging from a value of 1.0, i.e., a circle, to a value approaching zero, i.e., a slit or crack. A review of the test matrix given as Table 2.2 shows that the material orientation, θ, and the notch orientation, α, are varied from 0º through 90º in 45º intervals. The DIC analysis software utilized in this work (Vic-2D) is capable of providing the directional full-filed strain distribution at every

point in the gage section of the specimen. Strain distribution results are not immediately useful in determining the Stress Concentration Factor (SCF) of the specimen geometry, and so a constitutive model is required to relate the measured strains to the local stress levels. The use of the in-plane orthotropic stiffness matrix, i.e., the inverse of the compliance matrix presented in Eq. (1.2.2), along with the material properties given in Table 3.2, is proposed as an acceptable solutions to this problem given the relative continuity of the strain distribution on the macro-material scale for the subject material, and the agreement of the of the orthotropic models, i.e., Eqs. (3.1.2) and (3.1.3), with the experimental results presented in Section 3.1.

Uniaxial tensile testing proceeded initially with circular notched specimens, employing a test setup as described in Section 2.1. Clear variations in the regions of maximum and minimum elastic strain are observed as the material orientation is varied from warp (0º) to weft (90º), as shown in Fig. 3.12 below, which shows the strain in the *y-camera* direction.

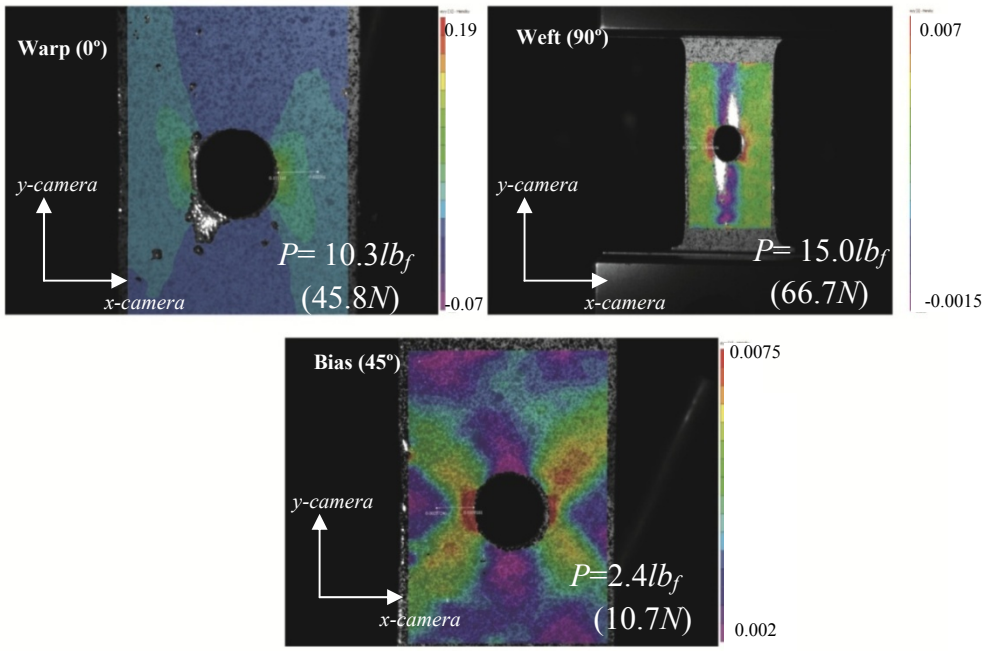

Figure 3.12: Elastic strain contours in the *y-camera* axis for SS136L micronic wire mesh with a central circular notch.

The circular notch diameter is 0.25in (6.35mm), and all notches are central to the specimen. Inspection of the *y-camera* elastic strain contours presented in Fig. 3.12 reveals that the macro scale strain distribution is greatly affected by the circular notch in all material orientations, and the direction of the propagation of the disturbance in the strain field from the notch is dependent in the material orientation. The appearance of the maximum strains in the bias (45º) oriented specimen occurring along the principle material directions, i.e., inclined at 45º, is consistent with the elasticity solutions presented by Lekhnitskii [Lekhnitskii, 1968], which predict the location of the maximum stress to be dependent on material orientation in directional materials. In the principle material orientations (warp (0º) and weft (90º)), the circular notches are flanked by regions of high tensile strains, adjacent to regions of compression on the loading axis of the specimen. The bias (45º) oriented specimen shows no compressive zones, but does have regions at the top and bottom of the notch surface with near zero strains in the *y-camera* axis.

Development of experimental SCFs for the circular notches incised into the principally-oriented subject material requires the quantification of the strain contours. This is facilitated by extracting the data along a horizontal line extending from one side of the notch to the edge of the specimen in the positive *x-camera* direction. Elastic strain data in the *y-camera*, and *x-camera* directions, as well as the respective tensorial shear strain, was extracted in this manner for all three experimentally treated material orientations, and this data is presented in Fig. 3.13. It must be noted that strain correlations near the edge of the circular notch in the warp (0º) and weft (90º) material orientations fail to converge due the high strain gradients in the region. This is made clear by inspection of Fig. 3.12, where the strain contours are undefined near the notch edge. Clearly, this has implications on the ability of the method to produce accurate SCF values at the notch edge, and this is dealt with subsequently. It is interesting to note that the shear strain, ε_{xy}, is

near zero at the notch in all of the material orientations, and that the axial strain, ε_{xx} and ε_{yy}, are symmetric in the 45º orientation about the transverse camera axis. This provides further support for the assumption of material orthotropy, i.e., the stiffness is equal in the $\pm 45^{\circ}$ material orientations. The strain distribution in the warp (0º) material orientation displays the unusual quality of positive transverse strain along the *y-camera = 0* axis. While the magnitude of the strain in the *x-camera* axis with respect to the other components is reasonable considering the sharp increase in *y-camera* direction strain expected in the failed convergence zone, the cause for a negative Poisson's effect is unclear. It is noted that this is not observed in smooth specimens, and that the transverse strain becomes negative, as expected, at higher load levels. Given these observations, it is postulated that this is a result of the inhomogeneity inherent to his structure, and the inability of the material to transfer strain information from the notch edge to the surrounding region at low gross stress levels. It is theorized that as the material is loaded, and the notched region elongates into an ellipse, the region near the free edge of the specimen is under considerably less deformation as a result of the low MSGC of the woven structure, i.e., the structure cannot efficiently transfer strain energy to neighboring wires due to the limited shear stiffness of the subject material. This behavior, dominated by frictional wire sliding and crimp interchange, results in the apparent expansion of the material as the mesh searches for an equilibrium configuration. Eventually, as the load increases and the energy reaches some critical value, the mesh locks and frictional sliding is replaced by direct mesh contact, resulting in transverse contraction of the material. The necessary condition of elasticity precludes data collection at higher load levels, and so it is elected to report results taken at lower load levels.

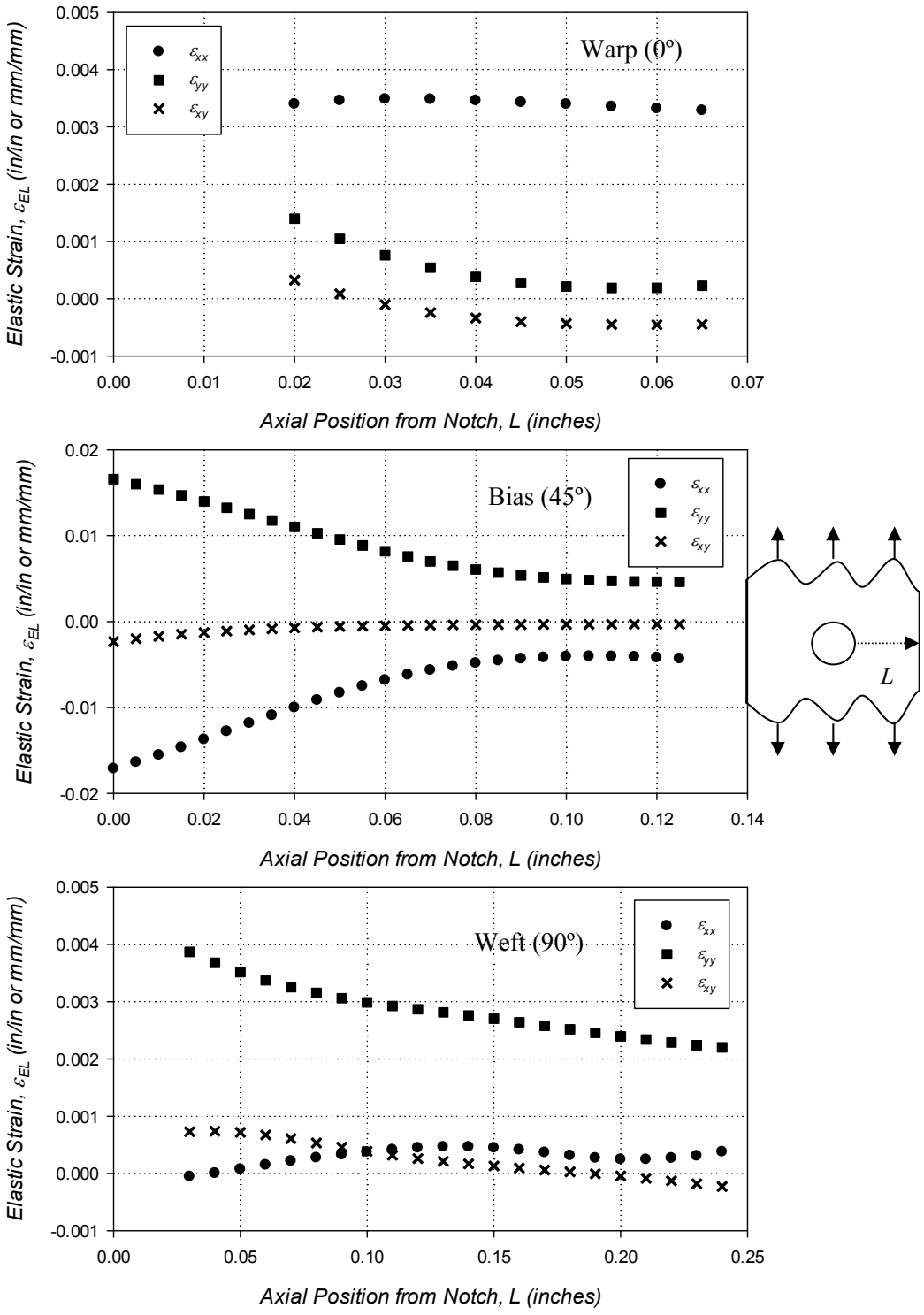

Figure 3.13: The tensorial elastic strain distribution along the *x-camera* axis at *y* = 0 in various material orientations for the 325x2300 twill dutch SS316L woven wire mesh material with a circular notch.

As failure in the bias (45º) material orientation is not observed to occur along an axis normal to the loading axis, but rather at some other angle relative to the *y-camera* axis, it is necessary to measure the strain at all points along the notch edge to determine the value and location of the maximum stress. In general, the stress distribution of an orthotropic body loaded at an angle to the principle direction is not symmetric with respect to the line parallel or perpendicular to the loading axis. Lekhnitskii [Lekhnitskii, 1968], however, does show that the stress distribution in an orthotropic sheet is symmetric with respect to the center of the notch, i.e., any line passed through the center of the notch will produce equal stress values at the edges where it intersect the opening contour. Thus, it is sufficient to measure the strain (and calculate the stress) on a range of π radians (180º) along this edge. Fig. 3.14 shows the distribution of the tensorial strains along the edge of the circular notch in the bias (45º) material orientation between the positive and negative *y-camera* axes.

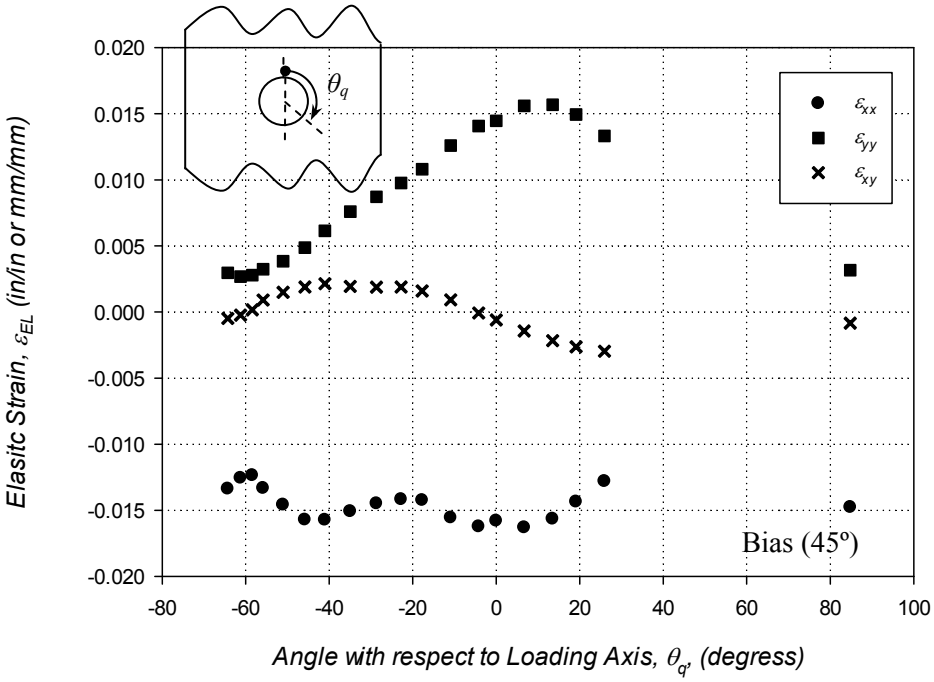

Figure 3.14: The tensorial elastic strain along the edge of the circular notch in the bias (45º) material orientation.

The angular position on the notch edge, θ_q is measured with respect to the positive loading axis. Note that the strain in the *x-camera* axis and the *y-camera* axis appear to follow opposing trends as a function of θ_q, and that the shear strain is zero near the axis aligned with the loading direction ($\theta_q = 0^o$).

With the maximum tensorial strain at the edge of the circular notches in each specimen quantified as shown in Figs. 3.13 and 3.14, it is straightforward to proceed with the calculation of the SCFs for a circular notch of 0.25in (6.35mm) in diameter centered in a 0.75in (19.05mm) wide uniaxial strip specimen of SS316L woven wire mesh. The definition of the SCF taken in the work is that presented in Eq. (1.3.1), i.e., the ratio of the maximum stress at the edge of the notch to the gross applied stress, σ_{gross}, which is defined in Eq. (3.2.1) as the load cell reading, P_{cell}, divided by the gross cross-section of the specimen, A_{gross}, i.e.,

$$\sigma_{gross} = \frac{P_{cell}}{A_{gross}} \tag{3.2.1}$$

As it is not immediately clear the edge position at which the stress will be at a maximum in material orientations other than principle, it is convenient to adopt a polar reference frame for stress component definition. For example, in the bias (45º) case, it cannot be assumed that the maximum stress occurs at a point perpendicular to the loading direction, and so it is necessary to employ the polar form of the stress tensor to investigate all points along the notch edge. The transformation from polar to Cartesian coordinates, given for the component σ_θ in Eq. (3.2.2), along with the observation from Fig. 3.13 that the shear strain, $\varepsilon_{xy,}$ is near zero near the notch edge in the warp (0º) and weft (90º) material orientations, allows for the assumption that σ_θ is equal to $\sigma_{y-camera}$ in the principle material orientations at the point of interest ($\theta_p = 0^o$).

$$\sigma_\theta = \sigma_y \cos^2 \theta_p + \sigma_x \sin^2 \theta_p - \tau_{xy} \sin 2\theta_p \tag{3.2.2}$$

The term θ_p refers to the angular coordinate in a fixed polar system at the center of the open notch, oriented such that 0º corresponds to the positive *x-camera* axis. Thus, comparison of SCFs calculated using $\sigma_{y-camera}$ (the loading direction) are equivalent to those calculated using σ_θ in the principle orientations, i.e.,

$$K_{t,g} = \frac{\sigma_{\max,y}}{\sigma_{gross}} = \left.\frac{\sigma_{\max,\theta}}{\sigma_{gross}}\right|_{\theta=0°,90°,\theta_p=0°} \tag{3.2.3}$$

Consequently, the σ_θ term is adopted as the stress component for SCF definition in the remainder of this work.

As the material orientation is being rotated with respect to the camera reference frame, careful attention must be paid to the transformation of the material stiffness matrix to assure the stress components are calculated properly. In general, the Hooke's Law relationship for a plane stress orthotropic material may be written in stiffness form for the principle material orientations as the following,

$$\begin{Bmatrix} \sigma_1 \\ \sigma_2 \\ \tau_{12} \end{Bmatrix} = \begin{bmatrix} Q_{11} & Q_{12} & 0 \\ Q_{21} & Q_{22} & 0 \\ 0 & 0 & 2Q_{66} \end{bmatrix} \begin{Bmatrix} \varepsilon_1 \\ \varepsilon_2 \\ \varepsilon_{12} \end{Bmatrix} \tag{3.2.4}$$

where the terms Q_{ij} are the components of the stiffness matrix. These components can be related to the elastic constants presented in Eq. (1.2.2) through an inversion of the compliance matrix, i.e.,

$$
\begin{aligned}
Q_{11} &= \frac{E_w}{1-\nu_{ws}\nu_{sw}} \\
Q_{12} = Q_{21} &= \frac{\nu_{ws}E_s}{1-\nu_{ws}\nu_{sw}} \\
Q_{22} &= \frac{E_s}{1-\nu_{ws}\nu_{sw}} \\
Q_{66} &= G_{ws}
\end{aligned}
\tag{3.2.5}
$$

While the form of Eq. (3.2.4) is useful for analysis of the stress state when one of the principle material orientations of the test specimen is aligned with the loading axis, analysis of the bias (45º) specimen requires a transformation of the stiffness matrix. Such a transformation can be accomplished via the following operation,

$$
\begin{Bmatrix} \sigma_x \\ \sigma_y \\ \tau_{xy} \end{Bmatrix} = [\mathbf{T}]^{-1}[\mathbf{Q}][\mathbf{T}] \begin{Bmatrix} \varepsilon_x \\ \varepsilon_y \\ \varepsilon_{xy} \end{Bmatrix} \tag{3.2.6}
$$

Where [**T**] is the transformation matrix, defined as follows:

$$
[\mathbf{T}] = \begin{bmatrix} c^2 & s^2 & 2cs \\ s^2 & c^2 & -2cs \\ -cs & cs & c^2 - s^2 \end{bmatrix} \tag{3.2.7}
$$

and the term s is sine θ and c is cosine θ. Use of Eq. (3.2.6) allows for the calculation of the stress state at the edge of the circular notch for all tested material orientations, and hence for the calculation of the experimental stress concentration factor via Eq. (1.3.1). These results are tabulated for the circular notch in Table 3.4. It must be conceded, as previously mentioned, that inspection of the DIC contour plots in Fig. 3.12 reveals that the correlation failed to produce strain values at the actual edge of the notch. Due to the high gradients expected in the region of the notch, it is likely that the SCF values calculated with this method do not represent the

maximum stresses at the notch edge, but rather are indicative of the stress levels very close to the notch edge. Thus, the DIC experimental stress concentration factors are given the subscript *n*, indicating that the value is valid at some distance from the notch, but not at its edge. The value of the DIC experiments is not diminished by this, however; as the experimental contours provide validation of the continuum based FEM approach outlined in Chapter 4. Note that the maximum stress values for the principle material orientations are calculated at the position *x* is equal to *r*, *y* is equal to 0, where *r* is 0.125in, and θ_p is 0º. The position in space is measured with respect to the center of the opening and relative to the camera axes. The bias (45º) specimen was found to have a maximum σ_θ component of stress at an angle, θ_p equal to 67.5º on the notch edge.

Table 3.4: Stress values near a circular notch in the SS316L woven wire mesh along with the calculated near notch SCF values.

Material Orientation, θ (º)	**Near Notch Max Stress, $\sigma_{max,\theta\text{-component}}$ (ksi)**	**Gross Stress, σ_{gross} (ksi)**	**SCF_n, $K_{t,gn}$**
0 (Warp)	9.4	3.92	2.39
45 (Bias)	6.85	0.913	6.85
90 (Weft)	12.7	5.71	2.21

While the experimental elastic strain and stress values determined via full field DIC provide detailed insight into the deformation mechanisms of the subject material in the presence of a circular stress riser, and give an idea of the magnitude of the stress concentration factor in the vicinity of a notch, the results presented in Table 3.4 likely do not correspond to the maximum stress that can be expected at the edge of circular notch in 325x2300 SS316L twill dutch woven wire mesh material. To address this deficiency while simultaneously investigating the application of classical continuum mechanics theory to this class of materials, the analytic

solution supplied by Tan [Tan, 1988] for the *y*-component of stress along the line at *y* equals 0 (measured from a coordinate system position at the center of the opening) in an orthotropic body with an elliptical notch is employed. The solution provided by Tan,

$$\sigma_y^{\infty}(x,0) = \overline{\sigma_y} + \overline{\sigma_y}\,\mathrm{Re}\left\{\frac{1}{\mu_1-\mu_2}\left[\begin{array}{c}\dfrac{-\mu_2\left(1-i\mu_1\lambda\right)}{\sqrt{\gamma^2-1-\mu_1^2\lambda^2}\left(\gamma+\sqrt{\gamma^2-1-\mu_1^2\lambda^2}\right)}+\\ \dfrac{\mu_1\left(1-i\mu_2\lambda\right)}{\sqrt{\gamma^2-1-\mu_2^2\lambda^2}\left(\gamma+\sqrt{\gamma^2-1-\mu_2^2\lambda^2}\right)}\end{array}\right]\right\} \tag{3.2.8}$$

which can be shown equivalent to the one provided by Lekhnitskii in Eq. (1.3.10) in the case of an infinite body and a circular notch, is ideal for this comparison as it provides for a finite width correction factor that can be used to scale the results, as shown in Eq. (1.3.11), accounting for the effects of the free edge boundary conditions on the stress distribution. Here, σ_y^{∞} is the maximum *y*-component of stress at the notch edge in an infinite orthotropic body with an elliptical hole, $\overline{\sigma}_y$ is the remotely applied gross stress, λ is the ratio of the major radius, *b*, to the minor radius, *a*, of the notch, μ_1 and μ_2 are parameters accounting for the anisotropy of the material, γ, is the notch distance ratio, *x/a*, and the term Re denotes that the real part of the complex expression is to be taken. The characteristic equation given for determining the factors μ_1 and μ_2 is,

$$a_{22}\mu^4 - 2a_{26}\mu^3 + \left(2a_{12}+a_{66}\right)\mu^2 - 2a_{16}\mu + a_{11} \tag{3.2.9}$$

where a_{ij} are the terms of the compliance matrix as given in Eq. (1.2.2). The FWC for a circular notch ($\lambda = 1$ only) takes the form shown in Eq. (3.2.10), where *W* is the overall specimen width, *a* is the minor radius of the notch, and *M* is a magnification factor given as Eq. (3.2.11)

$$\frac{K_T^{\infty}}{K_T} = \frac{3\left(1-2\frac{a}{W}\right)}{2+\left(1-2\frac{a}{W}\right)^3} + \frac{1}{2}\left(\frac{2a}{W}M\right)^6\left(K_T^{\infty}-3\right)\left[1-\left(\frac{2a}{W}M\right)^2\right] \tag{3.2.10}$$

$$M^2 = \frac{\sqrt{1-8\left[\frac{3\left(1-2\frac{a}{W}\right)}{2+\left(1-2\frac{a}{W}\right)^3}-1\right]}-1}{2\left(2\frac{a}{w}\right)^2} \tag{3.2.11}$$

By solving for the stress distribution along the line at $y = 0$, and then applying the FWC factor appropriate for the specimen geometry outlined in Fig. 2.1, it is possible to compare the analytic solution to the experimentally determined stress distribution along the same line, as shown in Fig. 3.15. It is clear that the analytic solution predicts considerably higher stresses at the edge of the notch than the maximum values measured using DIC. Inspection of the warp (0º) and weft (90º) stress distributions in Fig, 3.15 supports the assumption that this discrepancy is caused by the inability of the DIC measurement technique to correlate the displacement fields in regions of large gradients, as the stress distributions appear to converge in regions away from the notch edge. Based on this observation, it is concluded that the DIC measurements are not indicative of the maximum stress at the edge of the notch, but should be considered rather as near notch values. Given the apparent accuracy of the DIC results away from the notch edge, it is likely that the correlated stress field away from the notch could be used to directly estimate the stress at the notch edge via a least squares fit of the DIC data to the theoretical stress distribution. A similar technique has been successfully employed by Mogadpalli [Mogadpalli and Parameswaran, 2008]

to experimentally determine stress intensity factors (SIF) for a notched orthotropic plate using DIC. Such a method is beyond the scope of this thesis, however, and is left for future work.

Given the apparent agreement between the analytic solution and the DIC experimental results away from the notch edge, it is reasonable to extrapolate the experimental results to the notch edge using the analytic solution. In the case of the warp (0º) and weft (90º) material orientations ($\sigma_y = \sigma_\theta$), Eqs. (3.2.8) through (3.2.11) may be used for this purpose. Considering Eq. (3.2.3), the relationship presented in Eq. (1.3.10) can be used to predict the maximum stress, in the θ-component, along the notch edge in the bias (45º) case.

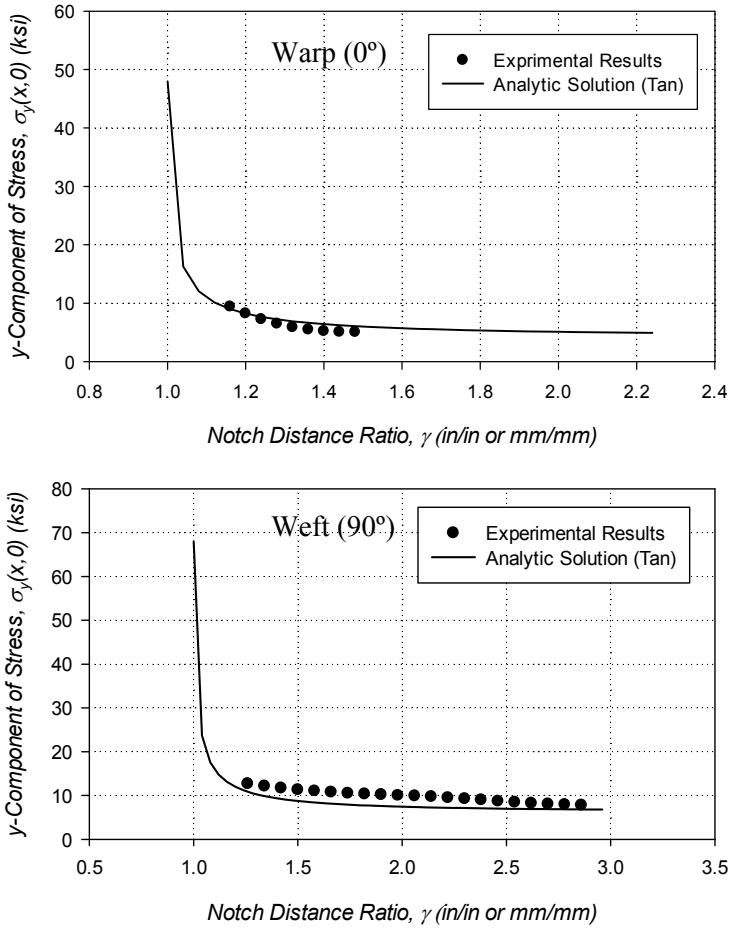

Figure 3.15: Experimental stress distribution along the line $y = 0$ for principal direction specimens of 325x2300 twill dutch woven wire mesh containing a circular hole with respect to the analytic solution as provided by Tan [Tan, 1988}.

The prediction for the θ-component of stress in the bias (45º) material orientation is presented in Fig. 3.16, along with the experimentally determined values. The DIC data was extracted along a contour near the edge of the notch [approximately 0.019in (0.48mm) away], along a 180º arc, i.e., ($r \cong a$, θ_p = -90º - 90º). Note that the experimental θ-component of stress has been determined from the DIC data by first employing Eq. (3.2.6) to calculate the Cartesian components, and then using Eq. (3.2.2) to covert to polar form.

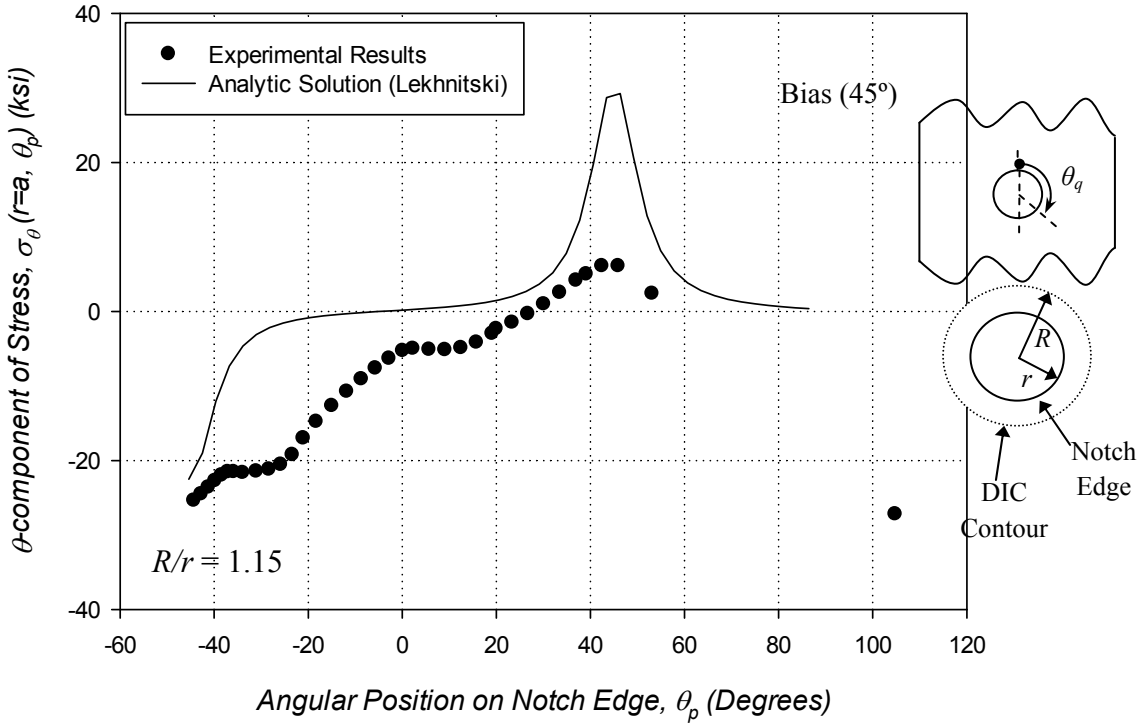

Figure 3.16: Distribution of the Theta-Component of stress along the edge of a circular notch in the SS316L woven wire mesh in the bias (45º) material orientation from both the DIC measurements and the solution presented by Lekhnitskii [Lekhnitskii, 1986].

The extrapolated SCFs for a circular notch in the subject material as a function of material orientation are presented in tabular form in Table 3.5. These values are given the subscript *a,* indicating that they are analytic in nature, and again it is noted that the stress values reflect the component σ_θ, and the reported SCF values are calculated accordingly. Clearly these values are

significantly higher than the isotropic case, $K_{t,g}$ = 3.0, and, as expected, are considerably higher than the near notch values presented in Table 3.4. It is interesting to note, that both the DIC results (Table 3.4) and the analytic solution predict the value of $K_{t,g}$ in the 45º (bias) material orientation to be significantly higher than in principle material orientations, indicating that this material orientation could be considerably more sensitive to the presence of a macro-scale defect.

Table 3.5: Analytic SCF values for a circular notch in SS316L twill dutch woven wire mesh

Material Orientation, θ (º)	**Predicted Notch Edge Stress, $\sigma_{edge,\ \theta\text{-component}}$ (ksi)**	**Gross Stress, σ_{gross} (ksi)**	**SCF_a, $K_{t,ga}$**
0 (Warp)	47.93	4.74	10.11
45 (Bias)	22.5	0.913	24.6
90 (Weft)	68.03	7.13	9.54

3.2.2 Experimental SCF Curves for Elliptical and Slit Notched Strip Specimens

With the experimental and analytic SCFs defined for circular notched specimens, testing continued with notches of varying λ ratio. As described in the experimental test matrix presented Table 2.2, the sharpness of the notch was varied from a λ value of 1.0, or a circle, to a value of near 0.0, or a slit, with an intermediate value of 0.5. For the cases of non-circular notches, the orientation of the notch root with respect to the loading axis, α, is of interest, and was also considered as a parameter in the test sequence. Thus, a series of 15 experiments, in addition to the circular notch experiments, were carried out using the full field DIC strain measurement technique. Strain contours for the λ equals 0.5 notches, again in the *y-camera* direction, have been correlated from the raw DIC data, and are presented in Figs. 3.17-3.19. Frames have been chosen in the early stages of loading, such that the contours represent nominally elastic material

behavior in all cases. Clearly in the case of elliptical notches (λ=0.5), the presence of the discontinuity causes severe perturbation of the strain field in all material and notch orientations.

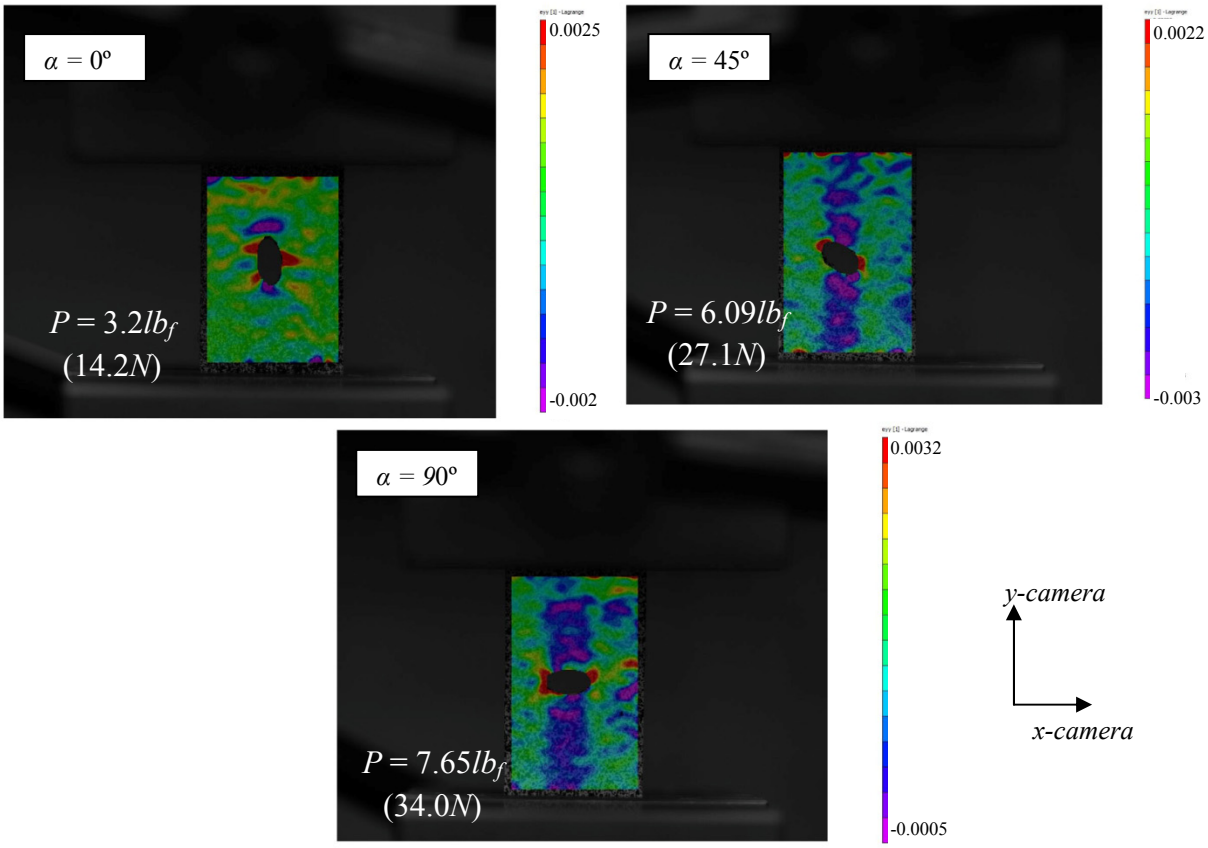

Figure 3.17: Mechanical strain contours in the *y-camera* axis for SS316L woven wire mesh in the warp (0º) material orientation, containing elliptical stress risers at various orientations with respect to the loading axis.

Figure 3.17 shows the *y-camera* axis strain contours in the area of elliptical notches in warp (0º) oriented woven wire mesh. It is interesting to note that the maximum strain in vicinity of the α = 0º notch is not at the center of the opening curvature as would be expected in a homogenous material, but rather is slightly above the center line, and symmetric about the *y-camera* axis. This is attributable to the discontinuous nature of this class of materials, and in particular, the relatively large gaps between load bearing wires in the warp (0º) material

orientation. For this class of materials, it is reasonable to assume that the location of the maximum *y-camera* direction strain is determined not only by the notch geometry, but also by the continuity of the wires in the vicinity of the notch. For example, if the wires at the center line of the notch radius are cut in the process of incising the notch in the specimen, these wires cannot transfer traction near the notch edge, and so this load must be picked up by the next fully continuous wire close to the point of maximum stress. Similarly, the discontinuity of wires cut-off by the notch edge explains the appearance of the strain contours in the α = 45º and α = 90º cases in Fig. 3.17, which all appear to be somewhat removed from the exact root of the notch perpendicular to the loading direction.

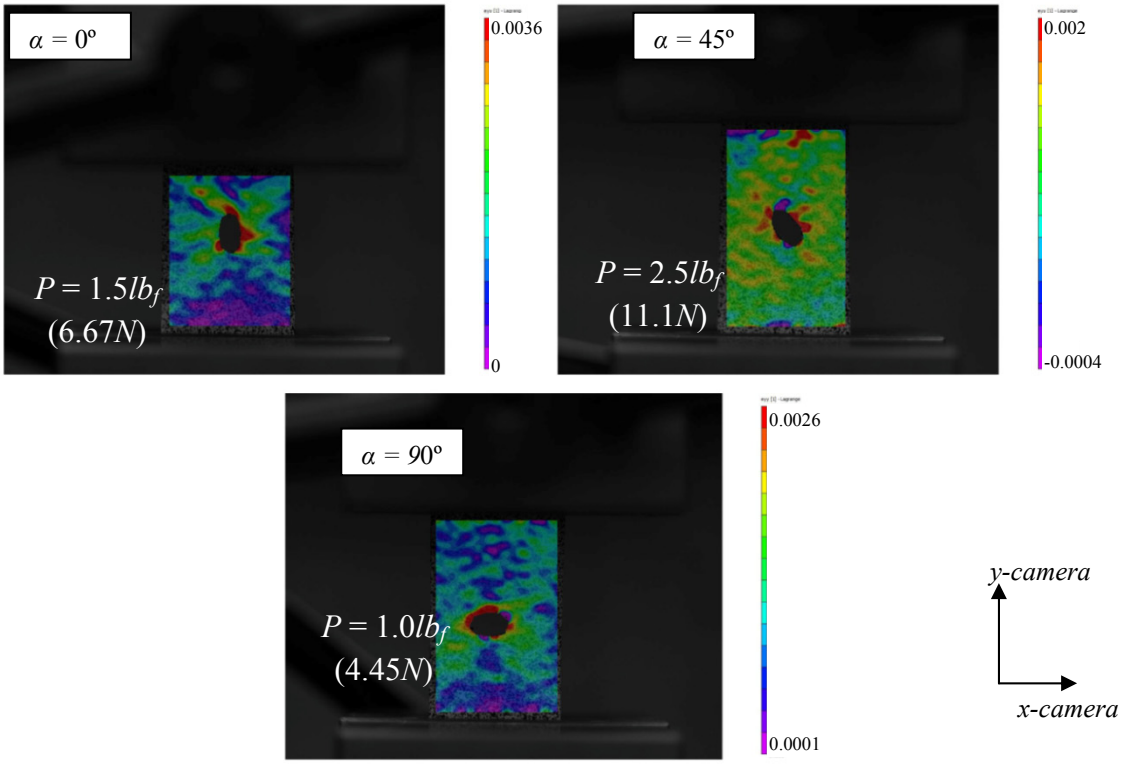

Figure 3.18: Mechanical strain contours in the *y-camera* axis for SS316L woven wire mesh in the bias (45º) material orientation, containing elliptical stress risers at various orientations with respect to the loading axis.

The strain distribution in the *y*-camera direction for elliptical notched specimens of the woven wire mesh material, incised in the bias (45º) material orientation, is shown Figure 3.18. Again, the elliptical notches are varied by orientation with respect to the loading axis. Inspection of Fig. 3.18 reveals that the strain distribution around the various elliptical notches in the bias (45º) orientated specimens is less uniform than in the warp (0º) case, with the maximum values not necessarily occurring at the notch roots, and with a general lack of symmetry about the loading axis. Close inspection, however, reveals that the strain distribution does appear nearly symmetric about the center point of the ellipse, particularly in the α = 45º and 90º cases, as is expected from analytic results. The relative size of the process zone in the region of the elliptical notches in the bias (45º) oriented specimens indicates that the failure mode in these specimens is likely yield dominant, i.e., characterized by a large plastic zone and high ductility. Conversely, the process zones for the elliptical notches in the warp (0º) oriented cases are more concentrated, indicating that the mesh rupture may show increased characteristics of brittle fracture. Such an observation can be easily confirmed via post-mortem inspection of the fracture surface, and inspection of the tensile response of the various notched specimens, and these aspects are treated in detail in subsequent sections.

The strain distribution in the *y-camera* direction around elliptical notches in the woven wire mesh subject material incised into weft (90º) oriented specimens is shown in Fig. 3.19. In general, the strain fields are symmetric about the center of the notch as expected, and the location of maximum strain is at the notch root perpendicular to the loading direction as expected. Again, in the α = 90º case, the area of maximum strain is somewhat more distributed. This is attributed to the increased load at the notch edge being redistributed and carried by the surrounding continuous wires in the vicinity of the maximum stress. Clear compressive zones develop in the

regions above and below the notch edge, suggesting some level of strain information transference from the notch to the surrounding structure, even in areas where the wires have been completely severed by the defect. The α equals 45º and α equals 0º cases show considerably smaller process zones, indicating that only a few wires are actively participating with the notch edge in these cases. Such an observation again lends itself towards the conclusion that this material orientation behaves more like a brittle material in the presence of a notch, and that the failure in the weft (90º) material orientation tends to be fracture dominant. Again, this observation is investigated using post-mortem fractography and detailed analysis of the tensile response in later sections of this chapter.

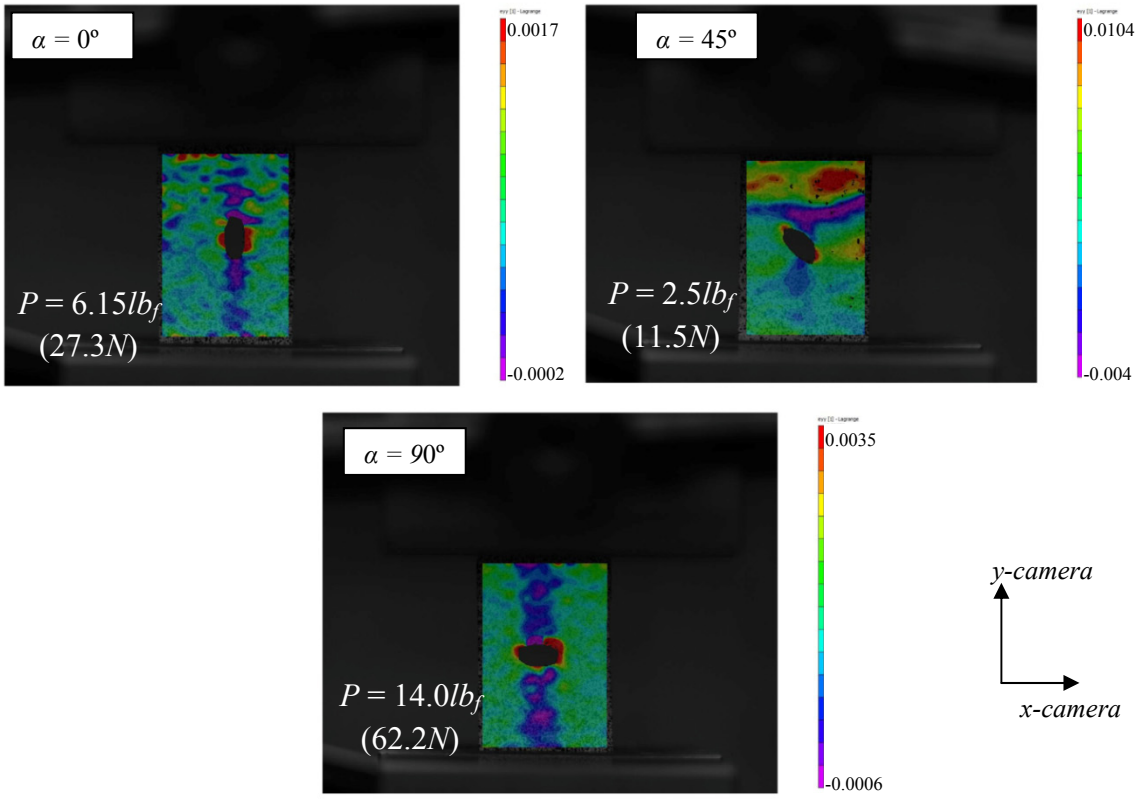

Figure 3.19: Mechanical strain contours in the *y-camera* axis for SS316L woven wire mesh in the weft (90º) material orientation, containing elliptical stress risers at various orientations with respect to the loading axis.

Strain correlations in the *y-camera* direction have also been developed for the slit notches (λ = 0.0), again with the notch orientation with respect to the loading axis, α, varying from 0º to 90º in 45º intervals. These contours are presented in Figs. 3.20 through 3.22, and all cases have been selected from frames early in the loading sequences to assure nominally elastic behavior near the notch root. In general, it can be observed that the slit notches aligned with the loading direction (α = 0º) cause very little disturbance in the strain field, which can be attributed to both the discontinuous structure of the subject material, and the fact that the radius of curvature of the notch perpendicular to the loading direction is along the order of the pore size between the wires. The lack of sensitivity of the strain field to the presence of the α = 0º slits is also evident in the failure location of these cases, which tended to be in the grip rather than at the notch. In all cases where the slit notch does appear to affect the strain distribution, the perturbation in the field is very local, and does not appear to favor a position on the notch edge, but rather creates a fairly uniform increase in strain over the entire open contour. Such an observation can be attributed to the fact that the root radius of the slit notch in the α = 45º and 90º cases is small enough to impact only a single wire, negating to a certain extent the singularity effects of the sharp slit notch in this class of materials.

The strain in the *y-camera* direction for a slit notch cut into material specimens oriented in the warp (0º) material orientation is shown in Fig. 3.20. Clearly, the slit notch oriented with the loading axis, α = 0º, has very little affect on the strain distribution in the structure. Even in the α = 90º case, the effect of the slit on the strain distribution is highly localized, and evenly distributed around the open contour. The uniform distribution of the strain field around the slit opening in the subject material is not restricted to the warp (0º) material orientation, but can also be observed in Fig. 3.21, bias (45º) material orientation, and Fig. 3.22, weft (90º) material

orientation. This presents a difficulty in the extraction of the strain data from the region of the contour, as it is not clear from inspection where the actual notch edge is located. To solve this problem, strain data was extracted from the full-field results as shown in Fig. 3.21 , with an inner contour and an outer contour along the basic path of the maximum strain region, and with strain lines that extend perpendicular to the loading region. In future work, such data could be used to extrapolate strain or stress fields to the notch edge by fitting analytic solutions to the experimental results, as proposed by Mogadpalli [Mogadpalli and Parameswaran, 2008].

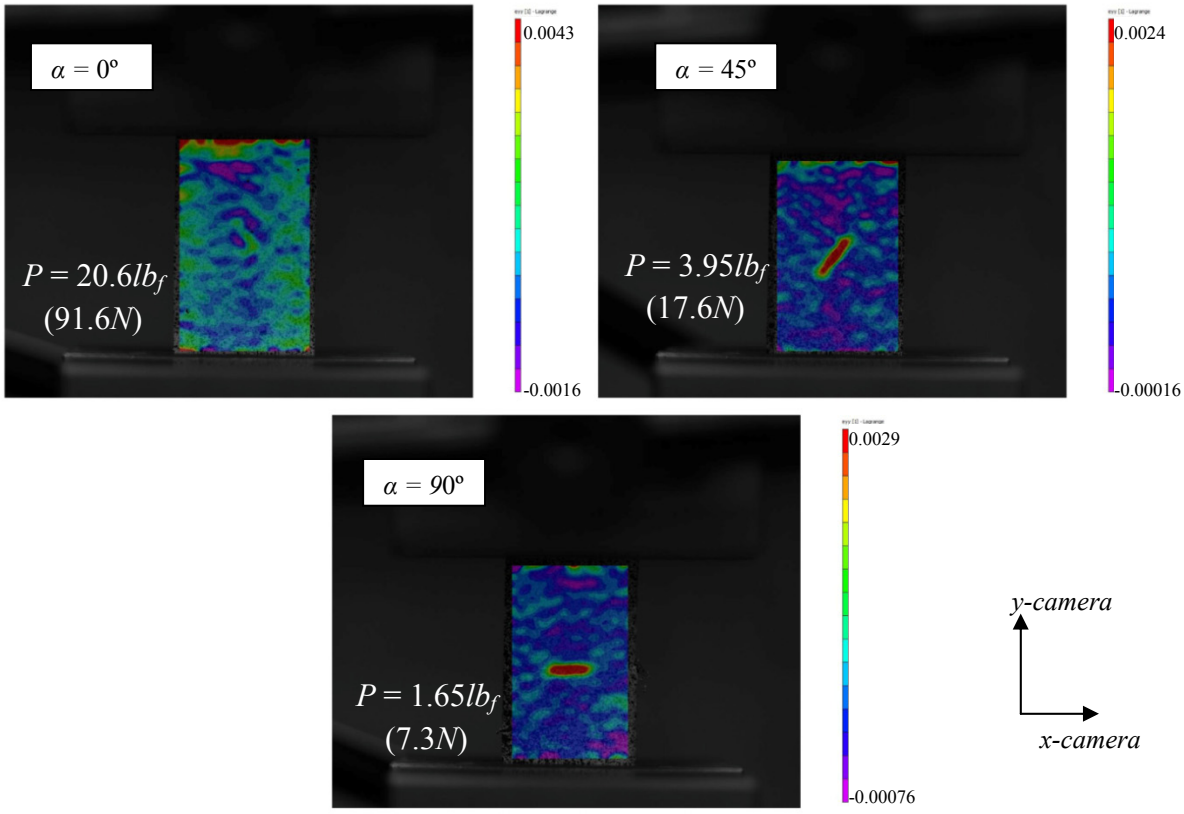

Figure 3.20: Mechanical strain contours in the *y-camera* axis for SS316L woven wire mesh in the warp (0°) material orientation, containing slit notch stress risers at various orientations with respect to the loading axis.

For the purpose of this current work, however, the inner contour is taken as the near notch field contour, and used to define the near notch SCF for this geometry. For the cases of α = 0º, the notch location was identified by investigating frames at higher load value, where the presence of the notch in the inelastic strain field becomes more evident. For the bias (45º) material orientation shown in Fig. 3.21, the α = 0º notch has no visible effect on the strain field, even at higher load levels, and so no contour can be accurately placed, and the value of SCF prescribed for this geometry and material orientation is 1.0. This observation is particularly interesting, as it implies that this material is tolerant to slit notches aligned with the loading direction.

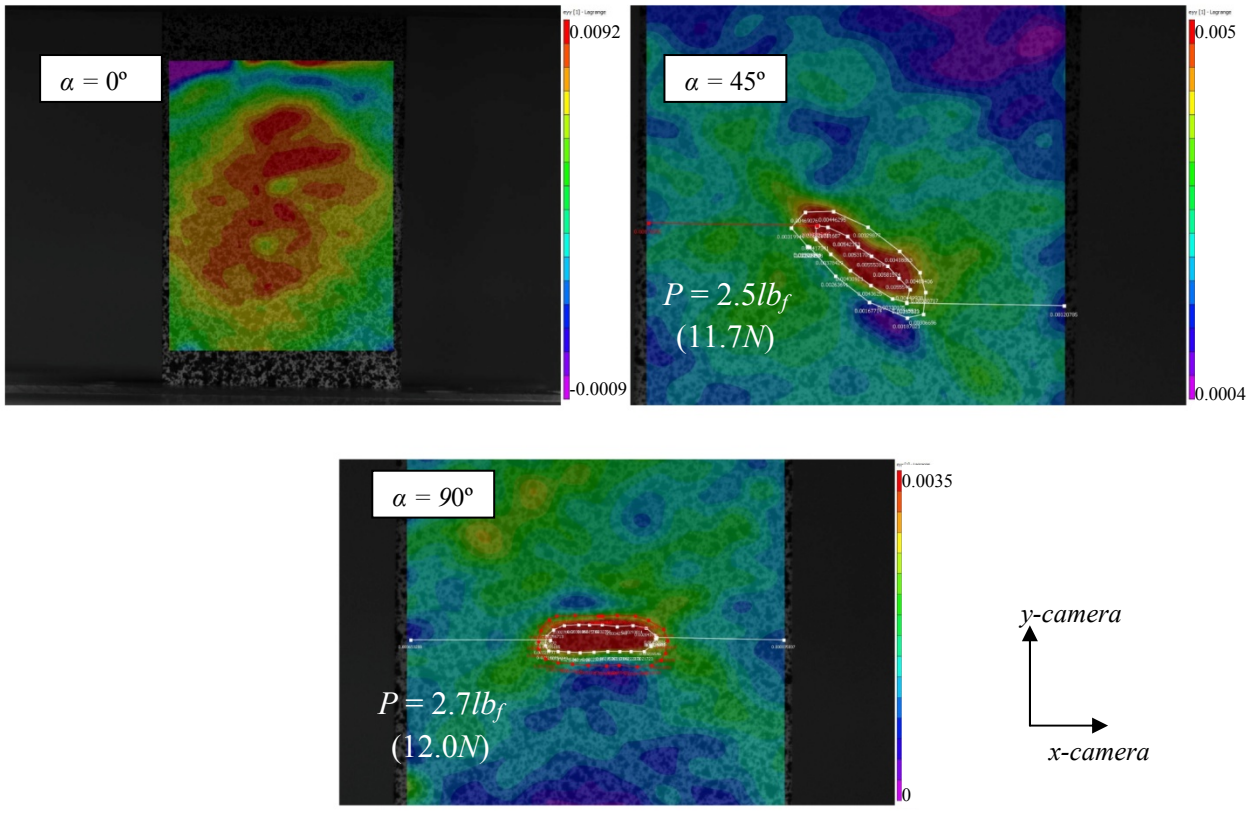

Figure 3.21: Mechanical strain contours in the *y-camera* axis for SS316L woven wire mesh in the bias (45º) material orientation, containing slit notch stress risers at various orientations with respect to the loading axis.

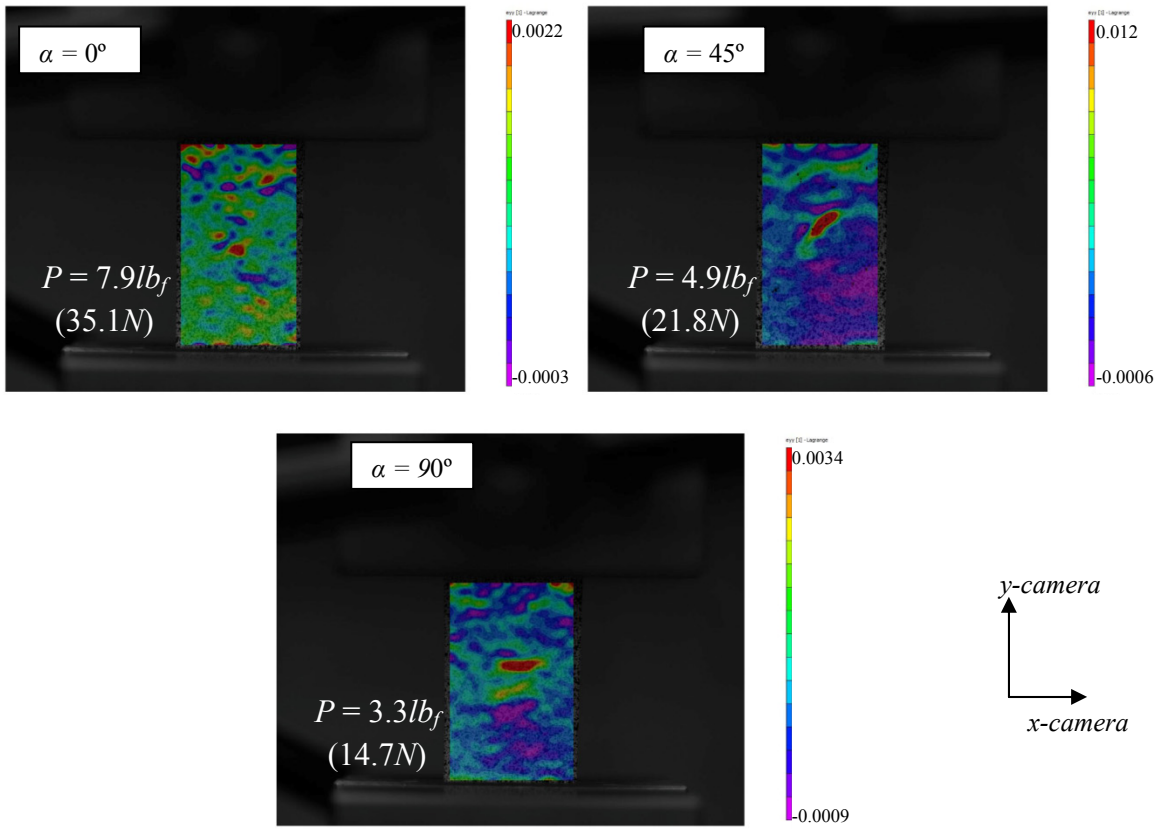

Figure 3.22: Mechanical strain contours in the *y-camera* axis for SS316L woven wire mesh in the weft (90º) material orientation, containing slit notch stress risers at various orientations with respect to the loading axis.

Given the variation in the observed strain fields in the region of the notch from what is expected for a continuous body, particularly in the location of the maximum strain, it is not possible to investigate the degree of stress concentration in the elliptically notched specimens by simply considering a line of interest at the notch root perpendicular to the loading direction, as was done in the case of circular notches. Even in the case of specimens incised in the principle material orientations, the varying inclination of the notch with respect to the loading direction forces inspection of the stress fields around the entire open contour. Thus, two sets of correlations have been extracted from the raw DIC data to investigate the strain and stress fields

around the elliptical notches. Figure 3.21 illustrates the method used for extraction of the tensorial strain components in all elliptical and slit notch cases, with data taken along nearly elliptically-shaped contours, and along lines of interest from the notch root to the specimen edge perpendicular to the loading direction. The elastic tensorial strain values taken along the elliptical contours have been leveraged to formulate the state of stress along the near notch edge as was done in the case of circular notches using Eqs. (3.2.4 - 3.2.7). These values are then used along with Eqs. (3.2.2 and 3.2.3) to the calculate the SCF for each respective case from the maximum value of σ_θ along the notch edge. The strain distributions calculated along the straight line paths from the notch tip to the specimen edge serve as indicators of the size of the region of the strain field perturbation, which ultimately can be used as an indication of mesh failure behavior in the presence of the various notch geometries.

The elastic tensorial strain distributions along the line of interest for the various notch orientations and λ values are shown in Figs. 3.23-2.28. For the elliptical notches in general, it is observed that the component of strain impacted the most severely by the stress riser is dependent on the notch orientation, α, with α = 0º producing significant increases in the shear strain component near the notch, and α = 90º degrees typically characterized by maximum strain in the *y-camera* component. The slit notches tend to produce highly localized increase in strain magnitudes near the notch tip when α = 90º, but very little impact when the notch is aligned with the loading axis (α = 0º). Figure 3.23 shows the strain distribution along the line of interest from the notch tip to the specimen edge for the warp (0º) oriented elliptical notched specimens. Inspection of Fig, 3.23 reveals the location of the maximum strain is slightly off of the notch

edge in the α = 0º case, which is also observed in the weft (90º) material orientation, as shown in Fig. 3.25.

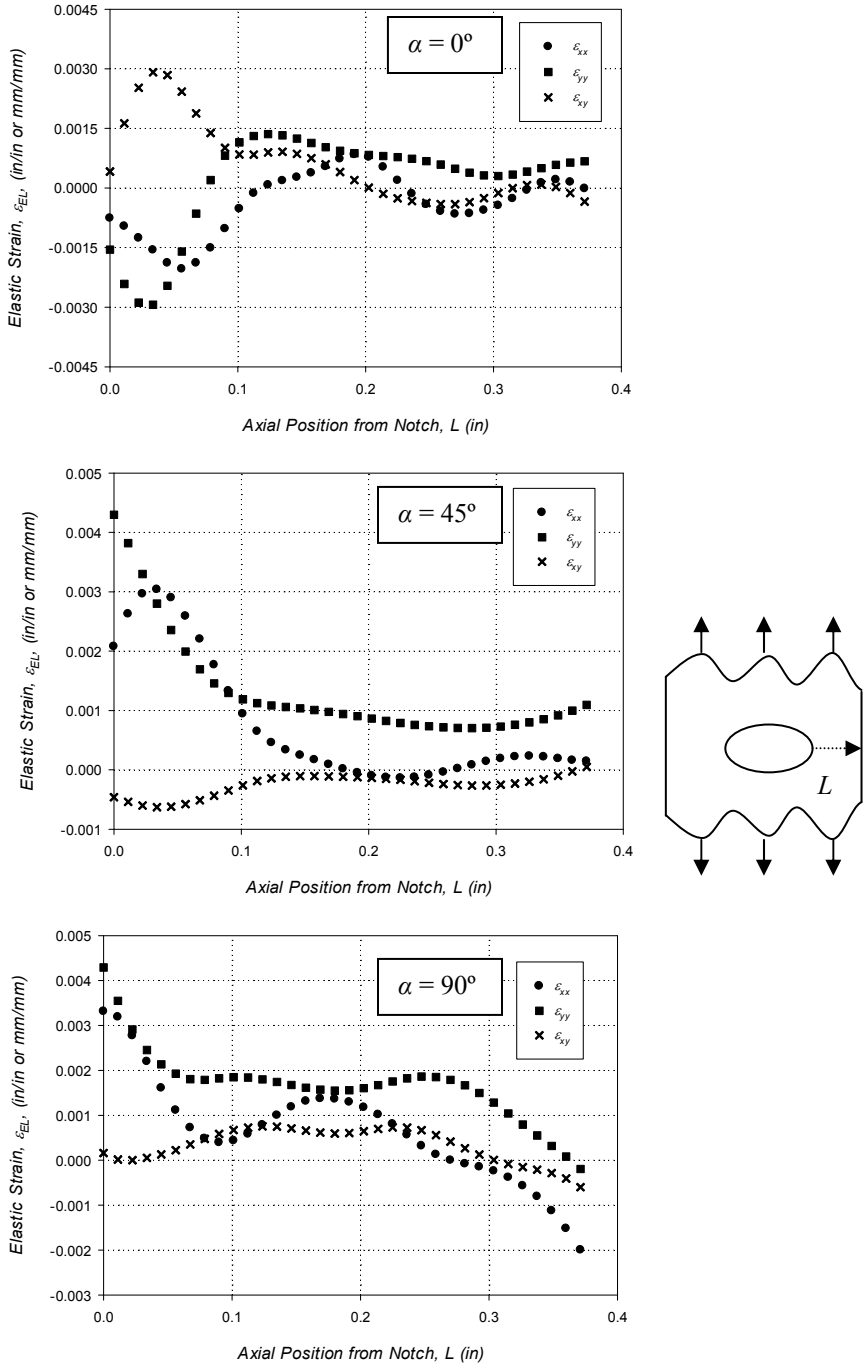

Figure 3.23: The tensorial elastic strain distribution along a line in the *x-camera* direction from the notch root to the specimen edge for various elliptical (λ= 0.5) notch inclinations in warp (0º) oriented specimens.

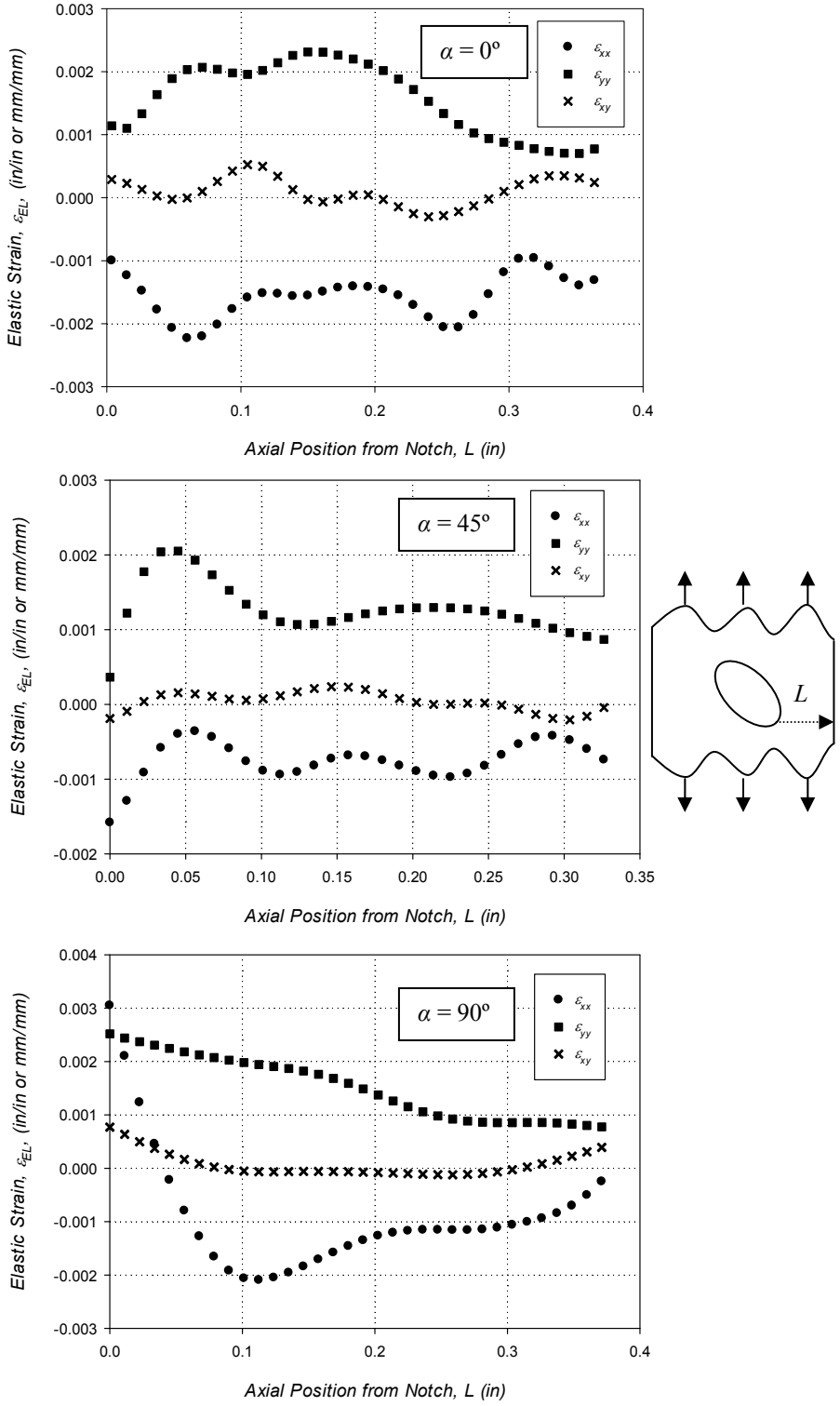

Figure 3.24: The tensorial elastic strain distribution along a line in the *x-camera* direction from the notch root to the specimen edge for various elliptical (λ= 0.5) notch inclinations in bias (45º) oriented specimens.

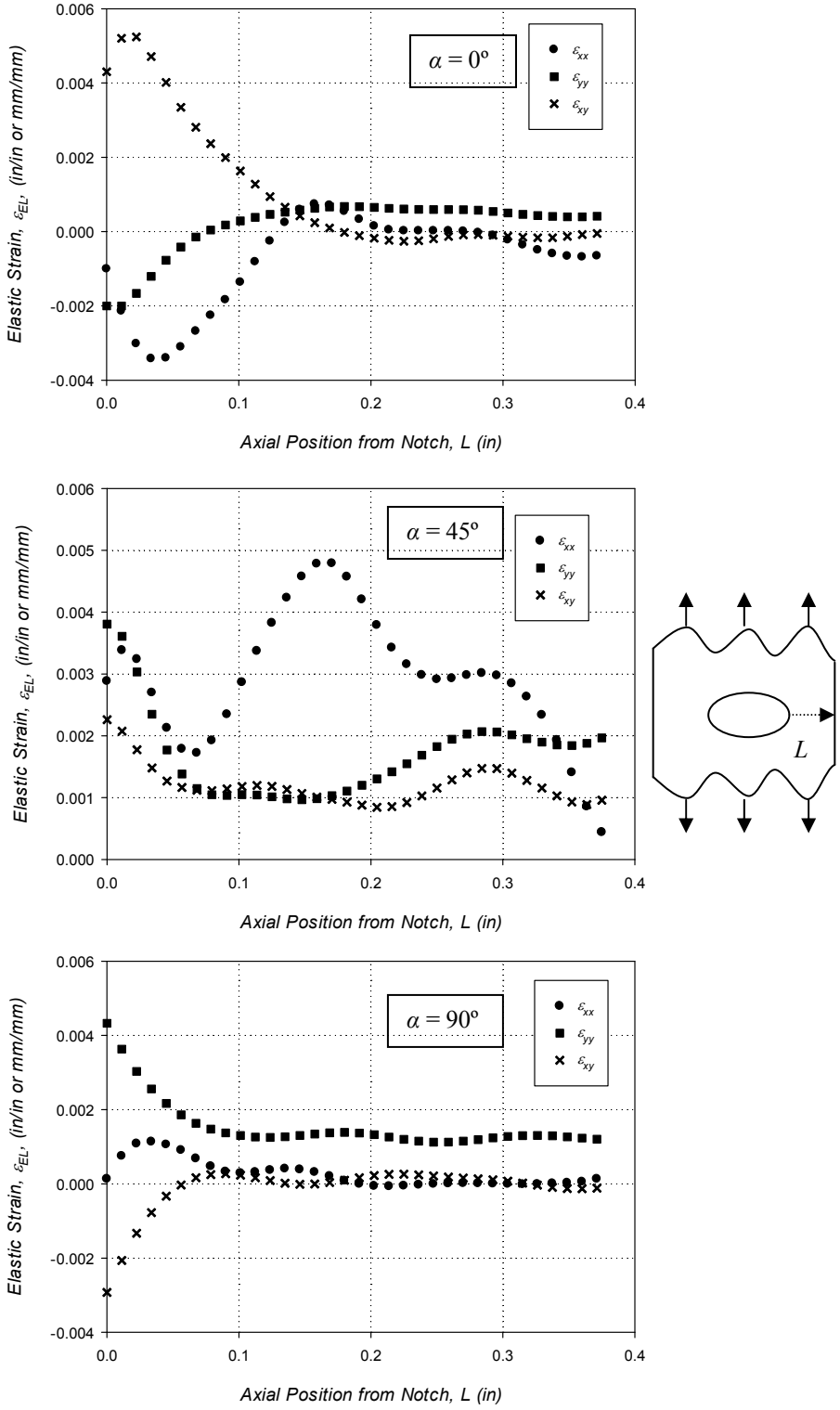

Figure 3.25: The tensorial elastic strain distribution along a line in the *x-camera* direction from the notch root to the specimen edge for various elliptical (λ= 0.5) notch inclinations in weft (90º) oriented specimens.

This observation is likely attributable to the inevitable cut-off of wires near the notch edge, clearly demonstrating the inhibited strain redistribution capabilities amongst contacting wires in the subject material. Figure 3.24 shows the respective strain distribution for the bias (45º) oriented specimens containing an elliptical notch, and it is interesting to note that, similar to the distributions shown in Fig. 3.14, the *x-camera* and *y-camera* axis strain distributions are nearly equal but of opposite sign, while the shear strain is near zero for both the α = 0º and the α = 45º cases. For the case where the notch is oriented orthogonally to the loading direction (α = 90º) in the bias (45º) oriented specimen (Fig. 3.24), the location of the maximum strain is at the notch edge, and the magnitude of the strains in the *x-camera* and *y-camera* directions at the notch tip are nearly equal but of opposite sign. The most atypical strain distribution found in the ellipse notched specimens is shown in Figure 3.25 (θ = 90º, α = 45º), where the maximum strain value 0.05% occurs in the *x-camera* direction, approximately 0.15 in. (3.81mm) from the notch edge, while in the same location the strain in the *y-camera* direction, i.e., the loading axis, is near zero. This may be attributable to the high stresses imparted on the relatively few warp wires (aligned with the *x-camera* axis) in the region of the notch tip, causing an asymmetric extension of the notch into the *x-camera* direction. This is supported by the general asymmetric appearance of the notch post-fracture.

The distribution of the tensorial strain in the region of the slit type notches (λ = 0.0) at various inclinations to the loading axis and in various material orientations is shown in Figs. 3.26 through 3.28. In all material orientations, minimum affect on the strain field occurs with the slit oriented with the loading axis (α = 0º). This fact is most pronounced in the bias (45º) and the weft (90º) material orientations, where the strain distribution is nearly constant across the specimen width.

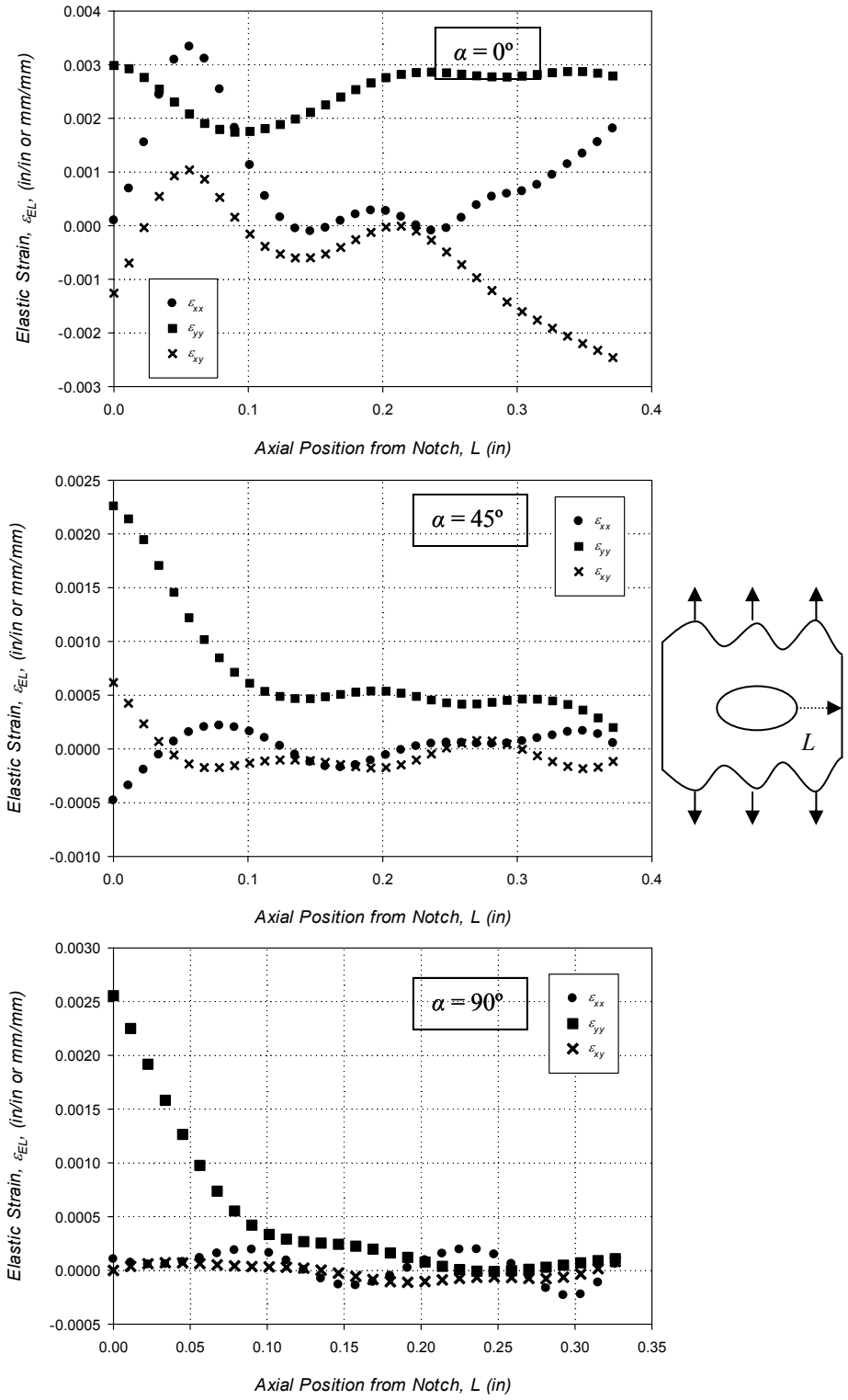

Figure 3.26: The tensorial elastic strain distribution along a line in the *x-camera* direction from the notch root to the specimen edge for various slit (λ= 0.0) notch inclinations in warp (0°) oriented specimens.

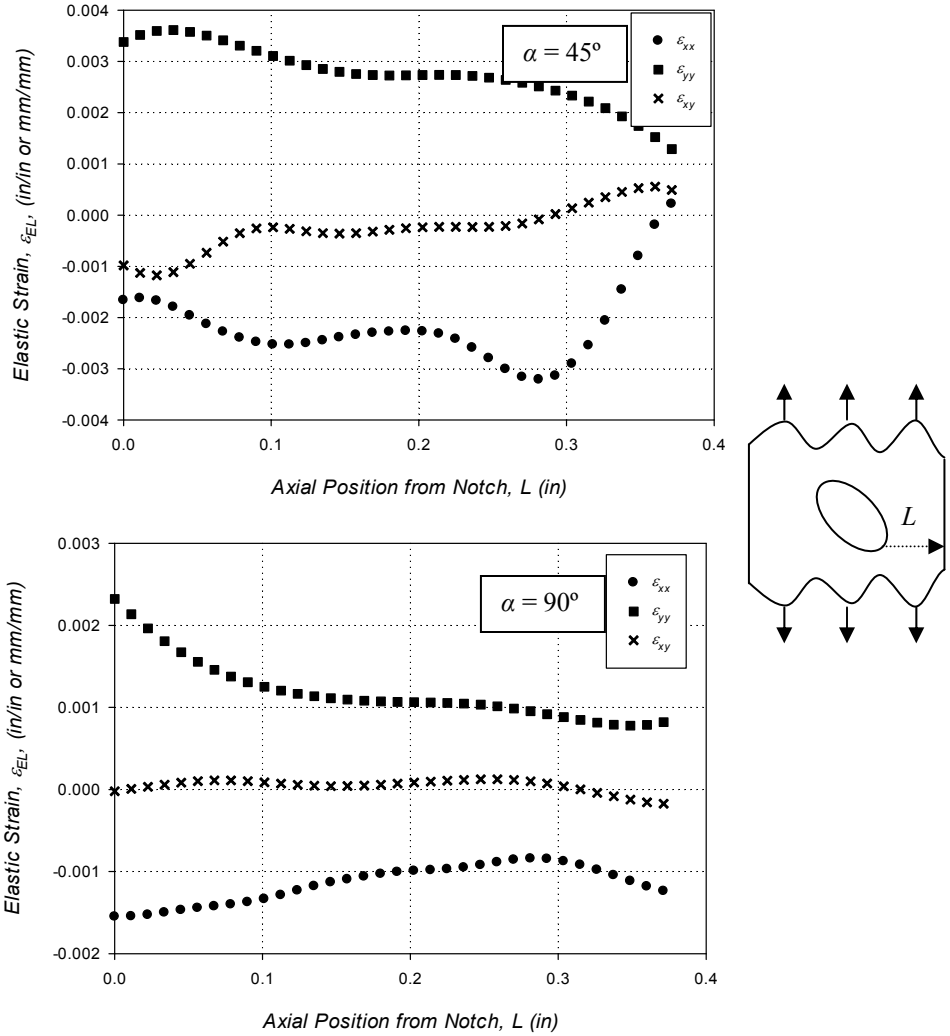

Figure 3.27: The tensorial elastic strain distribution along a line in the *x-camera* direction from the notch root to the specimen edge for various slit (λ= 0.0) notch inclinations in bias (45º) oriented specimens.

Inspection of Fig. 28 (θ = 90º, α = 0º) shows that there is no difference between the strain state at the notch tip and at the edge of the specimen, and the maximum value of 0.06% strain in the *y-camera* direction occurs 0.07 in. (1.78mm) from the notch edge. Figure 3.27, which shows the strain distribution along the line of interest from the notch tip to the specimen edge for bias (45º) oriented slit notch specimens, does not include a plot of the strain distribution for the α = 0º case, owing to the lack of significant strain disturbance in field around the slit.

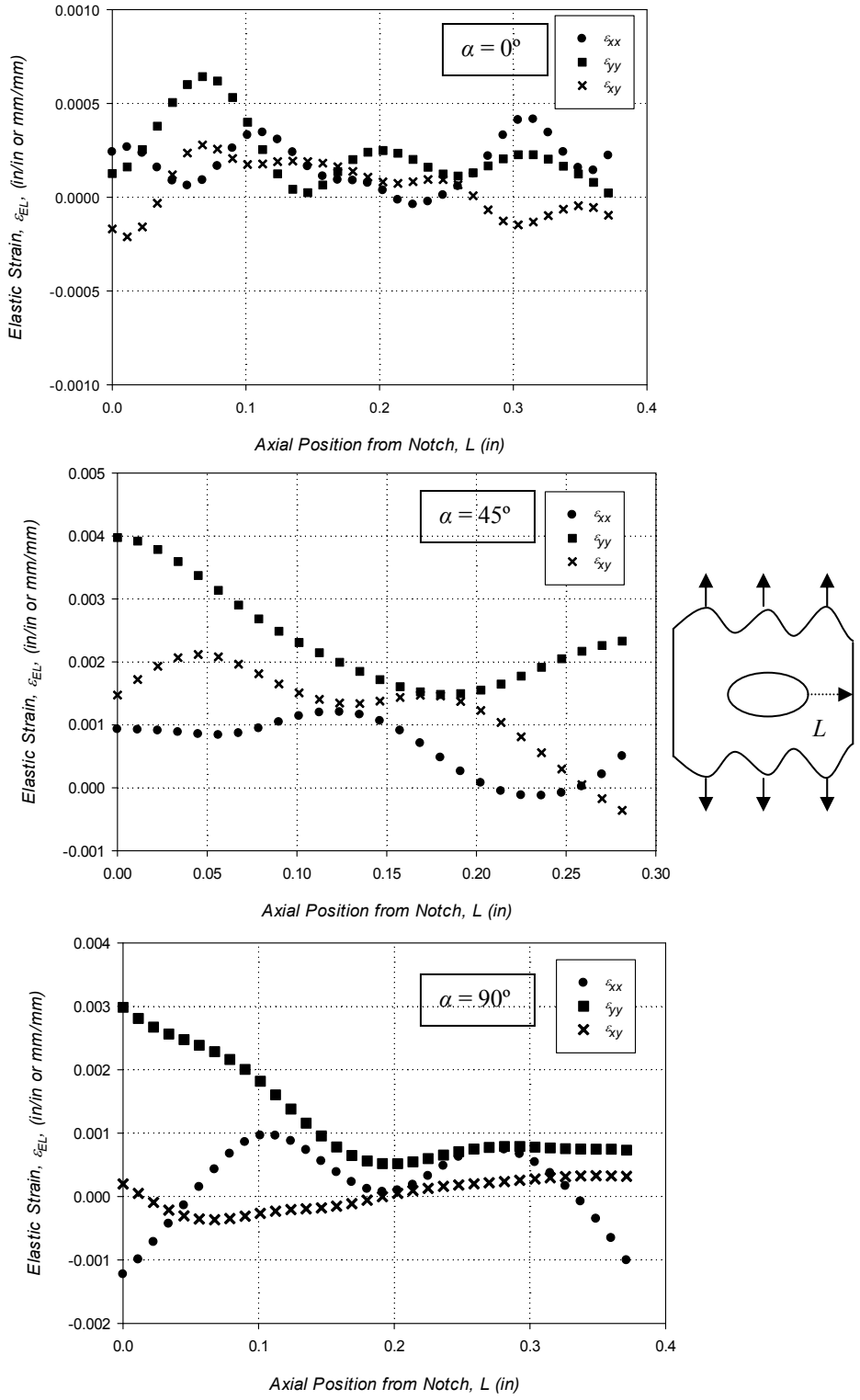

Figure 3.28: The tensorial elastic strain distribution along a line in the *x-camera* direction from the notch root to the specimen edge for various slit (λ= 0.0) notch inclinations in weft (90º) oriented specimens.

It is interesting to note that the difference in the maximum *y-camera* component of strain, typically found close to the notch edge, and the minimum *y-camera* component of strain, usually some distance from the notch edge, is relatively comparable between the α = 45º and α = 90º degree notch inclinations. For example, in Fig 3.28 (θ = 90º (weft)) the percent difference between the maximum and minimum *y-camera* direction strains when α = 45º is 91.3%, while the difference in the α = 90º case is 141.2%.

As previously described, the θ-component of the elastic stress distribution was taken around the open contour of the notch for all elliptical and slit notched specimens for calculation of the near notch SCF as defined in Eq. 3.2.3. The polar-coordinate system used to reference the θ-component of stress is similar to the system defined for the circular notches, but rotated 90º ($\pi/2$ radians) such that 0º (0 radians) indicates the loading axis. To reflect this difference, the θ-axis for the elliptical and slit notch specimens is given the subscript *q*. In all cases, the Hill yield criterion, Eq. (2.1.1), was employed to ensure notch tip elasticity, and hence an accurate representation of the SCF. As was the case for the circular notch specimens, the elasticity solutions proposed by Lekhnitskii [Lekhnitskii, 1968] for an infinite orthotropic plate with an elliptical notch have been leveraged to garner comparison to the DIC results. In most cases, the analytic infinite plate solutions are relatively comparable to the experimental results, however, differences in location of peak stress, and, particularly in the bias (45º) material orientations, a general difference in stress distribution, is observed in some cases. These inconstancies with the analytic stress distribution are attributed to both the finite geometry of the test specimens, and the degree of material discontinuity at the edge of the sharp elliptical notches in the bias (45º) material orientations. For the case of the elliptical notch specimens, comparison to the analytic

results is emphasized, and so the plots of stress are represented individually, with each set of figures representing a single material orientation, θ, and containing the various notch inclinations, α, similarly to the presentation of the strain distributions. For the case of the slit notched specimens, the analytic solutions presented by Lekhnitskii were found to be adversely affected by the apparent singularity of the notch tip. As the DIC strain distributions in Figs. 3.20 through 3.22 indicate, taking an analytic solution around a contour some distance from the notch edge, while possible, would not properly represent the behavior of this class of materials due to the lack of field perturbation away from the notch. Thus, the slit notch results are presented without analytic solutions, and are consolidated by notch orientation into a single figure.

The analytic solution used for comparison to the DIC stress contour is taken from the solution proposed by Lekhnitskii [Lekhnitskii, 1968], where it is presented in general form as an infinite series solution to the problem of complex potentials which satisfy Eq. 1.3.8, as well as the boundary conditions of the problem. It is well known that, for the case of complex potential functions in anisotropic materials, the stress components can be related to the potentials by [Lekhnitskii, 1968],

$$\begin{aligned}
\sigma_x &= 2\,\mathrm{Re}\left[\mu_1^2\Phi_1'(z_1)+\mu_2\Phi_2'(z_2)\right],\\
\sigma_y &= 2\,\mathrm{Re}\left[\Phi_1'(z_1)+\Phi_2'(z_2)\right],\\
\tau_{xy} &= -2\,\mathrm{Re}\left[\mu_1\Phi_1'(z_1)+\mu_2\Phi_2'(z_2)\right]
\end{aligned} \tag{3.2.12}$$

where z_1 and z_2 are complex variables given as,

$$\begin{aligned}
z_1 &= x+\mu_1 y,\\
z_2 &= x+\mu_2 y
\end{aligned} \tag{3.2.13}$$

and μ is defined as in Eq. 3.2.9. As is suggested by Lekhnitskii, only the first term of the infinite series solution is taken, and the complex potentials are given as,

$$\begin{aligned}\Phi_1(z_1) &= \frac{\overline{\beta}_1 - \mu_2\overline{\alpha}_1}{\mu_1 - \mu_2}\cdot\frac{1}{\zeta_1},\\ \Phi_2(z_2) &= -\frac{\overline{\beta}_1 - \mu_1\overline{\alpha}_1}{\mu_1 - \mu_2}\cdot\frac{1}{\zeta_2}\end{aligned} \tag{3.2.14}$$

where the terms $\overline{\alpha}_1$ and $\overline{\beta}_1$ are related to the boundary conditions of the problem, and for the case of uniaxial tensions are given as,

$$\begin{aligned}\overline{\alpha}_1 &= \frac{-p\sin\theta_q}{2}\left(a\sin\theta_q - ib\cos\theta_q\right),\\ \overline{\beta}_1 &= \frac{p\cos\theta_q}{2}\left(a\sin\theta_q - ib\cos\theta_q\right)\end{aligned} \tag{3.2.15}$$

and p is the remotely applied gross stress. The terms ζ_1 and ζ_2 are given as the following,

$$\begin{aligned}\zeta_1 &= \frac{z_1 + \sqrt{z_1^2 - a^2 - \mu_1^2 b^2}}{a - i\mu_1 b},\\ \zeta_2 &= \frac{z_2 + \sqrt{z_2^2 - a^2 - \mu_2^2 b^2}}{a - i\mu_2 b}\end{aligned} \tag{3.2.16}$$

By substituting Eq. 3.2.15 and 3.2.16 into Eq. 3.2.14, the complex potential functions characterizing the stress distributions in an infinite orthotropic plate with an elliptical notch can be formulated. Finally, by taking the derivative of Eq. 3.2.14 and substituting into Eq. 3.2.12, the Cartesian stress components can be found for every point in the infinite body. By employing the proper relationships for x and y, the stress contour around the edge of the elliptical notch can be generated, i.e.,

$$x = a\cos\theta_q,$$
$$y = b\sin\theta_q \tag{3.2.17}$$

All that remains is to employ the simple stress transformation from Cartesian to Polar coordinates, as shown in Eq. 3.2.2, such that σ_θ can be calculated. Figures 3.29 through 3.31 show the θ-component of the stress distribution as calculated using the DIC strain data, in comparison to the analytic stress distribution as predicted by Eq. 3.2.12. Inspection of Figures 3.29 through 3.31 reveal some interesting aspects of the mechanical behavior of this class of material in the presence of a stress riser. It is observed that in cases where the elliptical notch is in line with a principle material orientation, i.e., when α = 0º or 90º, the maximum stress tends to occur at θ_q = 90º (measured from the loading axis), which is as expected in an isotropic material. However, when the notch is oriented at an inclination to one of the principle axes, i.e., when α = 45º, the location of the maximum stress varies with material orientation, and tends to occur around 115º measured from the loading axis. Two distinct differences between the DIC stress results and the infinite analytic solutions are clear upon inspection of the Figs. 3.29 through 3.31. The most significant difference with regards to the mechanical behavior of this class of materials is the size of the area affected by the stress riser. For example, in the case of warp (0º) material orientation and α = 90º (Fig. 3.29), the analytic solution predicts the region of increased stress to occur over approximately 20º (0.35 radians) of the notch edge, while the experimental results show the area of stress perturbation caused by the elliptical notch is actually nearly 86.0º (1.50 radians). Additionally, the analytic solutions tend to predict areas of compressive stress adjacent to areas of tensile stress, particularly in the bias (45º) material orientations, and when the notch is orientated at α = 90º. This behavior is not generally observed in the subject material, indicating that compressive loads are not transferred well in the woven structure. It must also be noted that

correlation in the weft (90º) specimen failed for the α = 90º elliptical notch case over a portion of the specimen, resulting in the plot ranging from θ_q = 90-180 (π/2 - π radians).

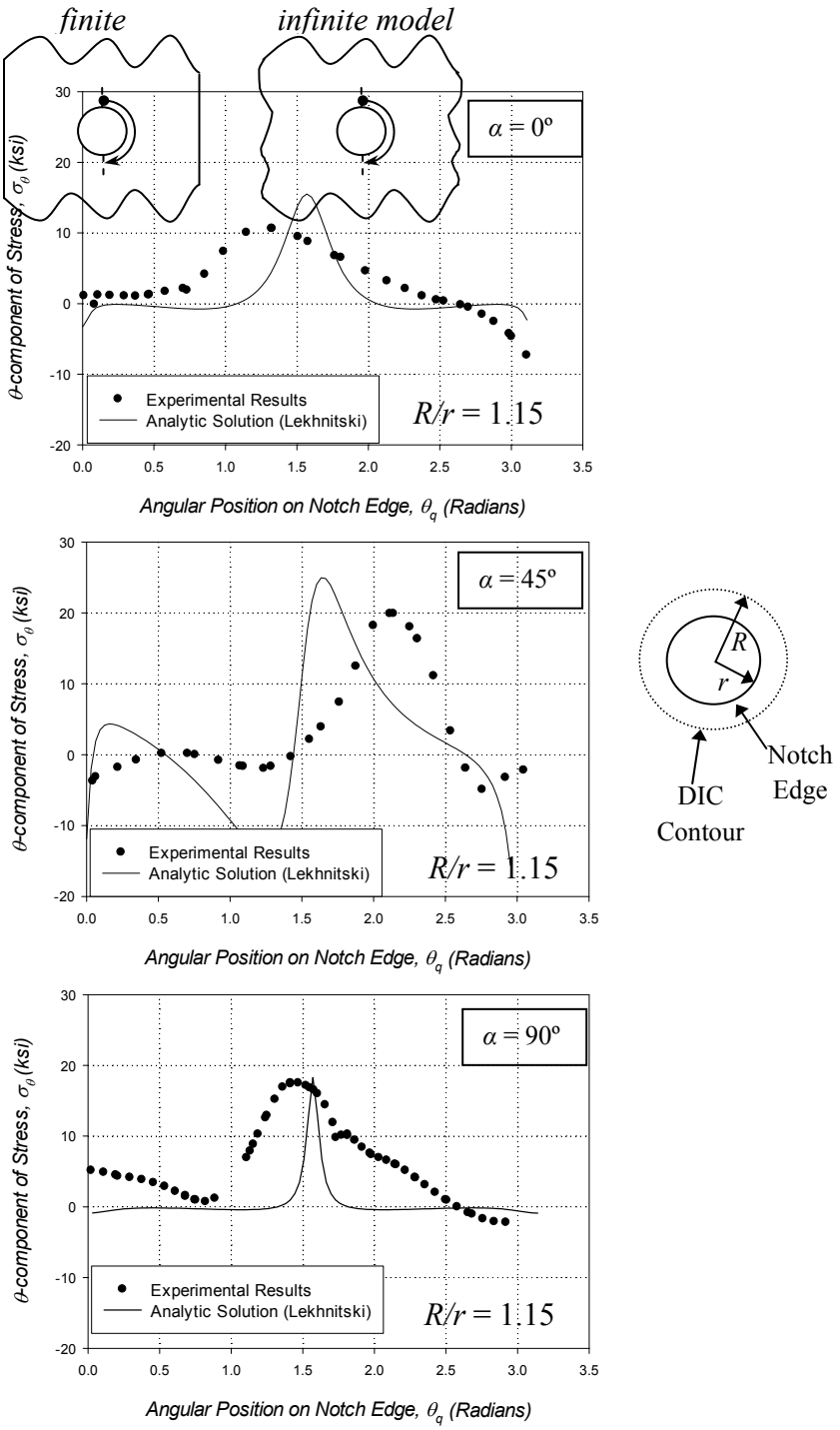

Figure 3.29: Experimental and infinite analytic distribution of the theta component of stress along the edge of an elliptical notch, inclined with respect to the loading axis at various angles, in warp (0º) oriented SS316L woven wire mesh.

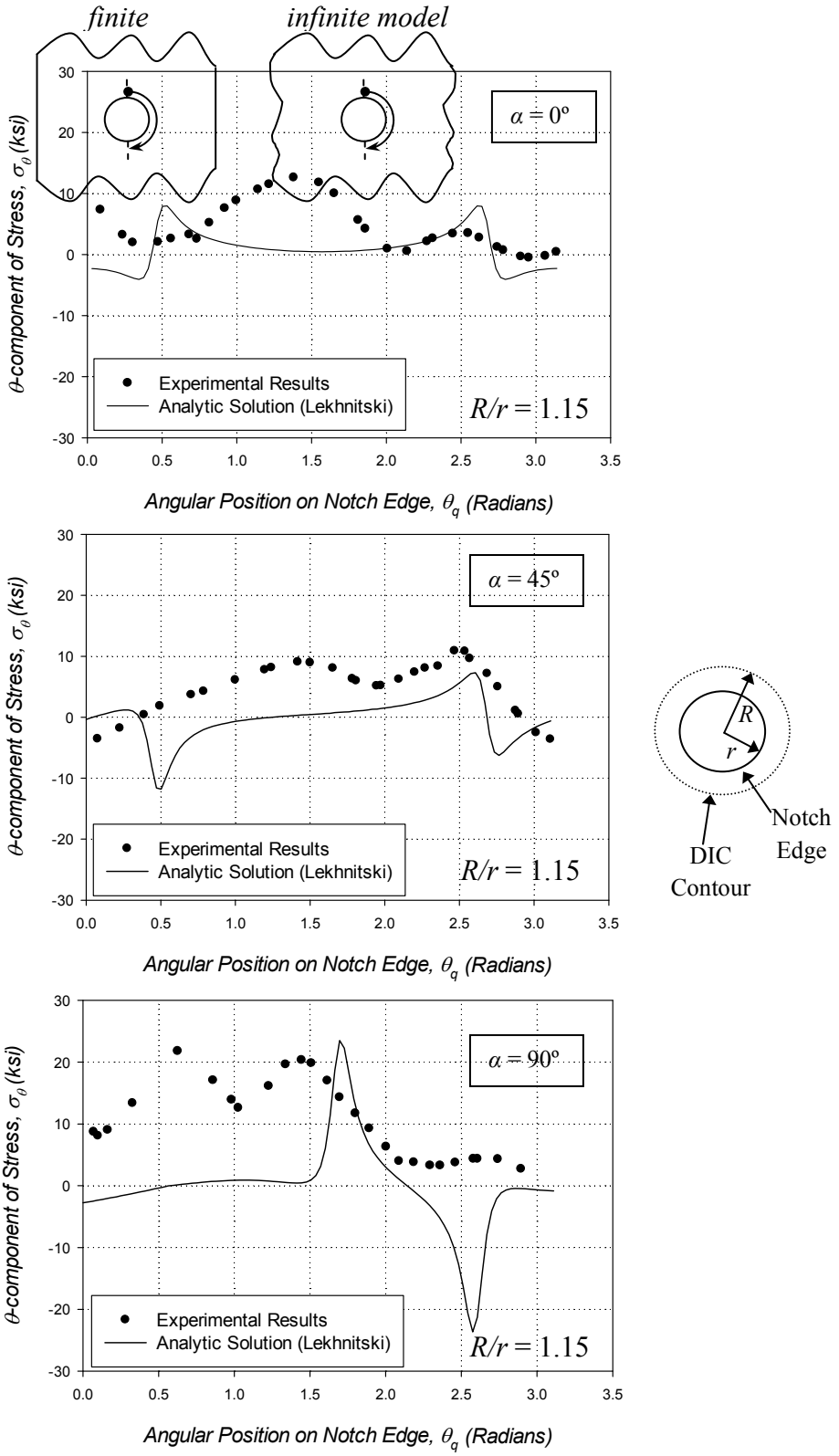

Figure 3.30: Experimental and infinite analytic distribution of the theta component of stress along the edge of an elliptical notch, inclined with respect to the loading axis at various angles, in bias (45º) oriented SS316L woven wire mesh.

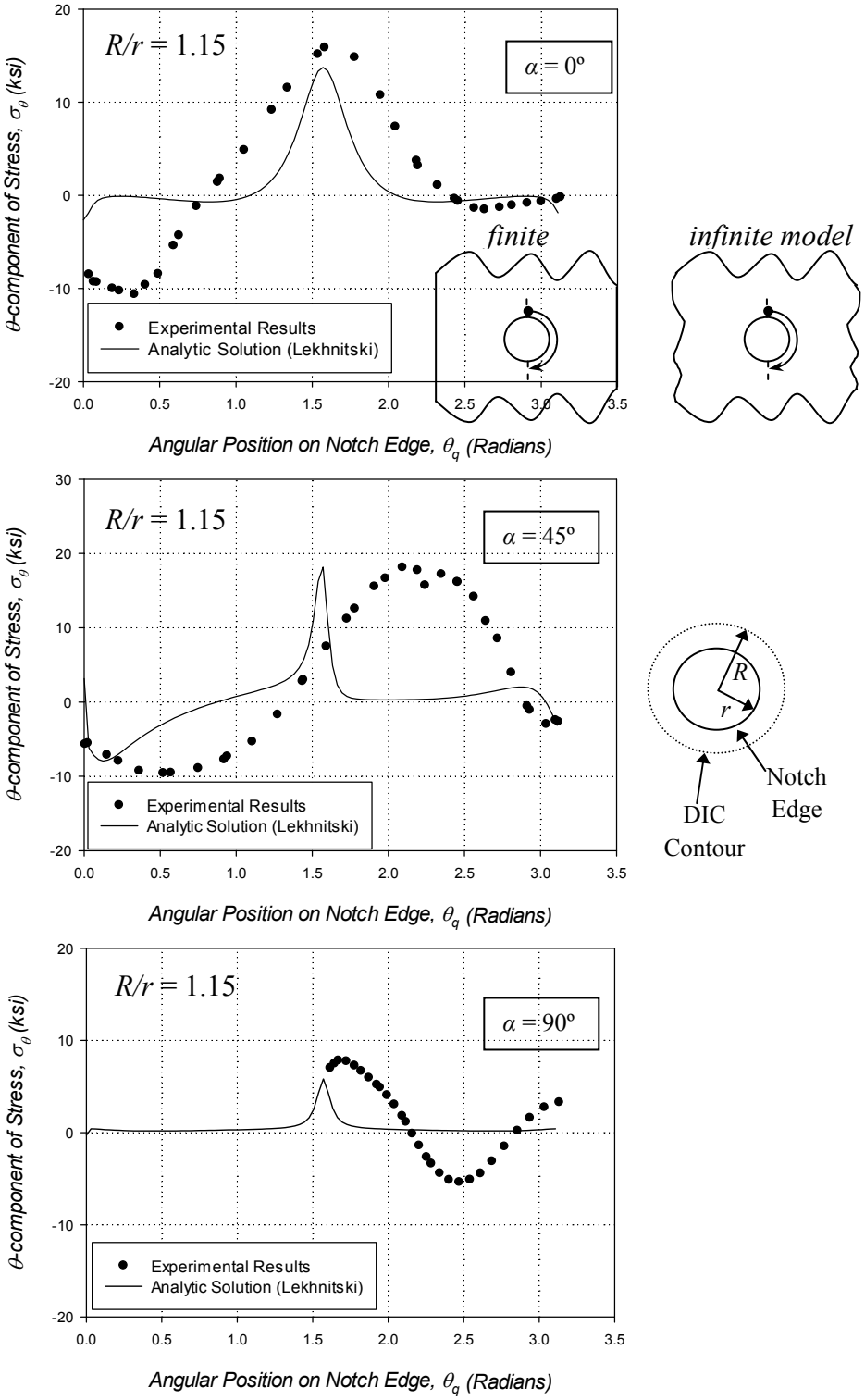

Figure 3.31: Experimental and infinite analytic distribution of the theta component of stress along the edge of an elliptical notch, inclined with respect to the loading axis at various angles, in weft (90º) oriented SS316L woven wire mesh.

As all of the results presented here are fully elastic, i.e., $P < P_{yield}$, it is reasonable to assume the stress distributions are scalable in magnitude up or down, depending on the applied load. This fact was leveraged to facilitate the analytic modeling of the stress distribution around the notch, in which a unit load value was used for P in every case. The application of this unit load produced the distribution of stress around the notch edge, which was then scaled in magnitude to match the maximum value of the DIC results. As such, the analytic solution cannot be used as a metric to gage the validity of the magnitude of the maximum stresses found in the region of the notch, but instead serves the purpose to validate the general shape of the distribution, the location of the measured maximum stress.

The process of extracting strain data and calculating the elastic strain distribution was repeated for the slit notch cases, and this data is presented in Fig. 3.32. Inspection of Figure 3.32 reveals that, particularly in the case of the bias (45º) and weft (90º) material orientations, a slit notch aligned with the loading axis (α = 0º) has little effect on the stress distribution in the structure. It must be noted that the angular reference θ_p, as opposed to θ_q, was used in the case of the circular notches. Recalling that θ_p references the positive *x-camera* axis as shown in the figure inset, it is concluded that me maximum stress in the slit notch cases is at the point of minimum notch radius of curvature, as expected, i.e., at $\theta_p = \pi/2$ radians. It should be noted that brittle type fracture is observed to occur at the slit notch tip in all cases where α = 45º or 90º, which serves to support the theory that a very localized zone of high stress is present at the tip of the notch, while the surrounding area is under nominal loading conditions. Nevertheless, the maximum value of the theta component of stress, regardless of position on the edge, is taken as the value for the calculation of the SCF.

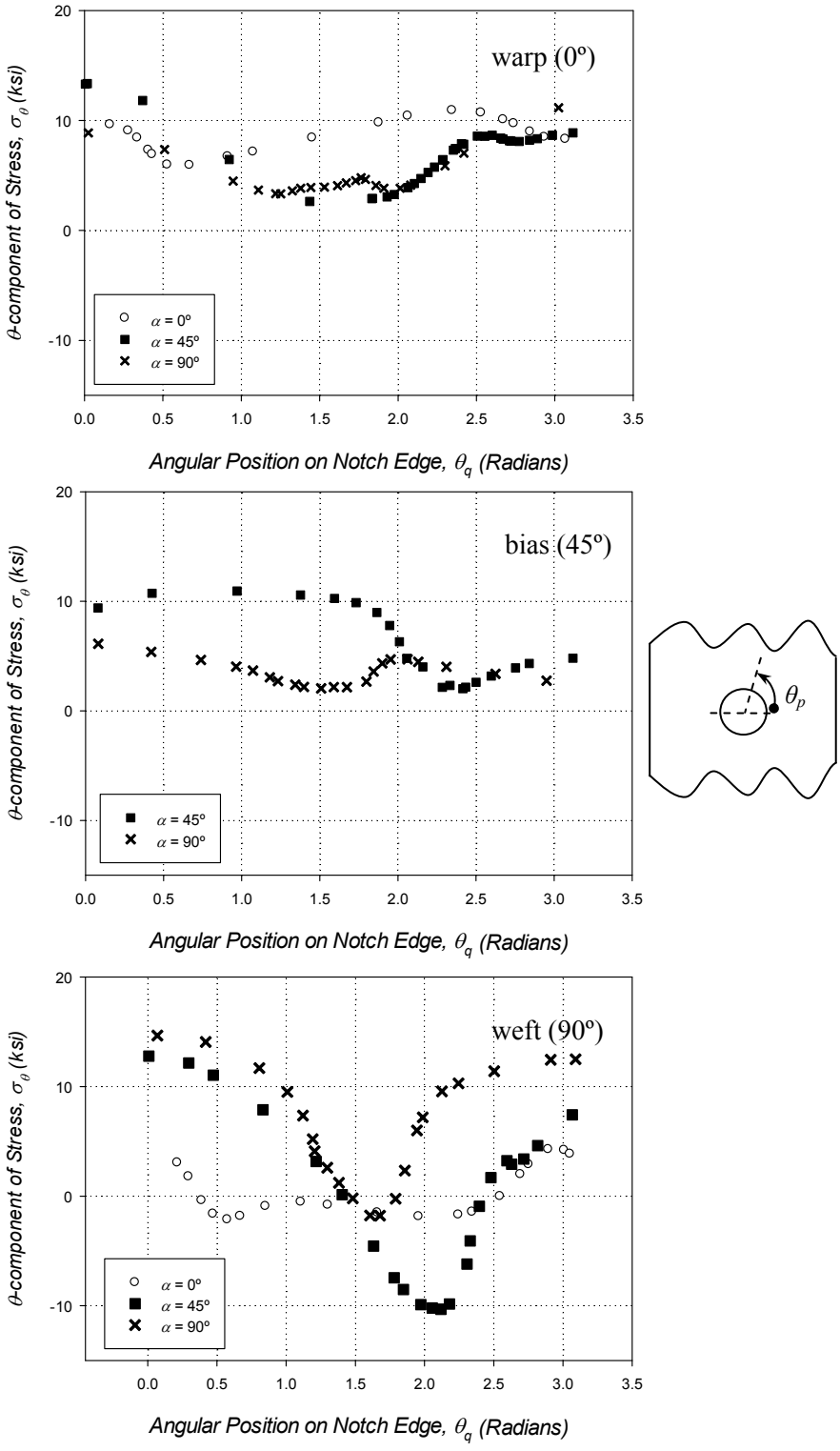

Figure 3.32: Experimentally-determined distribution of the theta component of stress along the edge of a slit notch, inclined with respect to the loading axis at various angles, in various material orientations of SS316L woven wire mesh.

With the stress distribution now known for the area near the edge of the notch for all experimentally treated geometries, development of the experimental SCF curves for this class of material is possible. As the SCF in this case is dependent on three experimentally treated variables; the material orientation, θ, the notch orientation, α, and the notch aspect ratio, λ, it is of great interest to characterize the SCF as a function of the various parameters using graphs. This allows for functional relationships to be observed, and provides clear insight into the combination of parameters that lead to the highest, and lowest, concentration of stress. Figures 3.33 through 3.35 show the relationship between the near field gross SCF and the notch aspect ratio, λ, the notch orientation, α, and the material orientation, θ, respectively. It is immediately clear upon inspection of Fig. 3.33 that the results from the bias (45º) material orientation have produced SCF values that appear unreasonable. While it should be noted that the maximum stress values for these cases have been calculated from DIC frames corresponding to very low gross loads, and that the Hill criterion for yielding has not been exceeded at the measurement contour close to the notch edge, i.e., the use of an elastic constitutive relationship is justified, such a high SCF value dictates that the wires at the notch edge are yielding almost immediately upon loading. As the first few DIC frames from which these results have been calculated are dominated by non-linear wire interactions, it is not ideal to extract data from these frames. Furthermore, it is conceded that the fixed grip conditions in the bias (45°) material orientation experiments inherently introduce a high level of specimen buckling as a result of the shear coupling exhibited by this material [Basset et al., 1999]. This specimen buckling produces out of plane displacement in the vicinity of the notch during tensile testing, even at low gross loads. Thus, it is possible that the results indicating SCF values near sixty may be erroneous.

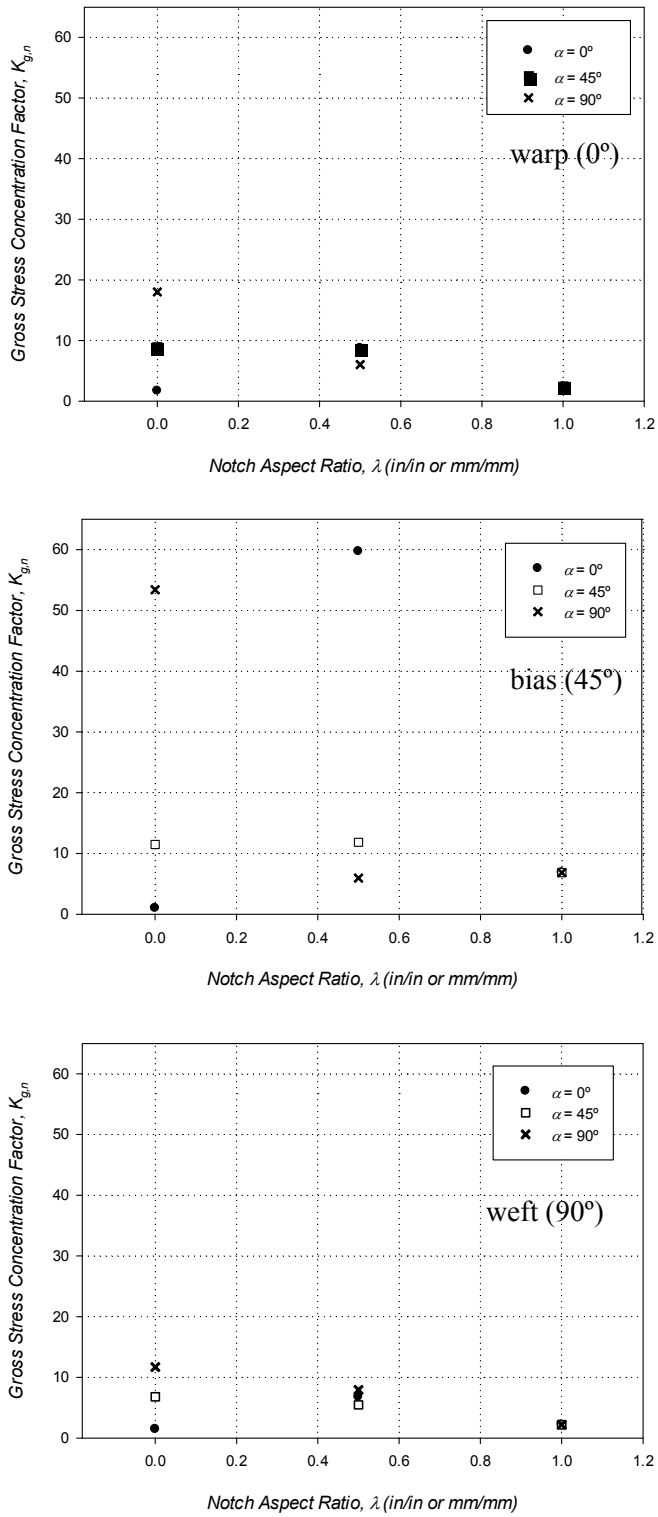

Figure 3.33: The near notch gross SCF present in the SS316L woven wire mesh plotted as a function of the notch aspect ratio at various material and notch orientations.

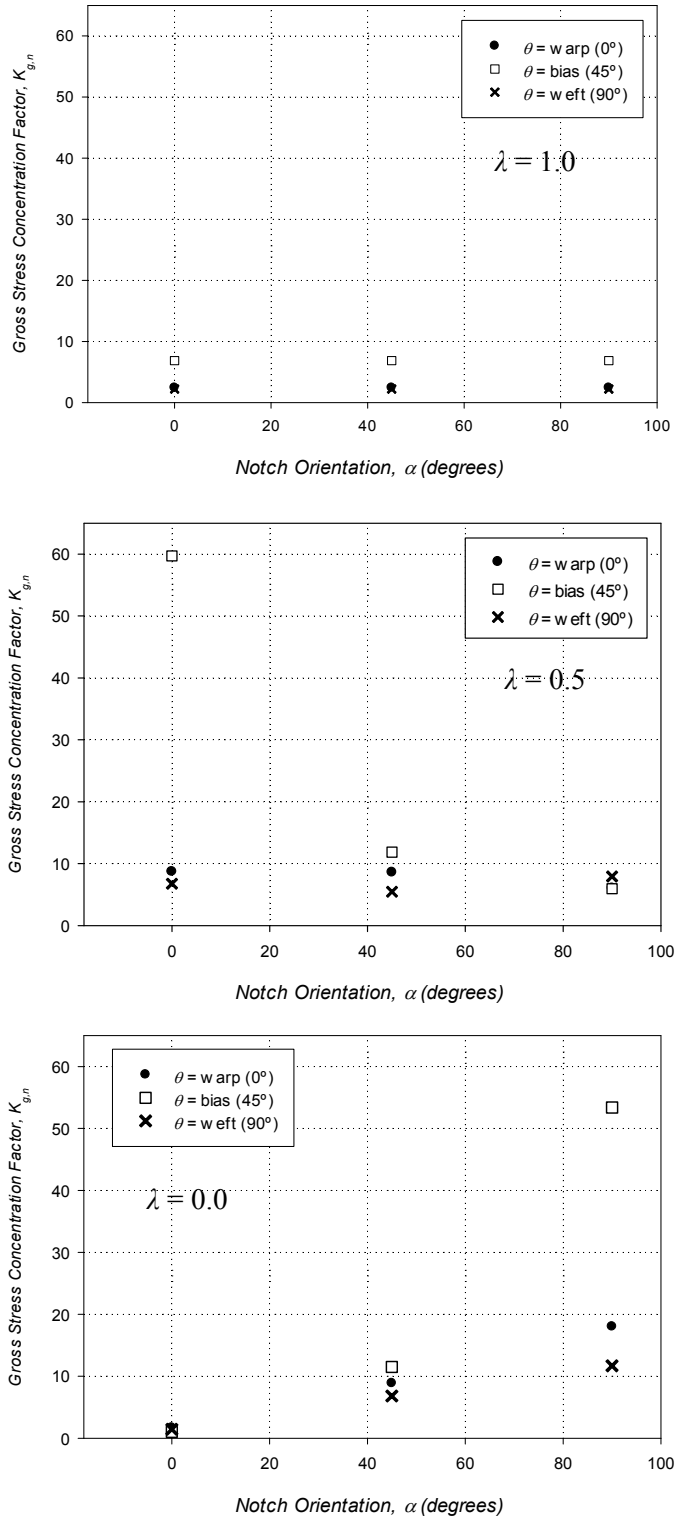

Figure 3.34: The near notch gross SCF present in the SS316L woven wire mesh plotted as a function of the notch orientation at various material orientations and notch aspect ratios.

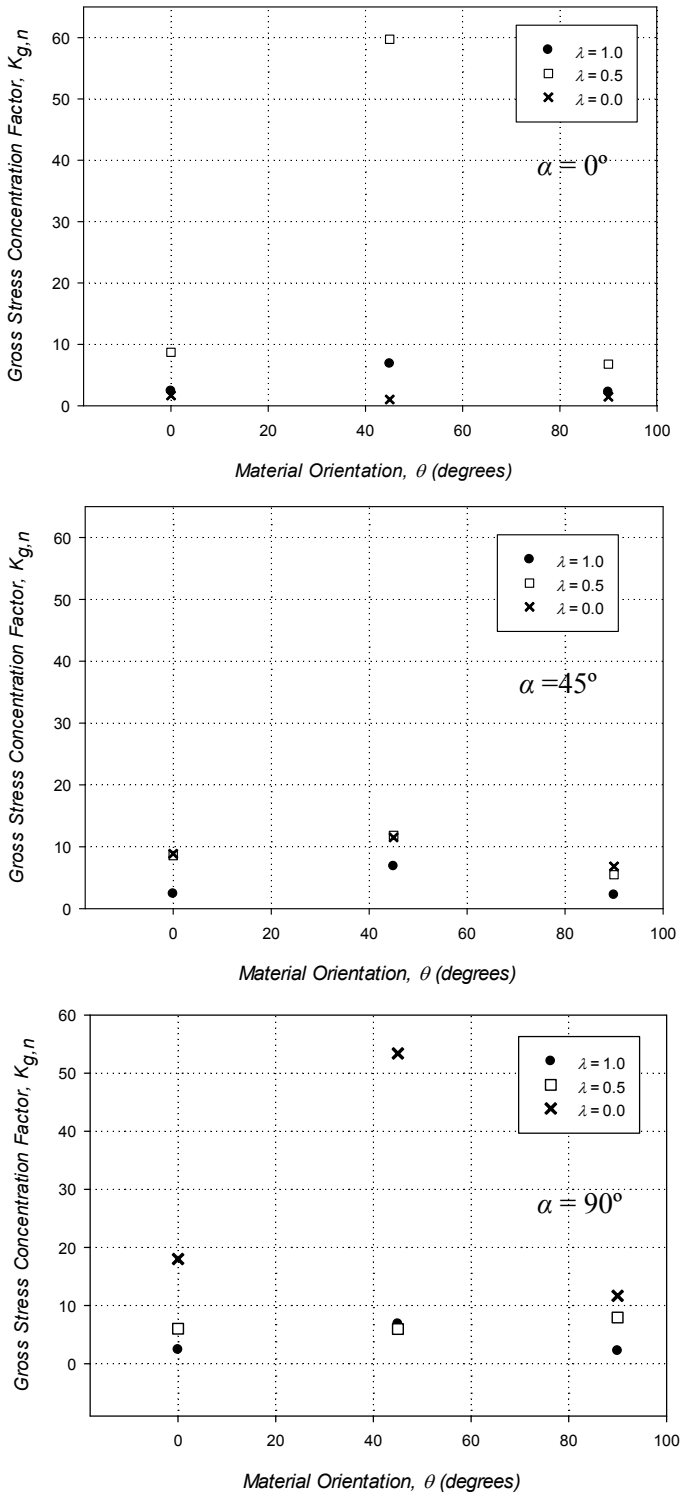

Figure 3.35: The near notch gross SCF present in the SS316L woven wire mesh plotted as a function of the material orientation at various notch orientations and notch aspect ratios.

Future work must be pursued to investigate this problem further, perhaps by employing an alternative test setup, a modified set of wave gripes, or by conducting experiments at material orientations intermediate to the ones treated herein, i.e., at θ = 15º intervals. This study is left to future research, and possible remedies are expounded on in the future work section of this thesis.

The set of SCF plots which most resemble the classical relationships between notch geometry and the concentration factor in isotropic homogenous materials is Fig. 3.34, which shows the SCF plotted as a function of notch orientation at various material orientations. It can be observed that the most damaging notch case, if the outliers of the bias (45º) material orientation are not considered, is the case of the slit notch (λ = 0.0) oriented at 90º to the loading axis (α = 90º) in the warp (0º) material orientation, which produces a near notch SCF value of 18.02. In contrast, the lowest SCF value is found to be 1.45, which corresponds to a weft (90º) material orientation, a notch aspect ratio of λ = 0.0, and a notch orientation of α = 0º. It is interesting to note that there is very little difference in the SCF value for the various notch and material orientations (again excluding the outlier values) in the case of the elliptical (λ= 0.5) notch. The maximum SCF value in the case is 11.85, which occurs in the bias (45º) material orientation, and in the 45º notch orientation. If the results from the bias (45º) are discounted completely, then the maximum value for the elliptical notch case is again found at a notch angle of 45º, but in the warp (0º) material orientation at 8.60. In general, the lack of variation of the SCF with notch orientation is indicative of the fact that this material is not highly sensitive to the radius of curvature of a defect, which is attributable to the lack of mechanical coupling between the adjacent warp wires (low inter-wire coupling). Inspection of Figure 3.35, which plots the SCF as a function of the material orientation, θ, at various degrees of notch aspect ratio, λ, and notch orientation, α, reveals a transition in the value of the notch aspect ratio that produces the

highest SCF in a given material orientation. For example, in the case where α = 0º, all of the material orientations have a minimum SCF for the slit notch case (λ = 0), and a maximum SCF for the case of an elliptical notch case (λ=0.5), whereas in the case where the notch orientation is 90º, the maximum SCF values are seen to occur in the slit notch cases. A clear transition is observable in this behavior upon inspection of the intermediate α = 45º notch orientation. The near notch gross SCF data for all of the various cases is arranged in tabular form in Tables 3.6 through 3.8, which comprise data from the warp (0º), bias (45º), and weft (90º) cases, respectively. Inspection of Table 3.7 clearly shows that the bias (45º) material orientation produces SCF values that are outliers to the rest of the data, and so these values have been asterisked to indicate that further testing is needed for confirmation.

Table 3.6: Near notch gross Stress Concentration Factors for SS316L woven wire mesh in the warp (0º) material orientation.

Material Orientation, θ (Degrees)	Notch Orientation, α, (Degrees)	Notch Aspect Ratio, λ, (in/in or mm/mm)	Near Notch Gross SCF, $K_{t,gn}$
0	0	1.0	2.39
		0.5	8.07
		0.0	1.67
	45	1.0	2.39
		0.5	8.58
		0.0	8.86
	90	1.0	2.39
		0.5	6.02
		0.0	18.02

Table 3.7: Near notch gross Stress Concentration Factors for SS316L woven wire mesh in the bias (45º) material orientation.

Material Orientation, θ (Degrees)	Notch Orientation, α, (Degrees)	Notch Aspect Ratio, λ, (in/in or mm/mm)	Near Notch Gross SCF, $K_{t,gn}$
45	0	1.0	6.85
		0.5	59.7
		0.0	1.0
	45	1.0	6.85
		0.5	11.85
		0.0	11.49
	90	1.0	6.85
		0.5	5.96
		0.0	53.39

Table 3.8: Near notch gross Stress Concentration Factors for SS316L woven wire mesh in the weft (0º) material orientation.

Material Orientation, θ (Degrees)	Notch Orientation, α, (Degrees)	Notch Aspect Ratio, λ, (in/in or mm/mm)	Near Notch Gross SCF, $K_{t,gn}$
90	0	1.0	2.21
		0.5	6.77
		0.0	1.45
	45	1.0	2.21
		0.5	5.47
		0.0	6.81
	90	1.0	2.21
		0.5	7.94
		0.0	11.69

3.3 Fractography of Notched Uniaxial Specimens

In an effort to understand the mechanisms behind the failure of the various notched woven wire mesh specimens, considerable attention has been paid to the post-mortem fracture characteristics. Fractography has been performed on the failed woven wire mesh specimens, using a DinoLite Model AM7015MT at 70 times magnification. These images are presented below in Figs. 3.36 through 3.42, differentiated by notch orientations and aspect ratio.

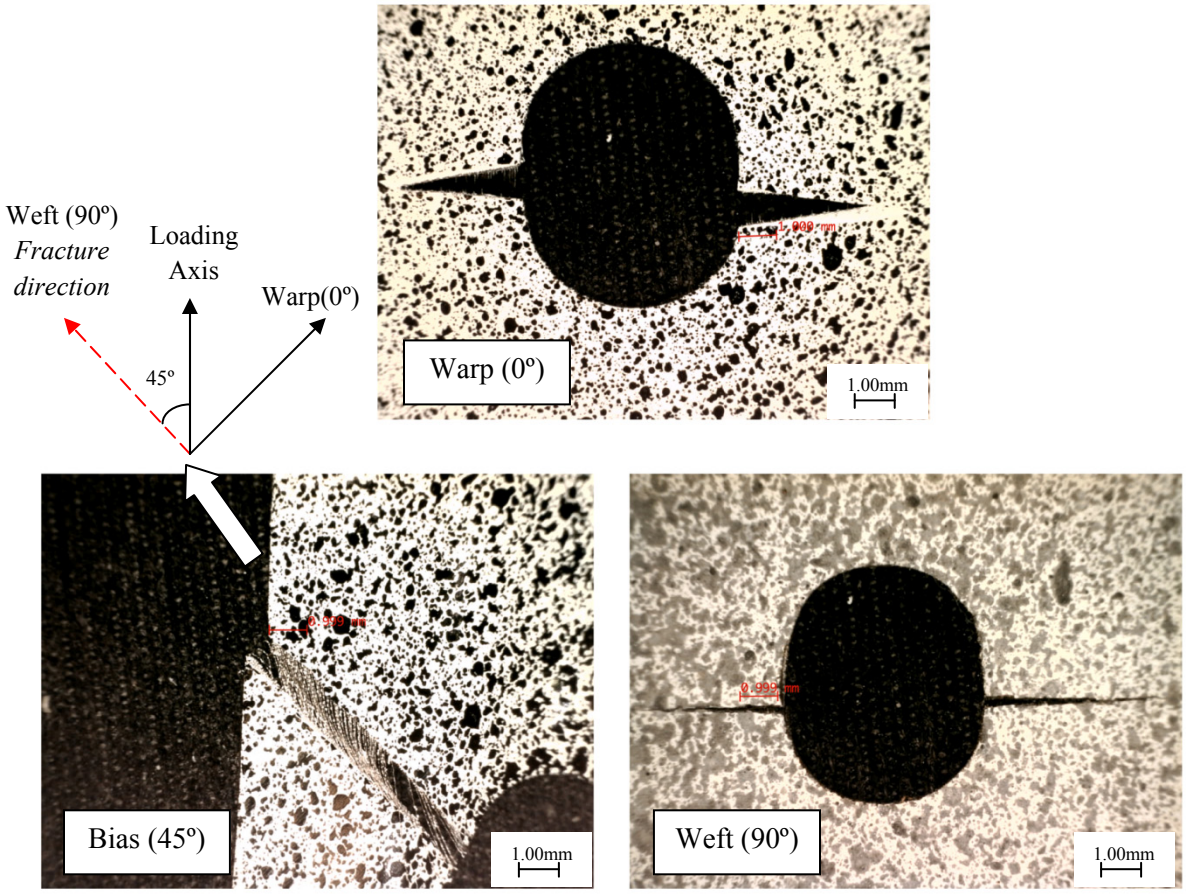

Figure 3.36: Fracture surface images for circle notched SS316L woven wire mesh specimens in various material orientations.

This investigation revealed a strong dependence of fracture orientation and appearance on material orientation. Observations were made from detailed inspection of the failure surfaces

post fracture for each specimen tested, with focus on the degree of wire pull-out (fraying), waviness of the fracture surfaces, orientation of the fracture with respect to loading, and the direction of fracture propagation.

Inspection of Fig. 3.36 shows clear differences in appearance of the fracture surface of each material orientation for the case of a circular notch. The warp (0º) material orientation fractures with no discernable wire fray or pull out, and the fracture surface displays little waviness is terms of its propagation. Failure occurs in the warp wires only, with very little if any load being transferred to the weft. The initially observed fracture began at the edge of the notch, at the line of symmetry running perpendicular to the line of load, and progressed outward as adjacent warp wires failed and unloaded, forcing neighboring wires to accept more load. It is interesting to note that the wavy fray-type fracture typically associated with this material orientation [Kraft and Gordon, 2011] is not observed in the notched material case, indicating that the stress concentration has reduced the process zone, resulting in only localized yielding and fracture. Failure in the weft (90°) orientation is very concentrated around the stress riser. No wire fraying is observed, and fracture propagates through the material quickly and in a straight path. Again, the failure surface is orthogonal to the loading direction, and the fracture initiates at the edge of the notch along the line of symmetry of the circular notch. Failure in the bias (45º) orientation is characterized by combinations of the failure characteristics associated with the warp (0°) and the weft (90°). Shear coupling of the off-axis specimens leads to the formation of shear stresses in the uniaxially loaded samples [Kraft Gordon, 2011], and indication of this can be observed from the high degree of weft wire fray. Fracture propagates along a direction perpendicular to the weaker warp (0º) material direction, and initiates at some angle to *x-camera*

axis centered at the notch center point. This indicates that maximum stress in the bias (45º) material orientation cases is not necessarily at a point of minimal radius of curvature.

In general, the observations made in the case of the circular notch are consistent for the case of elliptical notches oriented in line with the principle material orientations, as can be observed in Figs. 3.37 and 3.38. Inspection of the weft (90º) material orientation case in Fig. 3.37 reveals a small amount of weft wire fray present at the rupture location away from the notch root (left fracture surface), indicating that fracture of the wires occurred away from the notch edge, a result of wire cut-off at the notch, and indicative of the structural nature of the woven material.

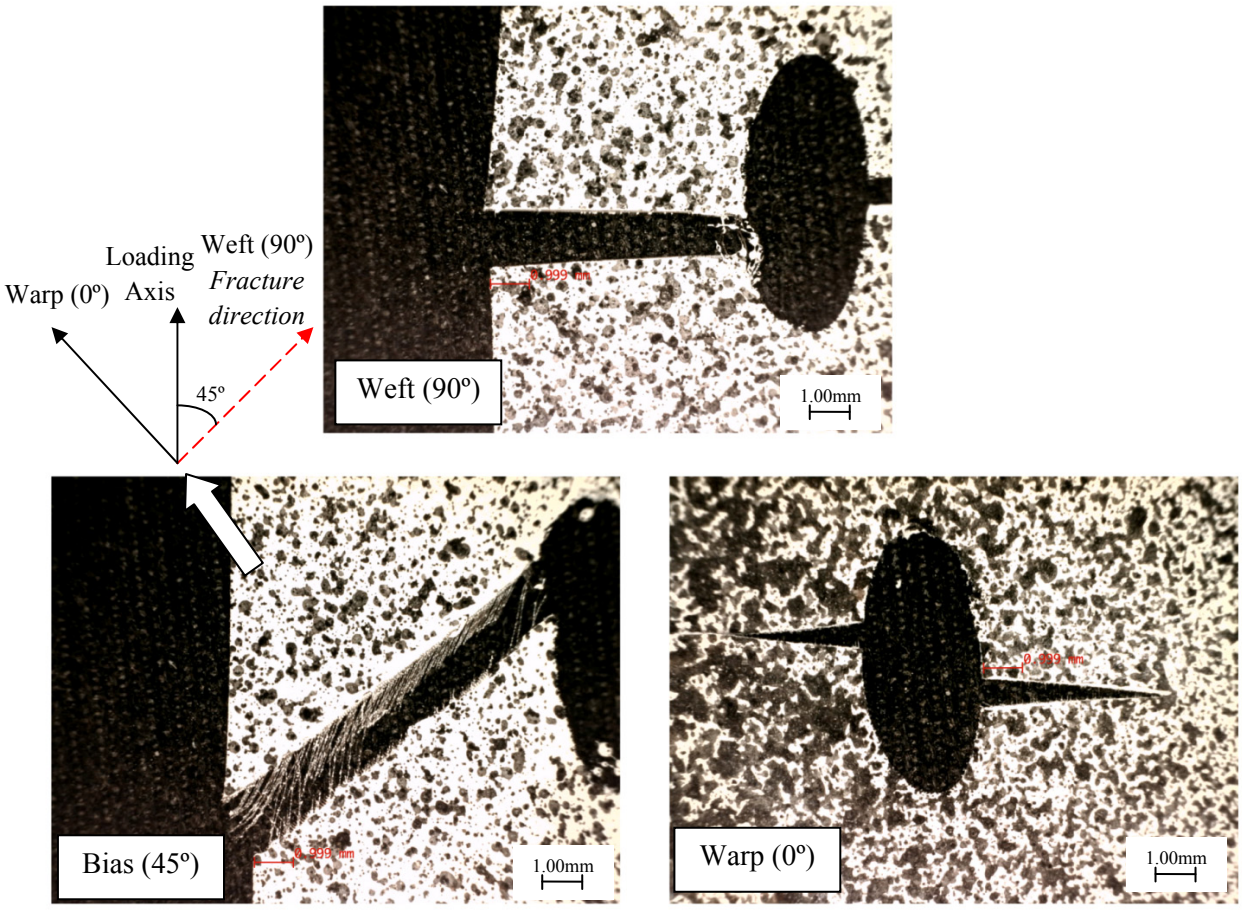

Figure 3.37: Fracture surface images for elliptical notched SS316L woven wire mesh specimens in various material orientation with α = 0º.

Also, slight variation in the symmetry of the fracture initiation zone on opposite sides of the notch is observed, and is most likely attributable to inconsistencies in the weave stricture, either naturally occurring or introduced during the notch punching process, in the vicinity of the notch. It is noted that the fracture occurring at the notch root in the weft (90º) case (right most fracture surface) shows no weft wire pull-out, indicating that a wire at the notch edge failed first.

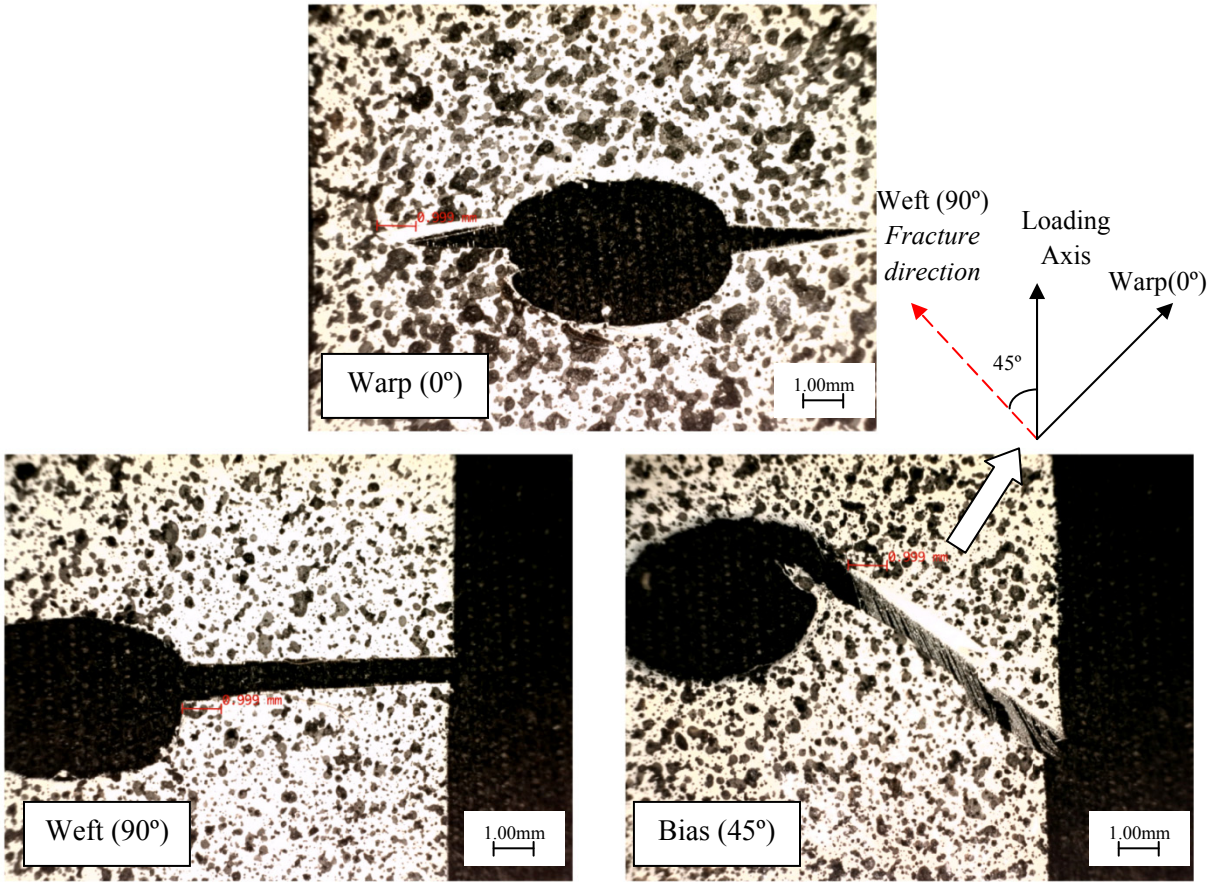

Figure 3.38: Fracture surface images for elliptical notched SS316L woven wire mesh specimens in various material orientation with α = 90º.

Inspection of Fig. 3.39, which shows the rupture associated with the 45º-oriented elliptical notches in various material orientations, also reveals that the location of maximum stress at the surface of the inclined notch is not at the notch root, but rather at some angle offset

from the minimum radius of curvature. Fracture at the notch edge in the warp (0º) and weft (90º) cases indicates that the amount of shear stiffness, i.e., the MSGC, in the material is sufficient to cause failure at the notch edge, otherwise, failure could be expected to initiate at any wire. Inspection of the process zone for the 45º inclined elliptical notch reveals that the location of the rupture is correlated with the location of the first continuous wire, and not necessarily on the edge of the notch, providing support for the previous observations regarding the asymmetry of the strain distributions provided in Figs 3.17 - 3.19 as being related to the distance from the notch edge to the first continuous wire.

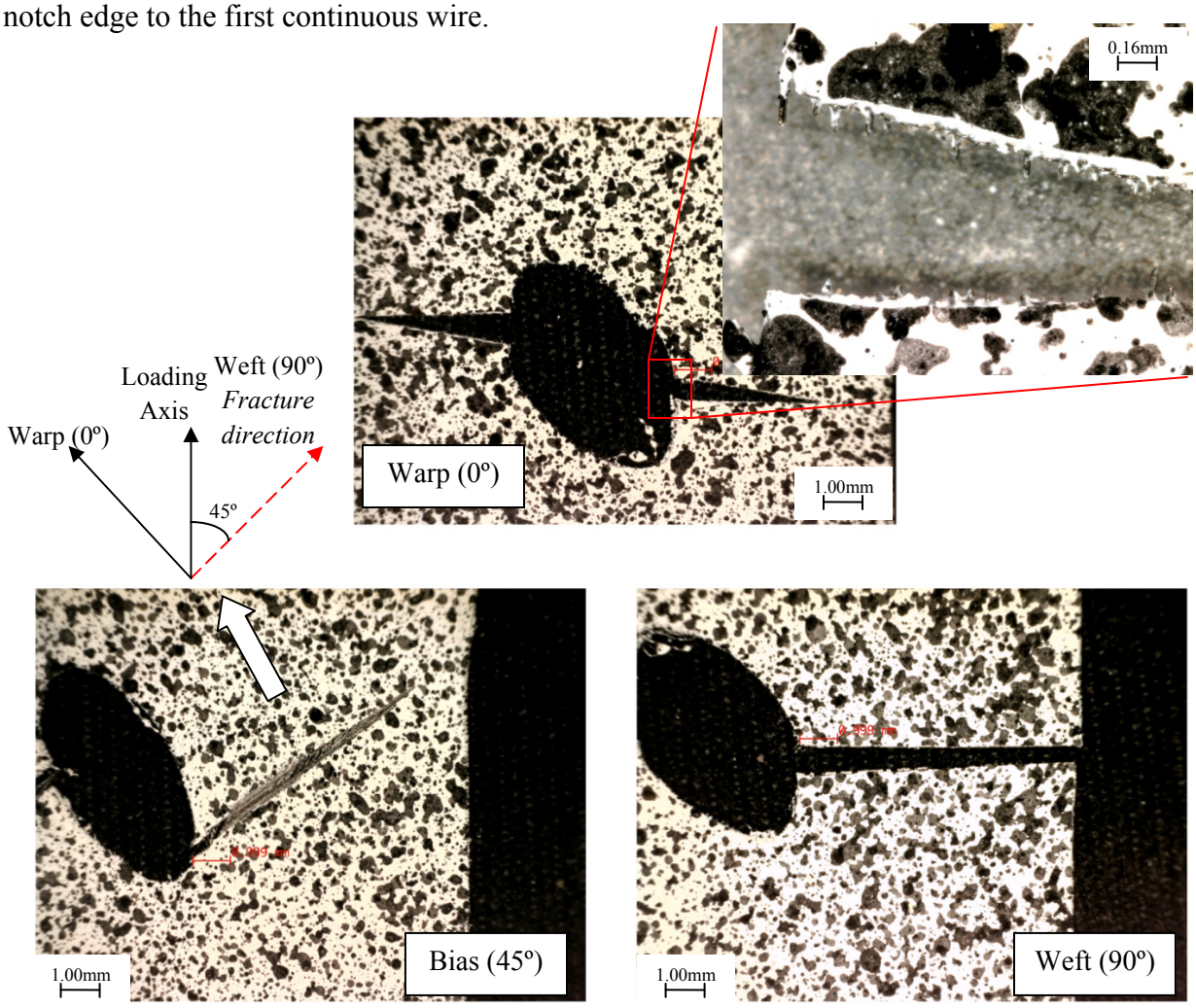

Figure 3.39: Fracture surface images for elliptical notched SS316L woven wire mesh specimens in various material orientation with α = 45º.

Fracture zones for the slit notched uniaxial specimens are shown in Figs. 3.40 though 3.42. In general, when mesh rupture was observed to occur at the location of the notch, the fracture is observed to initiate at the notch root, and to propagate in a similar fashion to the elliptical and circular notches. Inspection of the Fig. 3.40 shows that the α = 0º oriented notch failed to produce a stress concentration significant enough to cause mesh failure during the tensile tests in the warp (0º) and the weft (90º) material orientations, and rupture occurred in the grips. This observation supports the conclusion that slit notches oriented with the loading axis are not damaging to this class of material. Conversely, the failure location in the bias (45º) material orientation was at 0º oriented notch root.

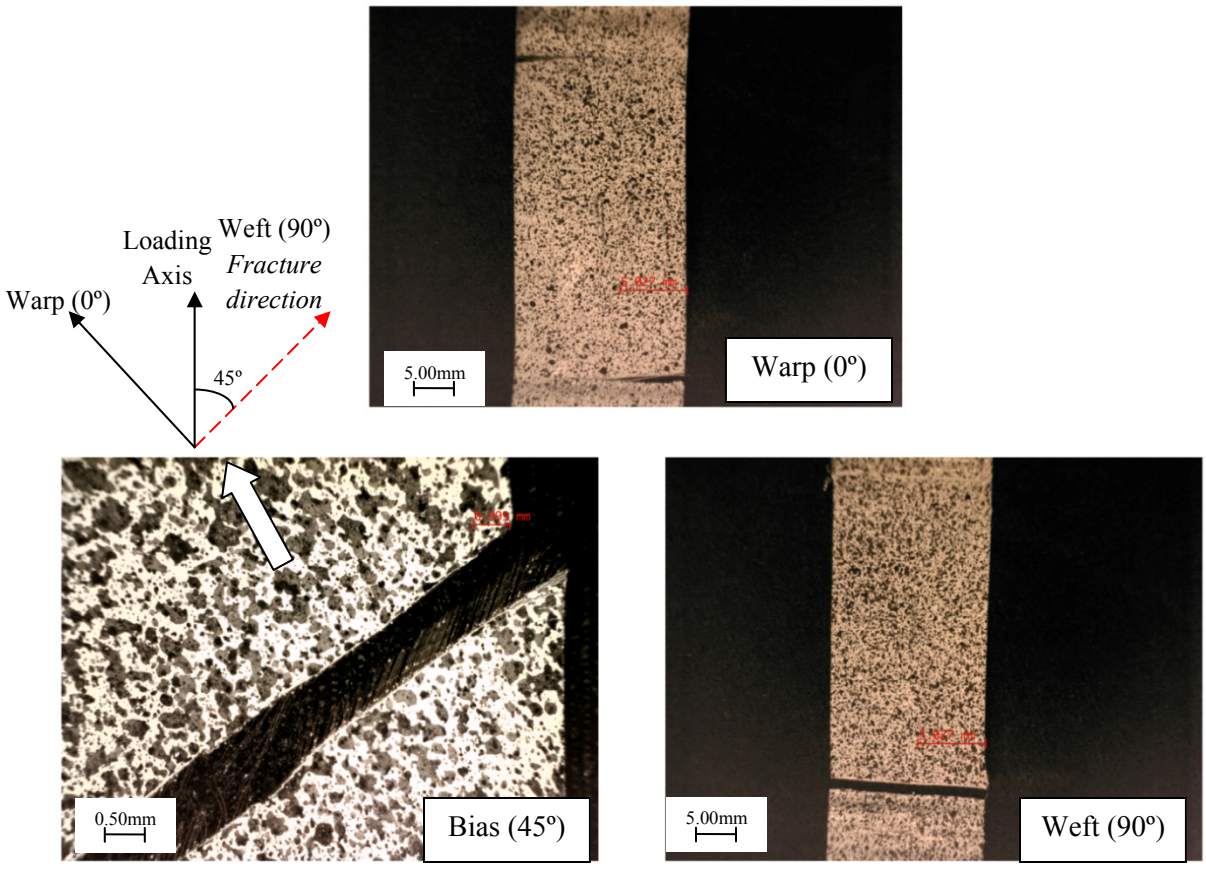

Figure 3.40: Fracture surface images for slit notched SS316L woven wire mesh specimens in various material orientation with α = 0º.

As stated in Section 3.2, the location of the rupture zone observed in the fractography of the slit notch specimens is not in agreement with the stress distributions taken from the DIC measurements for the weft (90º) case in both the inclined notch (α = 45º) and the perpendicular oriented notch (α = 90º) cases. This can be explained, by the inability of the DIC method to capture the strains directly at the notch tip, coupled with the extremely local stress concentration. Evidence to the fact of a highly localized process zone is seen in the degree of fracture surface sharpness in these cases, which indicates a brittle type fracture of the material, and in the consistency of the fracture initiation zone, in all material, θ, and notch, α, orientations, which is not observed in the circular or elliptical notch cases.

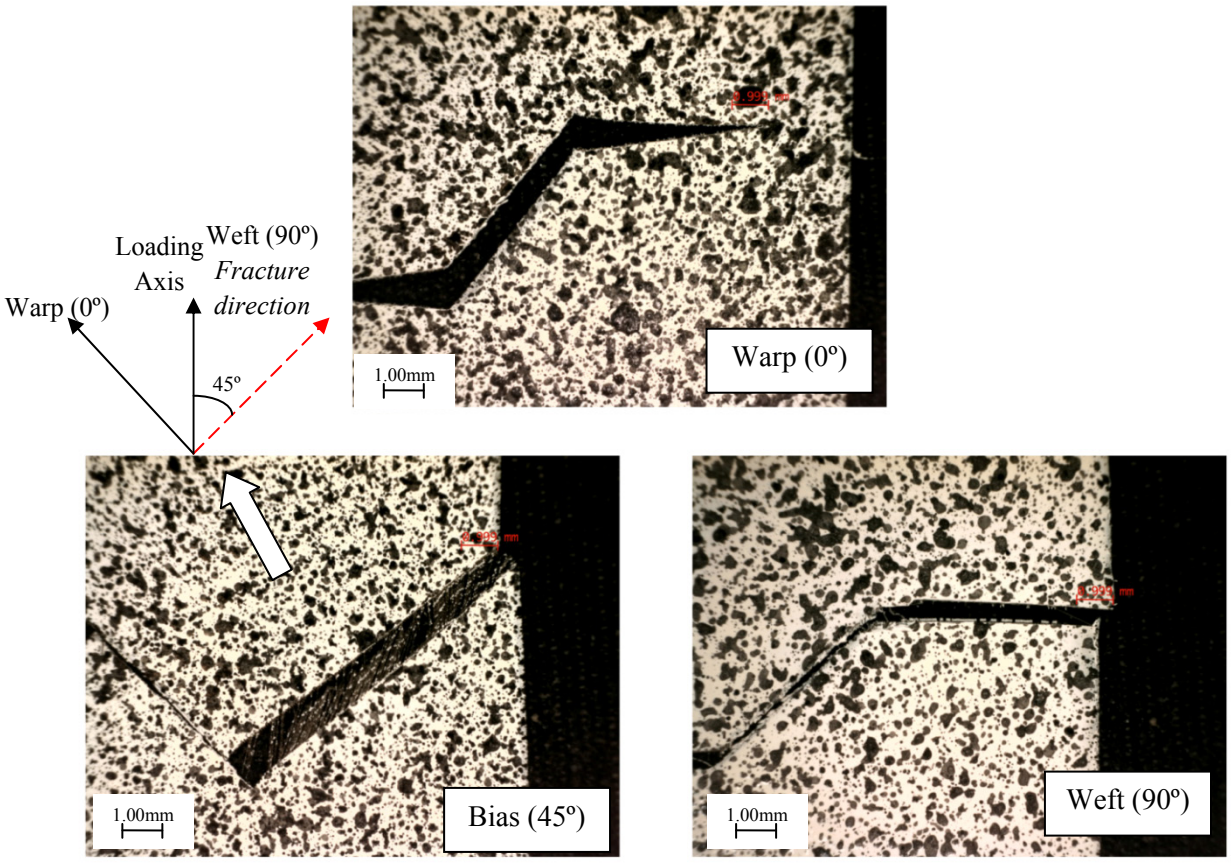

Figure 3.41: Fracture surface images for slit notched SS316L woven wire mesh specimens in various material orientation with α = 45º.

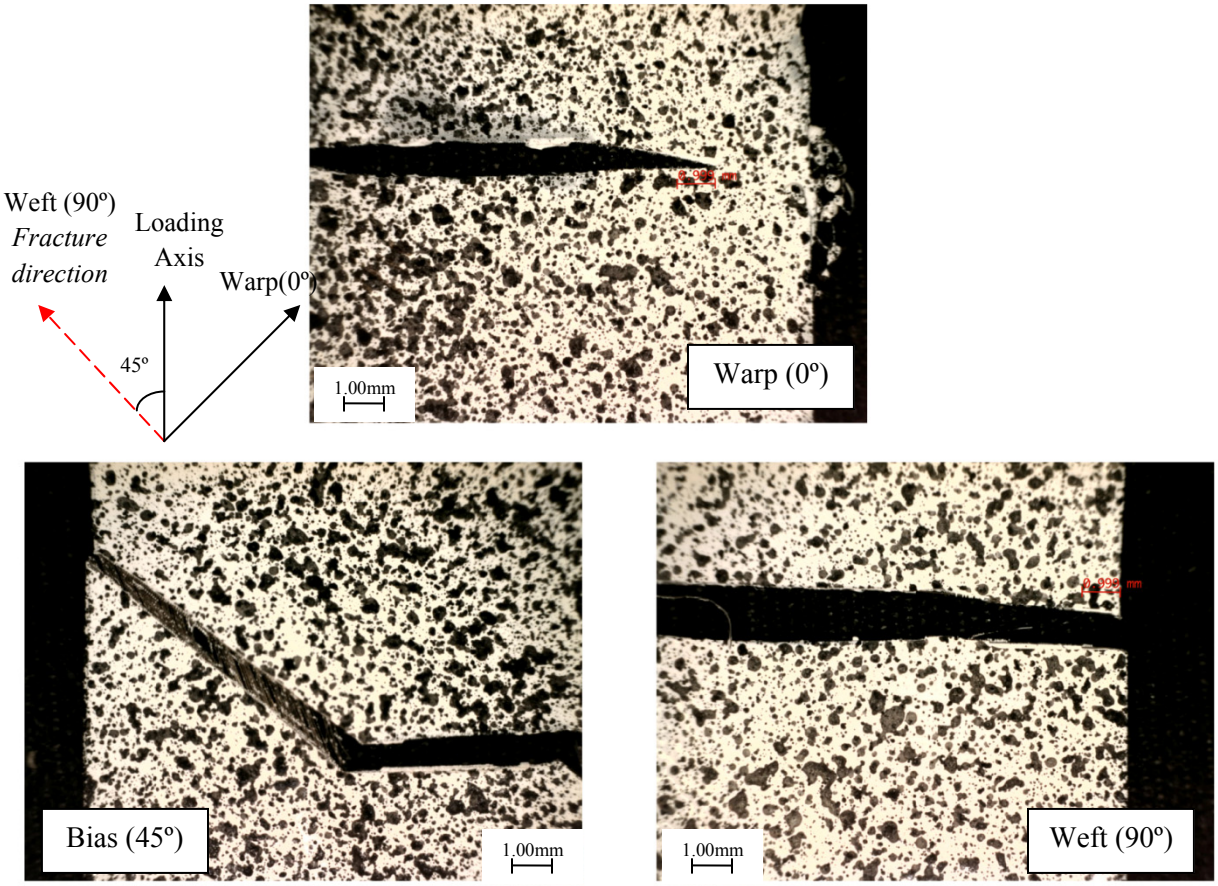

Figure 3.42: Fracture surface images for slit notched SS316L woven wire mesh specimens in various material orientation with α = 90º.

Further support for this hypothesis is provided by Fig. 3.43, which shows a close up view of the wires at the fracture location in an elliptical and slit α = 90º notches, in weft (90º) oriented specimen. The process zone in the case of the elliptical notch (Fig. 3.43(a)) clearly involves more wires, shows evidence of weft wire pull-out from the mesh, and is more evenly distributed around the areas of minimum curvature. The process zone in the case of the slit notch (Fig. 3.43(b)), distinguishable by the point of warp wire pull out from the mesh, is far more concentrated, and the surrounding wires exhibit very little sign of ductile deformation. From investigation of these images, it is plausible that the area of high stress in region of the notch tip

is confined to a small group of contacting wires, making it very difficult to discern using a near field approach as was employed to generate Figs. 3.17 - 3.19.

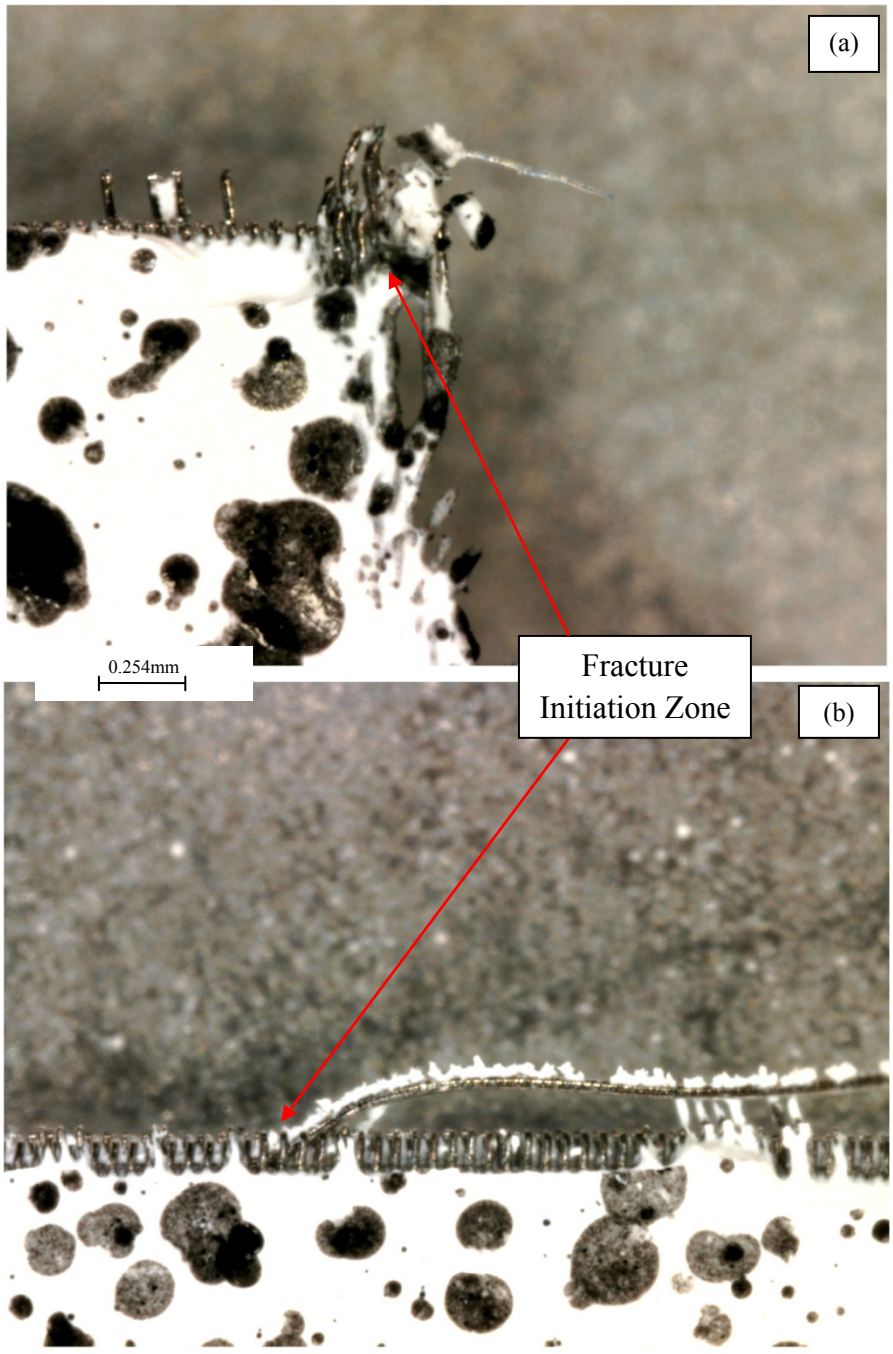

Figure 3.43: Fractographic image of the region of the notch root in the weft (90º) material orientation with (a) elliptical and (b) slit notches in the α = 90º direction.

3.4 Effective Stress Concentration Factors and Notch Sensitivity

An important metric in analyzing the effect that a stress concentration has on the mechanical behavior of a material is the change in the ultimate tensile strength between an un-notched nominal geometry and a notched geometry. This metric, which allows for the calculation of the effective SCF as per Eq. (1.4.1), can then be used to calculate the sensitivity of the material to the stress concentration by a ratio of the effective SCF to the measured SCF, as per Eq. (1.4.2). To facilitate this, a series of nine nominal cross section tests, given the specimen numbers *N*-θ-α, corresponding to the various material orientations, and to the notch orientation that produces the corresponding nominal cross section, have been run, and the results are presented in Figs. 3.44.

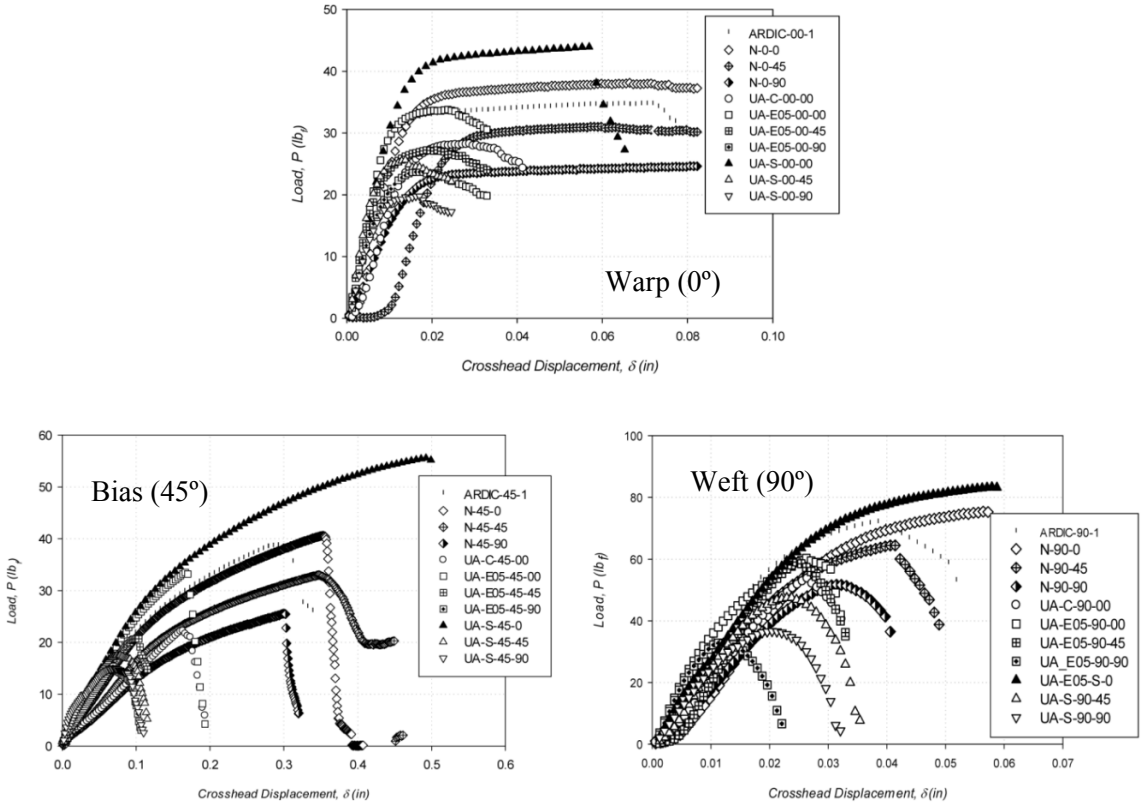

Figure 3.44: Uniaxial tensile response, in terms of load and crosshead displacement, of the SS316L woven wire mesh for various notched and nominal cross section geometries at various material orientations.

From Fig. 3.44, the ultimate tensile load, P_{ut}, of each specimen geometry can be extracted and used to calculate the effective SCF, and the sensitivity of the material to the respective notch geometry. These values are reported in Tables 3.9 through 3.11 with respect to material orientation. It is noted that some specimens display a notch sensitivity less than zero, which falls outside of the range of possible values, and these specimens are assigned a notch sensitivity of zero. In general, inspection of Tables 3.9 through 3.11 reveals that the ultimate load, P_{ut}, of SS316L woven wire mesh is not sensitive to the presence of a notch, particularly in the warp (0º) material orientation.

Table 3.9: The effective Stress Concentration Factors (SCF) and the resultant notch sensitivities of the subject material oriented in the warp (0º) direction.

material orientation, θ	specimen number	Notch Aspect Ratio, λ	notch orientation, α (º)	P_{ut}	Effective SCF, K_{eff}	Measured SCF, $K_{t,gn}$	Notch Sensitivity, q
	UA-E05-00-00	0.5	0	33.79	1.13	8.07	0.018
	UA-E05-00-45	0.5	45	27.24	1.14	8.58	0.019
	UA-E05-00-90	0.5	90	23.73	1.05	6.02	0.009
Warp (0°)	UA-S-00-00	0.0	0	43.95	0.87	1.67	0
	UA-S-00-45	0.0	45	25.65	1.21	8.86	0.027
	UA-S-00-90	0.0	90	19.82	1.2	18.02	0.015
	UA-C-00-00	1.0	-	28.35	0.88	2.39	0

Table 3.10: The effective Stress Concentration Factors (SCF) and the resultant notch sensitivities of the subject material oriented in the bias (45º) direction.

material orientation, θ	specimen number	Notch Aspect Ratio, λ	notch orientation, α (º)	P_{ut}	Effective SCF, K_{eff}	Measured SCF, $K_{t,gn}$	Notch Sensitivity, q
	UA-E05-45-00	0.5	0	33.63	1.21	59.7	0.004
	UA-E05-45-45	0.5	45	20.8	1.59	11.85	0.054
	UA-E05-45-90	0.5	90	15.56	1.65	5.96	0.131
Bias (45°)	UA-S-45-00	0.0	0	55.62	0.73	1.00	0
	UA-S-45-45	0.0	45	17.53	1.88	11.49	0.084
	UA-S-45-90	0.0	90	15.04	1.71	53.39	0.013
	UA-C-45-00	1.0	-	22.24	1.15	6.85	0.026

Table 3.11: The effective Stress Concentration Factors (SCF) and the resultant notch sensitivities of the subject material oriented in the weft (90º) direction.

material orientation, θ	specimen number	Notch Aspect Ratio, λ	notch orientation, α (º)	P_{ut}	Effective SCF, K_{eff}	Measured SCF, $K_{t,gn}$	Notch Sensitivity, q
	UA-E05-90-00	0.5	0	60.7	1.24	8.07	0.034
	UA-E05-90-45	0.5	45	59.32	1.09	8.58	0.012
	UA-E05-90-90	0.5	90	32.77	1.58	6.02	0.115
Weft (90º)	UA-S-90-00	0.0	0	83.47	0.90	1.67	0.000
	UA-S-90-45	0.0	45	47.5	1.36	8.86	0.046
	UA-S-90-90	0.0	90	36.74	1.41	18.02	0.024
	UA-C-90-00	1.0	-	53.67	0.96	2.39	0

The highest notch sensitivity is found in the bias (45º) material orientation for the case of an elliptical notch oriented at 90º to the loading axis, with a value of 0.131. This particular notch geometry and orientation also produces a relatively high notch sensitivity in the weft (90º) oriented specimen, with a value of 0.115. Interestingly, this notch geometry and orientation produces a very small notch sensitivity, 0.009, in the warp (0º) material orientation. It is also observed that the slit notches, which were expected to produce a more pronounced affect on the ultimate load than the elliptical notches, tend to produce smaller notch sensitivities than the elliptical notches. Again, this seems to be related to the MSGC factor, which suggests that the notch sensitivity factor, q, may play a role in the eventual functional form of this coefficient.

Insight into the mesh failure mechanisms can also be gained by inspecting the tensile curves presented in Fig. 3.44. In general, a mesh failure dominated by wire yielding mechanisms, characterized by individual wire necking, a large process zone, and a high level of overall macro ductility, can be identified by a tensile curve with a significant plastic strain region, i.e., a high elongation. Conversely, a brittle fracture type failure, characterized by a high level of structural interaction with the notch, can be identified by a tensile curve with a limited plastic strain region,

i.e., low elongation. To characterize the effect of the notch on the failure mode of the woven wire mesh material, the reduction in macro-scale elongation is considered.

In the warp (0º) material orientation, the largest reduction in elongation with respect to the AR specimen is observed to occur in the α = 90º slit notch, with a reduction of 76.9%. The minimum reduction is observed to occur in the case for the circular notch, while the α = 0º slit notch is seen to produce more plastic strain than the nominal cases. The bias (45º) material orientation also experiences the largest loss in ductility when notched with a slit oriented at α = 90º, with a loss in elongation of 66.6%. Large losses in ductility are also observed in the bias (45º) material orientation for the case of a slit notch in the 45º orientation, and for an elliptical notch oriented at 90º to the loading axis. Again, the minimum ductility loss is observed for the circular notch. The weft (90º) material orientation experiences the maximum loss in macro-scale ductility for the case of an elliptical notch oriented at α = 90º, with an elongation reduction of 62.5%. Again, the circular notch leads to the minimal reduction in elongation to failure in the weft (90º) material orientation.

CHAPTER 4: BIAXIAL TENSILE EXPERIMENTS

A regimen of biaxial testing has been performed on the SS316L woven wire mesh material, as per the test matrix outlined in Table 2.3, using the linkage based biaxial frame shown in Fig. 2.11. The biaxial testing performed provides data regarding the effects of both circular and slit type stress risers on the mechanical behavior of the subject material when incised into the cruciform geometry supplied in Fig. 2.9, and subjected to both equibiaxial and unequal-biaxial loads. Additionally, biaxial testing has been carried out on un-notched cruciform geometries such that the yield surface in tension-tension space could be experimentally ascertained, and compared to the Hill criterion. Ultimately, this testing sequence has shown that the Hill model provides a conservative estimate for the yield strength of the subject material under equibiaxial tension conditions, leading to a proposed modification to the Hill orientation model which improves the yield strength prediction capabilities of the Hill Analogy for the subject material. Also, the DIC results for notched cases have allowed for the production of near-notch SCF curves for SS316L woven wire mesh when incised into the given cruciform specimen geometry, and subjected to biaxial loads.

4.1 Woven Wire Mesh Yielding

Biaxial tensile testing (both unequal and equal) has been performed on un-notched specimens of the SS316L micronic woven wire mesh material to ascertain the tension-tension yield surface for the material. Two biaxial tests, one of equibiaxial tension and the other of unequal-biaxial tension, have been leveraged in conjunction with the uniaxial tensile tests in the principal material orientations (warp (0º) and weft (90º)) to characterize the yield behavior of SS316L woven wire mesh under tension. The results of the un-notched biaxial tension tests,

presented as stress-strain curves for each respective axis of loading, are provided in Fig. 4.1. It is noted that the stress-state imparted to the specimen is not controlled in the linkage-based biaxial testing performed in this work, but rather the crosshead displacement rate (stretch) is controlled, thus accounting for the unequal stresses observed in the equibiaxial case. The stretch rate, as defined in Sec. 2.2, is $\gamma = 1.2$ in all unequal-biaxial cases. It is also of interest to observe the differences between the equibiaxial loading case, and the case of uniaxial loading in the respective principle material orientations, which are plotted alongside the equibiaxial results in Fig. 4.1(a).

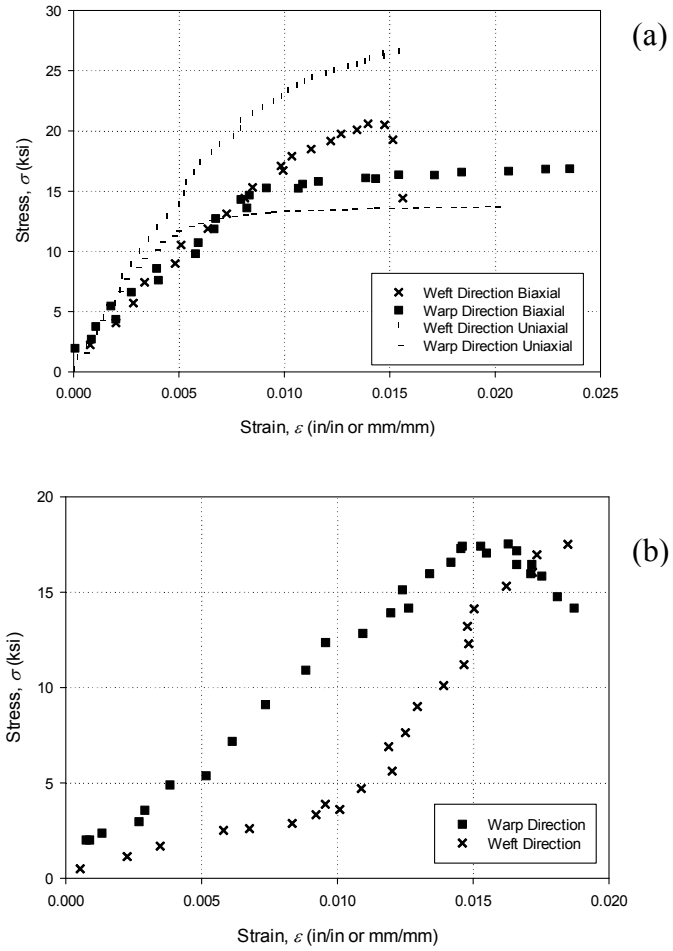

Figure 4.1: Tensile response of the SS316L twill dutch woven wire mesh subjected to (a) equibiaxial tension, and (b) unequal-biaxial tension

It is observed that the warp (0º) stiffness is slightly reduced when loaded equibiaxially, which can possibly be attributed to slight misalignment of the warp wires in the weave as they are bent and compressed by the de-crimping weft wires. The reduction in strength observed in the weft (90º) material orientation is attributed to the additional tensile load imparted to the warp wires, thus reducing their ability to carry the compressive loads imparted on them by the decrimping weft wires. The stiffness reduction observed in the weft (90º) case is also attributed to the tensioning of the warp wires, which effectively reduced the contact area of the overlapping wires, reducing the associated frictional forces. In general, the observations made from Fig. 4.1 work to underscore the fact that the SS316L woven wire mesh should ideally be treated as a structure composed of two independent materials, whose interactions determine global mechanical behavior, rather than as single orthotropic material.

Generation of an accurate yield surface from biaxial tensile test data requires that yielding of the gage section occurs prior to material rupture. It is clear from inspection of Figs. 4.1(a) and 4.1(b), showing the equibiaxial and the unequal-biaxial cases respectively, that yielding occurs prior to mesh rupture in both axes, thus allowing for the determination of the yield strengths, defined using a 0.2% strain offset technique. Figure 4.2 shows the experimentally determined yield strength results for the SS316L woven wire mesh material in tension-tension space, along with the first quadrant of the Hill yield surface, given in Eq. (2.1.1), generated using the constants provided in Table 3. 3. The axes of Fig. 4.2 have been normalized by the weft (90º) orientation yield strength of 22.8ksi (157.2MPa). The Hill criterion is found to be a conservative predictor of yielding for SS316L woven wire mesh material for the stretch ratios considered, suggesting its use as a first-order design criterion is reasonable and safe. While the current design of the biaxial load frame limits the values of γ to 1.0 and 1.2, additional stretch

ratios closer to 0.0 (weft (90º) uniaxial) and to ∞ (warp (0º) uniaxial) must be tested in future work such that the curvature of the yield envelope can be better established.

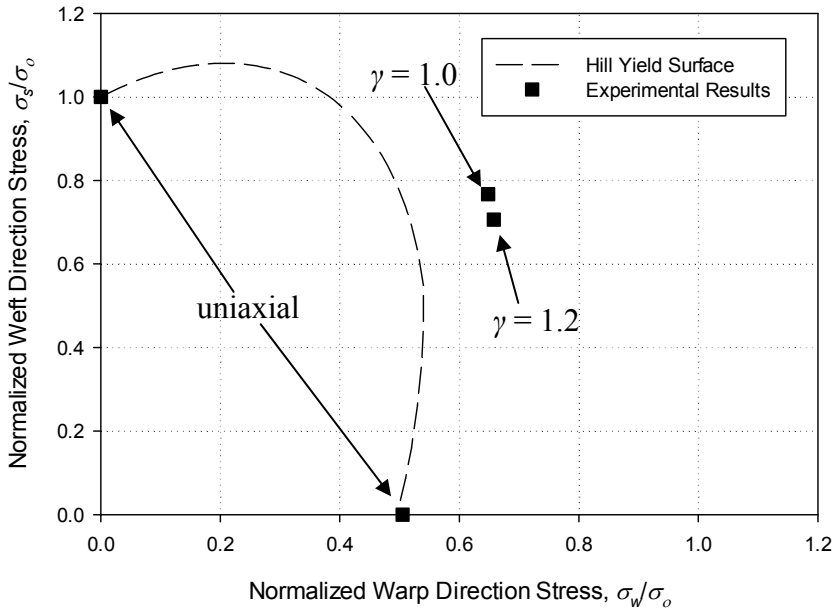

Figure 4.2: The normalized experimental yield stress of the SS316L woven wire mesh material in tension-tension space, along with the conservative Hill criterion yield surface.

The generally poor fit of the Hill criterion to the off-axis experimental results as evidenced by Fig. 3.11, along with the observation that the yield criterion is overly conservative in the case of biaxial tension, highlights the need for a modified form of the classical Hill yield criterion for accurate prediction of woven wire mesh yielding. While there are certainly many anisotropic yield criterions available in the literature, i.e., Tsai-Hill, Generalized Hill, Logan-Hosford, etc., a theory designed to account for various degrees of shear coupling, which is thought to be the prime contributor to the deviation from the Hill theory, is not known to exist [Meuwissen, 1995]. Evidence that the deviation from the Hill yield theory is based in coupling of the shear and normal stress terms is gained from the non-symmetrical nature of the material stiffness matrix as shown in Section 3.1, the general asymmetry of the structure as shown in Fig.

1.5, and from the fact that the Hill criterion fails to capture the yield behavior for this material in material orientations where coupling is known to occur, i.e., in off-axis orientations, as demonstrated in Fig 3.11. Asymmetry of the plastic material behavior suggests that terms should be added to the coupling positions in the plastic potential function. The matrix representation of the Hill criterion is given as Eq. (4.1.1) below, where **M** is the Hill coefficient tensor as given in Eq. (4.1.2). It is seen that the terms coupling the shear and normal stresses are zero, indicative of the fact that the Hill criterion as presented in Eq. (4.1.1) is formulated via an assumption of material orthotropy. As the Hill tensor relates some given stress state to the yield condition, it is postulated that adding terms to the shear stress coupling positions in the tensor, i.e., deviating from this orthotropic continuum assumption, will improve the ability of the Hill criterion to model the yield behavior of the woven wire mesh material.

$$\{\sigma\}^T [\mathbf{M}]\{\sigma\} = 1 \tag{4.1.1}$$

$$\mathbf{M} = \begin{bmatrix} G+H & -H & 0 \\ -H & F+H & 0 \\ 0 & 0 & 2N \end{bmatrix} \tag{4.1.2}$$

The effects of the stress coupling on the yield behavior of the SS316L woven wire mesh are theorized to be orientation-dependent, i.e., the degree to which the stresses are coupled is thought to be a function of the applied stress state. For example, when the material is loaded uniaxially, or in pure shear, the coupling terms must reduce to zero such that the case of special orthotropy is maintained. This is both consistent with the experimental and analytic modeling results presented in previous sections, and necessary to assure the model predicts either a maximum or a minimum yield strength in the principle material orientations, i.e., the derivative

of the yield strength orientation model must go to zero at both warp (0º) and weft (90º) material orientations. As such, the additional coupling terms must be functions of the applied stress state, and may not affect the definition of the classical Hill parameters, *F, G, H,* or *N.* To meet these requirements while allowing for easy comparison to the Hill orientation model derived using the assumption of uniaxial tensile loading, the coupling terms used to modify the Hill criterion have been assigned as functions of the material orientation, θ, as shown in (Eq. 4.1.3). It must be noted that the material orientation and the state of stress are related, and so development of a yield surface for the modified criterion similar to the one shown in Fig. 4.2 is possible. It can be shown that a yield surface generated via Eq. (4.1.3) will reduce to the Hill surface in a case of zero applied shear stress ($\theta = n\pi/2$, n = 0, 1, 2, etc.) and that the yield strength predicted by the modified model in pure shear is identical to the Hill criterion. Figure 4.3 shows the prediction of the yield strength with respect to material orientation for both the modified Hill criterion presented in Eq. (4.1.3), and the classical Hill criterion, in conjunction with the experimental data. The Hill constants used to generate the modified Hill yield strength prediction curve in Fig. 4.3 are identical to those supplied in Table 3.3, while the coupling terms *I* and *K* are given optimized values (based on regression analysis) of 22.9 and 5.98, respectively. Inspection of Fig. 4.3 shows that the fit to the experimental data is significantly improved by adding the coupling terms to the Hill criterion, and the ability of the modified model to predict the minimum yield strength at an orientation other than 45º is highly desirable. Further work is needed to investigate the mathematical stability of the proposed modifications to the Hill criterion, and to provide physical significance, i.e., a means to experimentally determine, the proposed constants *I* and *K*, as detailed in the future work section of this thesis.

$$\begin{Bmatrix}\sigma_x & \sigma_y & \tau_{xy}\end{Bmatrix}\begin{bmatrix} G+H & -H & I\sin(4\theta) \\ -H & F+H & K\sin(4\theta) \\ I\sin(4\theta) & K\sin(4\theta) & 2N \end{bmatrix}\begin{Bmatrix}\sigma_x \\ \sigma_y \\ \tau_{xy}\end{Bmatrix} = 1 \tag{4.1.3}$$

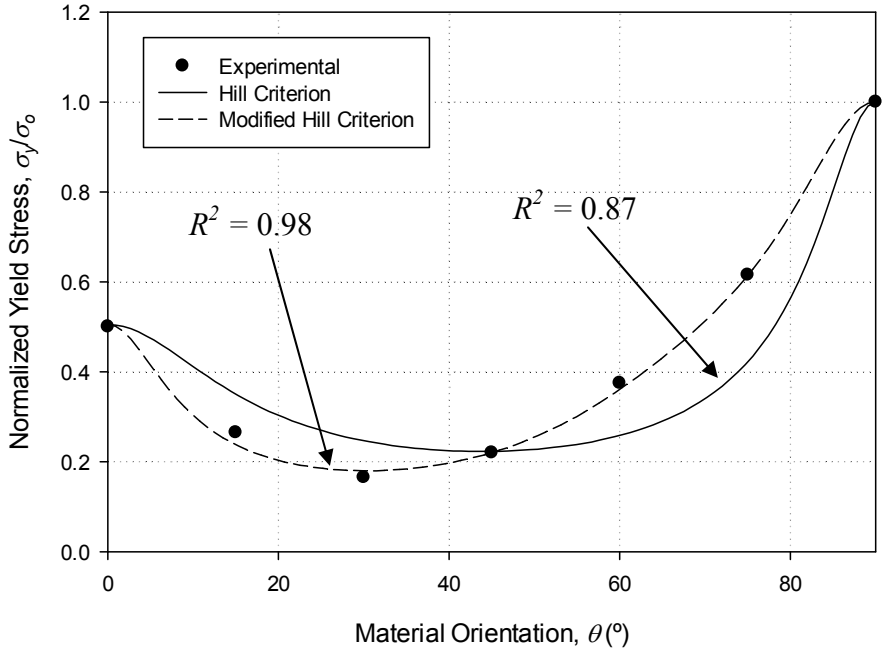

Figure 4.3: The prediction of yield strength as a function of material orientation for the SS316L woven wire mesh material using both the classical Hill criterion and the modified Hill Criterion in conjunction with the uniaxial experimental data.

4.2 The Notched Mechanical Behavior Under Biaxial Tension

The effect of notches on the mechanical behavior of the SS316L woven wire mesh material when loaded biaxially is of interest for practical application of the material in industry. The impact on the local (near notch) stresses of various notch geometries and orientations with respect to the weave axes is investigated using notched cruciform specimens, as illustrated in Fig. 2.9. In a similar manner to the uniaxial experiments, the notch aspect ratio, λ, is varied from a value of 1.0, or a circle, to a value of near 0.0, or a slit. Elliptical experiments are omitted in the biaxial testing regimen due to the lack of significant difference in circular and elliptical SCFs observed in uniaxial experiments. In all cases, the major diameter of the incised notched

measures 0.25in (6.35mm). Additionally, the slit notch orientation, α, is varied from warp aligned (0º) to weft aligned (90º) in 45º intervals as described in the biaxial test matrix provided in Table 2.3. Rather than varying the material orientation associated with the cruciform specimens, the stretch ratio, γ, was varied from equibiaxial ($\gamma = 1.0$) to unequal-biaxial ($\gamma = 1.2$) as described in Section 2.2. Similarly to the uniaxial tensile tests, DIC was employed using a camera mounted above the specimen, as shown in Fig. 2.14 (b), to allow for investigation of the full strain field in the gage section of the cruciform specimen. The recorded data was then leveraged to calculate the near-notch experimental SCFs for each case in a manner identical to that employed in Chapter 3. What follows is a detailed discussion of the effect of notches on the mechanical behavior of biaxially loaded SS316L twill dutch woven wire mesh, including experimental SCF curves for the given specimen geometry, as well as fractographic analysis of the process zones associated with mesh rupture in the gage section.

4.2.1 Near Notch Elastic Strain and Stress Distributions

The full field DIC strain measurement technique has been used to measure the strain distribution in the gage section of notched biaxial cruciform specimens subjected to equibiaxial and unequal-biaxial stretch ratios. Unlike the experimental setup previously outlined for the uniaxial test cases, the position of the camera in the biaxial linkage load frame with respect to the test specimen, as shown in Fig. 2.14, makes alignment of the camera axes with the specimen challenging. It is vital that the camera and the specimen be aligned, as even slight misalignment of the camera and specimen axes can lead to erroneous strain measurement, particularly in the form of artificial shear strains. Rather than defining a painstaking camera alignment and calibration process, it was elected to use the correlation software (VIC-2D, 2009) to calculate the

principle strains. In this way the DIC strain measurement tool behaves much like a rosette strain gage, making the alignment of the camera to the specimen inconsequential. In all cases, the misalignment was found to be slight, with very little difference observed between the principle and camera axis strains (within 5% in all cases). Thus, the principal axial strains are reported herein, along with the shear strain in the *x-camera - y-camera* plane.

The full field elastic principle strain distributions for the various notched cruciform specimen geometries and stretch ratios are provided in Figs. 4.4 through 4.12. In all cases, the weft (90º) material orientation is aligned with the 1-direction, while the warp (0º) material orientation is aligned with the 2-direction. Similarly to the uniaxial cases, the frames included in the subsequent figures have been selected based on an analysis of the near notch stress field indicating elasticity of the notch root, and the load level applied to the specimen at the time of the image capture, taken as the maximum of either the warp or the weft axes, is reported. Inspection of Fig. 4.4, which shows the case of the circular notched cruciform specimen subjected to equibiaxial stretch ratio ($\gamma = 1.0$) reveals distinct zones of strain concentration nearly aligned with the principle material axes, along with significant perturbation in the strain field caused by the presence of the circular uniaxial arm fillets. The locations of maximum strain appear to be slightly off of the main material axes for both the 1-direction and the 2-direction strains. This is attributed the effects of the fillet, which appear to be influencing the strain field near the circular notch. This observation indicates that the size of the notch selected for this series of experiments is likely too large with respect to the size of the specimen, and that it is not possible to ignore the boundary conditions in analysis of these results. Nonetheless, the major diameter of 0.25in (6.35mm) is maintained throughout this work for the sake of consistency and synergy with the uniaxial tensile tests. It is clear from inspection of Fig. 4.4 that the near notch

strain distribution is more affected in the 1-drection than in the 2-direction, with the maximum strain at the edge of the notch being nearly four times greater, despite the equivalency of the applied strains.

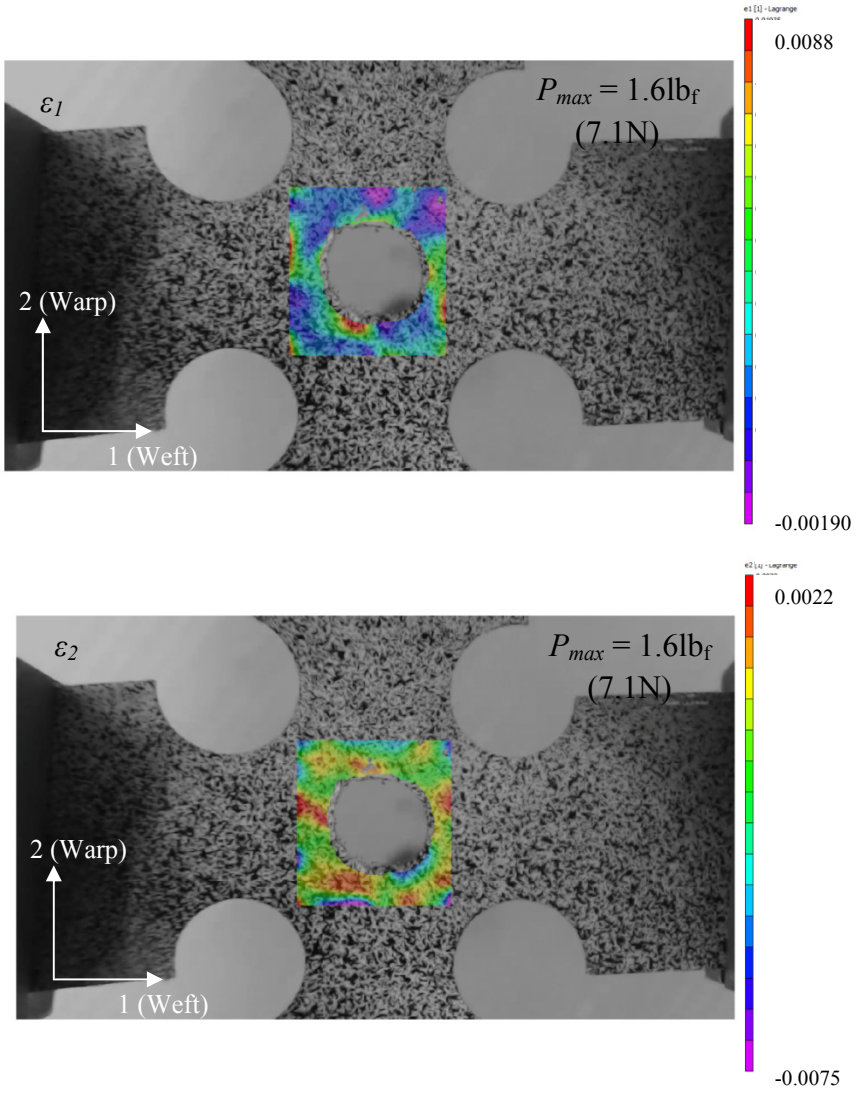

Figure 4.4: Principal elastic strain distribution in the gage section of a cruciform specimen loaded under equibiaxial stretch with a centrally located circular notch.

As the 1-drection corresponds to strain developing in the weft wire material orientation, this result indicates that the weft direction is more severely impacted by the presence of a circular

notch than the warp direction, which is likely owed to the significantly higher density of the weave in the weft (90º) material orientation. Figure 4.5 shows the principal strain contours around the region of a circular notch in the biaxial cruciform specimen subject to unequal-biaxial stretch ($\gamma = 1.2$).

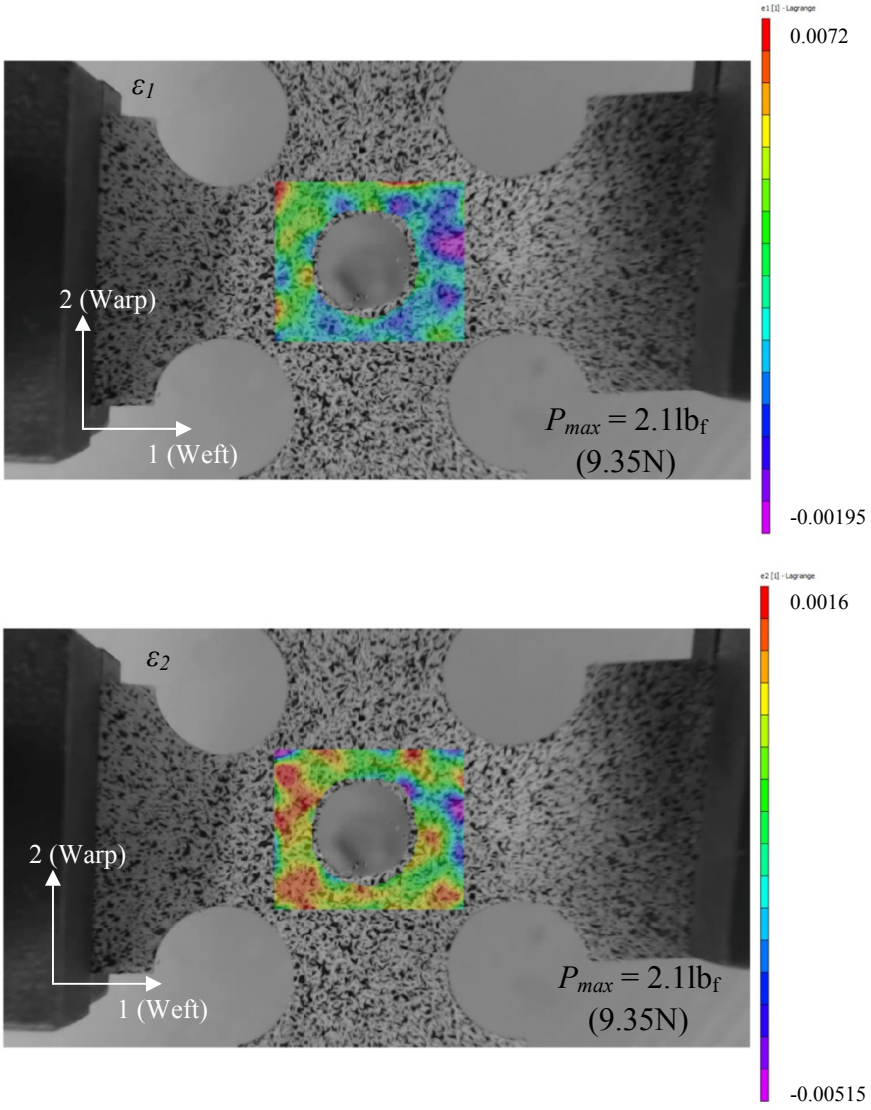

Figure 4.5: Principal elastic strain distribution in the gage section of a cruciform specimen loaded under unequal-biaxial stretch with a centrally located circular notch.

Several commonalities can be observed between the equibiaxial stretch case shown in Fig. 4.4, and the unequal-biaxial stretch case in Fig. 4.5, particularly in the strain distribution in the 2-diretion (warp direction). In general, the warp direction strain is characterized by larger and more evenly distributed areas of higher strain, with zones of field perturbation extending farther away from the notch edge than in the 1-direction (weft direction). Again, it is observed that the maximum strain in the 1-direction is approximately four times higher than the maximum strain in the 2-direction for the $\gamma = 1.2$ case. The effect of the increased stretch ratio appears to be a slight clock-wise shift the locations of the peak strains in both principal directions. This observation is consistent with the increased rate of strain in the warp direction, which has caused asymmetry to develop in the strain distributions with respect to the principal axes.

The presence of a crack or tear in the SS316L woven wire mesh is likely to present as a slit ($\lambda = 0$) type notch in service conditions, and so it is of particular interest to study this notch geometry in the biaxial experiments. Figures 4.6 through 4.11 show the DIC principal elastic strain results for the various slit notch orientations and stretch ratios. Inspection of Fig. 4.6, which shows the principal elastic strain distributions around a slit notch aligned with the 2-direction (warp), again demonstrates that the 1-direction (weft) strains are more locally affected by the presence of the stress riser. The 2-direction (warp) strains are relatively evenly distributed throughout the gage section, appearing nearly unaffected by the presence of the slit aligned with the warp wires. Again, the circular fillets appear to have significant strain concentration, particularly in the 1-direction (weft), where they account for the maximum strain in the gage region. Failure is observed to occur in the gage section of the specimen at the notch root, however; thus allowing for the subsequent analysis of the rupture zone using microscopy. It is noted that the peak strains in the gage section of the specimen are higher in the 1 -direction

(weft) than in the 2-direction (warp) for the α = 0º equibiaxial slit notch case, with values of 0.0035 and 0.0021 respectively.

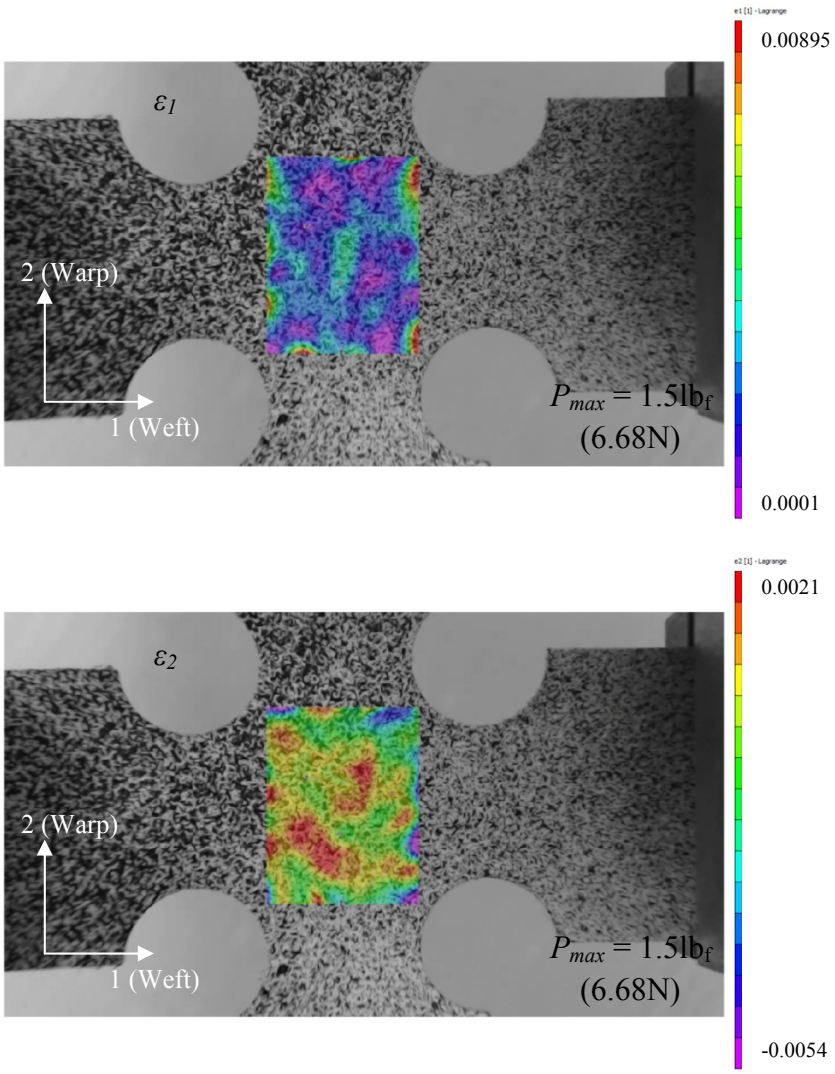

Figure 4.6: Principal elastic strain distribution in the gage section of a cruciform specimen loaded under equibiaxial stretch with a centrally located slit notch aligned with the warp direction (2-direction).

The α = 45º slit notch under equibiaxial stretch, provides an interesting case to study, as the orthotropic nature of the subject material allows for shear strains to develop along the face of the slit, i.e., the crack appears to be mixed mode in nature. The appearance of mixed-mode fracture conditions in equibiaxial tension tests of homogenous isotropic material is generally not

expected, as the edge shear traction terms cancel [Sih et al., 1962]; for non-homogenous material, however, it has been shown that mixed-mode loading conditions develop at the edge of a bias oriented crack under equibiaxial tension [Choi, 2001]. Mixed-mode conditions at the 45º oriented crack in the biaxially loaded SS316L woven wire mesh material are evidenced by the zone of transition between positive and negative 1-direction (weft) strains as shown in Fig. 4.7, which likely indicates mode-II type crack opening.

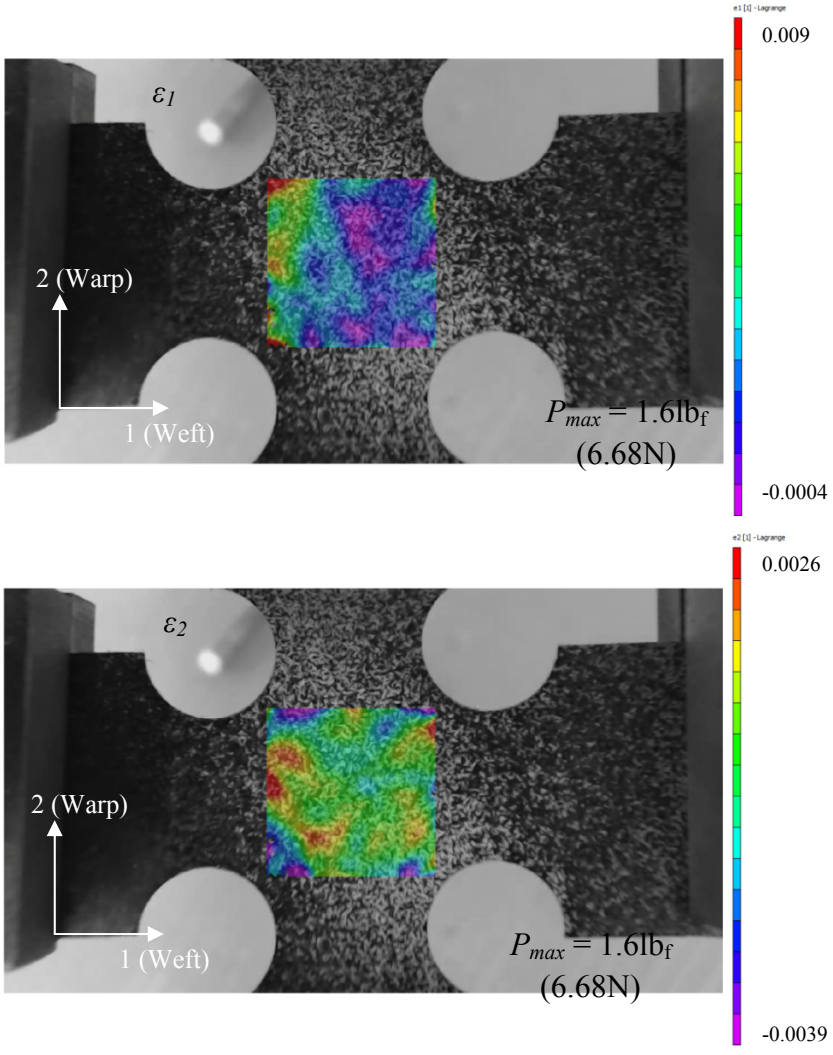

Figure 4.7: Principal elastic strain distribution in the gage section of a cruciform specimen loaded under equibiaxial stretch with a centrally located slit notch aligned at 45º to the warp direction (2-direction).

The 2-direction (warp) strain does not show similar visual evidence of mixed-mode behavior, but rather displays a uniform distribution of strain as seen in previous cases. Fractographic analysis, particularly regarding the direction of rupture propagation in the α = 45º, cases is necessary to confirm the mixed mode conditions, and this is discussed in detail in the subsequent section. The final equibiaxial case experimentally treated is the slit notch oriented at 90º to the warp axis (2-direction). The elastic principal strain contours for the α = 90º equibiaxial slit notch case is provided in Fig. 4.8.

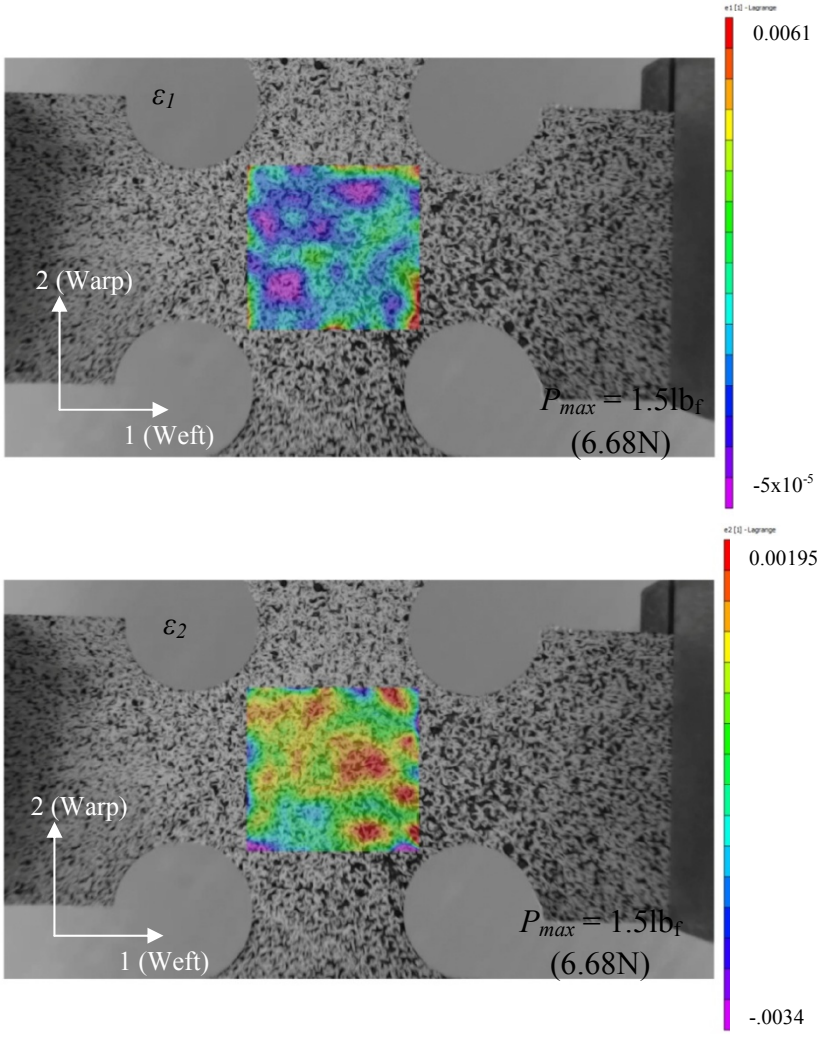

Figure 4.8: Principal elastic strain distribution in the gage section of a cruciform specimen loaded under equibiaxial stretch with a centrally located slit notch aligned at 90º to the warp direction (2-direction).

Inspection of Fig. 4.8 reveals no severe perturbation of the strain fields in the 1-direction (weft), which is as expected given the alignment of this direction with the notch roots. The lower mesh density in the warp orientation (2-direction) leads to the observed large distribution zone of higher strain near the notch root, as was similarly observed in uniaxial test cases.

The case of unequal stretch ratio, $\gamma = 1.2$, was also treated experimentally for the notch orientations of $\alpha = 0^{o}$, 45^{o}, and 90^{o}, and the DIC principal elastic strain contour plots associated with these experiments are provided as Figs. 4.9 through 4.11.

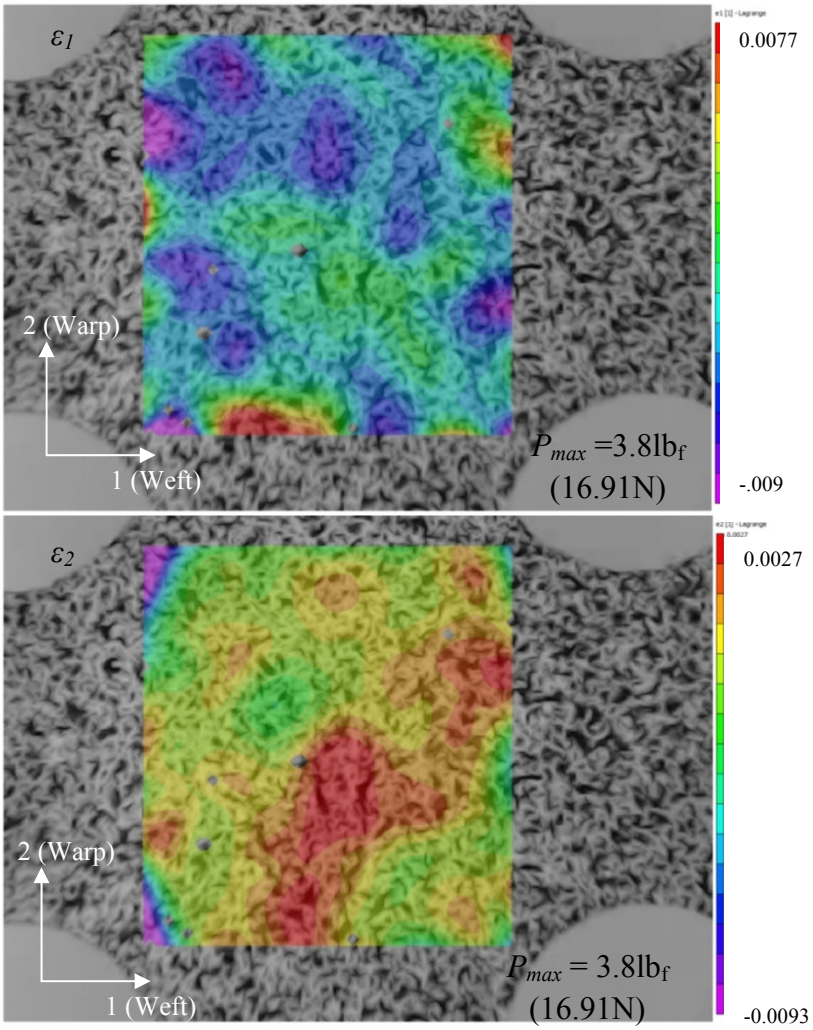

Figure 4.9: Principal elastic strain distribution in the gage section of a cruciform specimen loaded under unequal-biaxial stretch with a centrally located slit notch aligned at 0^{o} to the warp direction (2-direction).

The case of a slit aligned with the warp direction (α = 0º) is shown in Fig. 4.9, and it is clearly observed that the effect of the notch on the material response in the 1-direction (weft) is generally not strong in the elastic regime. This attributed to the increased stretch ratio in the 2-rection (warp), which is working to close the crack by Poisson's affect. Indeed, not until rupture was imminent was the slit observed to begin opening, and the affect on the 1-direction (weft) strain distribution observed to become significant. Figure 4.10 shows the principal elastic strain distribution for the unequal-biaxial case of a notch oriented at 45º to the warp axis (2-direction).

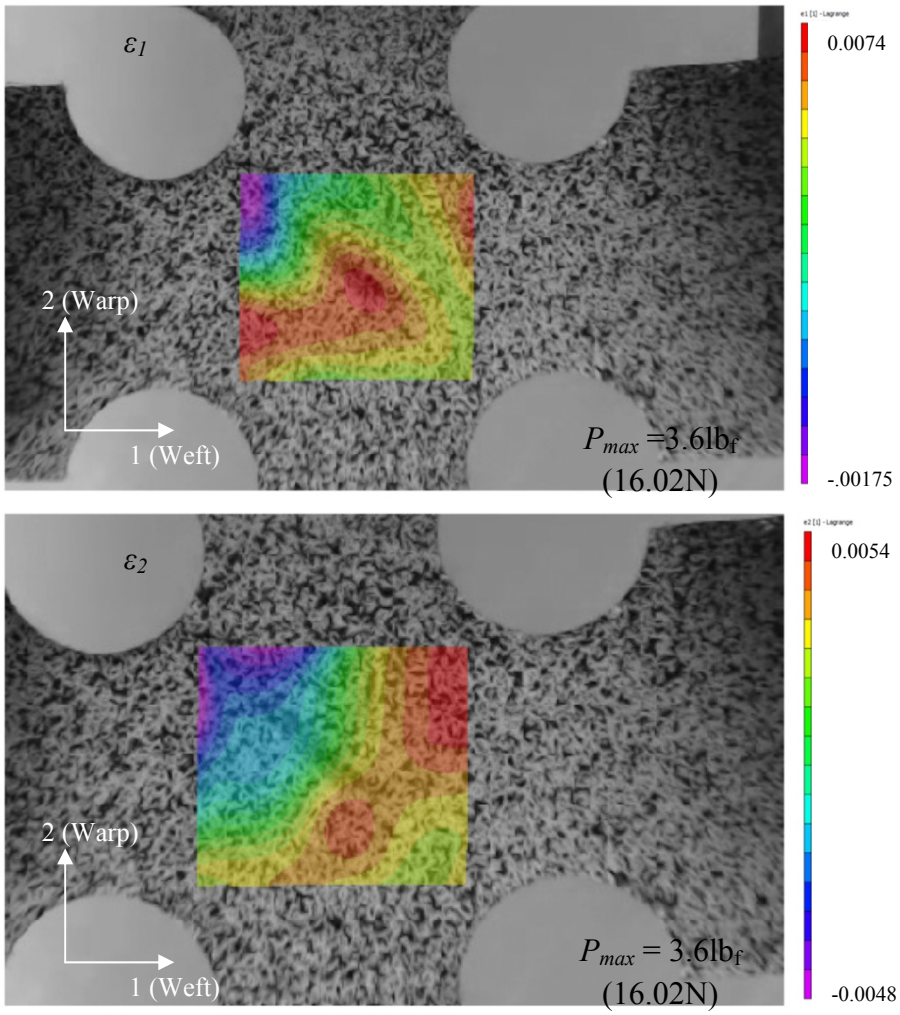

Figure 4.10: Principal elastic strain distribution in the gage section of a cruciform specimen loaded under unequal-biaxial stretch with a centrally located slit notch aligned at 45º to the warp direction (2-direction).

The notch strain contours are observed to interact with the fillet stress risers, making observations of the strain asymmetry associated with the equibiaxial 45º case difficult. It is noted that a general gradient of negative to positive strain exists in the gage section of the specimen starting in the upper left corner fillet, however, it is likely that such a strong gradient is a result of specimen misalignment in the grips. Future redesign of the biaxial test frame, outlined in detail in the future work section if this thesis, is necessary to aid in specimen alignment such that these anomalous measurements can be reduced.

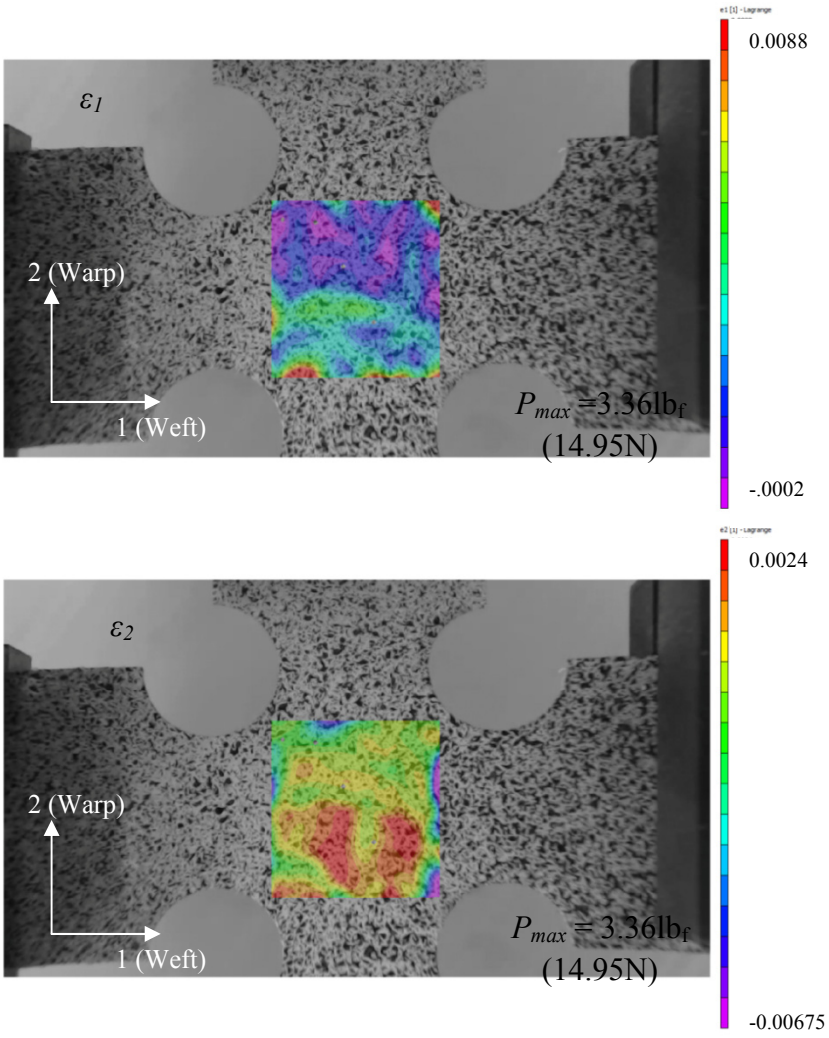

Figure 4.11: Principal elastic strain distribution in the gage section of a cruciform specimen loaded under unequal-biaxial stretch with a centrally located slit notch aligned at 90º to the warp direction (2-direction).

The principal elastic strain distribution for the case of a slit oriented at 90º to the warp axis (2-direction), and loaded by unequal-biaxial stretch, is shown in Fig. 4.11. Again, the effect of the unequal stretch rate is clear upon inspection of the DIC frames taken at low load levels, as the Poisson's affect form the higher warp direction (2-direction) stretch rate serves to reduce the weft direction (1-direction) strains. This is evidenced by the zone of near zero strain above the slit notch in the 1-direction (weft). It is noted that this zone of low strain is only observed at lower load levels, however the need to assure elasticity of the notch root in SCF calculations requires that low load levels be considered. In the warp direction (2-direction), the α = 90º slit produces large bean-shaped zones of increased strain in the region of the notch roots. While the shape of the strain distribution is consistent with homogenous isotropic theory, the size of the perturbed zone is very large with respect to the root radius, and is attributed to the inhomogeneous structure and low weave density in the warp direction, which has been shown to produce large process zones in uniaxial experiments [Kraft and Gordon, 2011].

In an effort to develop a more thorough understanding of the effects of stress risers in biaxially loaded SS316L woven wire mesh material, strain data has been extracted from the full-field DIC results along the various notch edges, allowing for the subsequent calculation of the respective stress distributions via Eq. (3.2.6), as was done in the uniaxial cases. As the slit notches are of particular interest, owing to the increased possibility of a tear or rip tip stress riser presenting itself in industry, particular attention is paid to these geometries, and the notch edge correlations are supplemented with correlations running through the notch roots. The various correlation paths are detailed in figure insets to provide clarity and reference to the reader. In all cases, the extracted strains and resulting stress states correspond to the loading condition detailed in the respective strain contour plot shown in Figs. 4.4 through 4.11. The angular position on the

notch edge is given in all biaxial cases as θ_w, which is defined as the angle with respect to warp axis (also the 1-axis or the *y*-axis). Figure 4.12 shows the distribution of tensorial elastic strain along the edge of a circular notch incised into both equibiaxially and unequal-biaxially loaded SS316L woven wire mesh material.

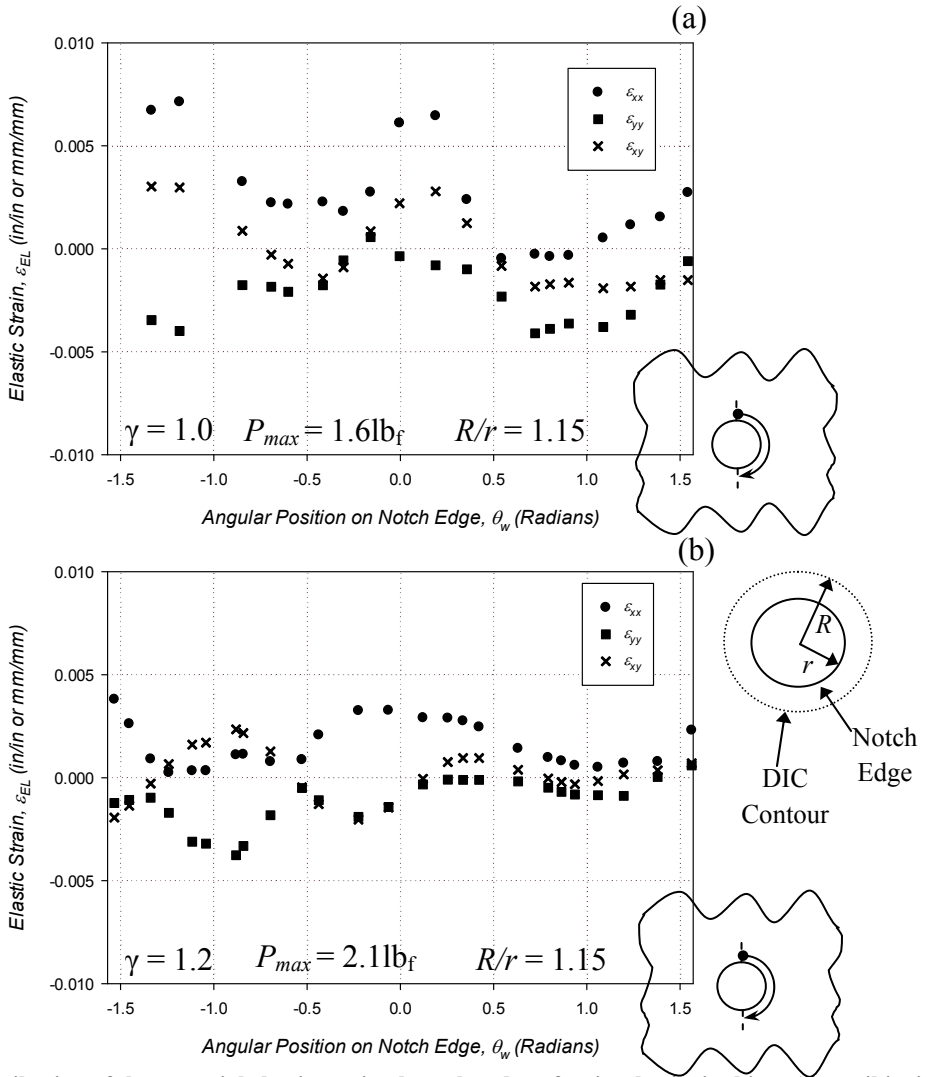

Figure 4.12: The distribution of the tensorial elastic strain along the edge of a circular incised into (a) equibiaxially loaded, and (b) unequal-biaxially loaded SS316L woven wire mesh material.

As was observed in the respective contour plots, the effect of the unequal-biaxial stretch ratio on the circular notched specimen is to shift the location of the tensorial peak strains for by approximately 0.25 radians. It is also interesting to note that the shear strain at the notch edge is

not negligible with respect to the axial strain values, and that the axial strain distributions are nearly out of phase with each other for both equibiaxial and unequal-biaxial cases. Also, a bigger range of strain magnitude is observed in the *x* and *y* directions for the case of equibiaxial tension than for unequal-biaxial tension, with values of 0.013 and 0.007, respectively. Figure 4.13 shows the strain distributions around the notch edge for the case of a slit notch oriented at $\alpha = 0^{o}$ to the warp direction for both the equibiaxial and unequal-biaxial cases, as described in the inset of each figure.

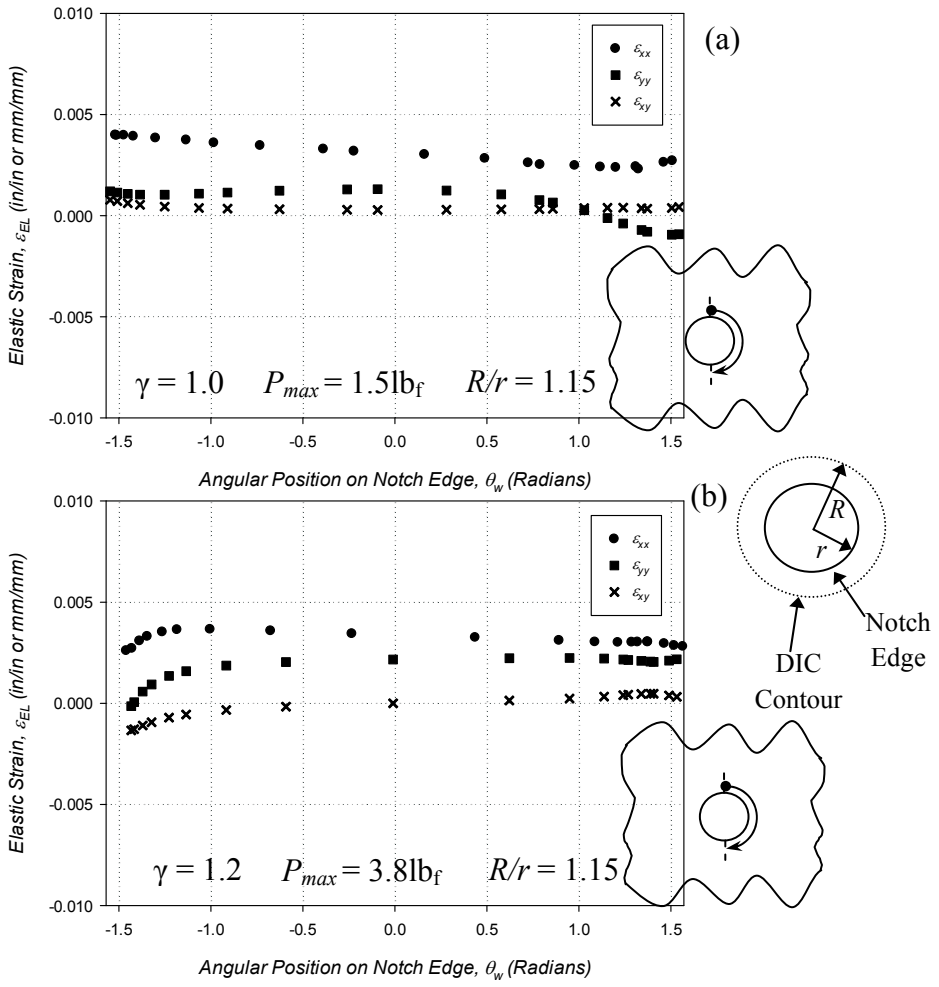

Figure 4.13: The distribution of the tensorial elastic strain along the edge of an $\alpha = 0^{o}$ oriented slit notch incised into (a) equibiaxially loaded, and (b) unequal-biaxially loaded SS316L woven wire mesh material.

Inspection of Fig. 4.13, reveals that the strain is relatively constant over a large portion of the notch edge. The *y*-direction axial strains are observed to increase slightly as the notch root is approached at $\theta_w = 0$ for both the $\gamma = 1.0$ and $\gamma = 1.2$ cases, but the increase is minimal considering the sharp radius of the slit notch. In general, the equibiaxial and the unequal-biaxial case produce very similar trends in elastic strain near the notch edge, with the only measurable difference being the slope of the strain distribution as the angle approaches $-\pi/2$ radians, where the $\gamma = 1.0$ case has a negative slope, and the $\gamma = 1.2$ case slope is positive. Again, this drop in strain at the notch face positions ($+/- \pi/2$ radians) in the $\gamma = 1.2$ case can be attribute to the increased strain the warp direction (*y*-direction) with respect to the weft direction (*x*-direction), causing a near traction free surface to develop along the face of the slit. The lack of symmetry observed in the strain distribution is attributed to misalignment of the specimen in the grips, and the effects of the circular fillets on the overall gage section strain distribution. The shear strain near the edge of the $\alpha = 0^o$ slit notch is near zero for both the equibiaxial and unequal-biaxial cases, which is consistent with the trend observed in the uniaxial loaded case. Figure 4.14 shows the distribution of strain along lines passed through the roots of the slit ($\alpha = 0^o$) notch along the axis of the slit, and through the central axis normal to the axis of the slit, as illustrated in the figure inset. The position along the line has been normalized by the length of the slit, 0.25in (6.35mm), such that the point $x_n = 0$ corresponds to the center of the notch. Figures 4.14 (a), which show the distribution of strain perpendicular to the major notch axis for the equibiaxial case, shows a maximum value occurring close to the notch edge, and is symmetric about the center of the notch. Minimums in the equibiaxial case occur just off of the notch edge for both axial strain components. This trend is reversed for the unequal-biaxial case shown in Fig. 4.14(b), where the maximum axial strains are shifted from the notch face edge, and the minimum

value occurs at the center of the open contour. For the case of the strains extracted along a line passing through the notch roots, as shown in Fig. 4.14 (c) and (d), peak strains are observed to occur over the entire range of the notch, rather than just at the notch roots. This observation communicates that the DIC setup used in the biaxial testing regimen is not of sufficient resolution to capture the small traction free zone at the center of the opening contour. Indeed, the peak strains in cases (c) and (d) are observed to correlate well with the peak values associated with the notch face strains extracted from cases (a) and (b). It is also noted that in the cases of strain distribution along the slit notch axis, the shear strain is not negligible, and is on the order of magnitude of the *y*-direction (warp direction) strains. This suggests mixed mode I-II type conditions at the slit for the case of biaxial loading, even in cases where the notch is oriented in one of the loading directions.

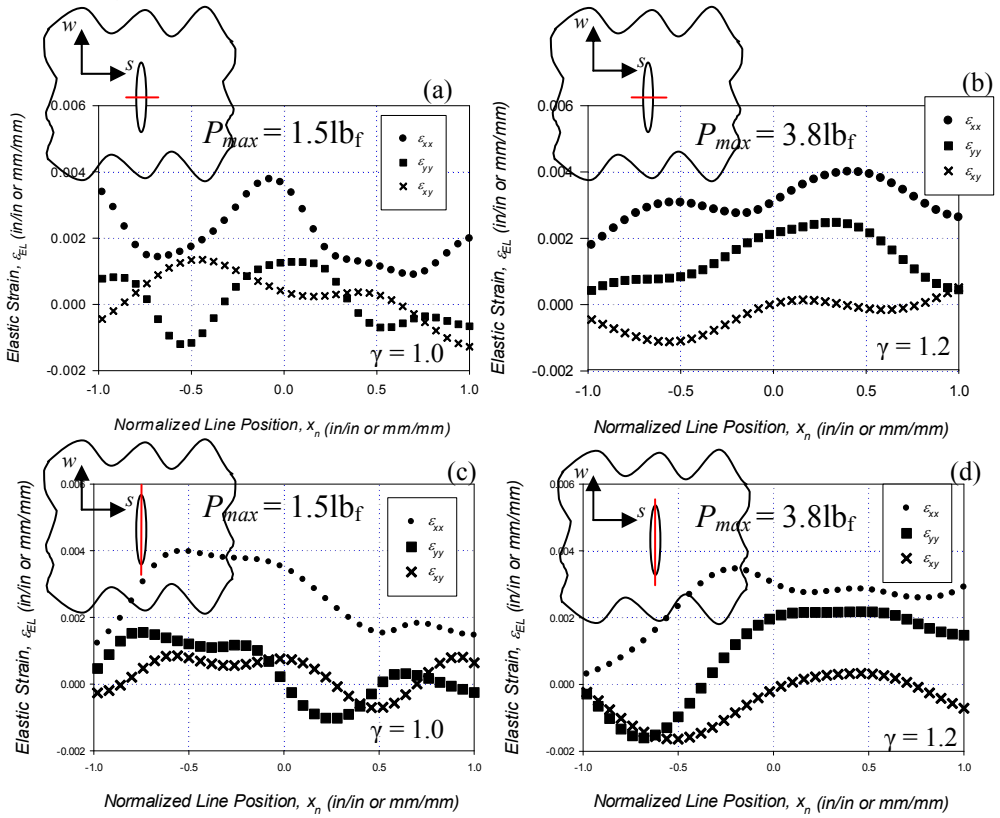

Figure 4.14: The strain distribution along lines passed through the notch roots (c, d), and perpendicular to the notch roots (a, b), for an $\alpha = 0^o$ oriented slit notch incised into (a, c) equibiaxial loaded, and (c, d) unequal-biaxally loaded specimens.

The strain distribution around the edge of the $\alpha = 45^{o}$ notch for both the equibiaxial and unequal-biaxial cases are shown in Fig. 4.15. Assessment of the strain distribution for the equibiaxial case shows a clear minimum of axial strain at an angular position of $\theta_w = -\pi/4$ radians, with the maximum strains occurring near +/- $\pi/2$ radians. These results suggest that the area of maximum stress concentration is not at the notch root in the $\alpha = 45^{o}$ notch cases.

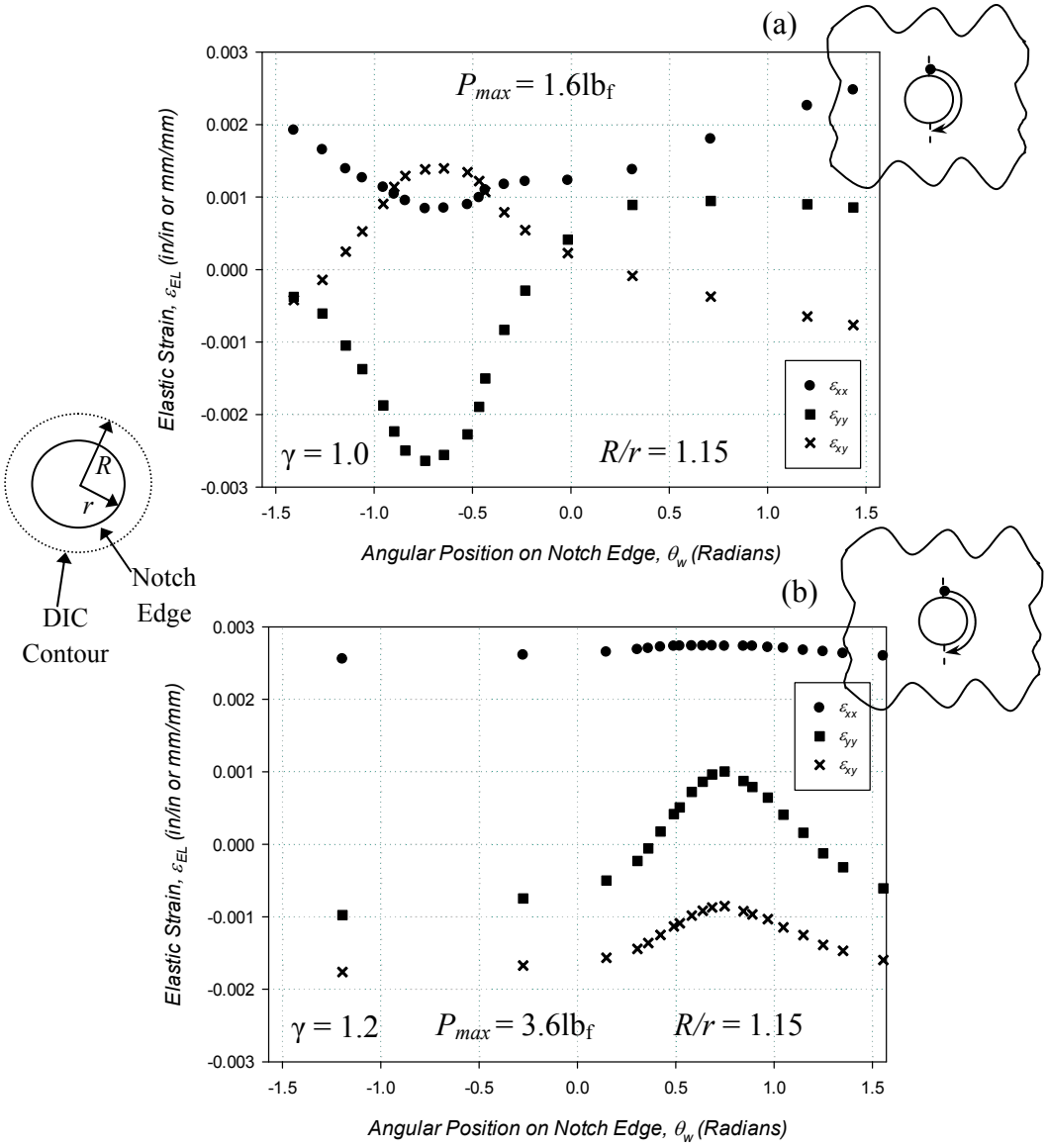

Figure 4.15: The distribution of the tensorial elastic strain along the edge of an $\alpha = 45^{o}$ oriented slit notch incised into (a) equibiaxial loaded, and (b) unequal-biaxially loaded SS316L woven wire mesh material.

It is interesting to note that the in-plane shear strains along the edge of the notch appear to be nearly exactly out of phase with the axial strains for the equibiaxial case, such that the maximum shear strain occurs near an angular position of $\theta_w = -\pi/4$ radians. The unequal-biaxial case initially appears dissimilar in appearance to the equibiaxial case, however, it must be noted that the specimen was flipped when input into the load frame, and thus the notch is oriented orthogonally to the equibiaxial case. Taking this into consideration, and shifting the unequal-biaxial trend accordingly, the strain distributions are actually quite similar in terms of the location of the peak axial strain magnitude. Comparison to the equibiaxial and unequal-biaxial strain contours, shown in Figs. 4.7 and 4.10 respectively, along with the understanding that the strain is taken in quadrants I and IV of the notch, justifies the differences in the sign of the axial strains in these locations. The exception to this observation is the location of the peak shear strain, which has shifted to be in phase with the axial strains. Again, to obtain a better understanding of the affect of an $\alpha = 45^{\circ}$ oriented notch on the mechanical behavior of biaxially loaded SS316L woven wire mesh material, strains have been extracted from lines both along and perpendicular to the major notch axis. The strain distributions for each respective path, and for both equibiaxial and unequal-biaxial stretch ratios, are provided in Fig. 4.16. The appearance of the strain plots in Fig. 4.16 are indicative of the fact that the $\gamma = 1.0$ and $\gamma = 1.2$ specimens are inverted, such that the trends for cases (c) and (d) are nearly exactly reversed. The asymmetry of strain distribution, particularly for cases (c) and (d), is pronounced, as the strain on opposite sides of the notch root are not equal. This may be attributed to slight misalignment of the specimen in the load frame grips, but may also be a product of structural asymmetry of the material, as was discussed in Chapter 3. Another possibility to consider is that this asymmetric behavior observed for cases (c) and (d) in Fig. 4.16 is a result of interaction of the strain field with the circular fillets

of the specimen. This conclusion is supported by noting the distribution for equibiaxial and the unequal-biaxial cases in Figs. 4.16 (c) and (d), in that one root appears to have negative *y*-direction (warp) strains, while the opposite root is in tension in the *y*-direction (warp direction). This suggests that further work is required to study the effects of specimen size and shape on the ability of this testing to produce valid results.

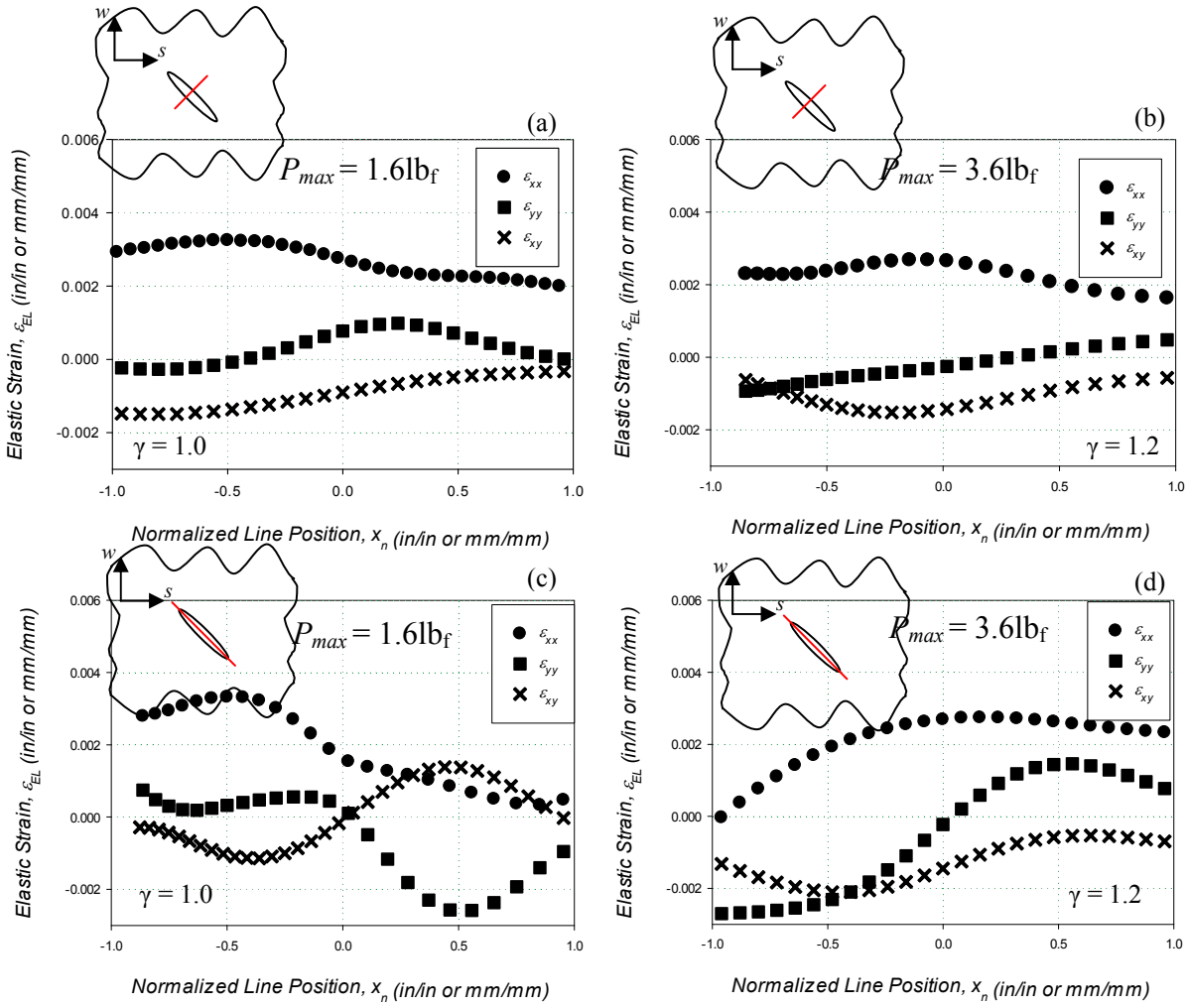

Figure 4.16: The strain distribution along lines passed through the notch roots (c, d), and perpendicular to the notch roots (a, b), for an $\alpha = 45^o$ oriented slit notch incised into (a, c) equibiaxial loaded, and (c, d) unequal-biaxally loaded specimens.

This final experimentally treated case is the $\alpha = 90^{o}$ slit type notch, for which the strains along the notch edge have been extracted as in the previous cases, and are plotted in Fig. 4.17. The equibiaxial case ($\gamma = 1.0$) shows peak axial strain values at the notch root ($\theta_w = 0$ radians) as expected. The unequal-biaxial case, however, shows that the location of peak strain has been shifted from the notch edge slightly. In both cases, the *x*-direction (weft or 1-direction) axial strain is higher than the warp direction, which speaks to the increased inter-wire coupling of this orientation. It is also noted that dips in strain occur near the notch root in the $\gamma = 1.2$ case that are not present in the equibiaxial case. To explain this measurement, reference must be made to the respective contour plots shown in Fig. 4.11. Inspection of Fig. 4.11 shows that areas of low strain are directly neighboring the notch root locations. Thus, even slight misalignment of the elliptical path used to extract the strain data is sufficient to cause the valley in strain observed in Fig. 4.17(b). It must be noted, however, that the location of the peak strains shown in Fig. 4.17(b) are reasonably close to the expected notch root locations, and are consistent with the peak values reported in the respective contour plot. Again, strains have been extracted from lines both along and normal to the major axis of the slit notch, and these plots are provided in Fig. 4.18 below. The lack of apparent strain concentration at the notch root as shown in Fig. 4.18(a) and (b) is attributed to the orientation of the notch in the weft direction, such that notch roots are composed of the less densely woven warp wires. This provides further evidence that the warp wire orientation possesses less inter-wire coupling than the weft wire orientation, and is consistent with the findings from Chapter 3. Inspection of Fig. 4.18(a) shows a severe compressive zone in the *x*-direction (weft) strain directly adjacent to the left notch edge. The fact that this behavior is not observed at the opposite notch edge, which shows elevated levels of *x*-direction (weft) strain as expected, leads to the conclusion that this observation is related to boundary condition

interference. Figure 4.18(b) shows clear regions of elevated strain corresponding to the notch locations, with nearly equal increases in magnitude at the notch roots. Figure 4.18(c) and (d) shows zones of higher *x*-direction (weft or 1-direction) strain at the notch faces, corresponding with regions of reduced shear strain. Inspection of Fig. 4.18(d) reveals clear evidence of the increased strain at the notch face, with an increase of 0.2% strain over the neighboring regions.

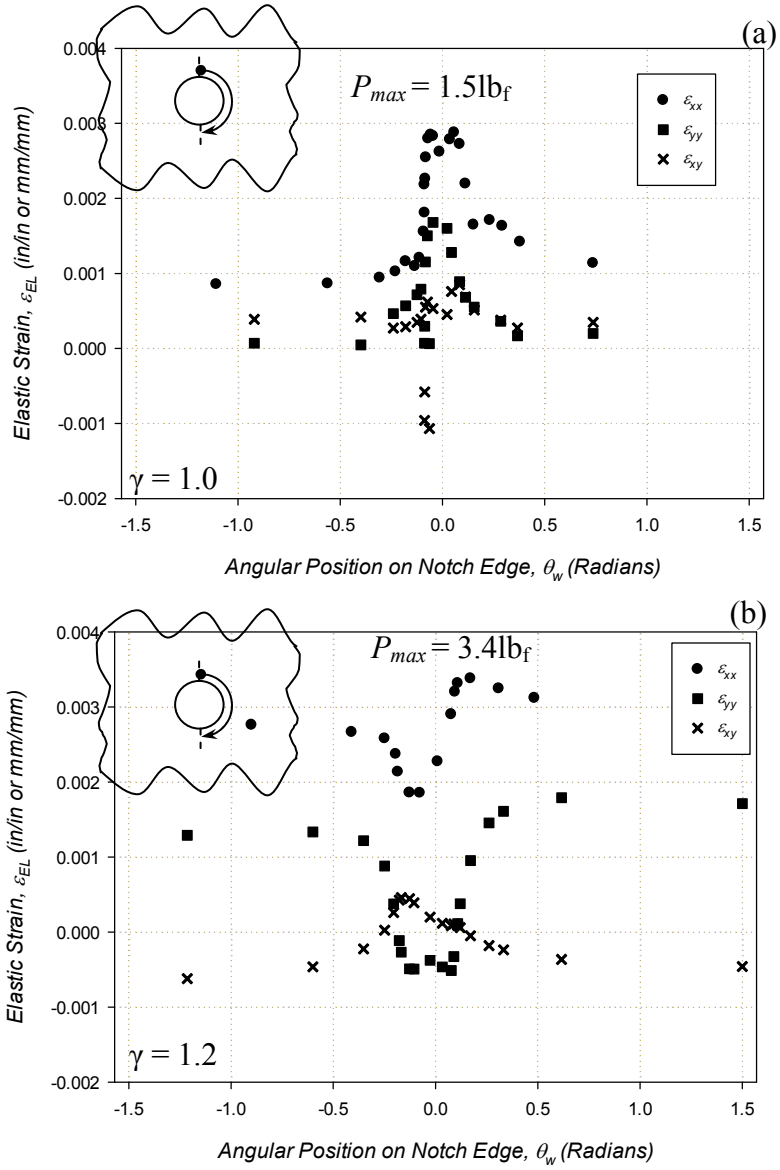

Figure 4.17: The distribution of the tensorial elastic strain along the edge of an α = 90º oriented slit notch incised into (a) equibiaxial loaded, and (b) unequal-biaxially loaded SS316L woven wire mesh material.

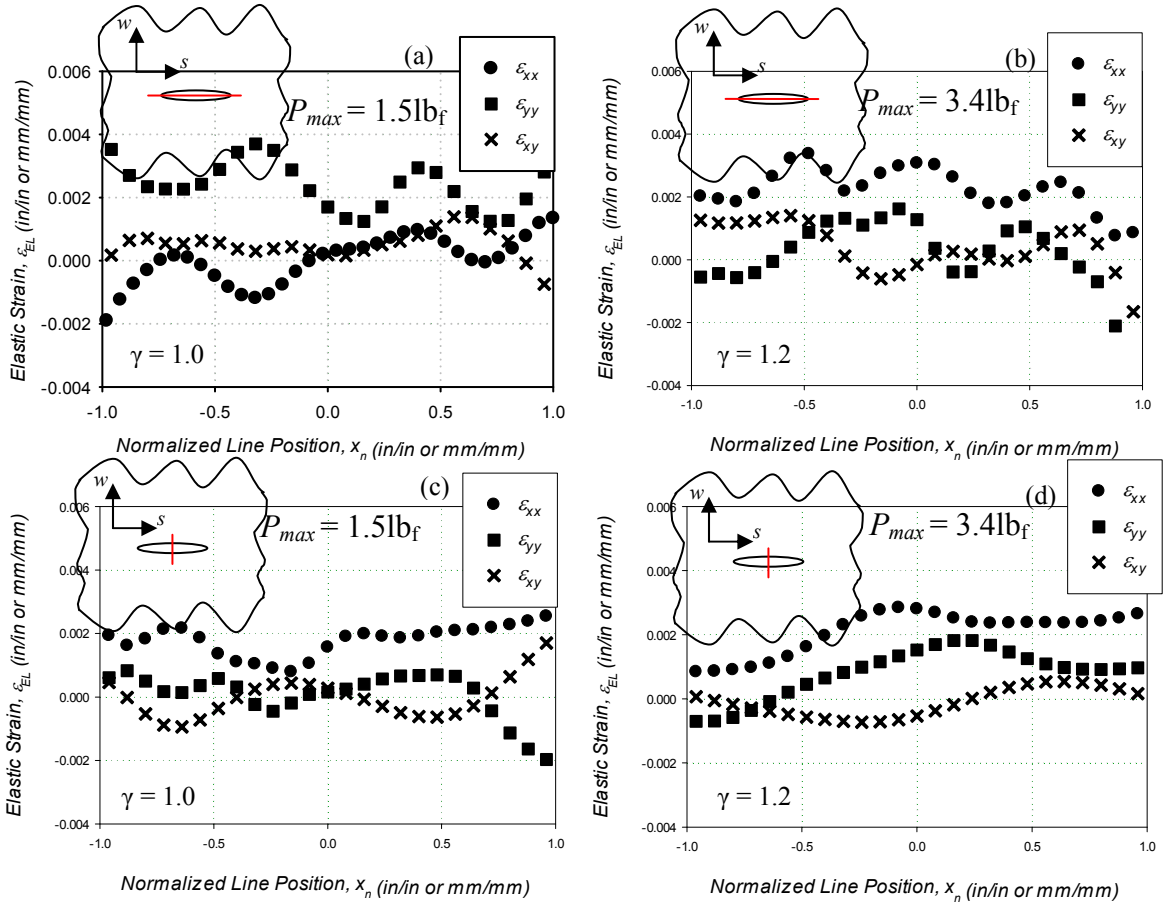

Figure 4.18: The strain distribution along lines passed through the notch roots (c, d), and perpendicular to the notch roots (a, b), for an $\alpha = 90^o$ oriented slit notch incised into (a, c) equibiaxial loaded, and (c, d) unequal-biaxally loaded specimens.

With the tensorial strains along the notch edge extracted and examined, Hook's Law, introduced previously as Eq. (3.2.6), can be employed to formulate the Cartesian strain components. As the state of stress in the biaxial specimen is somewhat complex, it is desirable to compare stress states amongst specimens using an equivalent measure of stress. Due to the assumed orthotropy of the subject material, and the previously displayed ability of the Hill Criterion to capture the yield behavior of the SS316L material reasonably well, the Hill equivalent stress, σ_{hill}, is chosen as the stress measure for comparison in this work. The equivalent Hill stress is formulated using the tensorial strain components taken near the notch

edge around the circumference of the notch, allowing for conclusions to be drawn regarding the effects of the circle and slit type notches in the stress state in the SS316L woven wire mesh material when loaded biaxially. Figures 4.19 through 4.21 show the distribution of the Hill equivalent stress as a function of angular position for the various notch geometries for both equibiaxial and unequal-biaxial cases. Figure 4.19, which shows the distribution of stress near the edge of the circular notched biaxial cruciform specimens, show zones of peak stress coinciding with the angular locations of the uniaxial tensile arms. The distribution of peak stress resembles the results obtained from the uniaxial tensile testing regimen, and the distribution can be thought of as a combination of two separate uniaxial tensile tests. This is thought to be a result of the size of the notch with respect to the size of the gage section of the biaxial cruciform specimens, and future work is necessary to investigate the relationship between circular notch size and stress distribution under biaxial tensile conditions. As was observed in the DIC contour plots, the location peak equivalent stress is rotated slightly for the unequal-biaxial case, which is thought to a product of both the unequal strain state, and the fillet regions interacting with the stress distribution around the notch edge. Figure 4.20 shows the distribution of the Hill equivalent stress near the notch edge for the case of various oriented slit notches in equibiaxially loaded SS316L woven wire mesh material. The location of peak stress is observed to shift as the notch orientation is varied, with the angular position of peak stress coinciding with the angular position of the notch edge in all cases. It is noted that the $\alpha = 0^{\circ}$ notch (aligned with the warp direction) produces a far less pronounced perturbation of the stress field near the notch tip, which is consistent with the observation made in uniaxial testing, and can be attributed to the reduced inter-wire coupling of the warp wires. In all cases except the $\alpha = 90^{\circ}$ case (notch aligned with the weft axis) the distribution of stress is asymmetric.

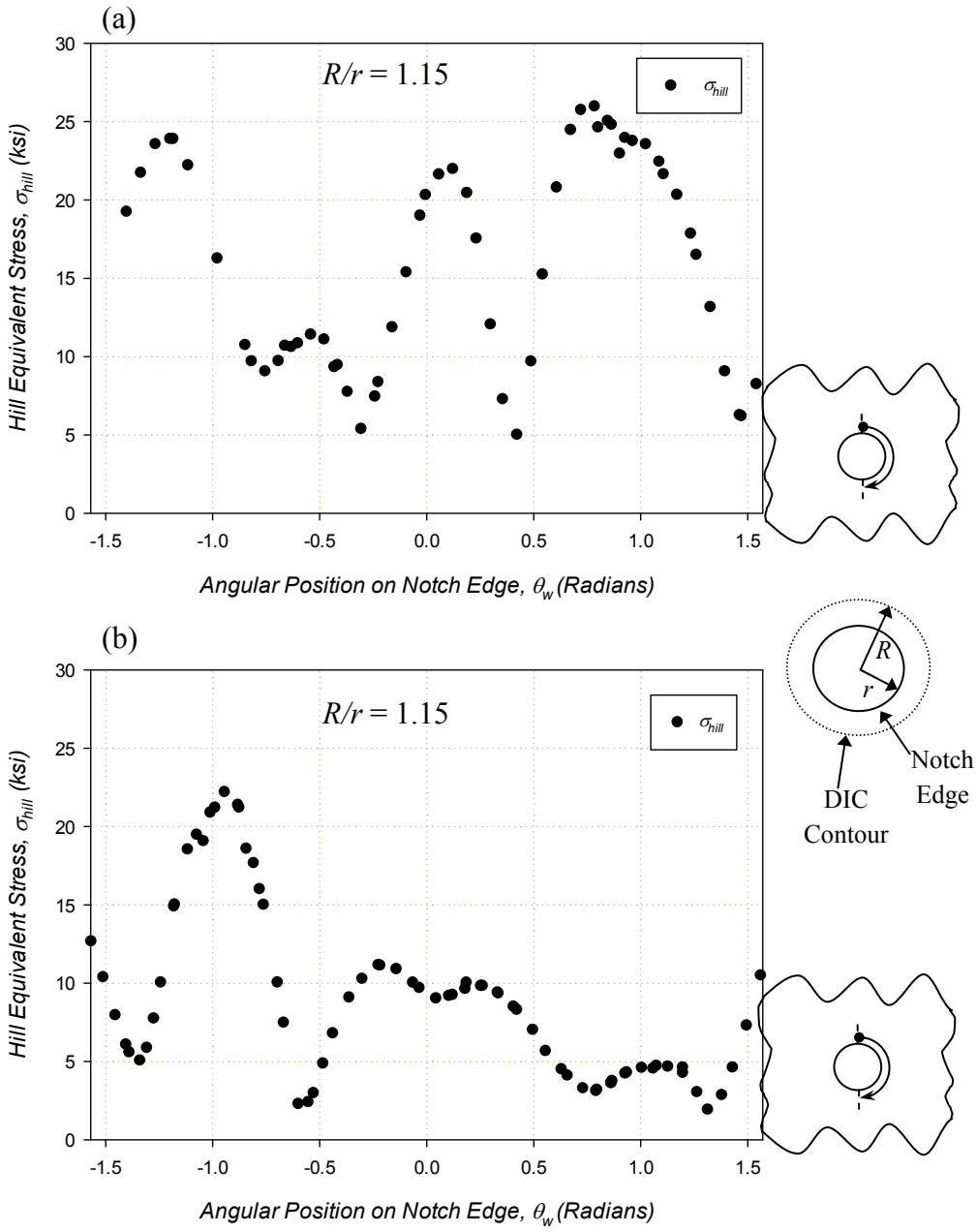

Figure 4.19: The Hill equivalent stress distribution near the edge of a circular notch in (a) equibiaxially loaded, and (b) unequal-biaxially loaded SS316L woven wire mesh material.

This result is unexpected, and again may be due to the relative size of the notch with respect to the gage section of the cruciform specimen. Numerical analysis of the notched cruciform

geometry is required to investigate this asymmetry further, and the results of this analysis are detailed in the subsequent chapter.

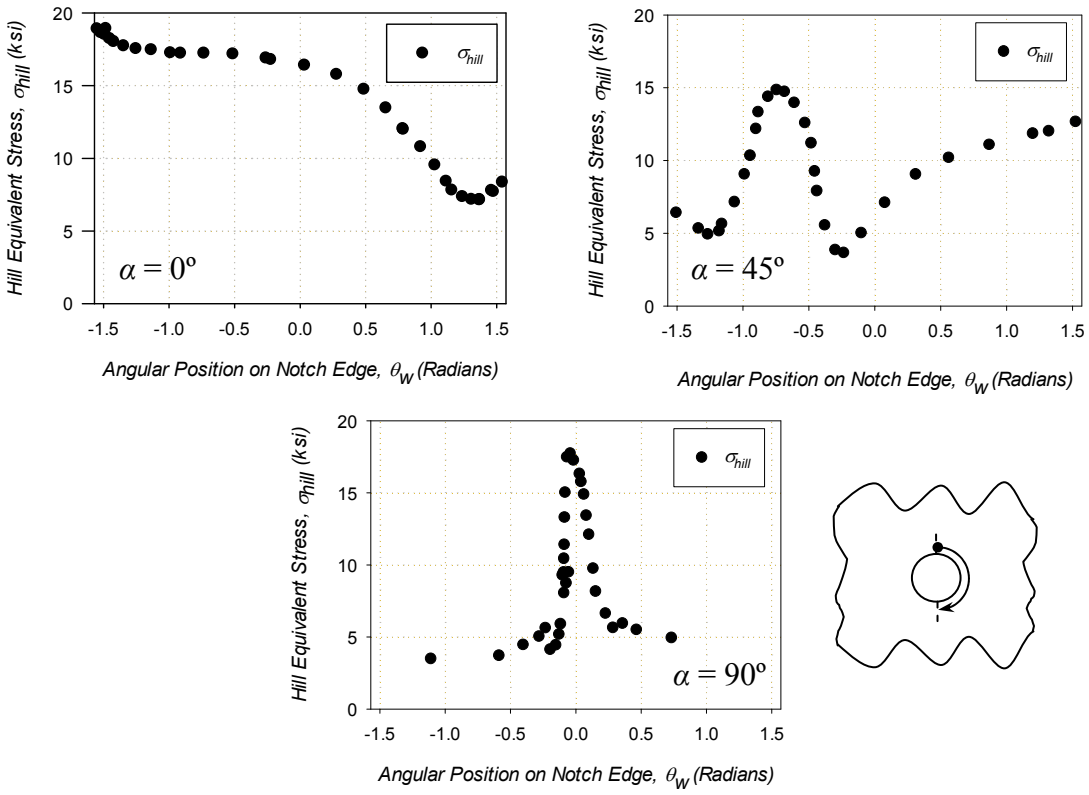

Figure 4.20: The Hill equivalent stress distribution near the edge of a slit type notch at various orientation with respect to the warp material direction in equibiaxially loaded SS316L woven wire mesh material.

The Hill equivalent stress distribution for the case of a slit notch at various orientations in unequal-biaxially loaded SS316L woven wire mesh material is provided in Fig. 4.21. Comparison of Fig. 4.21 with Fig. 4.20, which shows the equibiaxial case, reveal distinct differences in the location of peak and minimum stress values. The α = 0º case shows a minimum stress at the bottom notch root, and a near constant distribution of maximum stress that originates immediately off of the notch root. The maximum stress is observed to occur at the opposite notch root. The α = 45º case is quite similar to the equibiaxial case in trend, but the peak stress appears to occur on the opposite side of the notch. This is again attributed to the specimen

being input into the load frame with the opposite surface facing the camera with respect to the equibiaxial case, thus causing the inverted stress distribution.

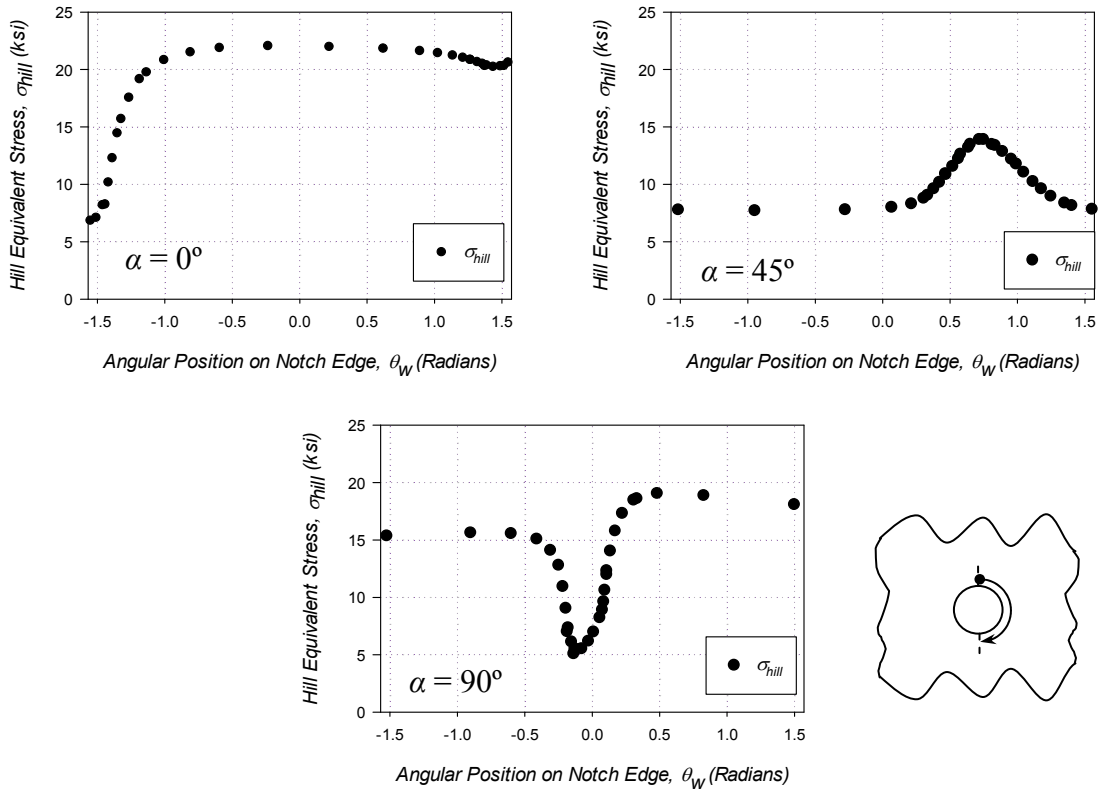

Figure 4.21: The Hill equivalent stress distribution near the edge of a slit type notch at various orientation with respect to the warp material direction in unequal-biaxially loaded SS316L woven wire mesh material.

Similar to the $\alpha = 0°$ case, the $\alpha = 90°$ case appears to have a minimum stress near the notch root. This observation was also made in investigation of the strain state in Fig. 4.17(b), where it was attributed to slight misalignment if the elliptical path used to extract the raw strain data. It is noted the location of peak stress is near to the notch root, but on the opposing notch edge. This shift in the location of the peak stress with respect to the equibiaxial case may be a result of the unequal-biaxial loading, as was observed in the case of the circular notches. It is also possible that the region of reduced stress near the notch root may be caused by constraint in the weft

direction due to the unequal stretch conditions and improper loading of the specimen in the grips. Clearly, this observation requires further investigation using numerical techniques, and this is provided in detail in the subsequent chapter.

4.2.2 Near Notch Experimental Stress Concentration Factors

As the SS316L woven wire mesh material is chiefly loaded in states of biaxial tension in industry, it is of great interest to develop an idea of the magnitude of the effects of a given stress riser has on the local stress field of this material when loaded biaxially. As previously defined, the near notch Stress Concentrations Factor (SCF) is a classical measure of the effect of a stress riser on the magnitude of the stress near a notch in a component, and this metric is utilized in the biaxial test cases to compare the stress states between un-notched and notched geometries at equivalent loading conditions. For the case of biaxial loading, the SCF is not clearly defined in literature, particularly in the case of anisotropic materials. A consistent definition of the SCF is necessary for accurate documentation of the effects of stress risers on the biaxially loaded woven wire mesh material, as the definition undoubtedly will affect the values predicted. Thus, the SCF is defined herein as the ratio of the maximum Hill equivalent stress near the edge of the notch to the Hill stress in the center of an un-notched biaxial specimen at the same load level, i.e.,

$$K_{g,n} = \frac{\sigma_{hill,\max}}{\sigma_{hill,gross}} \tag{4.2.1}$$

The trend of the SCF, $K_{g,n}$, with varying notch orientation, α, is plotted in Fig. 4.22 for the of equibiaxial stretch. The 1-direction (weft) principle strain contours, all equally scaled, are also included marking the location for SCF determination, and its proximity to and interaction with the stress perturbations caused by the neighboring circular fillets. Inspection of Fig. 4.22 reveals

that the maximum SCF, as defined in Eq. 4.2.1, is found in the case of circular notch. These results are, in general, not in agreement with uniaxial tensile testing results presented in Fig. 3.34, which shows the slit type notches as having higher SCF values, as would be expected.

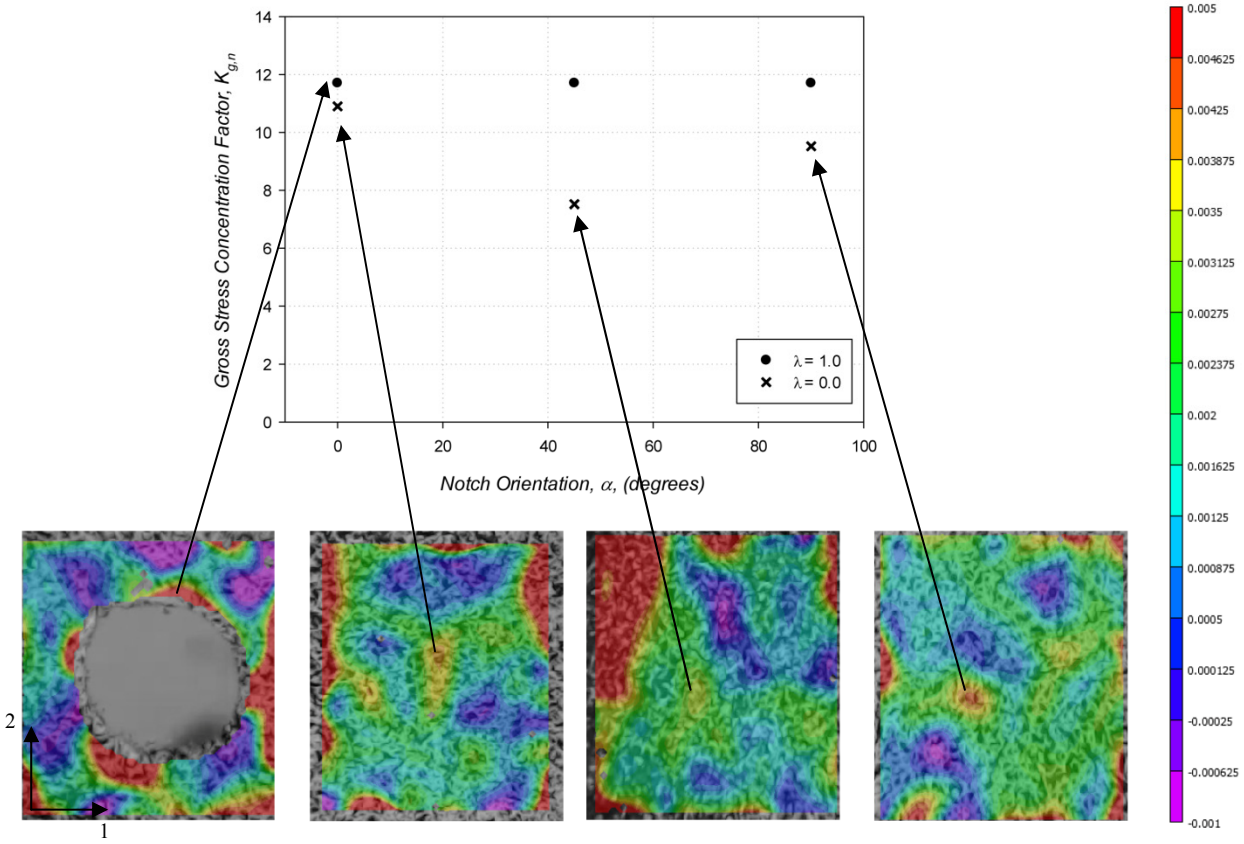

Figure 4.22: The near notch equibiaxial gross SCFs for circular and slit type notches in the biaxial cruciform specimen with respect to the notch orientation, and the corresponding 1-direction (weft direction) principle strain contours.

Inspection of the strain contour plot for the circular case provides a possible explanation for this observation, as the size of the notch is nearly equal in size of the measureable gage section, and clearly influenced by the high strain fields along the boundary. Further work is needed to explore the effects of reducing the size of the notch before definitive conclusions can be drawn regarding the SCF of this case. Figure 4.23 shows the trend of the SCF for the notched biaxial specimens with respect to the notch orientation for the unequal-biaxial stretch case. The trends of the SCF for the unequal biaxial case are observed to match those for the equibiaxial case, but with values

on the order of 50% lower for the slit notches. The reduction in the SCF for the $\gamma = 1.2$ case may be attributed to the fact that the amount of stretch applied in the weft direction, which has shown to posses higher inter-wire coupling and is known to be of higher weave density, has been reduced.

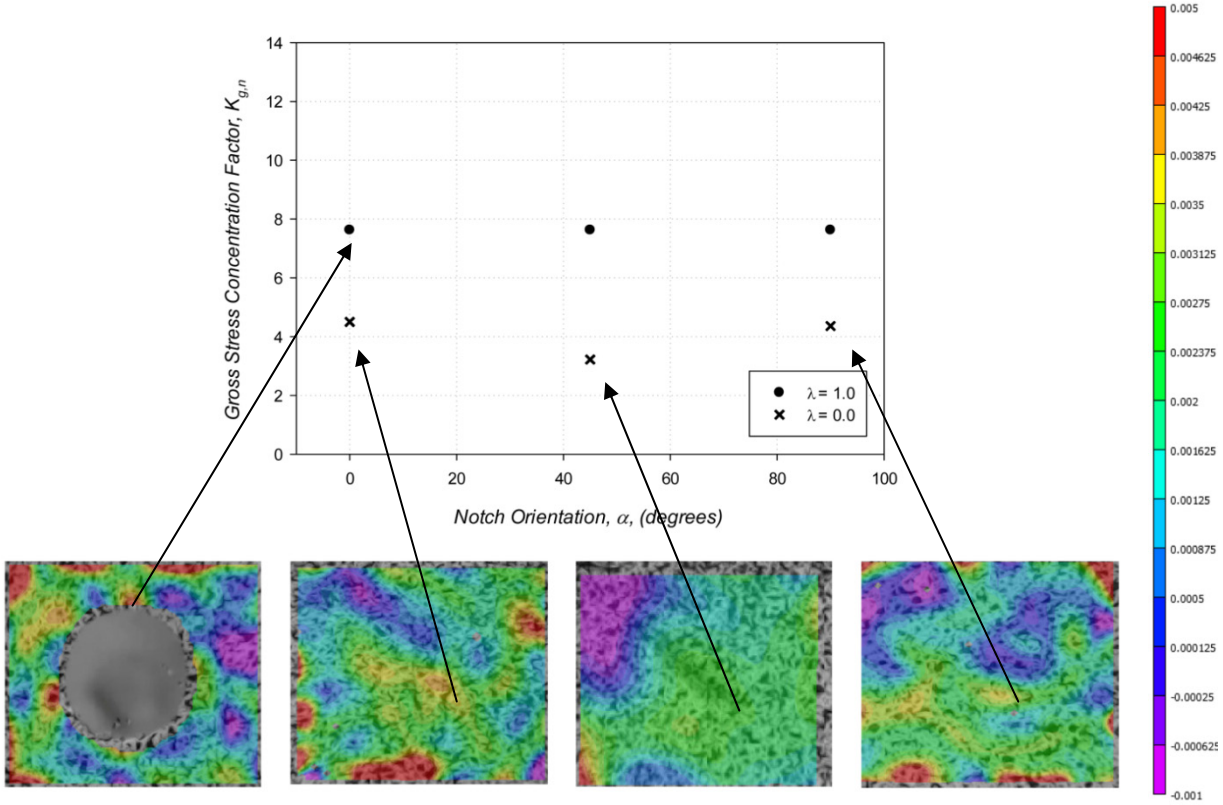

Figure 4.23: The near notch gross unequal-biaxial SCFs for circular and slit type notches in the biaxial cruciform specimen with respect to the notch orientation, and the corresponding 1-direction (weft direction) principle strain contours.

This assumption could easily be tested in future work via a simple rotation of the test specimen, such that the weft direction receives 20% more stretch than the warp direction, and then observing the trends in SCF with respect to the changing stretch ratio. In general, the maximum SCF for the slit notch cases are found to be at $\alpha = 0^{o}$, while the minimum SCF is found at $\alpha =$

45º. The SCF results presented in Figs. 4.22 and 4.23 are summarized in Table 4.1 for all experimentally treated conditions.

Table 4.1: Near Notch Gross Stress Concentration Factor for various notch geometries and orientations in both equibiaxially and unequal-biaxially loaded cruciform specimens incised from SS316L woven wire mesh material

Biaxial Stretch Ratio, γ	Notch Aspect Ratio, λ	Notch Orientation, α (º)	Near Notch Gross SCF, $K_{g,n}$
1	1	-	11.70
	0	0	10.90
		45	7.52
		90	9.52
1.2	1	-	7.62
	0	0	4.50
		45	3.22
		90	4.36

4.3 Fractography of Notched Biaxial Cruciform Specimens

Much knowledge regarding the effect of a stress concentration on the mechanical behavior of SS316L woven wire mesh material can be gained by inspection of the rupture zone. In particular, observations regarding the size of the process zone, the degree of wire pullout and fraying, and the waviness of the fracture surface are indicative of the mechanisms leading to mesh failure. To facilitate an investigation of the mechanisms leading to fracture in the notched biaxial cruciform specimens, post-mortem fractography has been performed using a DinoLite digital microscope, model number AM7015MT. The fracture surface images, shown in Figs. 4.24 through 4.31, are supplemented with the experimental DIC frames taken in situ at the onset of specimen rupture, showing the distribution of first principal stain around the notch location. The relative size of the area of the strain field perturbation is thought to be indicative of the sensitivity of the biaxially loaded woven wire mesh to the given notch geometry, and is also

correlated to the dominant material direction, for example, the warp (0º) material orientation is consistently observed to produce larger zones of strain field perturbation.

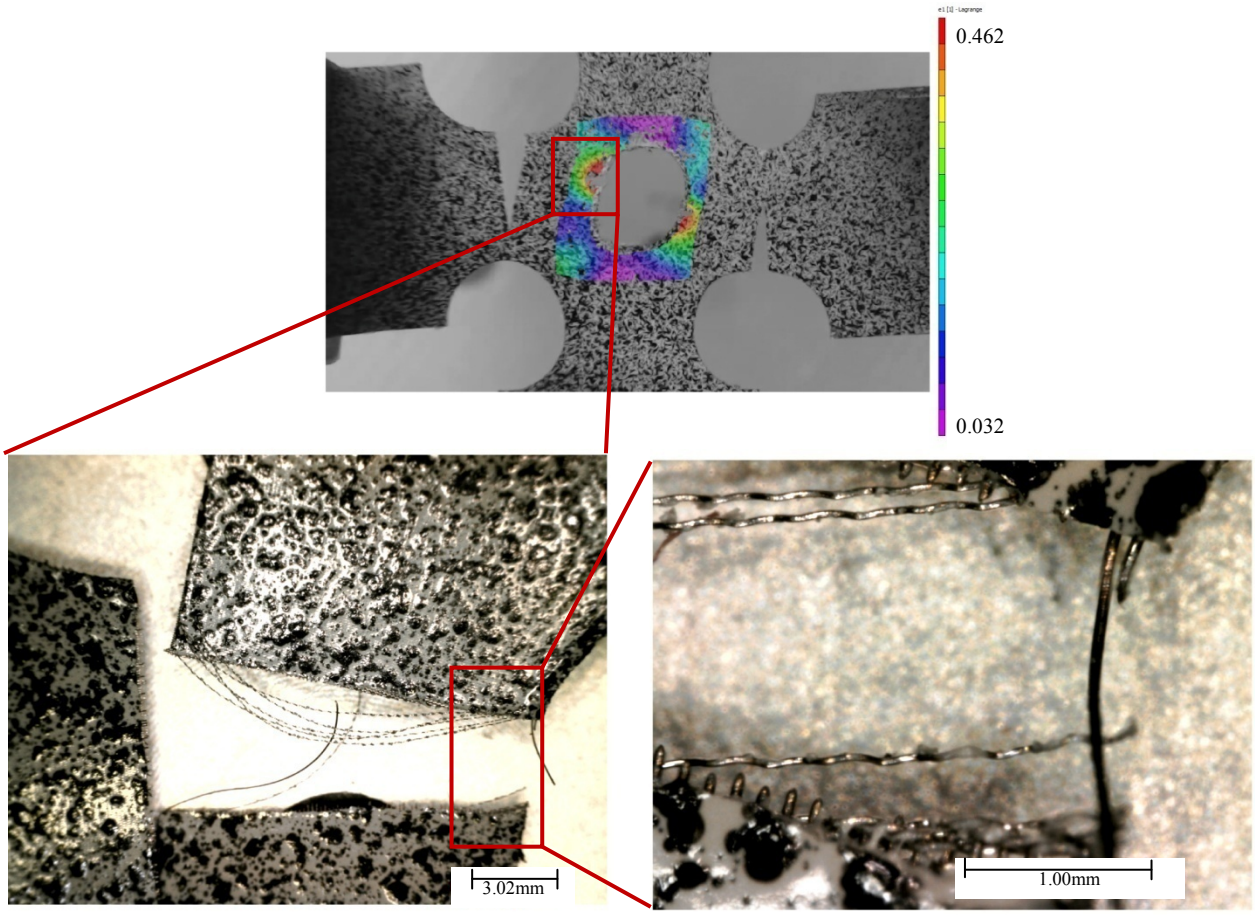

Figure 4.24: Post-mortem fracture surface images of equibiaxially loaded SS316L woven wire mesh incised with circle type notch, along with DIC contours of first principal strain at rupture.

In homogenous and continuous materials, the sharpness of the notch radius tends to correlate well with the observed failure mechanisms, with larger root radii leading to yield dominant failure, and lower root radii typically leading to fracture dominant failure modes. Inspection and comparison of the circular and slit notch rupture zones in the SS316L woven wire mesh material allows for conclusions to be drawn regarding the failure behavior of this class of

materials, and how this behavior is related to material orientation and boundary loading conditions. Figures 4.24 and 4.25 show the rupture zones for the $\lambda = 1.0$ circular notches in both equibiaxial and unequal-biaxial cases, respectively. Inspection of both Figs. 4.24 and 4.25 shows that the failure at the circular notch root is accompanied by simultaneous failure at the circular fillets, indicating that the severity of the stress concentration at the circular notch root is not sufficient to cause fracture type rupture at the notch.

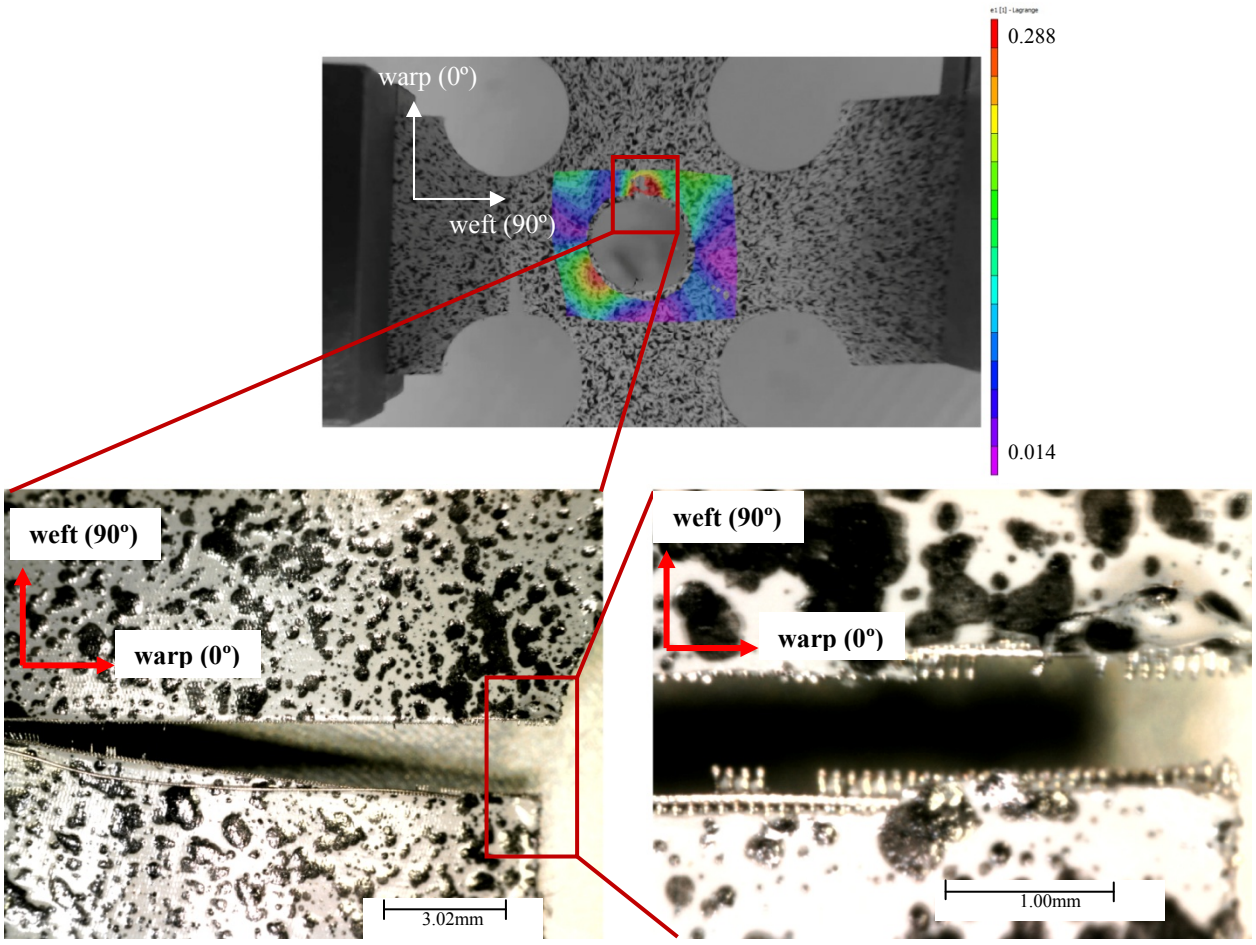

Figure 4.25: Post-mortem fracture surface images of unequal-biaxially loaded SS316L woven wire mesh incised with circle type notch, along with DIC contours of first principal strain at rupture.

Nonetheless, the zone of increased strain in the region of gage section failure is pronounced, being more than an order of magnitude larger then neighboring zones of minimum strain.

Inspection of the fracture surfaces shows that the orientation of the crack propagation changes with load ratio. In the equibiaxial case, the failure is observed to occur in the warp wires, and is characterized by a high degree of weft wire fray. Failure in the unequal-biaxial case shown in Fig. 4.25, occurs at a location nearly 90º to the equibiaxial case, and is characterized by the sharp and concise failure of the weft wires. Further inspection of the first principal strain contour plot provided in Fig. 4.25, however, indicates that the dominant fracture direction is likely in a state of transition at the stretch ratio of 1.2, as an additional zone of increased strain is observed to be developing at an angle of 90º to the fracture zone. In both cases, the fracture prorogation is observed to be normal to either the warp (0º) or weft (90º) principal directions, and is indicative of fracture occurring due to tensile dominant conditions.

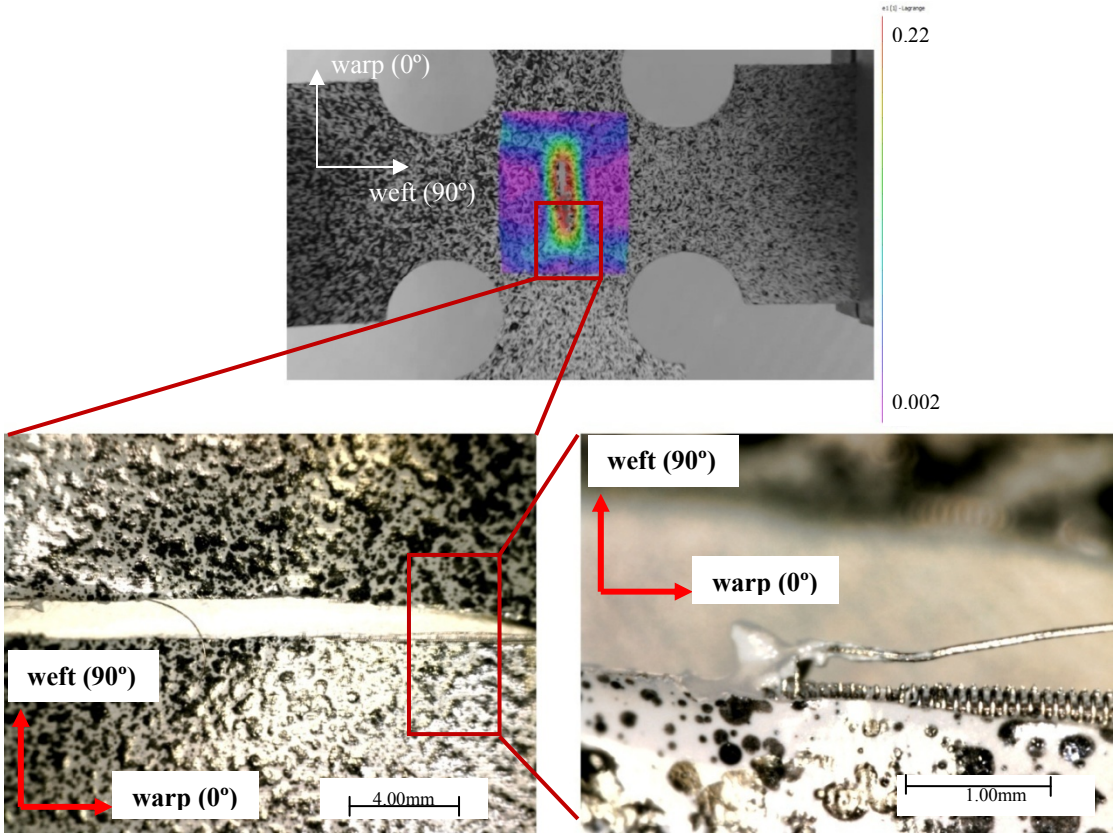

Figure 4.26: Post-mortem fracture surface images of equibiaxially loaded SS316L woven wire mesh incised with an α = 0º slit type notch, along with DIC contours of first principal strain at rupture.

To investigate the difference in rupture zone appearance associated with the extreme cases of the λ = 1.0 circle notch and the λ = 0.0 slit notch, fractography was also performed on the various slit notch cases. Figures 4.26 and 4.27 show the failure zones associated with the equibiaxial and unequal-biaxial α = 0º slit notch cases, respectively.

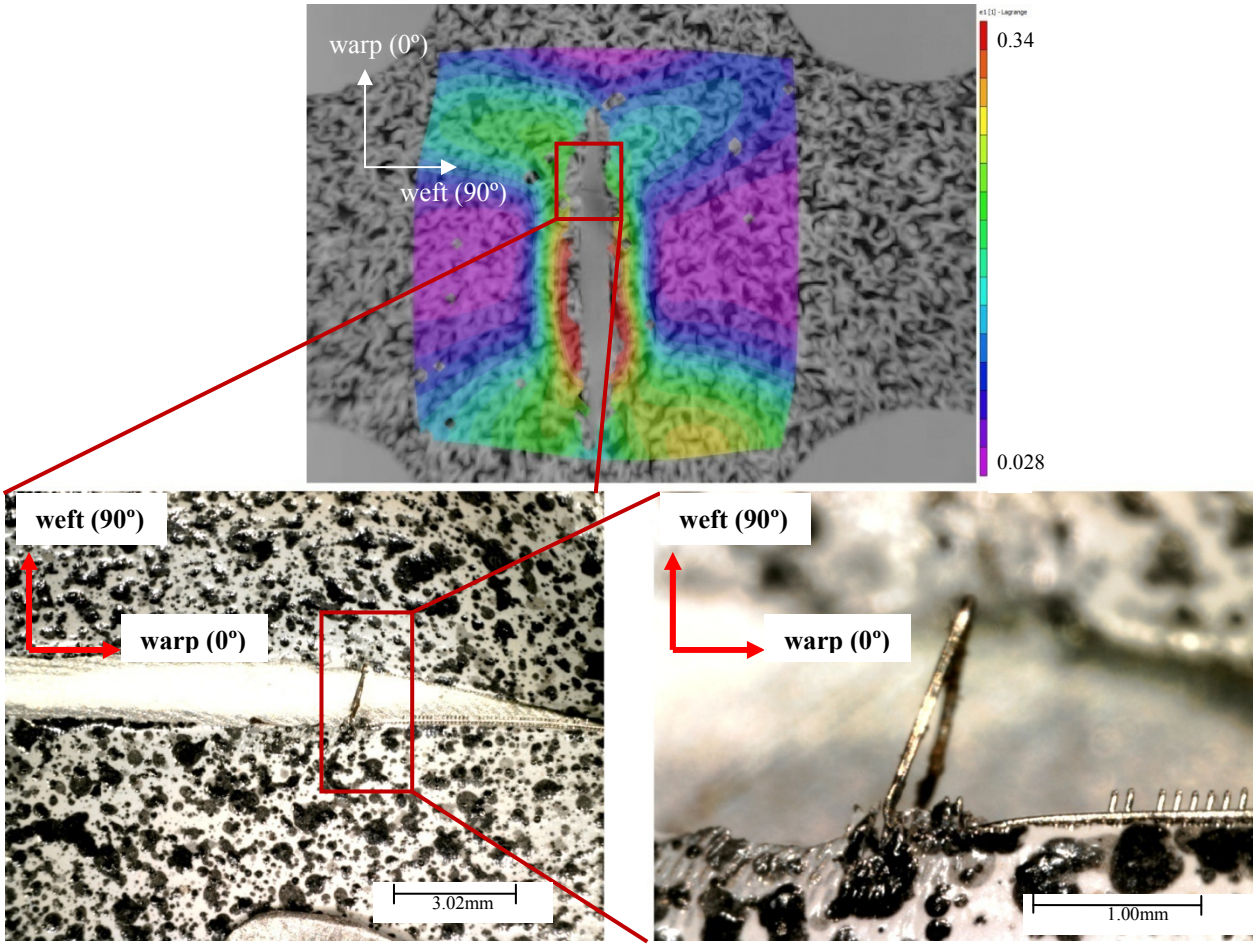

Figure 4.27: Post-mortem fracture surface images of unequal-biaxially loaded SS316L woven wire mesh incised with an α = 0º slit type notch, along with DIC contours of first principal strain at rupture

In both cases, the notch is observed to initiate fracture in the gage section of the specimen, which propagates normal to the weft wire direction. In both Fig. 4.26 and 4.27, the fracture initiation site is marked by an extremely tortured warp wire, which has been pulled out of the weave by failing weft wires at the notch root. This seems to indicate a zone of high inter-wire coupling at

the notch root, which is believed to be indicative of higher energy transference, and a higher degree of notch root yielding. Support for this conclusion, especially in the $\gamma = 1.2$ case shown in Fig. 4.27, is gained from the contour plots of first principal strain taken at the time of mesh rupture, which show zones of increased strain propagating away from the notch root. The increased area of strain distribution at the time of rupture observed in the uneqaul-biaxial case with respect to the equibiaxial case shown in Fig. 4.26 is attributed to the higher stretch imparted onto the warp wires, which invariably are characterized by lower inter-wire coupling, and a larger process zone.

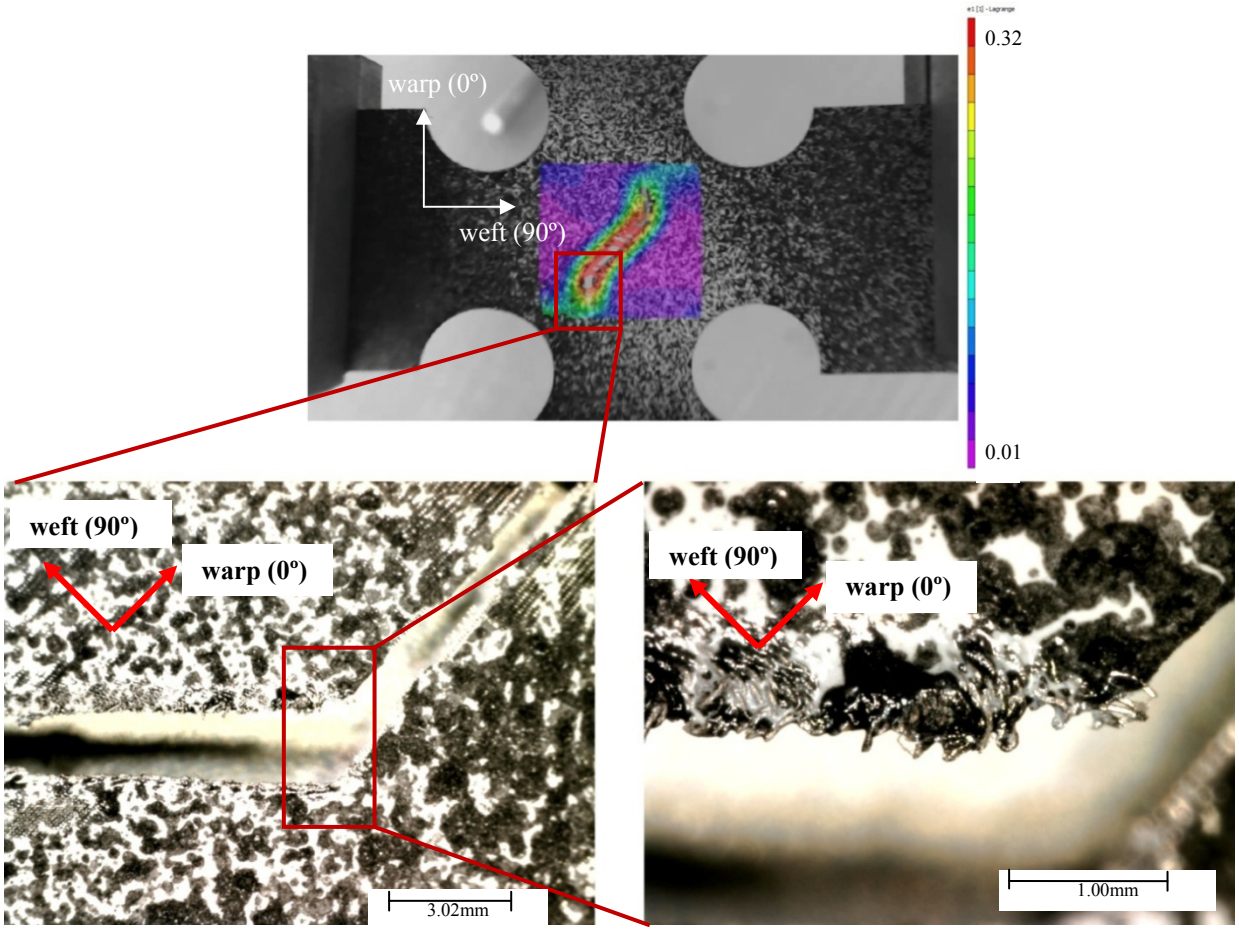

Figure 4.28: Post-mortem fracture surface images of equibiaxially loaded SS316L woven wire mesh incised with an α = 45º slit type notch, along with DIC contours of first principal strain at rupture.

Figures 4.28 and 4.29 show the failure regions associated with the α = 45º oriented slit type notch in equibiaxial loaded and unequal-biaxially loaded SS316L woven wire mesh material, respectively. In both cases, the fracture is observed to propagate normal to the weft wire direction, and is characterized by bending of the wires along the crack face. The observation of bending wires on the crack face is consistent with mode II type loading conditions, indicating that shearing of the notch face contributes to the failure of the material. As this material exhibits a much higher elongation to failure in shear than in tension, as evidenced by Fig. 3.1, it is likely that the rupture associated with the α = 45º slit is more ductile in nature.

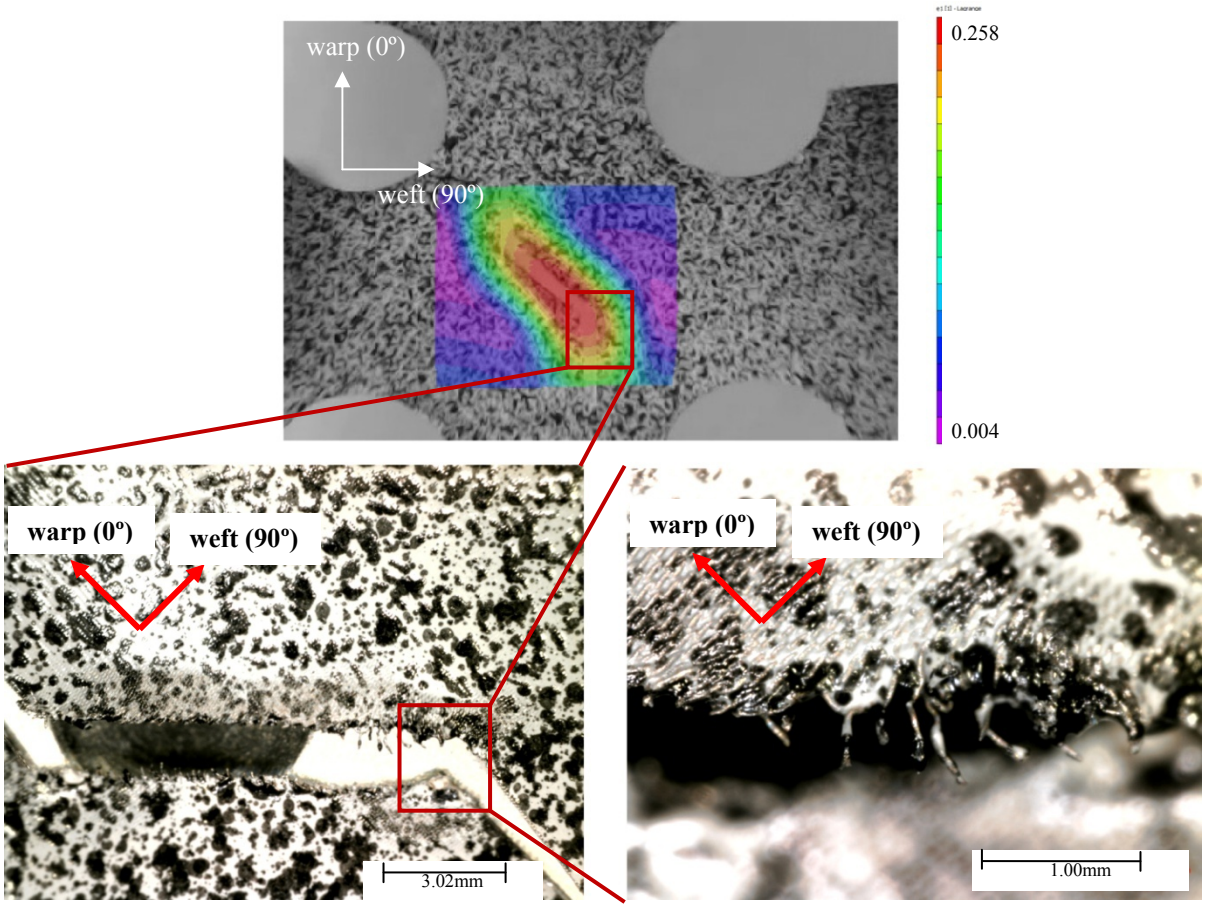

Figure 4.29: Post-mortem fracture surface images of unequal-biaxially loaded SS316L woven wire mesh incised with an α = 45º slit type notch, along with DIC contours of first principal strain at rupture.

As the fracture of the α = 45º slit notch cases are observed to propagate via weft wire failure, observation of the sharp and concise fracture surface is consistent with previous observations made from uniaxial tests. Again, a larger zone of increased strain is observed in the contours of first principal strain for the unequal-biaxial case shown in Fig. 4. 29 than is observed for the equibiaxial case in Fig. 4.28, which is attributed to the increased stretch imparted onto the warp wires. Figures 4. 30 and 4.31 show the rupture zones associated with the α = 90º slit type notch in the biaxial cruciform specimen of SS316L woven wire mesh under equibiaxial and unequal-biaxial tension, respectively.

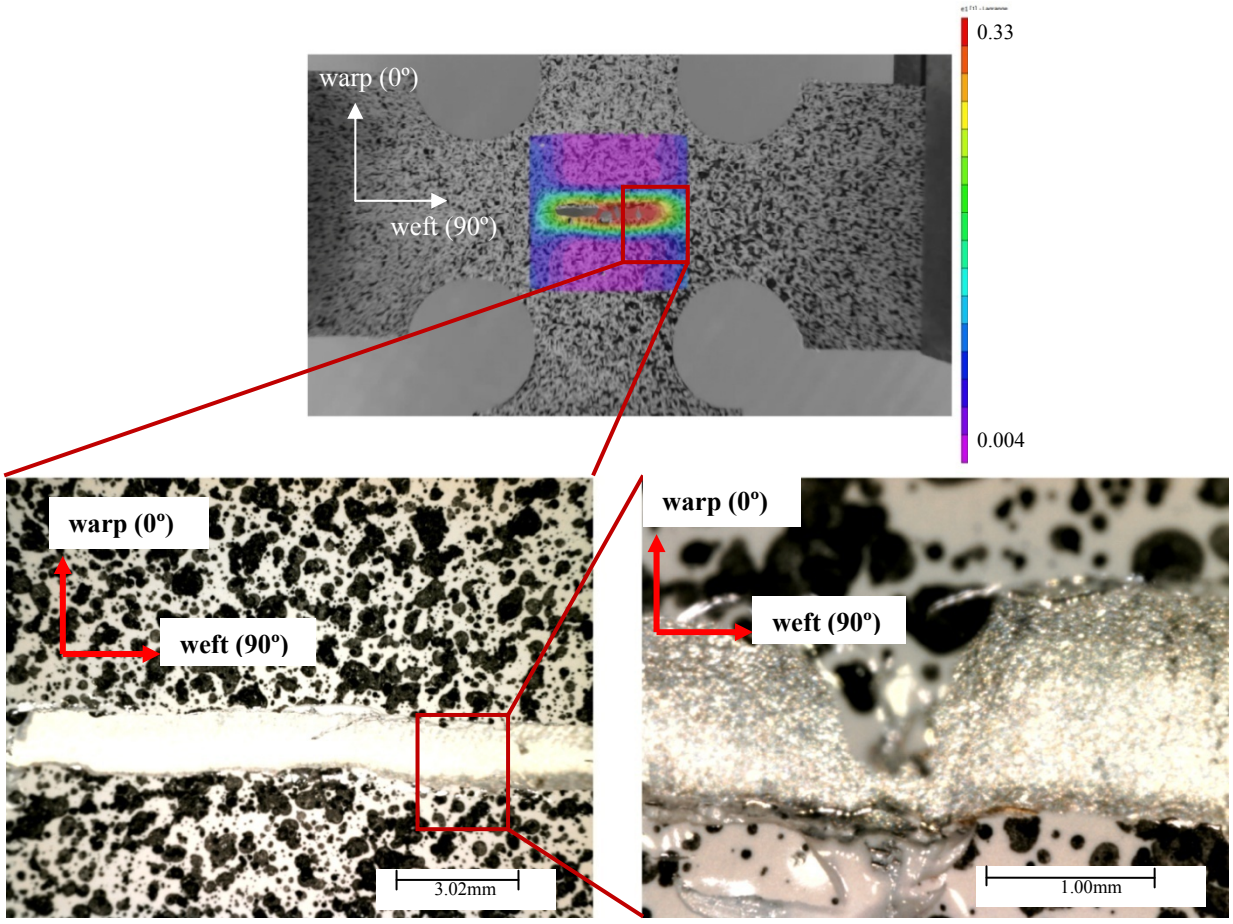

Figure 4.30: Post-mortem fracture surface images of equibiaxially loaded SS316L woven wire mesh incised with an α = 90º slit type notch, along with DIC contours of first principal strain at rupture.

In both cases, fracture is observed to propagate normal to the warp wire direction, and is characterized accordingly by a wavy fracture surface with areas of weft wire pull-out. The warp wire failure for the case of α = 90º notch cases in general presents as a more yield dominant failure condition, with a larger process zone evidenced by both inspection of the fracture surface images, and by the large zones of increased strain the respective DIC contour plots. Figure 4.31, in particular shows the ductile failure of the warp wires at the notch root, characterized by significant warp wire necking.

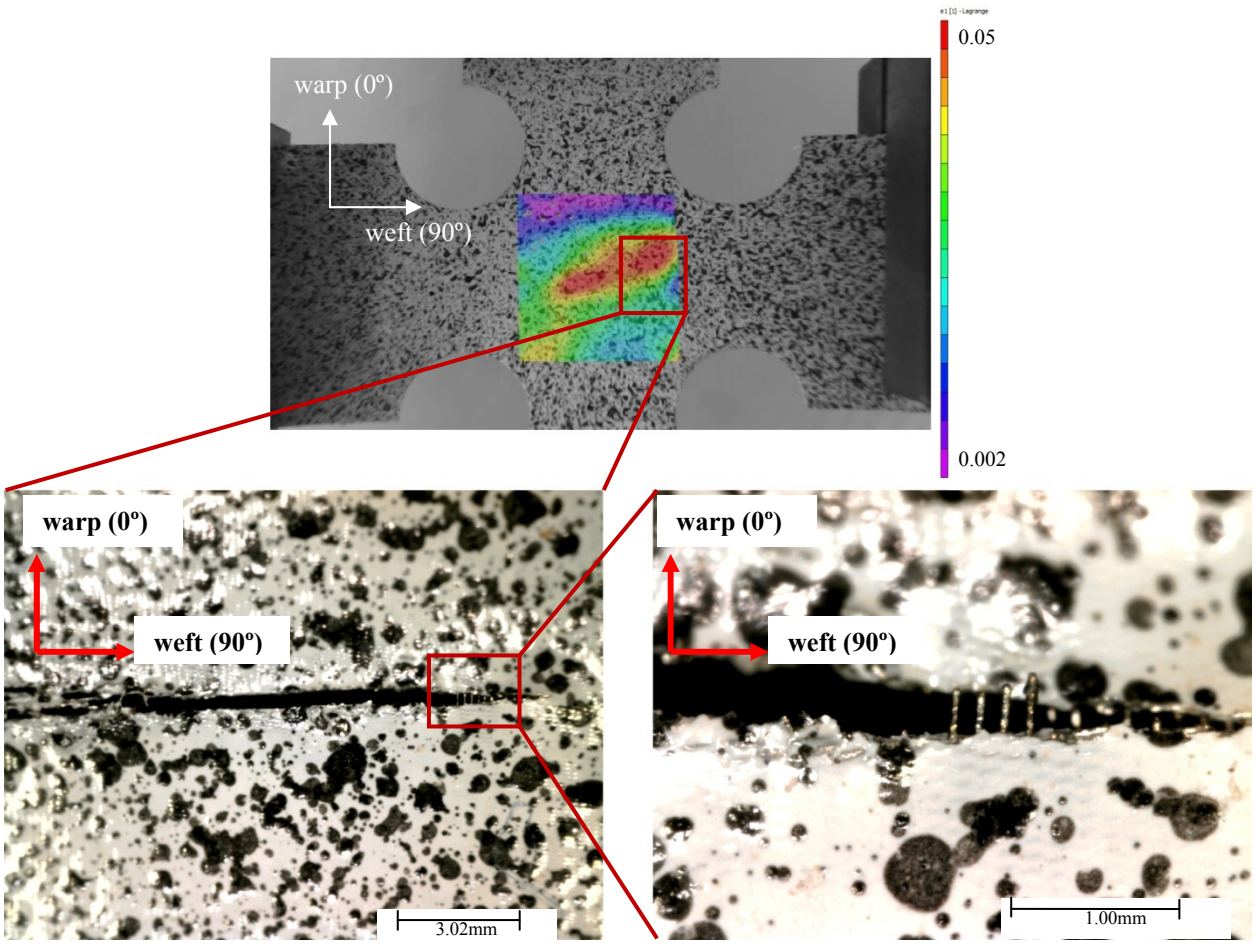

Figure 4.31: Post-mortem fracture surface images of unequal-biaxially loaded SS316L woven wire mesh incised with an α = 90º slit type notch, along with DIC contours of first principal strain at rupture.

In general, it is observed that the crack propagation orientation is not affected by the biaxial stretch ratios tested in the current experimental regimen. Fracture always is observed to occur along a principal material direction for the notch orientations treated here, with a transition in the dominant failure mode from weft wire dominant to warp wire dominant occurring between $\alpha = 45^{\circ}$ and $\alpha = 90^{\circ}$. The precise transition orientation is of great interest, and must be addressed by future experimental work incorporating intermediate notch orientations.

CHAPTER 5: MACRO-SCALE FINITE ELEMENT ANALYSIS

The finite element method has been leveraged as a platform for macro-scale simulation of the mechanical behavior of SS316L twill dutch woven wire mesh material in the presence of stress concentrations. While the mechanisms leading to ultimate mesh rupture are of great interest to this work, it is prudent for a number of reasons to begin this study in the elastic domain. Primary among the motivations for elastic simulation is the need to supplement the experimental regimen with intermediate material orientations, θ, and ellipse ratios, λ. Also, the elastic material constants have been experimentally-defined, as demonstrated in Ch. 3, making such a simulation technique relatively straightforward to implement. Furthermore, as the finite element method is built upon assumptions inherit to continuum theory, comparison of the Finite Element Model (FEM) results to the experimental contour plots provided in Ch. 3 allows for objective conclusions to be drawn regarding the practical use of such an idealization. To this end, a FEM code has been established in ANSYS to batch calculate the SCF based in the maximum σ_θ component of stress at the notch edge in relation to the gross applied stress, as was done in Ch. 3. Also, macro-scale strain contour plots are provided for comparison to the experimental DIC data. This analysis was performed parametrically, and data has been collected in material orientations varying from warp (0º) to weft (90º) in intervals of 15º, and at λ ratios of 1.0, 0.5, and 0.05 (approximating 0.0). In general, the results of this modeling effort show reasonable agreement between the FEM and the experimental results, justifying extension of the numerical modeling into the plastic domain in the subsequent chapter, such that mesh yielding and rupture can be studied.

5.1 Finite Element Model and Parameter Definition

5.1.1 The Uniaxial Model

A macro scale FE model has been generated to match the geometric specifications outlined in Fig. 2.1(b). An orthotropic linear elastic constitutive model has been employed, with elastic constants corresponding to those defined in Table 3.2. The FE mesh consists of 8-node isoparametric plane elements using the assumption of plane stress (PLANE82), and the mesh density is increased at the notch edge to capture the higher gradients in that region. For principal material orientation cases, the symmetry of the problem has been leveraged, and only one quarter of the geometry has been modeled. For cases off of the principle material orientations, the orthotropic material properties are not symmetric, and so the entire specimen geometry must be modeled. Figure 5.1 shows the FE models used for both the symmetric and asymmetric cases, along with the boundary conditions employed for the respective models.

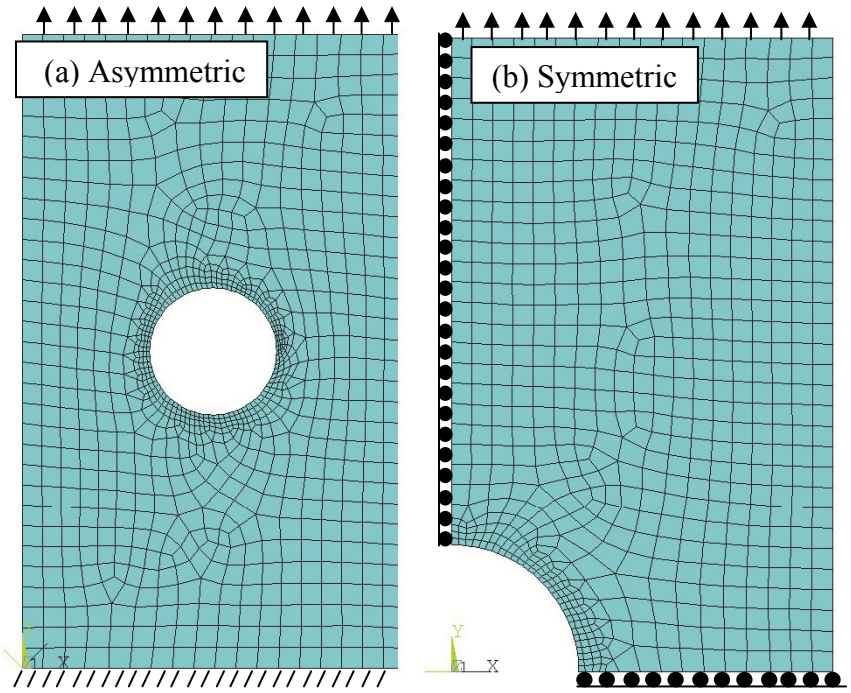

Figure 5.1: Macro scale Finite Element mesh used to simulate the linear elastic behavior of the woven wire mesh in the presence of a circular notch for the (a) off-axis cases, and (b) principle material orientations.

As seen in Fig, 5.1, loads were applied to the uniaxial model along the top edge, with careful attention being paid to assure the proper distribution of the load amongst the nodes on that edge. The applied load was ramped over a series of sub-steps to the desired level, which was set to match the load cell reading corresponding to the experimental DIC frame used for comparison. The asymmetric model, Fig. 5.1 (a), contains a total of 956 elements, while the symmetric model, Fig. 5.1(b) contains 653 elements. Comparison of the results from simulations run in the principal material orientations for the symmetric case and unsymmetrical case show that the fixed boundary condition in Fig. 5.1 (a) is far enough away from the notch to not have an effect on the simulation results. To facilitate parametric transformation of the material model for off-axis simulations, the element coordinate system was simply rotated with respect to the global Cartesian coordinate system. As the material properties in ANSYS are by default aligned to the element coordinate system, a transformation of the material model results. The model results were then rotated back into the global system for post-processing. The ANSYS APDL code used to develop this model is supplied in Appendix B.

5.1.2 The Biaxial Model

In a similar fashion to the uniaxial macro scale model, the biaxial cruciform geometry was also modeled elastically using the finite element method. Again, 8-node isoparametric (PLANE82) elements were employed, with the assumption of plane stress. Symmetry was employed for this modeling effort, as in all cases the principle material orientations, warp (0°) and weft (90º) are aligned with the uniaxial specimen arms. The material model is linear elastic orthotropic, with the material constants equal to those supplied in Table 3.2. The complete model contains 868 elements, and the applied boundary conditions are as shown in Fig. 5.2. For the

biaxial specimens, the stretch ratio, γ, is controlled as a parameter. The applied γ for each simulation is determined from the test matrix in Table 2.3 as either equal to 1.0 or 1.3, such that the results are directly comparable to the experiments. Again, the range of the stretch ratio, has been expended from the biaxial test matrix for the elastic simulations to supplement the experimental SCF values.

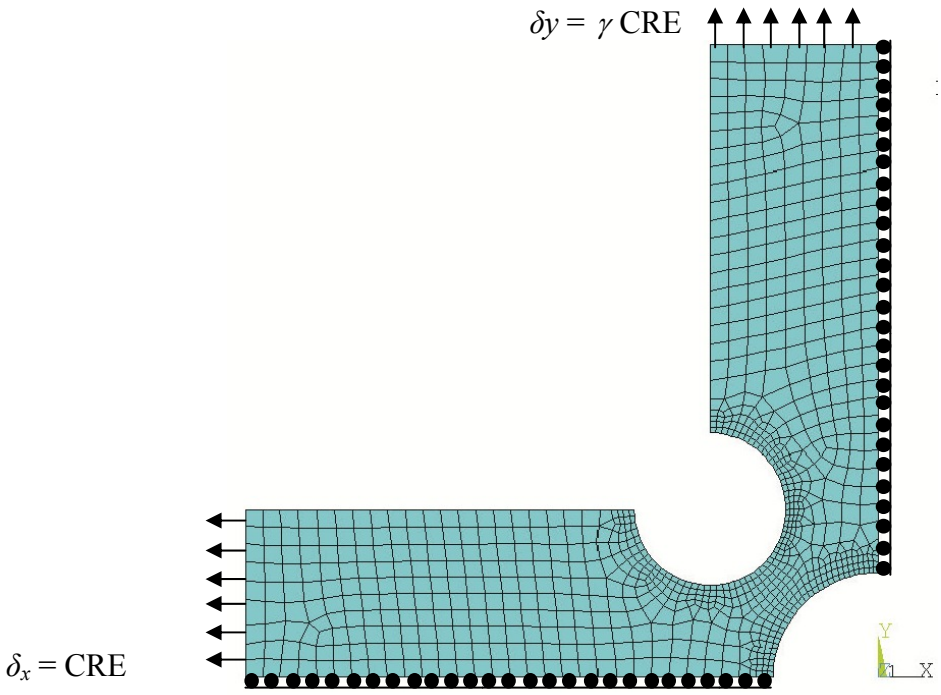

Figure 5.2: Macro scale finite element mesh used to simulate the linear elastic response of the biaxial cruciform specimen with a central circular notch and the applied boundary conditions.

5.2 Comparison of FEM Contour Plots to Experimental Data

5.2.1 Uniaxial Simulations

Prior to the use of the FEM model to interpolate or extrapolate SCF values outside of the test regime, it is prudent to compare the simulated strain fields to those measured using DIC. Agreement of the strain fields justifies progression to SCF determination from the finite element model, and gives credence to the use of the continuum assumption in macro-scale mechanical

modeling of this class of materials. For this comparison, one numerical simulation was run for each respective notched uniaxial tensile test, i.e., 21 simulations. The model was loaded and constrained as shown in Fig. 5.1, with the symmetric model (Fig. 5.1(b)), used only in circular notched cases where a principal material orientation is aligned with the loading axis. The magnitude of the uniaxial tensile load applied to the model was matched to the load cell output values corresponding to the DIC frame number chosen for data extraction in Ch. 3, such that the results are directly comparable. Care was taken to adjust the contour scales in the FEM post-processing module to match the contours from the DIC plots, so that the FEM results correspond directly to the DIC contours. This scaling facilitates comparison, making any differences in the simulated and experimental fields visually apparent. Figures 5.3 - 5.9 show the simulated and experimental elastic strain contours in the *y-camera* orientation for the various notch aspect ratios, λ, and notch orientations, α, and for all experimentally treated material orientations, θ.

The comparison between FEM and DIC for the circular notched cases reveals a clear agreement, both in magnitude and in distribution, between the predicted and measured elastic strain contours, as shown in Fig. 5.3. The gray zones of the FEM contours indicate regions subjected to higher strains than the DIC scale. The location of the gray zones in both the weft (90º) an bias (45º) material orientations is consistent with regions of high gradient that fail to correlate using DIC. The asymmetry of the strain distribution in the off-axis material orientation, evidenced by inspection of the bias (45º) material orientation case, where the strain distribution below the circular notch is not equal to the distribution above the notch, is likely owed to boundary condition effects. The consistency of the FEM contours, which are based on continuous and homogonous elements, with the DIC measured strain gives credence to the use of the analytical models presented in Chapters 1 and 3 to predict the stress distribution in this class

of materials in the presence of a circular notch. It must be noted that the FEM contour plot deformations presented herein have been automatically scaled by ANSYS, and are not representative of actual deformations in the material.

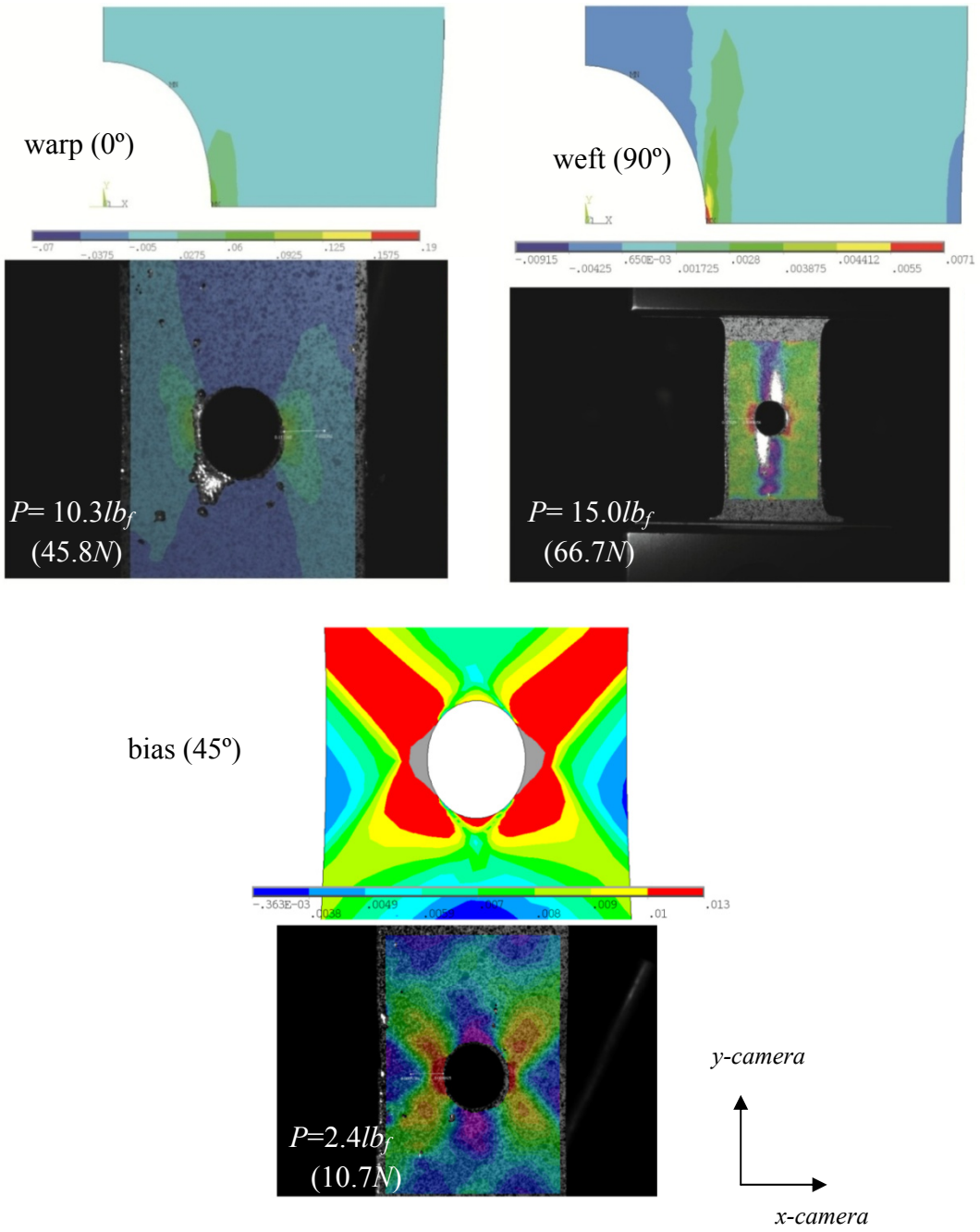

Figure 5.3: Comparison of the simulated elastic strain in the *y-camera* direction to the DIC *y-camera* direction strains for circular notched SS316L woven wire mesh in various material orientations

For the case of elliptical notches ($\lambda = 0.5$) in the SS316L woven wire mesh, it is observed that the homogenous FEM simulations, in general, are capable of predicting the location of maximum *y-direction* elastic strain, as shown in Figs. 5.4 through 5.6. Comparison of the FEM and DIC contours shows that the FE model captures the general shape and trend of the strain distribution, but tends to show more concentration and uniformity near the notch edge. The *y-camera* elastic strain contours tend to be in excellent agreement away from the notch edge, both in magnitude an in distribution. The difference in uniformity and concentration of the FEM contours with respect to the DIC contours at the edge of the elliptical notches can likely be attributed to the discontinuity of the cut-off wires near the notch edge, and their tendency to shift in the weave upon loading, producing parasitic strain information. These discontinuous deformation mechanisms are not accounted for in the continuous and homogonous FE model, as the effect of these discontinuities on the local stain distributions would require consideration of the meso-structure of the material. The bias (45º) material orientation is observed to have the most deviation from the simulated behavior near the notch edge, where the DIC fails to produce a clear location of maximum strain concentration. This is likely due to the high degree of shear coupling and relative rotational motion of the wires in this orientation, which cannot be directly accounted for in a homogenize modeling effort. Future work must be undertaken to improve the homogenized material model to account for the energy of these rotational and sliding motions. Again, investigation of the FEM contours confirm that, in the case of either bias (45º) material orientations, or in cases where the notch orientation, α, is 45º, the location of maximum strain is not at the location of minimum radius of curvature, but rather is offset by some angle. This highlights the need to consider the entire edge of the notch when investigating the degree of stress concentration.

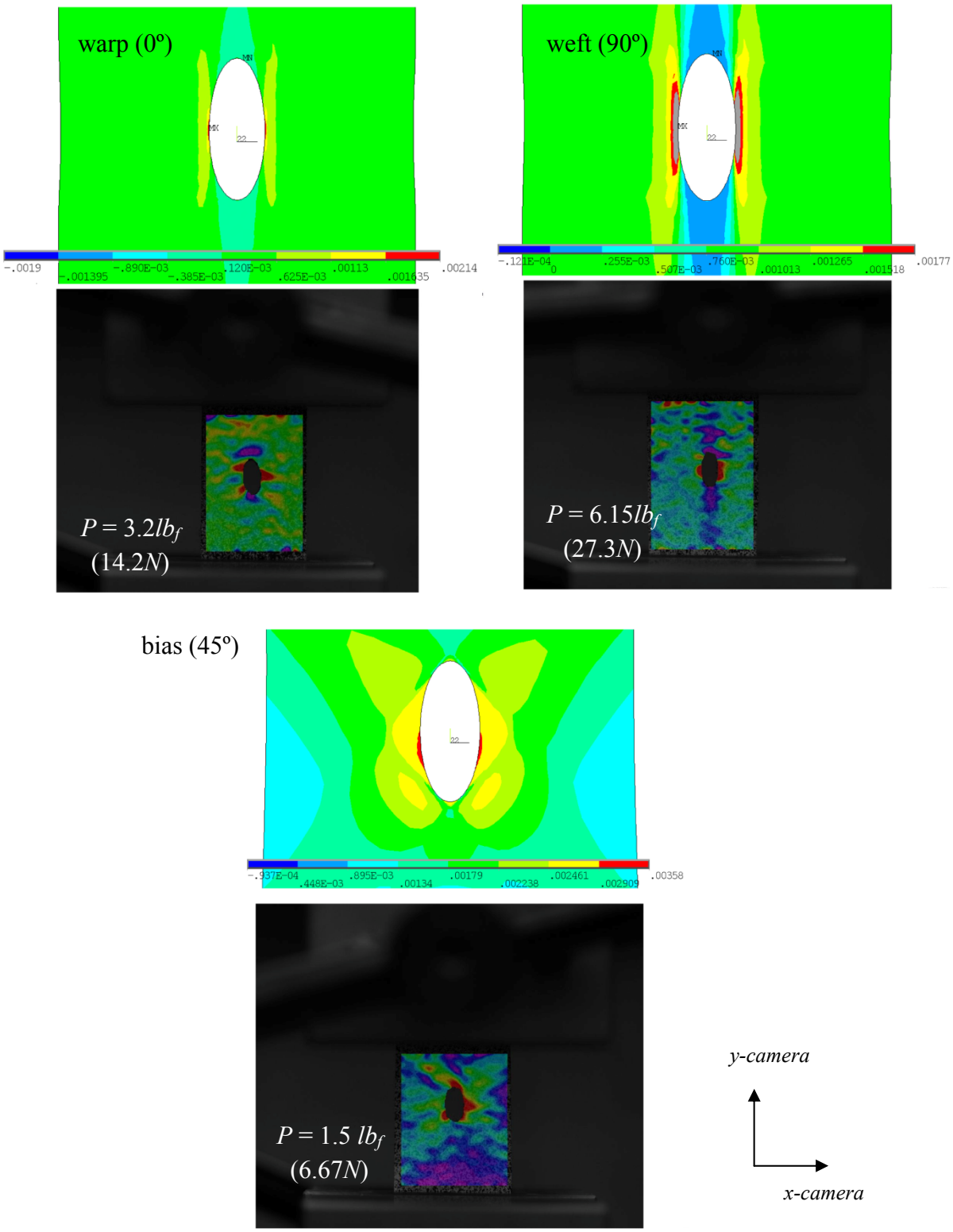

Figure 5.4: Comparison of the simulated elastic strain in the *y-camera* direction to the DIC *y-camera* direction strains for elliptical notched (α = 0º) SS316L woven wire mesh in various material orientations

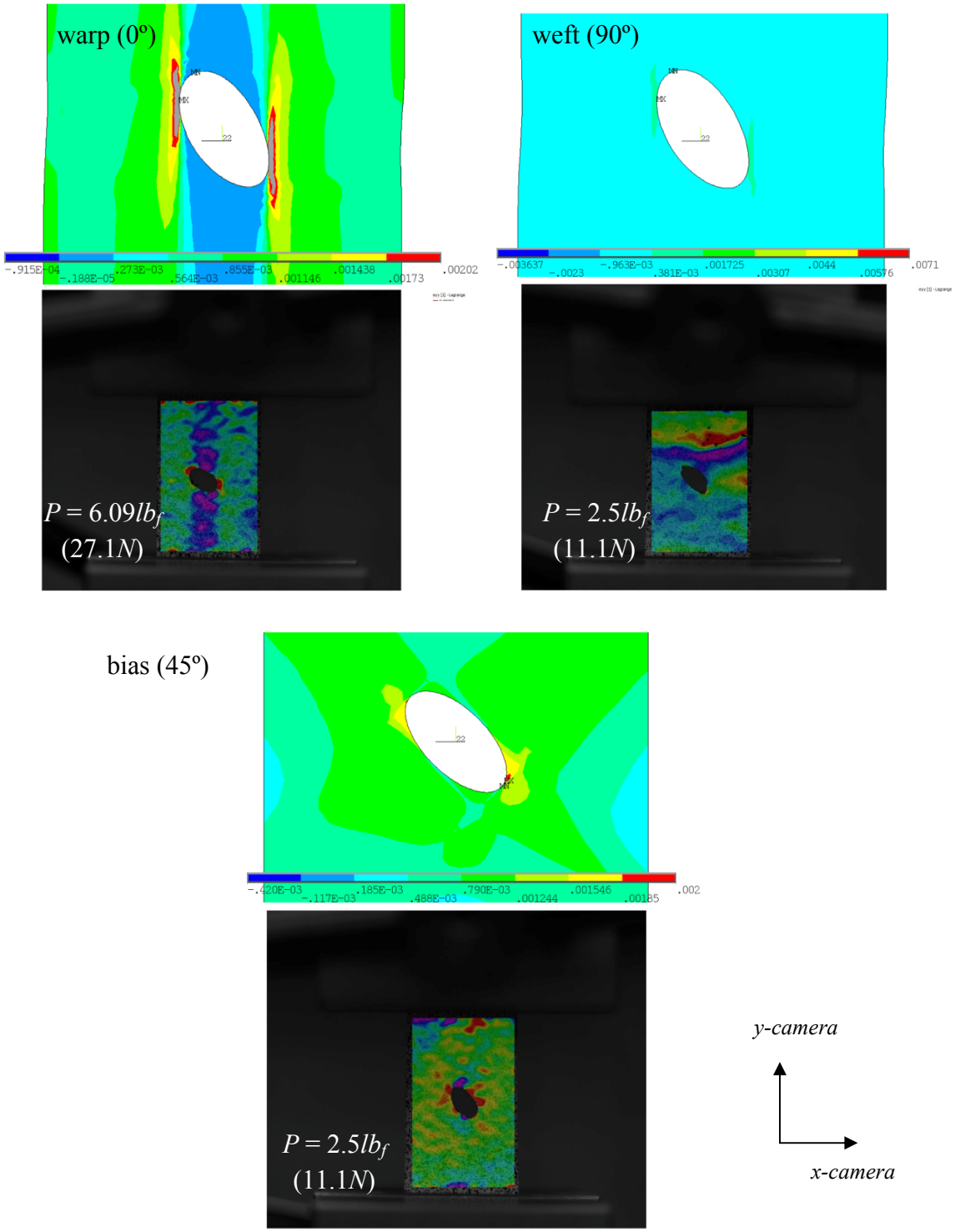

Figure 5.5: Comparison of the simulated elastic strain in the *y-camera* direction to the DIC *y-camera* direction strains for elliptical notched (α = 45º) SS316L woven wire mesh in various material orientations

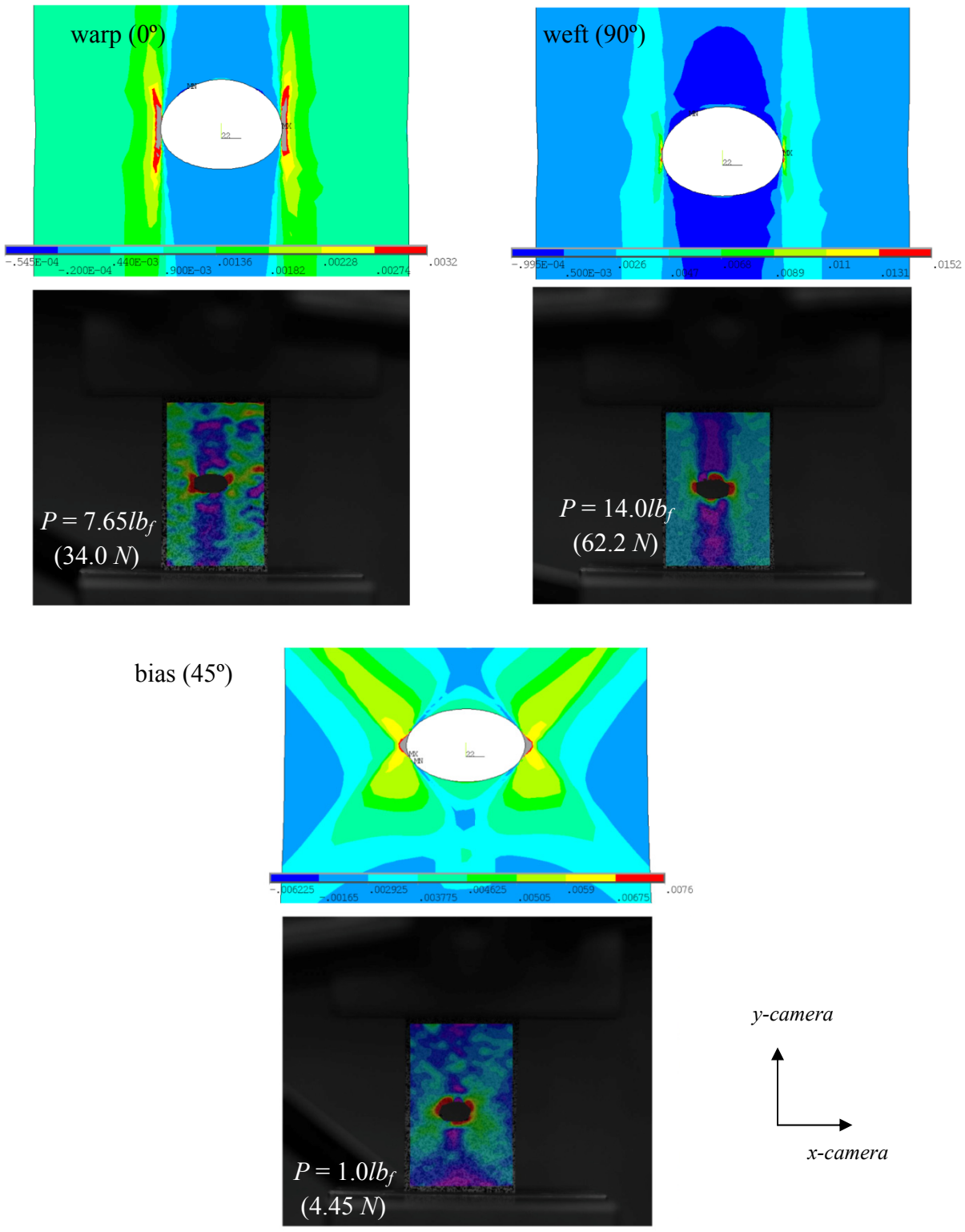

Figure 5.6: Comparison of the simulated elastic strain in the *y-camera* direction to the DIC *y-camera* direction strains for elliptical notched (α = 90º) SS316L woven wire mesh in various material orientations

For the case of slit notches ($\lambda = 0.0$) in the SS316L woven wire mesh, it is observed that the homogenous FEM simulations, in general, do not accurately predict the location or magnitude of the maximum *y-direction* elastic strain, as shown in Figs. 5.7 through 5.9. The slit notches were generated in the model geometry by reducing the length of the minor radius to 5.0% of the major radius. This method lends itself to simplistic parametric modeling of the system, while producing a reasonable approximation of the slit notch geometry. It was elected to model the slit notch root with very fine quadratic elements (10,000 nodes on notch edge) rather than using singular elements to capture the behavior of the material at the notch root, again for ease of parametric modeling. It is noted that the slit aligned with the warp axis is not represented for the $\theta = 45^{\circ}$ (bias) material orientation due to a lack of correlation data, as discussed in Ch. 3.

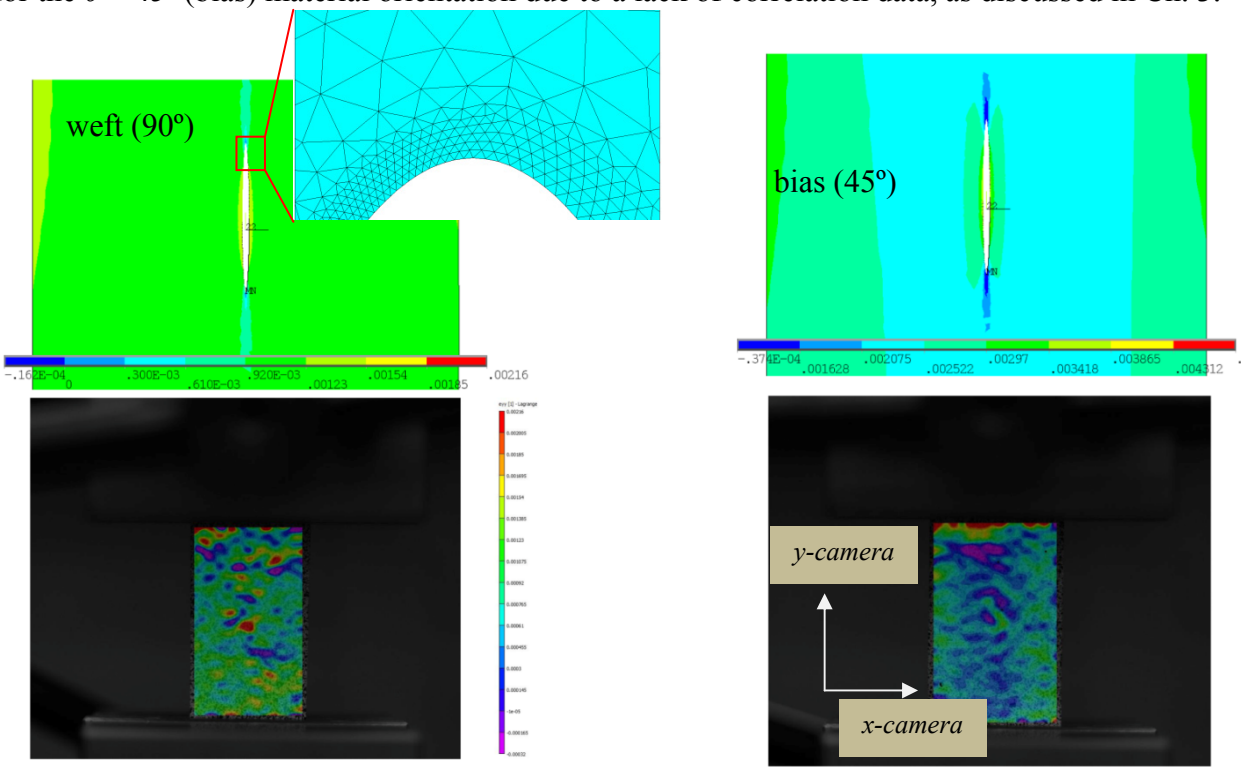

Figure 5.7: Comparison of the simulated elastic strain in the *y-camera* direction to the DIC *y-camera* direction strains for slit notched ($\alpha = 0^{\circ}$) SS316L woven wire mesh in various material orientations

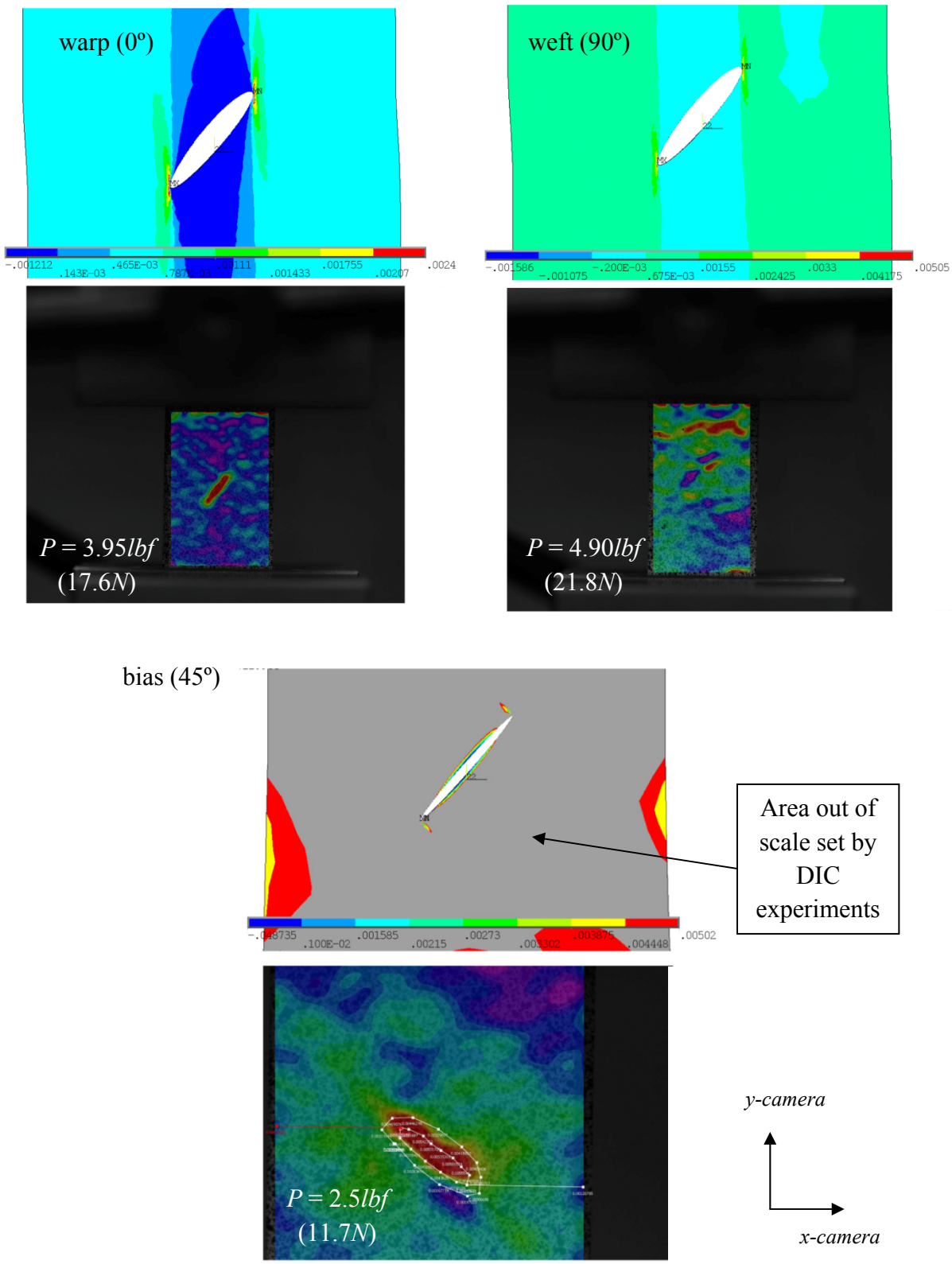

Figure 5.8: Comparison of the simulated elastic strain in the *y-camera* direction to the DIC *y-camera* direction strains for slit notched (α = 45º) SS316L woven wire mesh in various material orientations

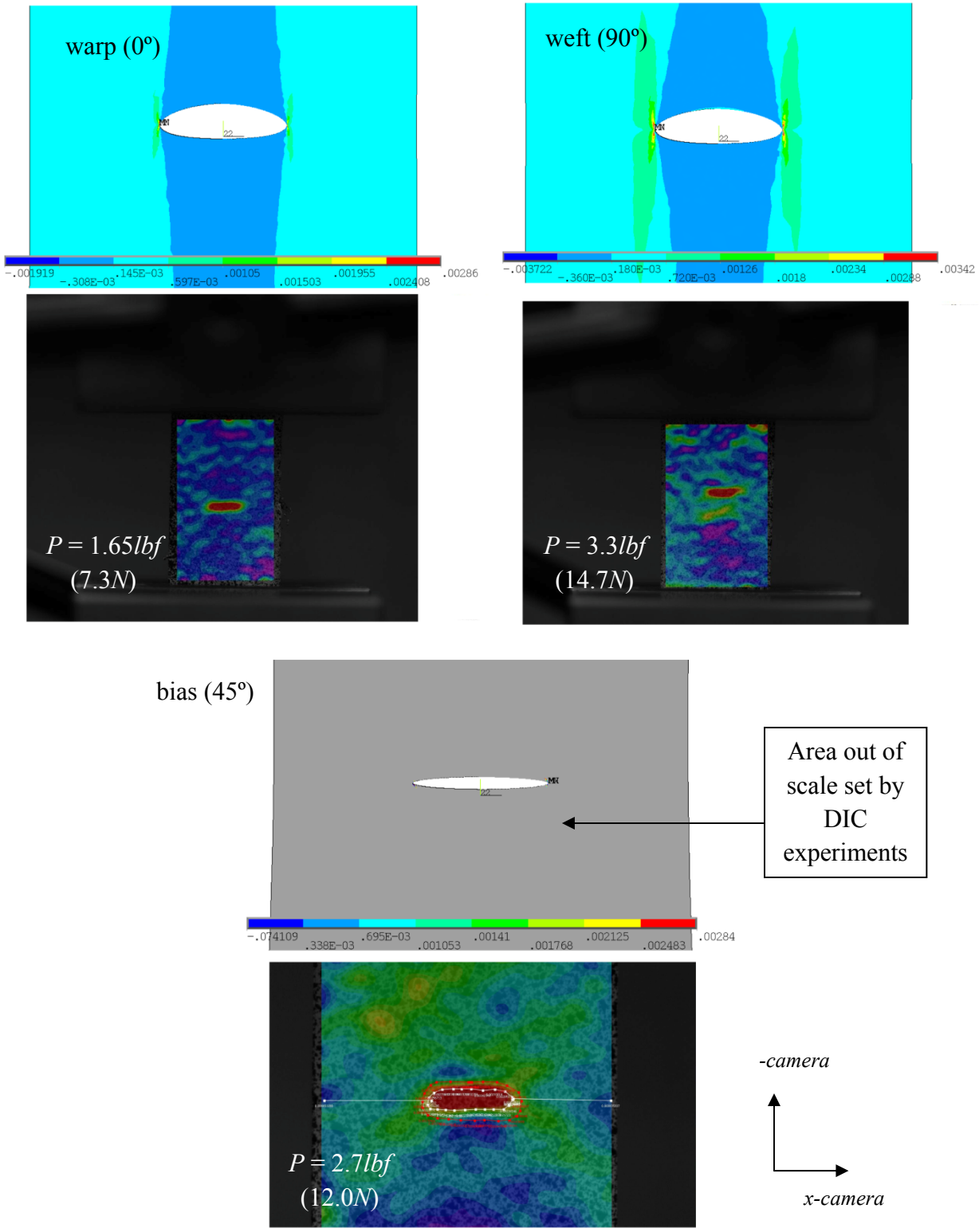

Figure 5.9: Comparison of the simulated elastic strain in the *y-camera* direction to the DIC *y-camera* direction strains for slit notched (α = 90º) SS316L woven wire mesh in various material orientations

The large zones of gray in the FEM contours of both Fig. 5.8 and 5.9 indicate that the FEM results do not correlate well with the scale of the DIC results in the bias (45º) slit notched cases. Again, this is attributed to the inability of the model to capture the large relative rotations of the discrete wires in the off-axis material orientation. For a qualitative comparison of the results in these cases, Fig. 5.10 is supplied, but it must be noted that the scales of the contours in this figure are not consistent with each other or with the respective DIC contours. In general, the FEM contours do not show the dispersion of the strain concentration over the entire edge of the notch as seen in the DIC contours, but rather show distinct regions of extremely localized high strain. Furthermore, the far-field effects of the notch are not consistent between DIC measurements and FEM in the slit notch cases, as the DIC plots show very little effect in the field away from the notch, while the FEM plots show a larger region of perturbation. Given these observations, caution must be exercised in using homogenized elastic FEM results to predict the magnitude and location of the maximum stresses in slit notched geometries of SS316L woven wire mesh material, particularly in the bias (45º) material orientation.

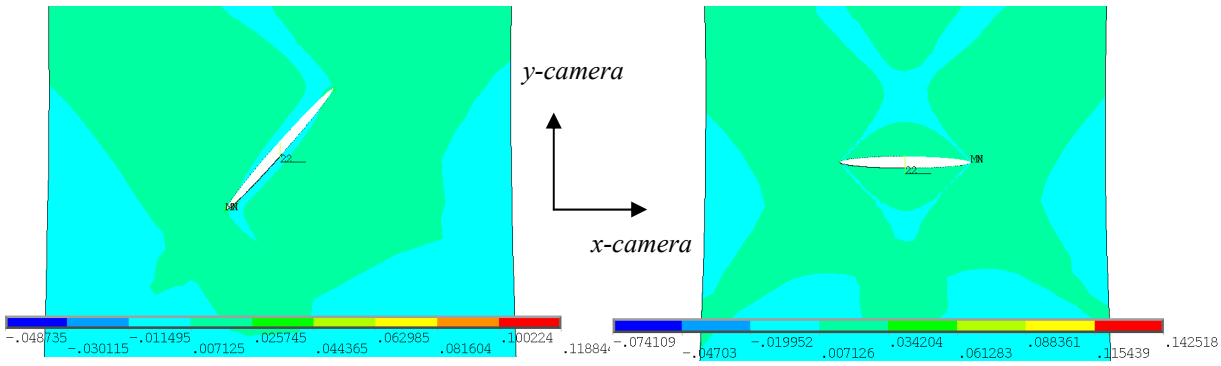

Figure 5.10: Re-scaled FEM strain contours in the *y-camera* direction for the case of (a) $\alpha = 45^{\circ}$, $\theta = 45^{\circ}$, and(b) $\alpha = 90^{\circ}$, $\theta = 45^{\circ}$

5.2.2 Biaxial Simulations

Similarly to the uniaxial case, comparison of experimental results from biaxial tensile tests performed on the SS316L woven wire mesh material to numerical results from homogenized macro-scale FEM simulations is key to furthering the understanding of how this class of materials behaves in the presence of a stress riser. Prior to detailed inspection of the stress state near the tip of a notch using the previously described FE model, it is advantageous to leverage the simulations for comparison to the full-field DIC strain contours. To facilitate this comparison, boundary conditions have been imparted onto the FE model that exactly match the conditions of the experiment at the time of image capture for SCF determination, and the scales of the strain contours for the DIC and FEM cases have been made to equal each other. Comparison of the first principal stress contours, where the 1-direction is equivalent to the weft direction as described in Chapter 4, are presented in Fig. 5.11 through 5. 14 for all experimentally treated cases.

The results of the uniaxial simulations, as presented in the previous section, indicate that the most likely notch case for acceptable comparability to exist between the macro-scale FE simulations and the experimental DIC results is for the λ = 1.0 circular notches. Figure 5.11 shows the results of the λ = 1.0 case, for both the equibiaxial (γ = 1.0) and unequal-biaxial (γ = 1.2) stretch ratios. Analysis of Fig, 5.11 reveals that the strain contours near the edge of the notch are similar both in magnitude and in distribution for both cases. Areas of negative strain present in the experimental case are not present in the simulations, but this is likely attributed to the inhomogeneity of the SS316L micronic mesh structure, i.e., this is indicative of poor strain

energy transference into certain zones near the notch edge, or low Meso-Scale Geometric Coupling (MSGC).

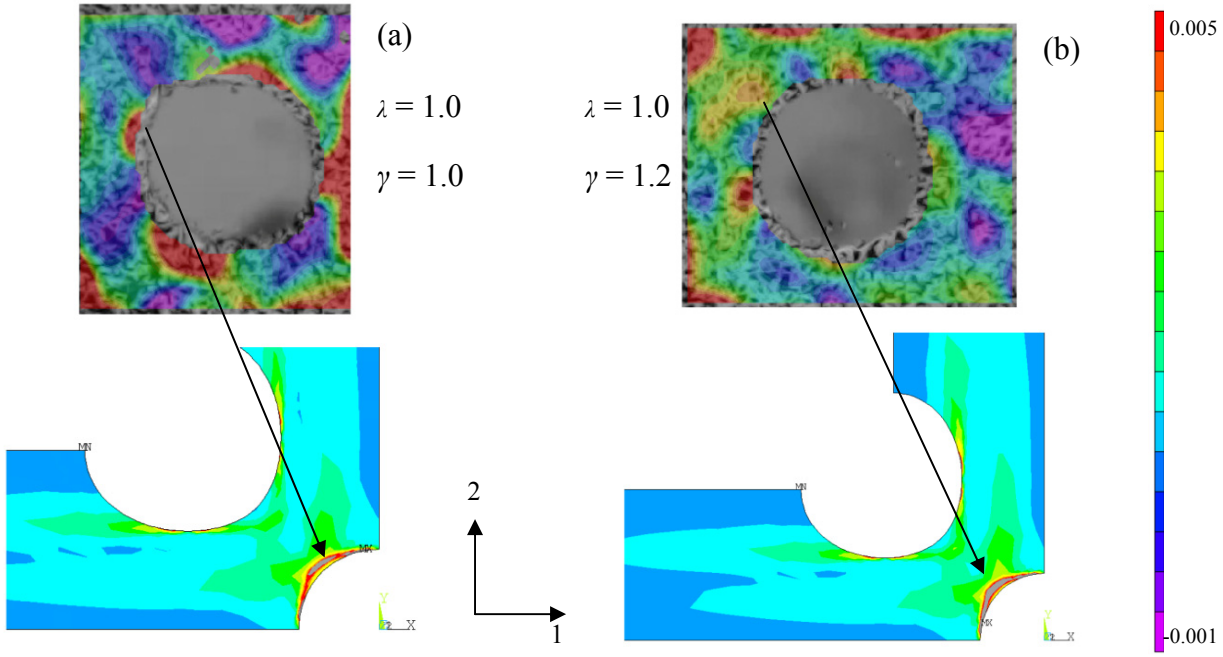

Figure 5.11: Experimental and simulated contours of first principal strain in the vicinity of a circular notch in (a) equibiaxially loaded, and (b) unequal-biaxially loaded SS316L woven wire mesh material.

In addition to the circular notched cases, the oriented slit notch cases were also treated via macro-scale FEM simulations. Figure 5.12 shows a comparison of the simulated and experimental results near the edge of a slit notch ($\lambda = 0.0$) oriented in line with the warp material orientation ($\alpha = 0^{o}$) for both equibiaxial and unequal-biaxial cases. Inspection of Fig. 5.12 shows that while the DIC and simulated strain contours generally agree in distribution and magnitude in the areas close to the notch root, the simulations predict higher strain values at the notch root. This is consistent with the uniaxial simulation results, and the high levels of strain at the near singularity of the slit type notch root is expected for the homogenized continuum model. Also, it is observed that the fillets tend to perturb the strain contours to a higher extent in the DIC

experiments than in the simulations predict. It is interesting to note that the levels of low strain observed just above the notch root in the DIC contours are also observed in the model results, however the magnitudes of the respective minimum strain values are again not consistent.

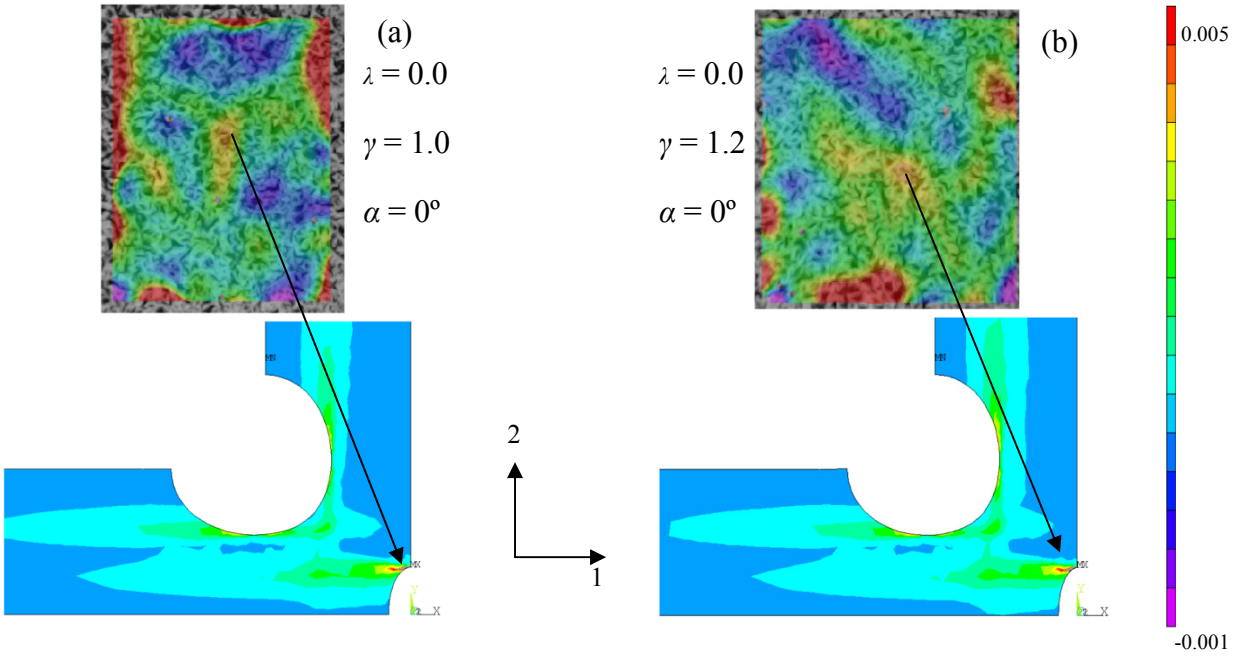

Figure 5.12: Experimental and simulated contours of first principal strain in the vicinity of an $\alpha = 0°$ slit notch in (a) equibiaxially loaded, and (b) unequal-biaxially loaded SS316L woven wire mesh material.

The modeled case which least resembles the DIC contour results is the $\alpha = 45°$ slit notch, shown in Fig. 5.13 for both the equibiaxial and unequal-biaxial cases. The divergence of the experimental and simulated strain distribution results for the inclined notch case is believed to be directly related to the lower level of inter-wire coupling associated with the bias (45°) material orientation, and the inability of the subject material to react mode II type loading. Additionally, it is likely that improved camera resolution and noise reduction is necessary for DIC to be capable of spatially resolving the highly localized region of increased strain predicted by the FEM simulations. Inspection of 5.13 shows that in both experimental cases, the first principal

strain distribution around the circular fillet interferes with the strain distribution around the root of the notch, making accurate determination of the effects of the inclined slit notch challenging. This is particularly evident in Fig. 5.13 (b), which shows the case of $\gamma = 1.2$, where the notch has no visually apparent affect on the strain field in the gage section of the material. Inspection of the equibiaxial case shown in Fig. 5.13 (a), however, does show a region near the notch root where the strain magnitude and distribution is similar to the simulated case.

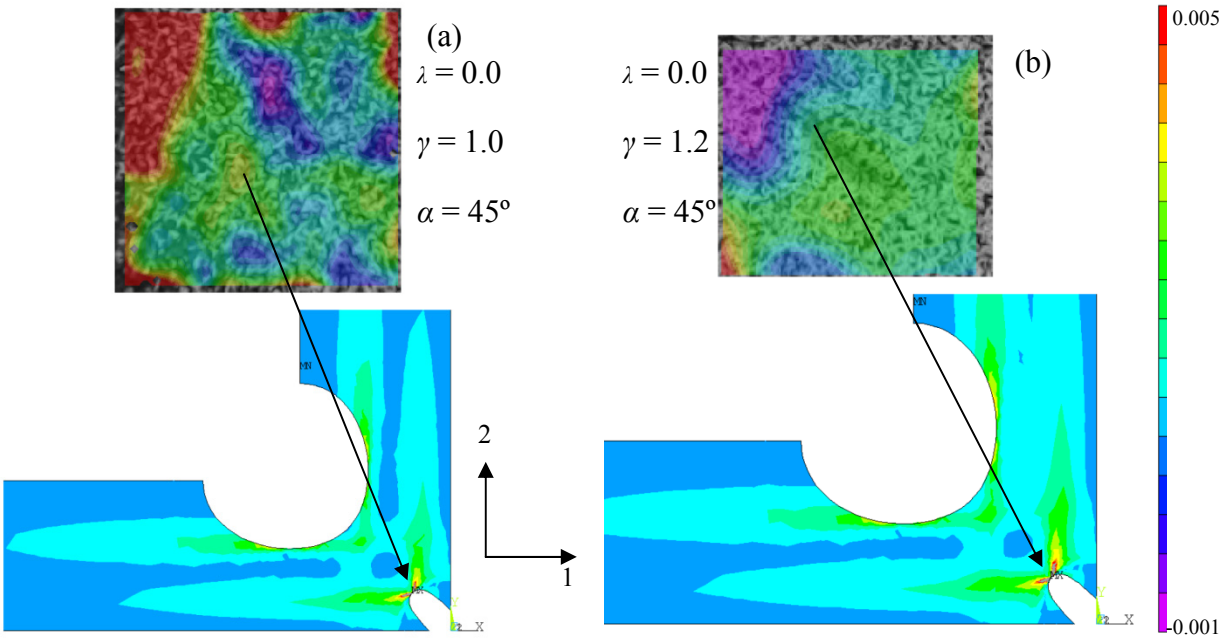

Figure 5.13: Experimental and simulated contours of first principal strain in the vicinity of an $\alpha = 45^{\circ}$ slit notch in (a) equibiaxially loaded, and (b) unequal-biaxially loaded SS316L woven wire mesh material.

The final experimental case available for comparison to the homogenized macro-scale mode results is the $\alpha = 90^{\circ}$ slit notch. Figure 5.14 shows the simulated and DIC experimental first principal strain contours in the region of a slit notch oriented with the weft axis for both equibiaxial and unequal-biaxial cases. Again it is observed that the general distribution in the vicinity of the notch edge is captured by the homogenized macro-scale FE model, however the model predicts significantly higher strains at the notch root than are measured experimentally via

DIC. These results highlight the ability of the DIC experimental method to predict the location of maximum strain, while pointing out the limitations of FEM for predicting realistic strain or stress values at the root of a notch approaching a singularity due to the considerable dependence of predicted field magnitude on mesh density. Use of numerical fracture mechanics approaches, such a defining a Stress Intensity Factor (SIF) in place of the SCF at the notch root, may improve the simulation results, but this is considered beyond the scope of this thesis and is left for future work.

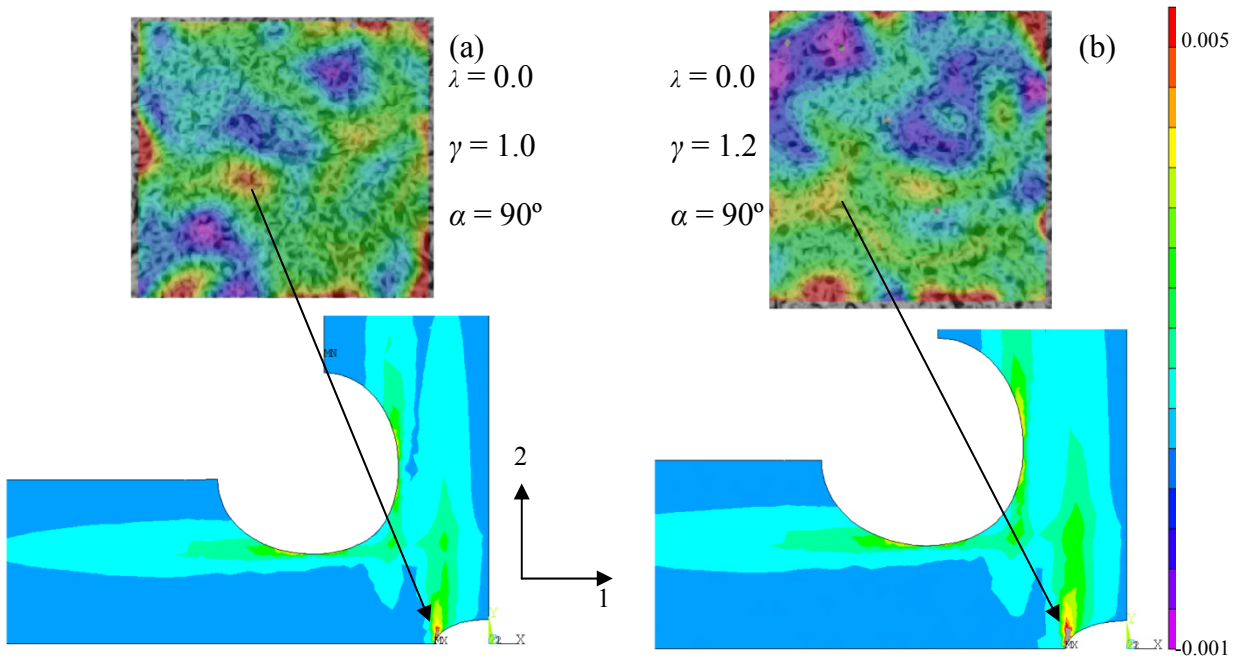

Figure 5.14: Experimental and simulated contours of first principal strain in the vicinity of an $\alpha = 90^{o}$ slit notch in (a) equibiaxially loaded, and (b) unequal-biaxially loaded SS316L woven wire mesh material.

5.3 Numerical Prediction of Intermediate SCF values

5.3.1 Uniaxial Tension Simulations

The ultimate goal of the elastic simulations outlined in this chapter is to extend the experimental SCF regime into untested material orientations, and to compare the results of homogenous numerical modeling efforts to those obtained experimentally though full-field DIC. To facilitate this, the model has been exercised parametrically in material orientations varying from warp (0º) to weft (90º) in increments of 15º. To determine the SCF of each respective notch geometry and material orientation, the theta component of the stress has been extracted at every node on the edge of the notch using a path operation (see Appendix B for details). The FEM derived SCF curves, plotted as a function of material orientation, are presented in Fig. 5.15 for the various experimentally treated notch aspect ratios and orientations. Comparison of these plots to the experientially derived SCF values as function of material orientation, shown in Fig. 3.35, reveals similarities in the trends of the SCF, particularly in the case of the circular notches. Figure 5.15 shows that the maximum SCF occurs at a material orientation, θ, of 30º in all cases. The bias (45º) orientation FEM simulation for the case of the elliptical ($\lambda = 0.5$) notch oriented with the loading axis ($\alpha = 0$º) does not produce the outlier value seen for the elliptical notch case in the experimental data. The slit notch ($\lambda = 0$) oriented at $\alpha = 90$º, however, does show an elevated value for the SCF of 120.0 in the bias (45º) material orientation, which is roughly twice the outlier value from the respective experimental case. This supports the high experimental SCF values, indicating that future work, perhaps using a full-field extrapolation approach as detailed in the future work section of this thesis, is necessary prior to concluding the DIC results are unreasonable. It is noted that as the notch root radius continues to approach a value of zero, i.e., a true slit or crack, the use of the SCF as an analytical tool becomes limited, as it would require the

stress to approach infinity at the notch root. Clearly this is not possible, and such a crack in a homogenous material requires analysis using fracture mechanics approaches. This is beyond the scope of this thesis, and such analysis is left to future work.

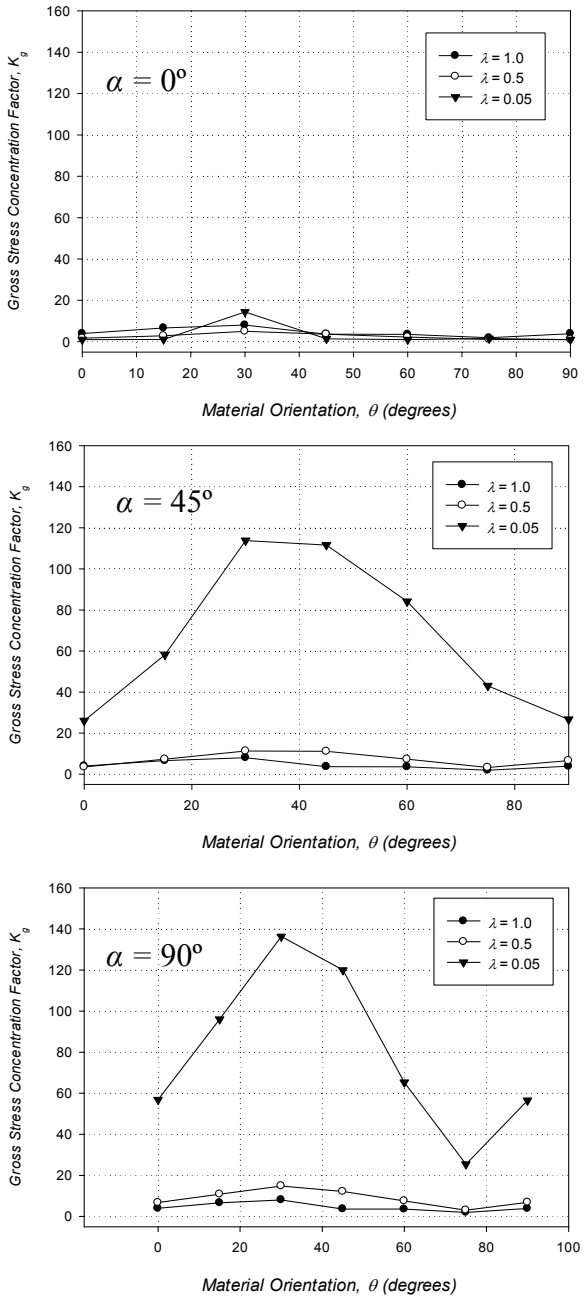

Figure 5.15: The stress concentration factor (SCF) as a function of SS316L woven wire mesh material orientation a various notch aspect ratios and orientations.

5.3.2 Biaxial Tension Simulations

As was the case for the uniaxial simulation regimen, it is desirable to employ the macro-scale simulation technique as a means to both expand the experimental test matrix, and to judge the effect of the homogenization assumption on the simulation results. To facilitate this, ANSYS Parametric Design Language (APDL) has been used to parametrically investigate the effects of slit notch orientation on the SCFs associated with a $\lambda = 0.0$ notch incised into both equibiaxially loaded and unequal-biaxially loaded SS316L wove wire mesh material. Figure 5.16 shows the numerically predicted SCF associated with various slit notch inclinations incised into the biaxial cruciform geometry shown in Fig. 5.2, as well as the baseline circle cases. The definition of the SCF in this case is consistent with Eq. (4.2.1), where the Hill equivalent stress is used as the stress comparator. For comparison, the SCF calculated using the Von Mises equivalent stress, which is isotropic in nature, is also plotted for each respective case in Fig. 5.16. Inspection of Figure 5.16 shows that the SCF for the biaxial case tends to be maximum when the notch is oriented with the warp axis ($\alpha = 0^{\circ}$). It is observed that the measures of SCF determined using the Hill and Von Mises equivalent stresses tend to follow similar trends for both the equibiaxial and unequal-biaxial stretch ratios from $\alpha = 0^{\circ}$ through $\alpha = 45^{\circ}$. The divergence observed at $\alpha = 60^{\circ}$ is attributed to the isotropy of the Von Mises Equivalent stress, which in general predicts a more symmetric SCF trend than the Hill stress. In comparison to the experimental results observed in Figs. 4.22 and 4.23, where the maximum SCF occurs at $\alpha = 0^{\circ}$ and the minimum occurs at $\alpha = 45^{\circ}$, the simulation trends are reasonably well consistent. Where the experimental and numerical results differ greatly is in magnitude, as the numerical simulations predict SCF values nearly an order of magnitude greater than is measured from the biaxial DIC experiments.

This difference in magnitude can be attributed to a combination of mesh sensitivity in the region of the slit notch singularity, and to divergence from the assumption of continuity of the actual material. Indeed, it is noted that the magnitude of the stress at the notch tip predicted by FEM is highly mesh dependent, with smaller element sizes producing higher levels of SCF, and vice versa. Again, note that the slit notches are approximated in the model, with the minor radius equal to 5.0% of the major radius.

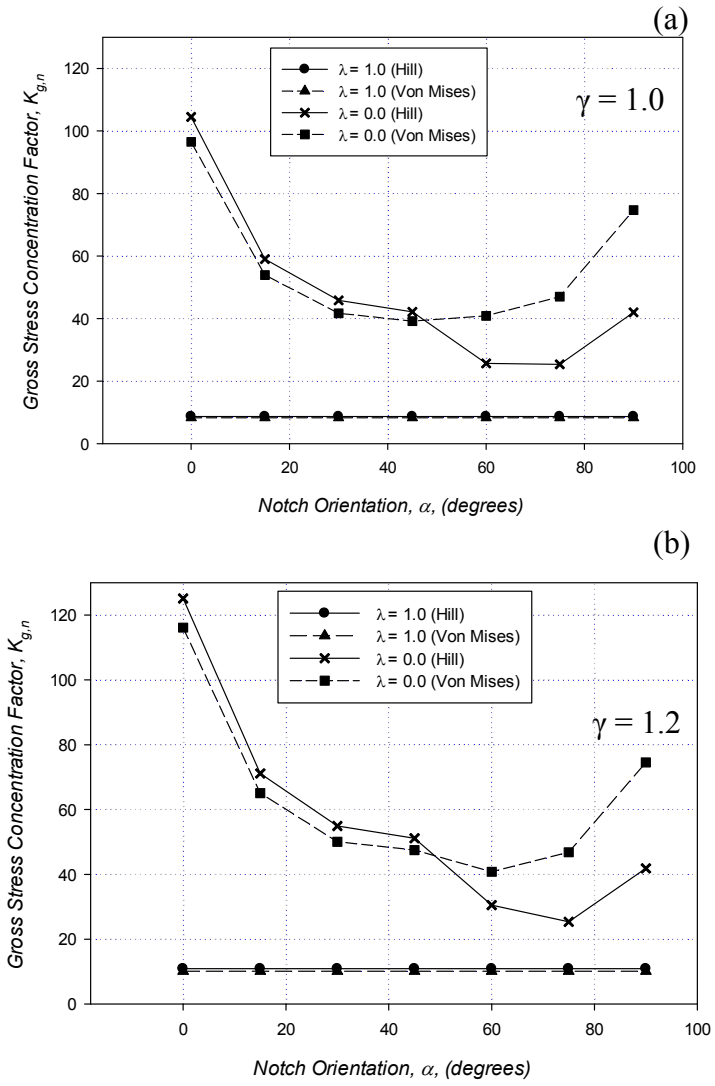

Figure 5.16: Simulated gross stress concentration factors for (a) equibiaxially loaded, and (b) unequal-biaxially loaded SS316L woven wire mesh material as a function of notch orientation for both circle (λ = 1.0) and slit (λ= 0.0) notch cases.

While the slit notch (λ at 0.0) case simulations produce accurate trends, but fail to capture magnitude of the experimental SCF values, the circle notch (λ at 1.0) case simulations predict the order of magnitude of the biaxial SCF with reasonable accuracy. The macro-scale simulations predict a SCF for the equibiaxially loaded circle notch case of 8.7, which represents a 29.4% difference with respect to the experimentally determined SCF of 11.7, while the simulations predict a SCF value of 10.9 or the unequal-biaxial case, compared to the experimental value of 7.6, with a percent difference of 35.7%. This provides further evidence to the fact that divergence of the simulated slit notch SCF magnitudes from the experimental cases is due in large part to a breakdown of the SCF as a viable tool for gauging the state of stress near a notch approaching the aspect ratio of a crack.

CHAPTER 6: MESO-SCALE ELASTO-PLASTIC FINITE ELEMENT ANALYSIS

6.1 Meso-Scale Model Definition

Meso-Scale numerical simulations were conducted to model the behavior of SS316L woven wire mesh subject to various stress states [Kraft and Gordon, 2011]. To carry out these simulations, a 3D meso-scale finite element model was created using ANSYS. This simulation technique requires that individual wires be modeled, both geometrically and constitutively, and employs 3D contact elements to define frictional wire contact and allow relative wire sliding. The model was designed to facilitate comparability to the tensile experiments, with controlled displacements being applied uniaxially to the mesh. Material properties were defined for each wire type (warp or weft) independently, with the goal being to match the material response of the tensile specimens from the warp (0°) and weft (90°) orientations. This entails a parametric process in which each property is iteratively selected to achieve optimal curve-fit to the experimental data. Defined elastic constants, such as the Elastic Modulus and Poisson's ratio, were forced to conform with the published properties for SS316L, while properties such as strength, friction coefficient, contact stiffness, and hardening parameters were optimized to achieve optimal correlation with experimental results. It must be noted that physical influences such as residual plasticity in the wires, or geometrical disparities in the mesh due to manufacturing processes as shown in Fig. 1.5, are not explicitly captured in this modeling effort, but instead are taken into account by iterative maximization of the regression coefficient between the numerical model and experimental load-deflection relationships, i.e., the model is phenomenological in nature. As predicted by Eq. (1.2.1), the wire strengths defined in the model

vary somewhat from published properties for SS316L, as shown in Table 1.1; but overall the response of the model is exceptional given the geometric complexity. To investigate the elasto-plastic response of the meso-structure, a multi-linear kinematic hardening (MKIN) model was employed for the warp and weft wires based on published tensile curves for SS316L [Blandford et al., 2007]. The boundary conditions chosen for this modeling effort reflect the need for easy comparison to experimental data. Displacement was applied to one face of the model via a scaled rate identical to the tensile experiments. Symmetry constraints were then applied to the free edges of the mesh geometry via frictionless supports, as illustrated in Fig. 6.1.

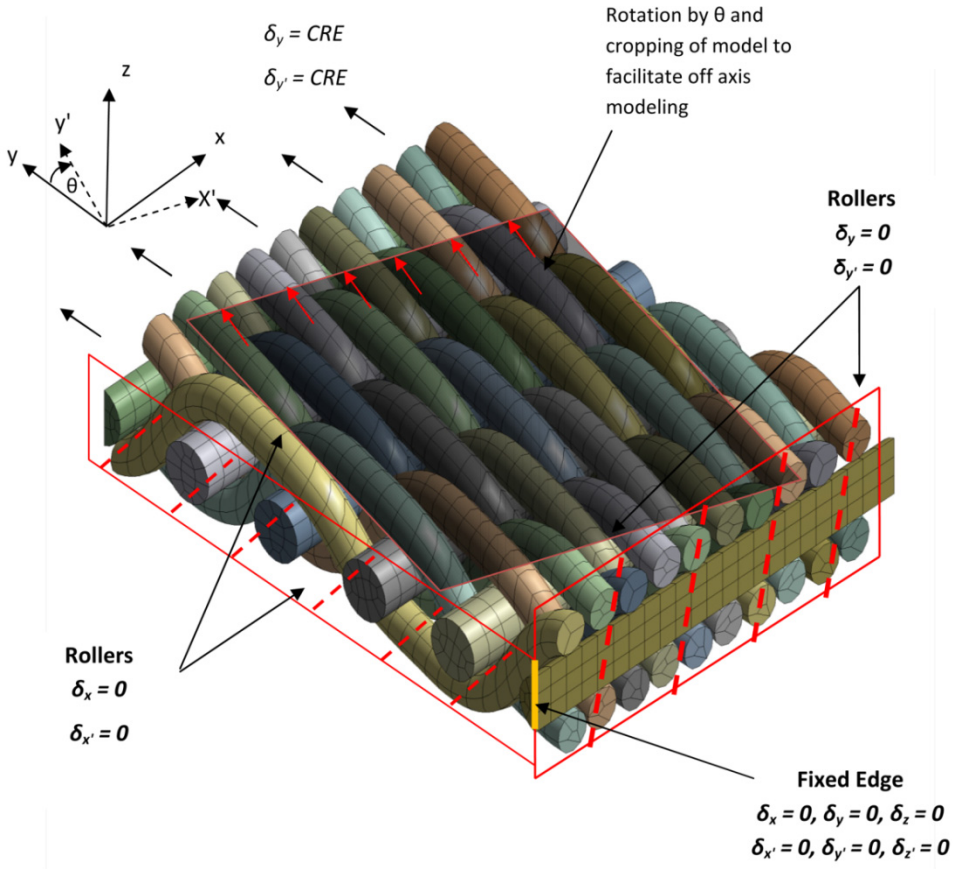

Figure 6.1: Finite element mesh of meso-scale model used to facilitate numerical modeling of the 316L SS woven wire mesh with boundary conditions used to simulate the tensile testing of the weft (90°) orientation sketched, along with illustration of rotation and cropping used to form off-axis simulation results.

To capture the behavior of the SS316L twill dutch woven wire mesh in the first quadrant of σ_1-σ_2 space, a series of uniaxial tensile experiments were conducted in various material orientations, ranging from 0° (warp) to 90° (weft) in 15° intervals. Capturing this behavior via the meso-scale finite element model can be realized through one of two methods. One option is to rotate the stress state imparted onto the model to match that of each experimental orientation. This method helps ensure proper stress distribution, and lends itself conveniently towards parametric modeling. The use of this method via controlled displacement boundary conditions, however, requires the definition of complex boundaries to ensure the applied displacement is dependent on the strain of previous load step. To eliminate this difficulty, it was elected to rotate and crop the model geometry to each respective orientation, and then to apply a uniaxial controlled displacement to the rotated specimen. This boundary condition, also illustrated in Fig. 6.1, assures easy comparison to the experimental data, and achieves shearing strains on the material through shear coupling effects as in the uniaxial experiments.

6.2 Meso-Scale Model Results

6.2.1 Load-Deflection Response of the Model

The model was exercised in a parametric fashion to test the meso-scale response of the woven wire mesh in every material orientation tested experimentally. The warp (0°) and weft (90°) orientations serve as benchmarks for the identification of the wire material properties, and so serve as good indicators of how well the model behaves with respect to experimental data. The simulated load versus displacement response of the main weave axes is provided in Fig. 6.2 in conjunction with the experimental results. The fit is exceptional through the elasto-plastic

region in both axes, validating the ability of the simplistic constitutive model to capture the macroscopic response of the material.

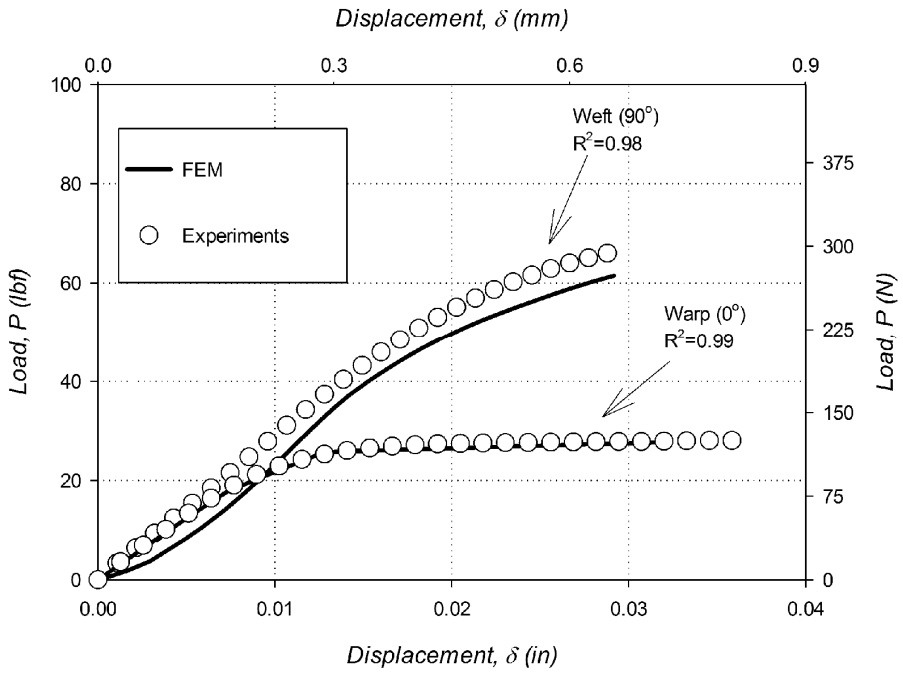

Figure 6.2: The elasto-plastic response of the meso-scale finite element model as compared to the mechanical response of the 325x2300 316L SS woven wire mesh subject to tensile testing in the warp (0º) and weft (90º) orientations.

Off-axis simulations were necessary to show that the meso-scale response of the SS 316L woven wire mesh could be related to the macro-scale response for all tension loading modes. Good agreement between meso-scale numerical results and macro-scale test results in all material orientations is necessary to justify the use of global constitutive assumptions to model this material. Such results in all orientations allow the design engineer to homogenize the meso-structure of the mesh, and develop strength and life predictions based solely on easily obtainable macro-scale material characteristics. The load versus displacement response of the numerical simulations in each off-axis orientation is provided in Fig. 6.3, along with their respective

experimental curve. Inspection of Fig. 6.3 shows that the meso-scale model response closely follows the response of the macro-scale in the elasto-plastic region.

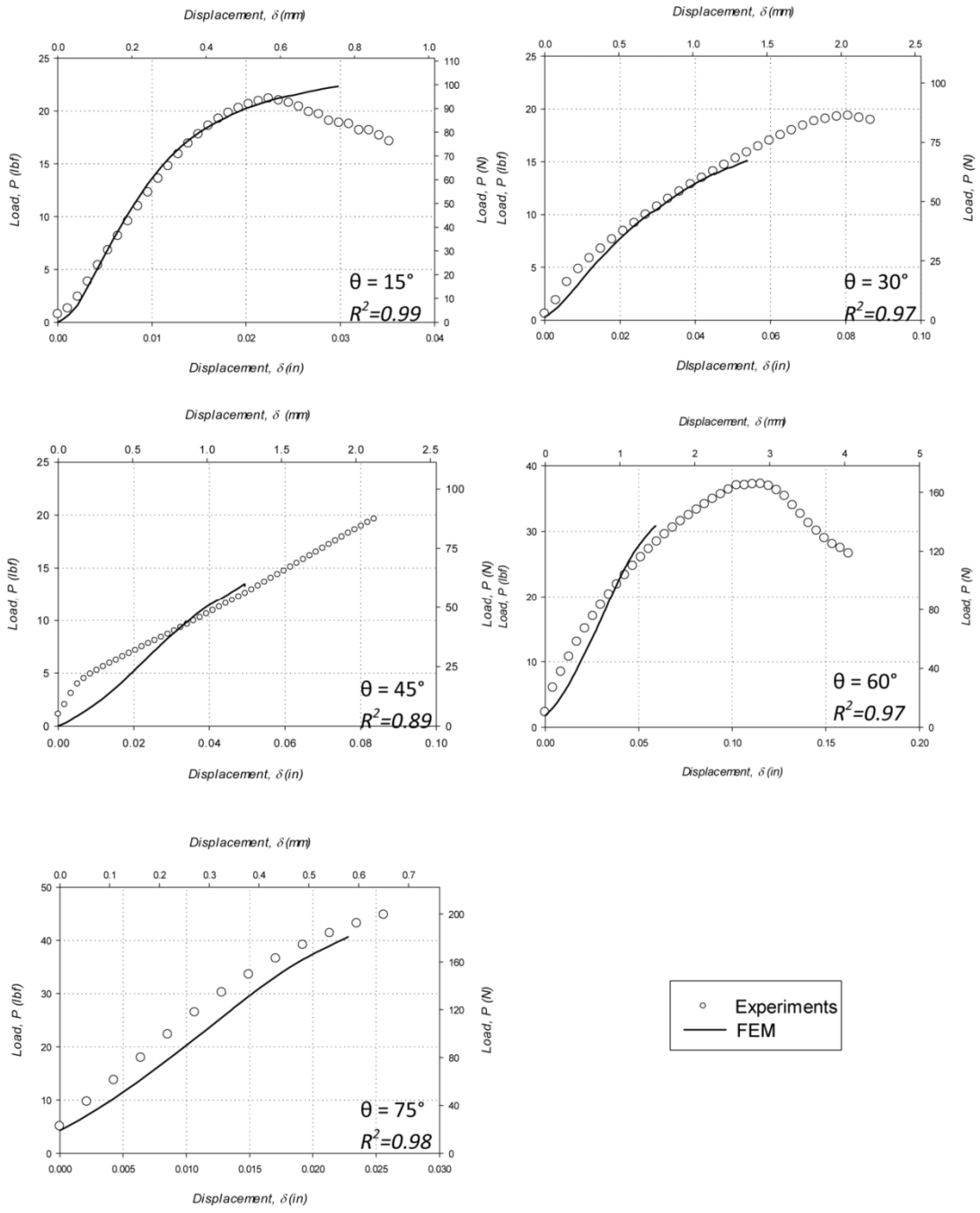

Figure 6.3: Load - Displacement curves from off-axis meso-scale numerical simulation of the 325x2300 SS316L woven wire mesh compared with experimental results.

This fact justifies the use of homogenized orthotropic material properties to model this material, alleviating the need to consider the geometry or characteristics of the ensemble of wires in the mesh. The exceptional fit of the meso-scale model response to experimental data in most orientations also justifies the development of a 2D orthotropic finite element to model higher-level mechanical aspects of this material, such as fatigue and damage characteristics. It must be noted that the R^2 values reported in Fig. 6.3 are calculated for the correlation up to ultimate tensile strength of the experimental case, or to the end of the simulation curve, whichever is first.

6.2.2 Meso-Scale Yield Behavior

The global mechanical behavior of a composite material is in general a function of its constituents. Typically, the material properties of the individual components and the interactions between the different substrates governs the global response of the material. Woven materials like the SS316L twill dutch woven wire mesh in question are similarly dependent on the behavior and interaction of their components. The meso-scale characteristics of the mesh, such as the weave pattern, tightness, and uniformity, ultimately determine its global behavior. Evolution of the global behavior of the mesh throughout elasto-plastic transition is a function of the behavior of the individual wires in the weave. The material properties, geometry, and contact parameters of the wires are important factors in the overall mesh behavior, and a thorough understanding of mesh yielding requires investigation of these influences. Woven materials possess an intermediate level of internal component interaction not encountered in homogenous materials. An intermediate scale of material evolution, in which individual wires begin to yield at the meso-scale, exists between the microstructural accumulation of defects and the global evolution of the material. In the same manner that accumulation of damage at the micro-scale

ultimately leads to global yielding in homogenous materials, accumulation of plasticity at the meso-scale leads to global yielding of the woven wire mesh. It is postulated that wire level yielding reaches some critical value prior to any discernable deviation of the macro-scale material response from elastic behavior. In this light, meso-scale plasticity accumulation prior to global mesh yielding can be viewed as macro-scale elastic damage accumulation.

To investigate the relationship between localized wire yielding and global yielding of the 325x2300 SS316L twill dutch woven wire mesh, further numerical simulations were conducted with the goal of mapping the progression of wire level plastic deformation with respect to the macro-scale response. The developed finite element model, constrained in an identical fashion as described in Fig. 6.1, was used along with the MKIN model to simulate the development of local plastic strain at the meso-scale of the mesh. Equivalent plastic strain was recorded at key areas on the individual wires, typically at points of contact where plasticity was the highest, as illustrated in Fig. 6.4. These areas were carefully chosen from central locations in the mesh such that boundary effects were minimal, but it must be noted that the reported plastic strains are local, and not indicative of overall wire plasticity. The progression of local equivalent plastic strain in the wire level is related to the global response of the woven mesh by plotting the global macro-level experimental stress-strain relationship with respect to meso-scale equivalent plastic strain accumulation. This relationship is illustrated in Fig. 6.5 for various material orientations.

Analysis of Fig. 6.5 reveals a definite dependence of wire plasticity evolution on material orientation, and provides some evidence to suggest that localized equivalent plastic deformation indeed reaches some critical value at the meso-scale prior to global yielding of the woven mesh. The high level of strain energy in the warp wires for both the 75º and weft (90º) cases is surprising considering the dominant loading direction is weft, however, it must be considered

that the compressive stresses in the warp wires due to crimp interchange and contact with the weft wires are quite large. It is observed, particularly in the weft dominant orientations (60° - 90°), that significant wire level plasticity develops prior to the material exhibiting signs of global yielding. This behavior indicates that individual wire yielding is indeed a source of elastic damage that may affect the global elasticity of the woven mesh.

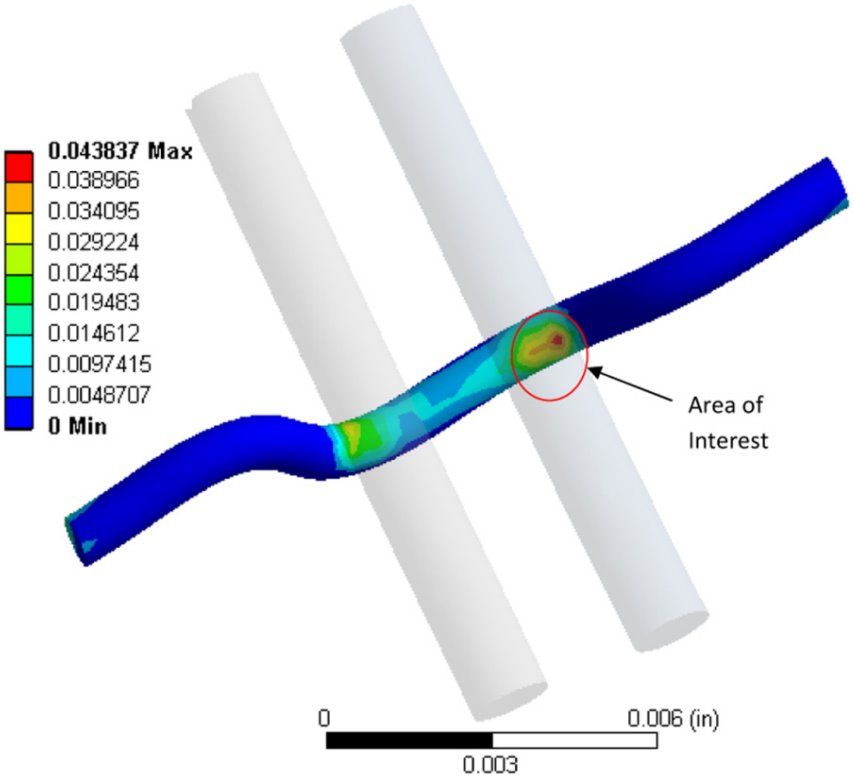

Figure 6.4: Example area of interest for investigation of meso-scale equivalent plastic strain development in the 325x2300 SS316L woven wire mesh.

Damage, typically defined as the accumulation of microstructural defects within a material, in this case could be defined by plasticity developing at the intermediate meso-scale. Future work is planned to develop a relationship for the development of wire level plasticity to macro-scale elastic damage through continuum damage mechanics.

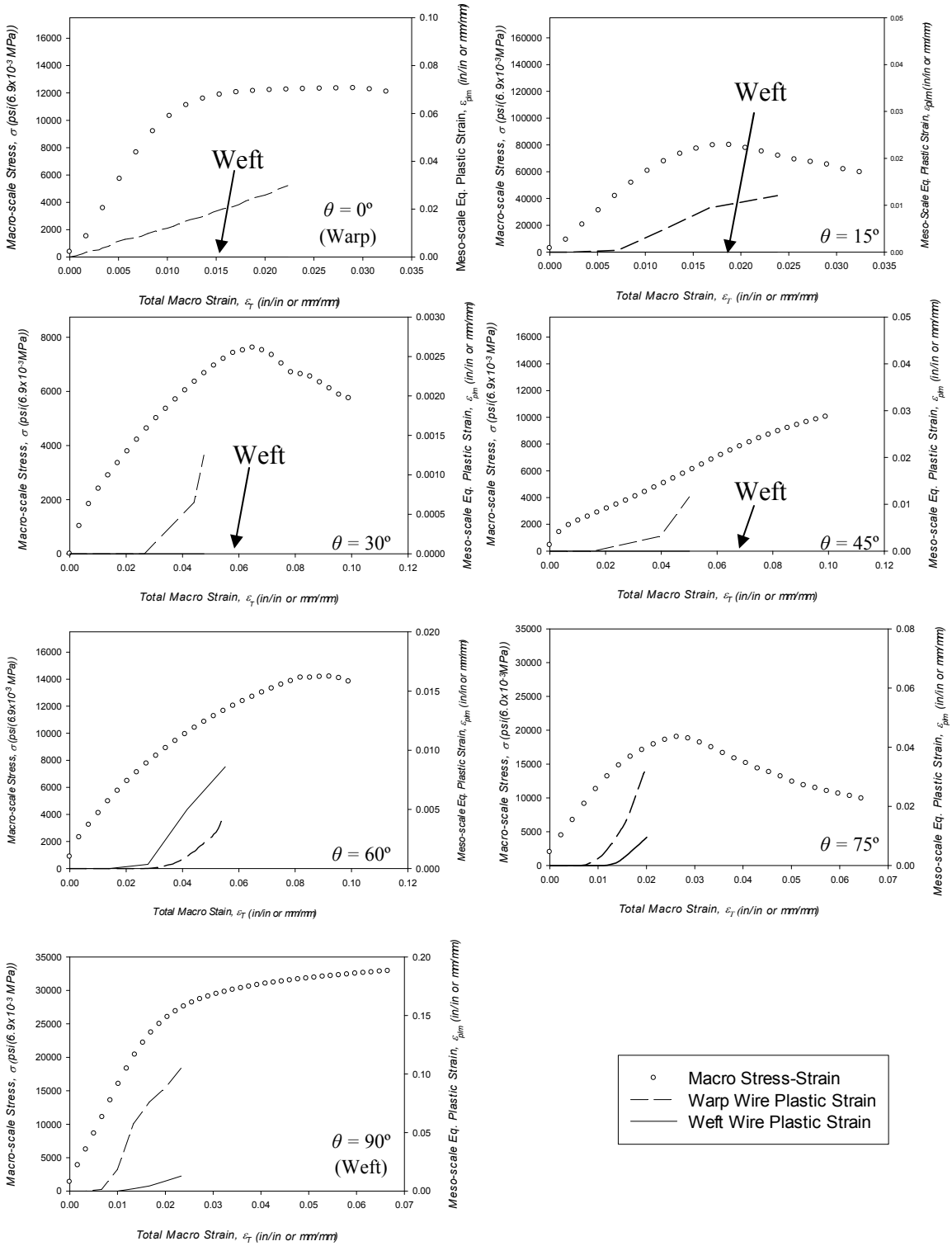

Figure 6.5: The development of plastic strain at the meso-scale predicted by the numerical simulations with respect to the global stress-strain relationship of the 325x2300 SS316L woven wire mesh at various material orientations.

6.2.3 Mathematical Modeling of Meso-Scale Plastic Strain

As in the case of fiber-reinforced composite materials, the mechanical behavior of micronic woven wire mesh material is dominated by the deformation and failure mechanisms of the individual wires constituting the mesh, and the interaction between these wires. As is evidenced in Fig. 6.5, the macro-scale plastic flow and eventual rupture behavior of the subject material is driven in the meso-structure of the material. In this respect, global yielding of the woven wire mesh is not a function of the movement of microscopic atomic level dislocations as in homogenous materials, but rather is realized through the wire yielding, individual wire failure, and load redistribution occurring on the meso-scale. This suggests that macro-scale mesh failure can be modeled by considering meso-scale plastic strain as a driving mechanism behind global yielding. On this premise, it is proposed that the development of a model relating the meso-scale equivalent plastic strain to the total global tensile strain of the material would allow for the prediction of mesh rupture due to meso-scale plasticity. The prediction of mesh failure could then be realized by simply tracking the total strain state in a region of interest, which lends itself particularly well to the previously introduced macro-scale homogenous FE modeling of a notched geometry. The ability to predict the level of meso-scale plasticity in a material from macro-scale strain measurements could also potentially be leveraged as a damage indicator in Non Destructive Evaluation (NDE) of this class of materials, or to determine the state of a material subjected to complex loading conditions. Such a model, in conjunction with the measured wire or fiber tensile properties, i.e., ultimate wire plastic strain, could provide a high caliber correlation for failure modeling. To this end, an analytical model has been developed

based on the trends observed in Fig. 6.5 to predict the level of meso-scale plastic strain, $\varepsilon_{pl,meso}$, present locally in the material as a function of the total global strain, $\varepsilon_{T,macro}$, i.e.,

$$\varepsilon_{pl,meso} = ae^{b\left(\varepsilon_{T,macro}-\varepsilon_{y,macro}\right)} + c\varepsilon_{T,macro} \tag{6.2.1}$$

It is noted that the model presented in Eq. (6.2.1) is not based on physical mechanisms, and that the proposed constants in their present form are simply chosen via regression analysis optimization. The term $\varepsilon_{y,macro}$ here is the macroscopic yield strain of the material, which is dependent on material orientation. Furthermore, it must be noted that the hardening behavior prescribed to the SS316L wires in the MKIN model used to predict the plastic strain in the meso-scale FE model is not reflective of actual SS316L tensile results, but rather has been selected via an optimization of the overall FE model response as described in Section 6.1. Thus, the use of the current optimized constants, provided in Table 6.1, must be cautioned, and the model as proposed herein can be treated as a first-order approximation only. To provide increased physical meaning to the plasticity model, and to lay the groundwork for future improvements, an initial attempt has been made to provide functional forms of the constants with respect to the material orientation. Ideally, the constants, which are different for the warp and weft wires, should be symmetric about the perpendicular material axes, and should be governed by periodic functions of the material orientation, θ, taking into consideration parameters such as power law or voce hardening coefficients [Kraft and Gordon, 2011]. As the form of the model proposed in Eq. (6.2.1) represents only a first order mathematical approximation, however, the form of the equations governing the constants as a function of material orientation are not constrained as such, and are presented herein merely to demonstrate that the parameters provided in Table 6.1

do in fact hold functional forms in theta. Improvements to the meso-scale FE model will provide for improvements to the constant formulations, and this is discussed in detail in the future work section of this thesis. The formulations of the constants are expressed as follows.

$$a_{warp} = 0.0003e^{3.325\left(\theta-\frac{\pi}{4}\right)} \tag{6.2.2}$$

$$a_{weft} = 0.0025e^{5.00\left(\theta-\frac{5\pi}{12}\right)} \tag{6.2.3}$$

$$b_{warp} = -61.92\theta^3 + 171.0\theta^2 - 55.55\theta + 121.1 \tag{6.2.4}$$

$$b_{weft} = -46.44\theta^3 + 241.4\theta^2 - 137.3\theta + 6.6 \tag{6.2.5}$$

$$c_{weft} = 0.284\theta^4 - 1.118\theta^3 + 1.102\theta^2 - 0.294\theta + 0.004 \tag{6.2.6}$$

$$c_{weft} = 0.284\theta^4 - 1.118\theta^3 + 1.102\theta^2 - 0.294\theta + 0.004 \tag{6.2.7}$$

The functional forms of Eqs. (6.2.2 - 6.2.7) are determined via regression analysis fit of the constants to the optimized parameters presented in Table 6.1, and are not representative of any physical material behavior. The fit of the coefficient models to the optimized meso-scale plasticity model constants is shown in Figs. 6.6 through 6.8 for the parameters *a*, termed the meso-scale plastic strain scale factor, *b*, termed the meso-scale plastic strain exponential coefficient, and *c*, the meso-scale plastic strain linear coefficient, respectively. In all cases, the fit is found to be acceptable, and the parameter fitting functions are found to produce reasonable trends capable of predicting the constants in intermediate material orientations. The largest deviation of the predicting functions from the optimized constants is seen for the case of the exponential coefficient, *b*, in orientations where the plasticity is largely dominated by the warp wires, i.e., where b_{weft} should ideally equal zero. The fit produced by Eq. (6.2.1) with respect to

the meso-scale plasticity level predicted by the FE model is provided in Fig. 6.9 for all treated material orientations.

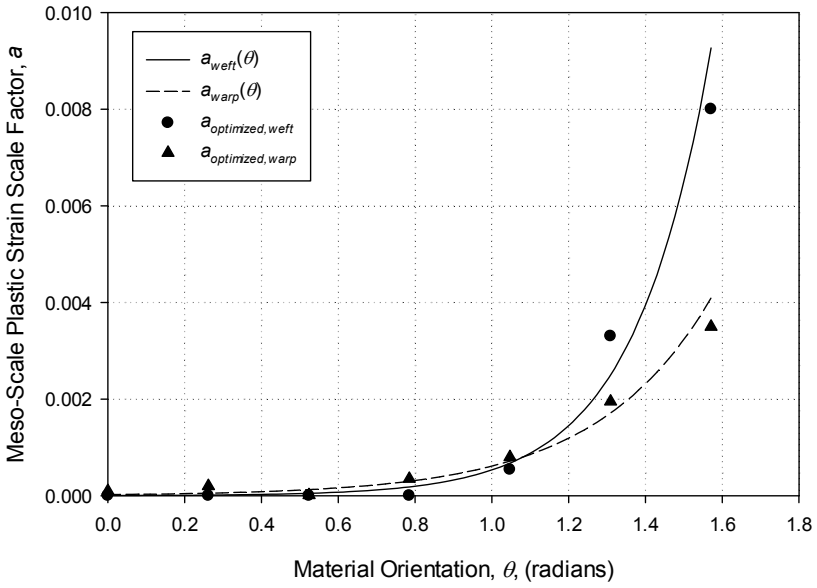

Figure 6.6: The orientation dependence of the meso-scale plastic strain scale factor, *a*, as predicted by Eqs. (6.2.2) and (6.2.3), with respect to the parameters values developed from regression optimization of Eq. (6.2.1).

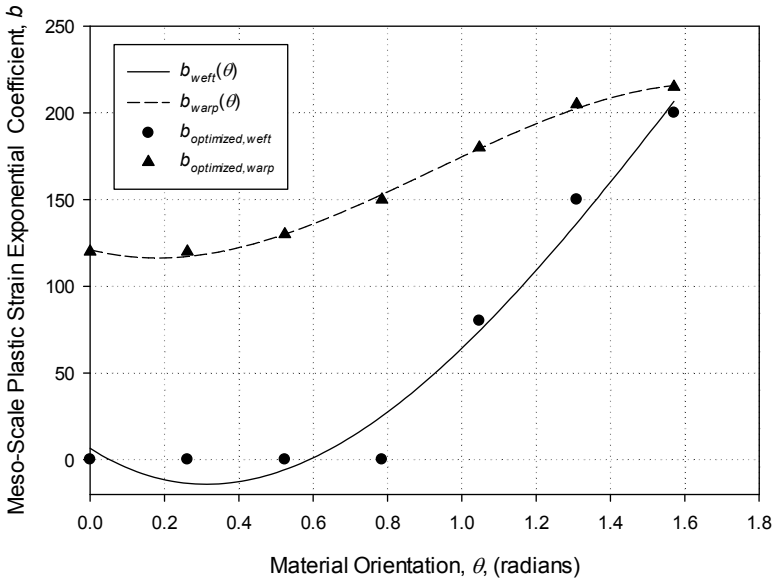

Figure 6.7: The orientation dependence of the meso-scale plastic strain exponential coefficient, *b*, as predicted by Eqs. (6.2.4) and (6.2.5), with respect to the parameters values developed from regression optimization of Eq. (6.2.1).

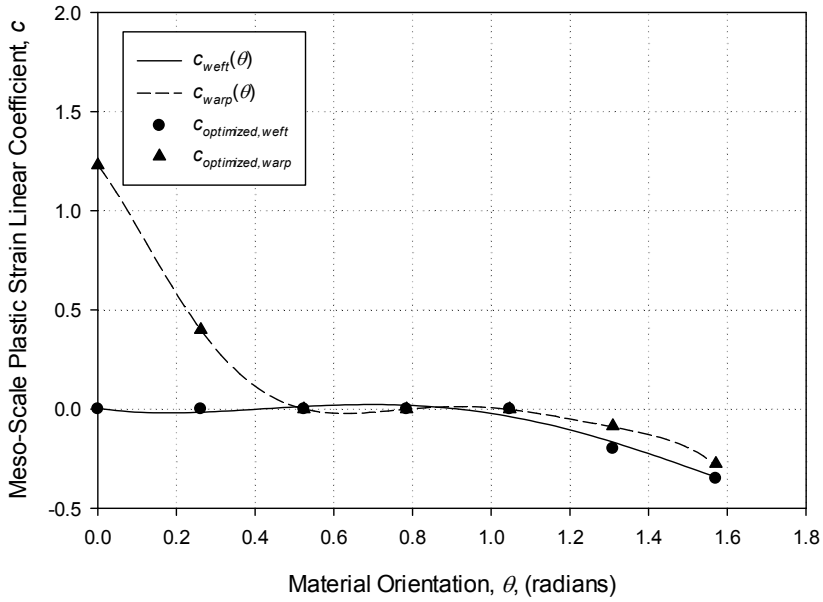

Figure 6.8: The orientation dependence of the meso-scale plastic strain linear coefficient, *c*, as predicted by Eqs. (6.2.6) and (6.2.7), with respect to the parameters values developed from regression optimization of Eq. (6.2.1).

To demonstrate the ability of the parameter prediction functions to formulate reasonable model parameters in all material orientations, Figure 6.9 has been generated using constants formulated via the prediction functions. Inspection of Fig. 6.9 reveals that the fit of the mathematical model to the simulation results is sufficient to treat the model as a first order approximation for predicting meso-scale material failure in both the warp and the weft wires. Note that the different wires posses their own constants for each respective material orientation, which is reflective of the varying deformation mechanisms amongst the weft and warp wires. It is also noted that a clear transition occurs at the 60º material orientation, where plasticity in the weft wires becomes significant enough to contribute to mesh rupture. This observation is consistent with the rupture behavior observed form uniaxial tensile tests [Kraft and Gordon, 2011].

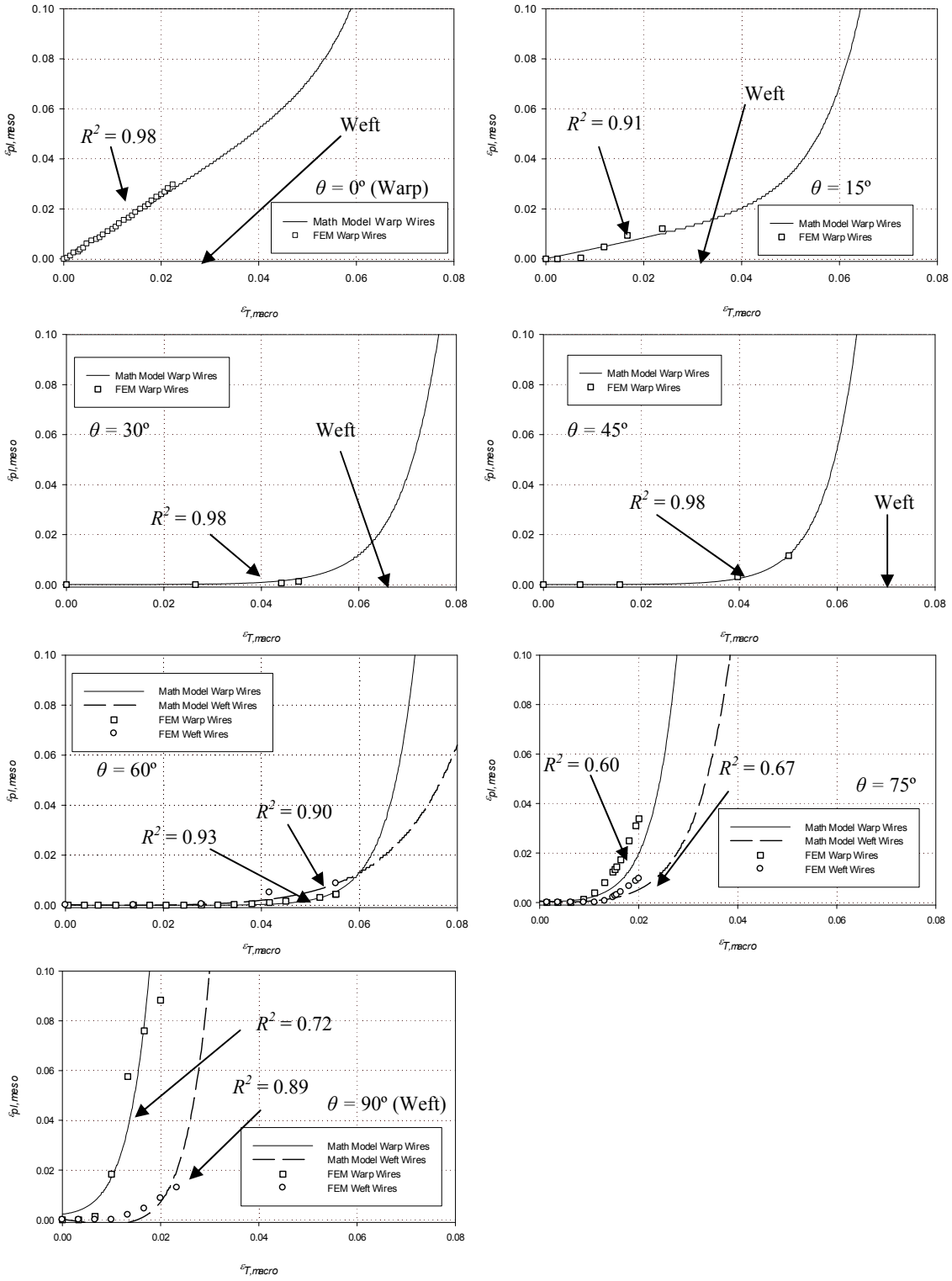

Figure 6.9: Comparison of the finite element and mathematical models of the progression of the meso-scale plastic strain as a function of the total global strain applied to the material

Table 6.1: Optimized parameters for the mathematical model relating meso-scale wire plasticity to the applied macro-scale total strain

Material Orientation, θ (º)	Wire Type	a	b	c
0	Warp	1.00×10^{-4}	120.0	1.230
	Weft	0	0	0
15	Warp	2.00×10^{-4}	120.0	0.400
	Weft	0	0	0
30	Warp	1.25×10^{-5}	130.0	0
	Weft	0	0	0
45	Warp	3.50×10^{-4}	150.0	0
	Weft	0	0	0
60	Warp	8.00×10^{-4}	180.0	0
	Weft	5.40×10^{-4}	80.0	0
75	Warp	1.95×10^{-3}	205.0	-0.085
	Weft	3.30×10^{-3}	150.0	-0.200
90	Warp	3.50×10^{-3}	215.0	-0.275
	Weft	8.00×10^{-3}	200.0	-0.350

6.3 Numerical Implementation of a Meso-Scale Plasticity Model to Predict Mesh Rupture

The meso-scale plasticity model presented in Eq. (6.2.1) is ideal for implementation into the macro-scale finite element model previously introduced in Chapter 5, as it relates the failure of individual wires in the SS316L woven wire mesh to the global strain state of the material. As the strain state near the region of a notch is straightforward to track using the finite element method, it is possible to use Eq. (6.2.1) to relate the state of total mechanical strain in an element to the meso-scale equivalent plasticity of the wires that would ideally comprise that element. When the equivalent meso-scale plastic strain is predicted to have reached some predefined criterion, taken in this case as the elongation to failure of SS316L, as shown in Table 1.1, then the wires, either warp or weft, in that element are said to have failed. Thus, the element is

considered to have lost stiffness, and should be disregarded in further load steps of the analysis. The commercial FEM software package, ANSYS, provides a built-in functionality for reducing element stiffness based on a user defined criterion known as Element Death, and this feature has been leveraged to facilitate element failure based on predicted wire plastic strain levels using the meso-scale plasticity model in Eq. (6.2.1). It should be emphasized that the Element Death feature in ANSYS does not remove any elements from the mesh that have exceeded the failure criterion, but rather reduces their associated stiffness by multiplying the element stiffness matrix by a severe reduction factor, $1x10^{-6}$ in this case, such that the elements not longer contribute to the solution. To maintain continuity of the solution throughout subsequent load steps, the deactivated element loads, mass, specific heat, etc., are immediately reduced to zero. Additionally, the energy of the deactivated elements are not considered in the total model energy [ANSYS, 2012]. By selecting and plotting only the "live" elements remaining in the mesh for each load step, crack propagation in the SS316L woven wire mesh material can be simulated using the macro-scale FE model. Additionally, the reduction in "killed" element stiffness effectively reduces the overall stiffness of the model, allowing for the global unloading of the material due to mesh rupture to be simulated. To illustrate the constitutive response of an element being killed by the Element Death routine, a single element model, incorporating a single unit square PLANE82 element with boundary conditions as illustrated in Fig. 6.10(a), has been exercised in ANSYS. The element is observed to display a typical elasto-plastic response until the maximum total strain criterion (0.8% strain in this case) is exceeded, as shown in Fig. 6.10(b). Upon the criterion being reached, the element stiffness is immediately reduced to near zero through the remainder of the applied displacement. While the Element Death feature in ANSYS is a very useful simulation tool, it is relatively poorly developed in the ANSYS

catalogue [ANSYS, 2012] , and employment in a parametric simulation routine is somewhat cumbersome. As such, it is pertinent that the logic used to implement the meso-scale plastic model be documented, and this is provided in the form of a flow-chart in Fig. 6.11. Additionally, the ANSYS APDL code used to generate the simulation results in this section is provided in Appendix B. The model geometry employed in the mesh failure simulations is identical to that shown in Fig. 5.1(a), however, the mesh has been greatly refined to facilitate accurate crack growth. The FE mesh used to discretize the circular notched specimen geometry is provided in Fig. 6.12, along with a sketch of the boundary conditions applied to the model. It is noted that while roller type conditions at the boundary shown in Fig. 6.12 would be ideal, the notch is far enough removed from the bottom edge of the specimen so as to not be affected by the clamped conditions.

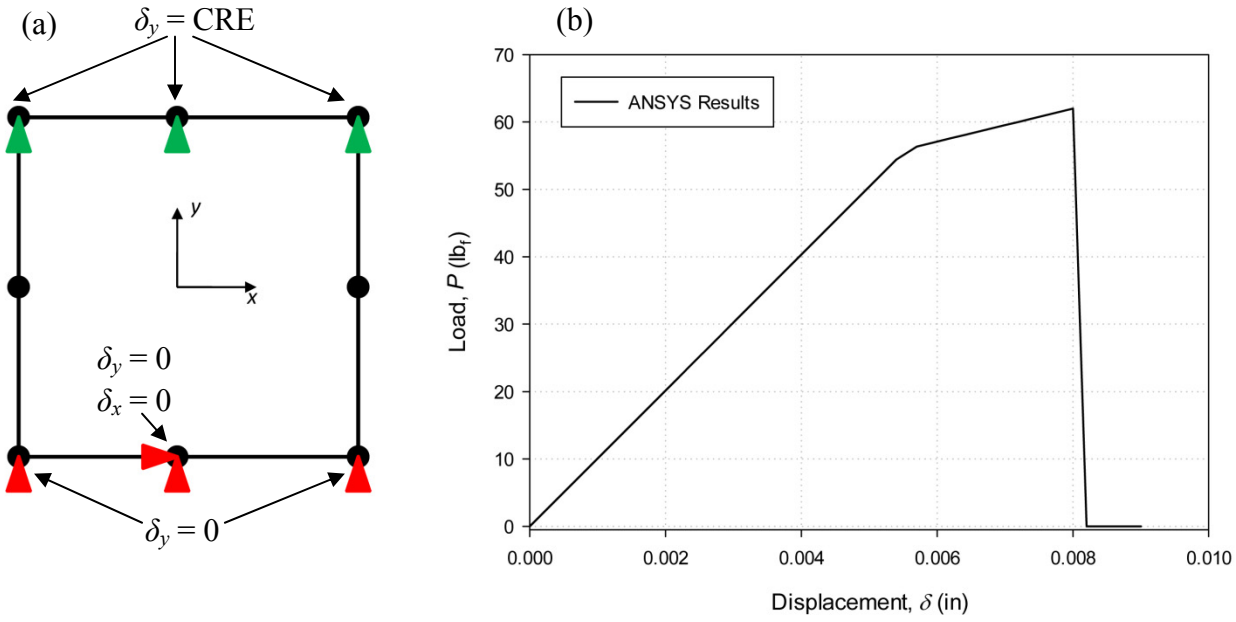

Figure 6.10: The elasto-plastic response of a single PLANE82 element being deactivated using the ANSYS Element Death routine, along with the applied boundary conditions.

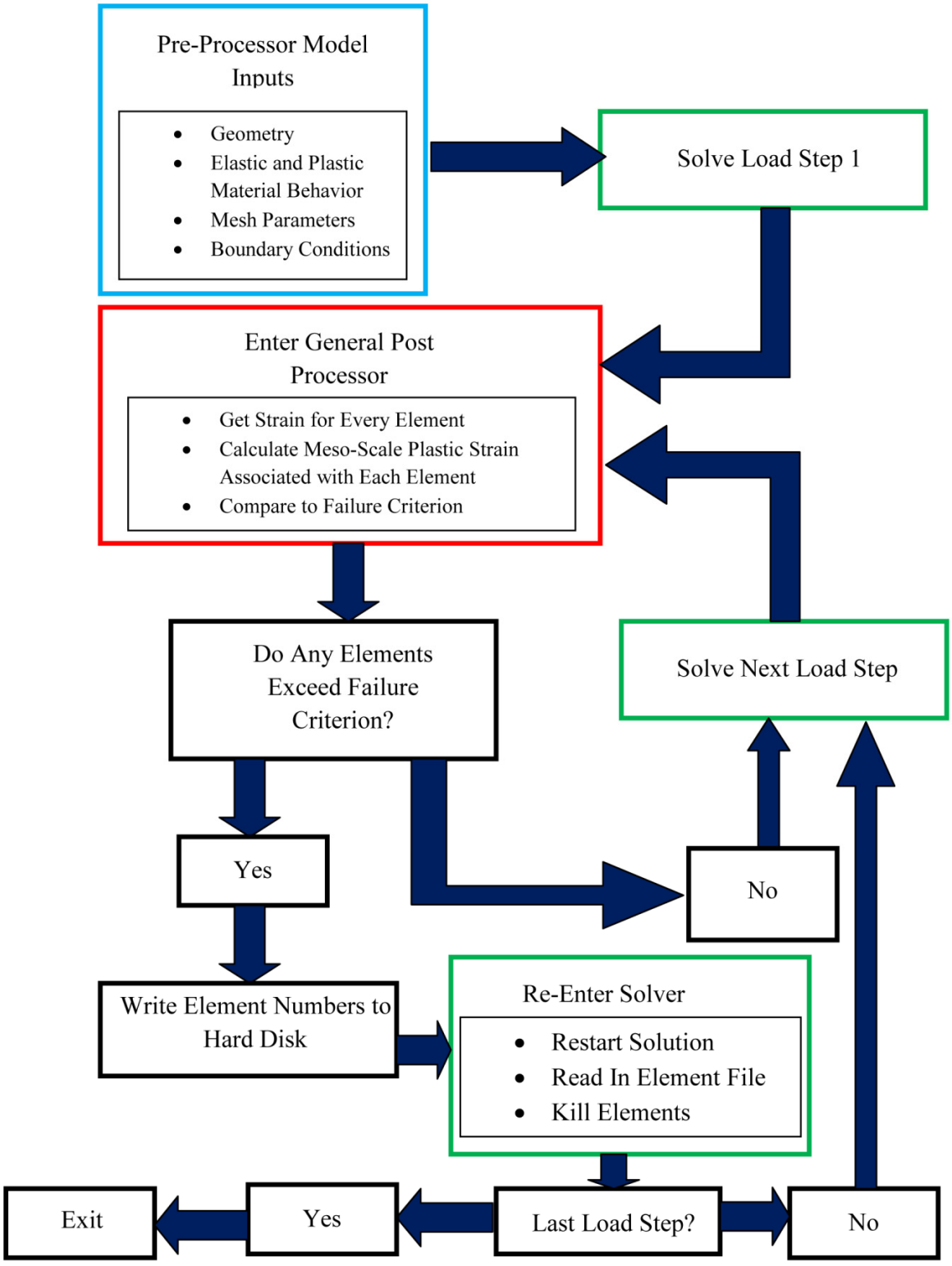

Figure 6.11: Flow chart outlining the logic steps used to kill elements in the macro-scale FE model using the meso-scale plastic strain model

The linear elastic material model used for this case is orthotropic, and identical to the one used in modeling the strain distribution around various notches in Chapter 5. Additionally, plastic material behavior is captured in this modeling effort using anisotropic hardening, i.e., the ANSYS model ANISO, which allows for different yield strengths and different tangent moduli to be defined for the respective principal material orientations, and for the case of pure shear. The ANISO plasticity parameters defined for the mesh failure simulations are provided in Table 6.2. As the anisotropic plasticity model requires the definition of a pure shear yield strength, and pure shear testing of thin materials such as the SS316L woven wire mesh is challenging due the tendency of the material to buckle, this parameter has been estimated using the bias (45º) tensile yield strength via a model proposed by Chen [Chen et al., 2007], i.e.,

$$S_{xy} = k \sin \omega \frac{S_{45}}{\sqrt{2}} \tag{6.3.1}$$

where the term S_{xy} is the yield strength under pure shear, S_{45} is the bias (45º) uniaxial tensile yield strength (5.0ksi), k is a converting coefficient set at 0.7 as recommended in the literature [Chen et al., 2007], and ω is the angle between the warp and weft directions, which is assumed to be 90º in this case. The tangent moduli for each case is treated as a model optimization parameter, and so has been selected via an error reduction study with respect to the uniaxial experimental results.

Table 6.2: Parameters defined for the anisotropic plasticity model used for the macro-scale failure simulations of SS316L woven wire mesh material

Loading Condition	Yield Strength, S_y (ksi)	Tangent Modulus, T (ksi)
Uniaxial Warp (0º)	11.7	280.0×10^3
Uniaxial Weft (90º)	22.8	700.0×10^3
Pure Shear	4.69	15.0×10^3

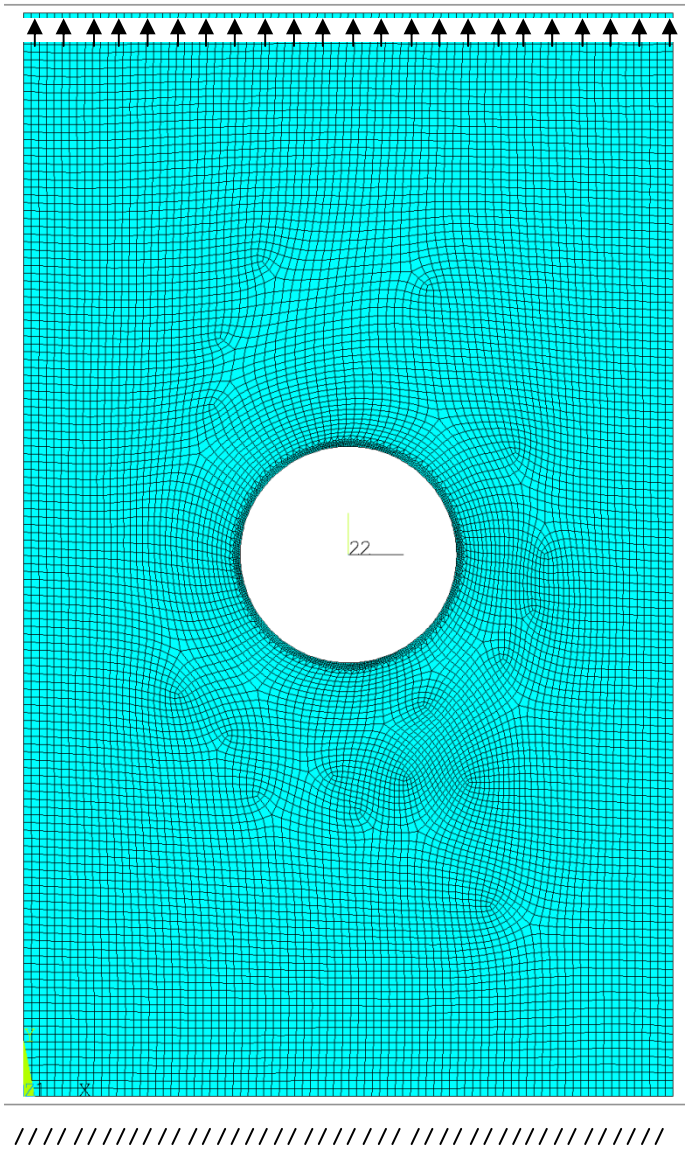

Figure 6.12: The finite element mesh used to simulate the failure of SS316L woven wire mesh material when notched with a circular stress riser, and the applied boundary conditions.

To demonstrate the ability of the meso-scale plasticity model to provide a first-order prediction of the failure of the SS316L woven wire mesh material, the described FEM implementation has been exercised for the cases of circular notched uniaxial specimens loaded in both the warp (0º) and weft (90º) material orientations. The numerical prediction of crack growth in the warp (0º) oriented SS316L woven wire mesh is provided in Fig. 6.13, along with contours

of damage in the warp wires, defined as the ratio of meso-scale plastic strain level in the element to the failure criterion. Values of damage greater than one indicate elements that are to be killed in the subsequent load step.

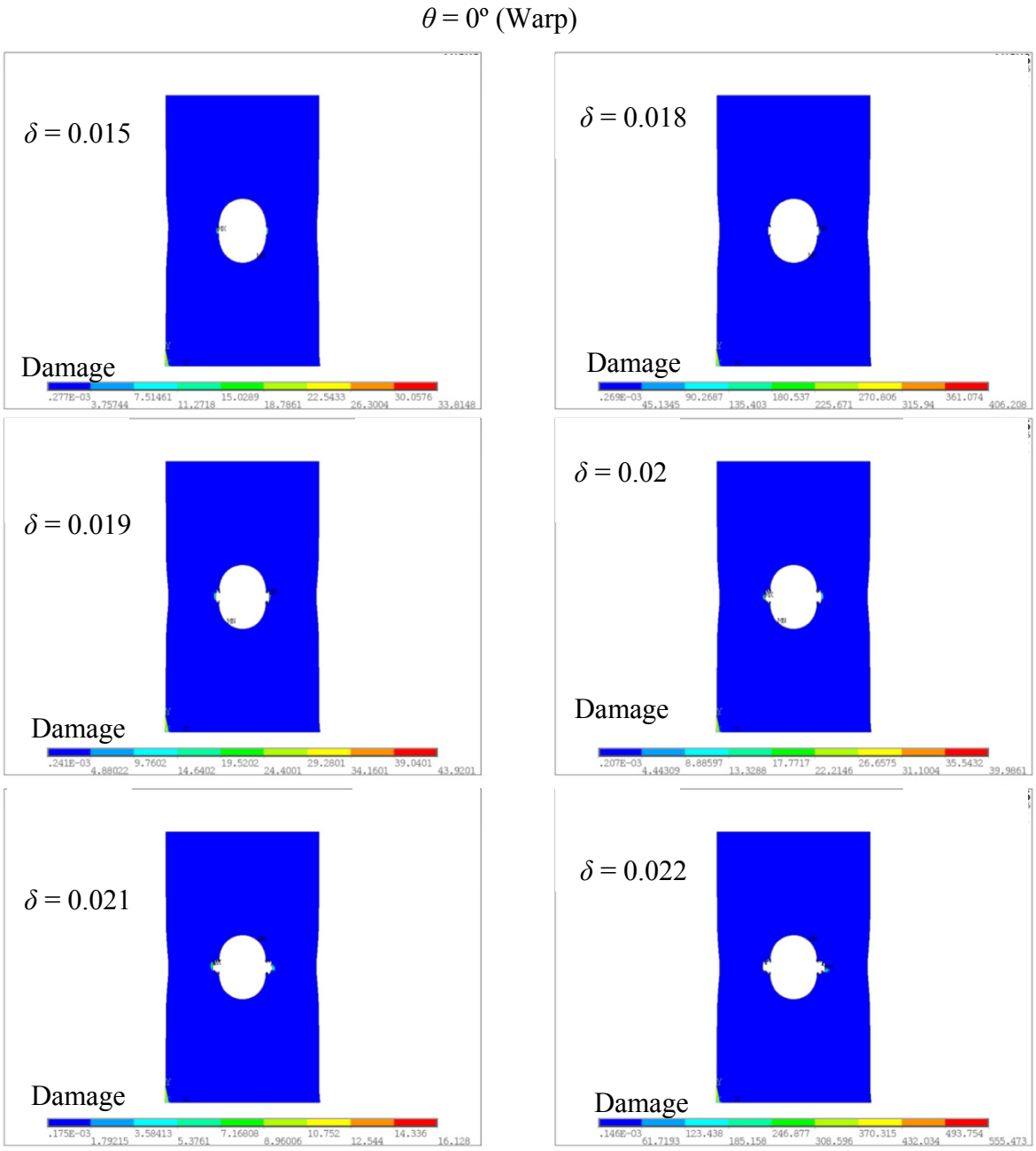

Figure 6.13: Simulated crack growth from a circular notch in SS316L woven wire mesh material loaded in the warp (0º) material orientation.

The observation that in some instances the damage value is much larger than one indicates that this simulation could benefit from an adaptive time stepping routine, such that the load step could be automatically bisected to achieve better refinement of the crack growth path, and this modification is suggested for future work. Inspection of Fig. 6.13 shows that the crack growth is symmetric on either side of the notch, and generally progresses along a path normal to the loading direction as would be expected. The simulations shows a large process zone as is expected in the warp (0º) material orientation, and overall the simulation conforms well to the experimental rupture zone shown in Fig. 3.36 with regards to appearance. In an effort to make a more objective assessment of the performance of the meso-scale plasticity model in predicting mesh failure in the warp (0º) material orientation, the plastic load-displacement response of the simulation is compared to the experimental results in Fig. 6.14.

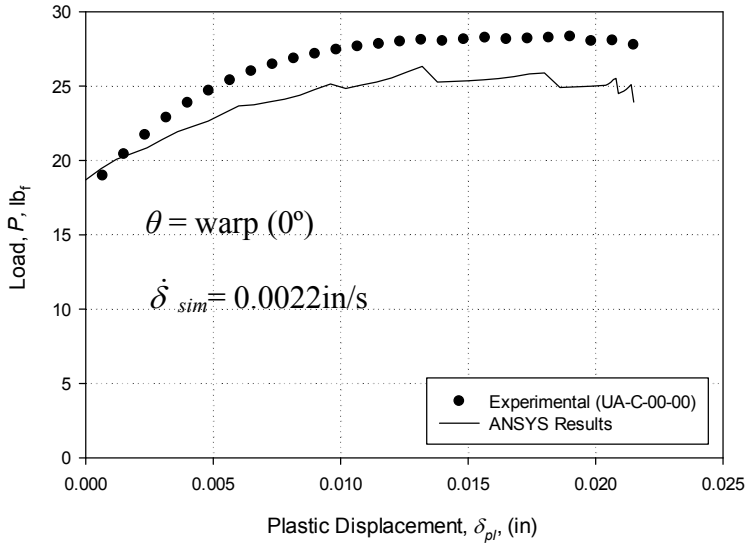

Figure 6.14: The experimental and simulated load - plastic deformation response of circular notched SS316L woven wire mesh material in the warp (0º) material orientation.

Key features to compare in assessment of the performance of the model are the strain hardening, ultimate tensile strength, and unloading behavior of the model with respect to the experimental

results. The model appears to perform well in all respects for the warp (0º) material orientation, clearly showing the gradual unloading and low strain hardening associated with the warp (0º) material orientation.

The weft (90º) direction failure is characterized by brittle type material behavior, with very little global plastic strain and quick unloading upon reaching the ultimate tensile strength. The process zone is generally observed to be more compact than the warp (0º) case, and tends to progress along a sharp and well defined path. The failure prediction at a circular notch in the SS316L woven wire mesh material loaded in the weft (90º) material axis is presented Fig. 6.15, along with contours of weft wire damage, defined similarly as in the warp (0º) orientation case. Again, the failure surface is observed to be symmetric with respect to the circular notch, and is observed to generally progress in a direction normal to the loading axis. The sharpness of the rupture zone observed in experiments is not captured by the simulations, however, and in fact the process zone appears to be larger in the weft (90º) degree simulation than for the warp (0º) case. This is attributed to the rapidity of the growth of meso-scale plastic strain in this material orientation, and the lack of an adaptive load stepping routine to reduce the plastic strain step size. Indeed, if the load step size is too large, it is observed that the natural distribution of strain begins to dominate the element death progression rather than the small zone of increased global strain at the growing crack tip. It is speculated that the addition of an automatically bisecting load step algorithm into the simulation in future work will improve the appearance of the simulated crack growth by ensuring that only the elements at the crack tip exceed the criterion for each given load step. Nonetheless, inspection of the plastic load - displacement curves for the experimental case and the simulated case, presented in Fig. 6.16, does show that the brittle type failure and rapid unloading associated with the weft (90º) material orientation is captured by the model.

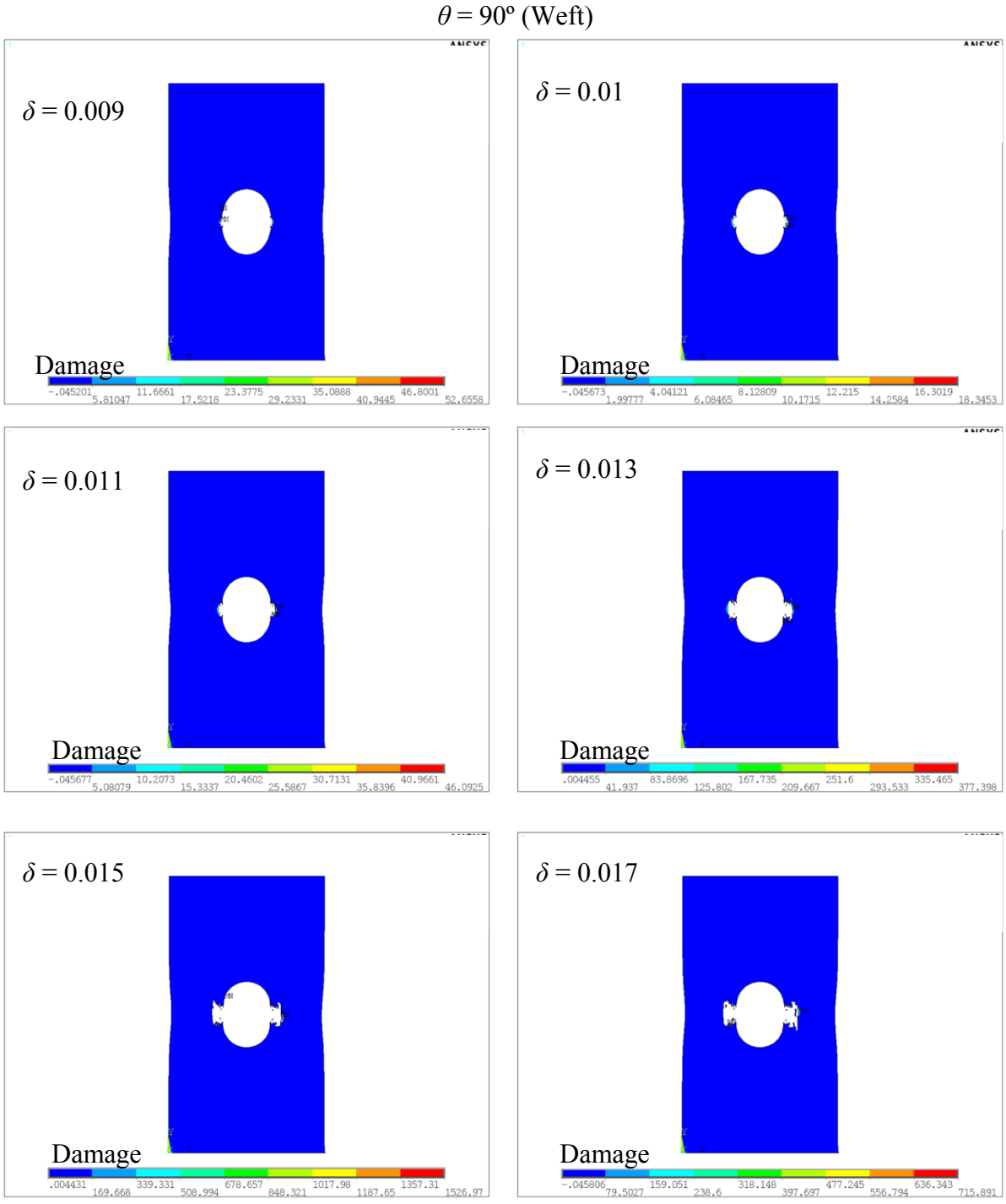

Figure 6.15: Simulated crack growth from a circular notch in SS316L woven wire mesh material loaded in the weft (90º) material orientation.

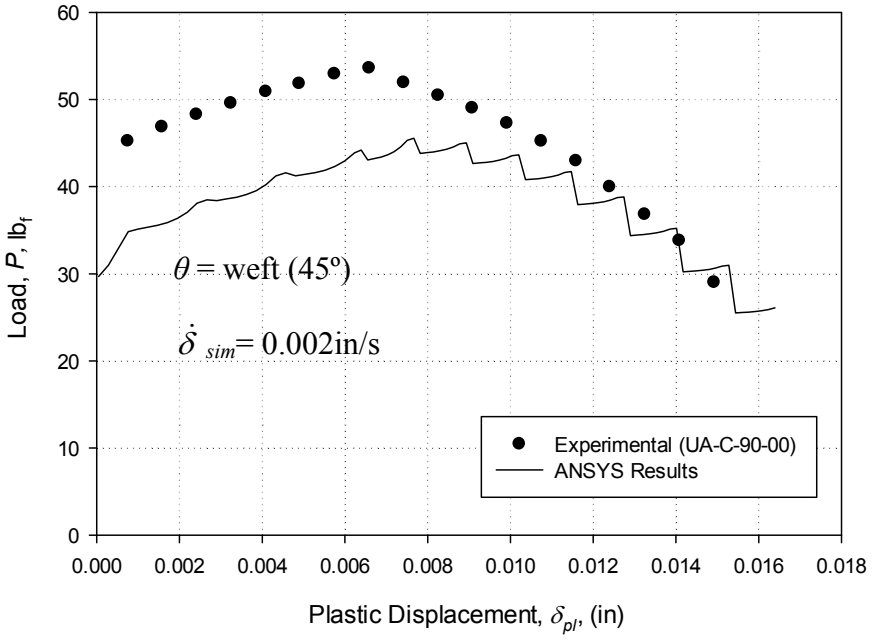

Figure 6.16: The experimental and simulated plastic load - plastic deformation response of circular notched SS316L woven wire mesh material in the weft (90º) material orientation.

Inspection of Fig. 6.16 also demonstrated that the hardening model prescribed for the simulations captures the behavior of the weft (90º) oriented material observed in experiments. Overall, the model results for the weft (90º) case indicate that, while improvements to both the meso-scale plasticity model and the numerical implementation routine are needed to obtain accurate crack growth behavior, the model is capable of capturing the global behavior of the material using meso-scale simulation results, and future work is warranted in honing this multi-scale approach.

CHAPTER 7: CONCLUSIONS AND RECOMMENDATIONS FOR FUTURE WORK

Woven metallic materials hold significant promise for use in high performance filtration and trace detection applications, and are excellent candidates for use as reinforcement in emerging composites. Prior to implementation of this class of material into new technologies, however, there must exist a general understanding of their mechanical behavior, and of the applicability of classical mechanics of materials models to extrapolate design scenarios. Accordingly, this thesis, which focused on a representative 325x2300 SS316L twill dutch micronic woven wire mesh, has worked to address knowledge gaps in several fundamental areas that are key to expanded use of this class of material in industry. Three key aspects of the mechanical behavior of the representative micronic metallic woven structure have been studied in depth in this work, namely (1) the applicability of an in-plane linear elastic orthotropic model to govern the elasticity of the woven mesh, (2) the effect of stress concentrations on the mechanical behavior and ultimate rupture of the mesh, and (3) the yielding behavior of the woven structure at the macro and meso scales. While these aspects have been studied independently in this research through a rigorous experimental testing and numerical simulation regimen, consideration of the combination of these characteristics is necessary to understand, and ultimately to model, the elasto-plastic mechanical behavior of this class of materials. Thus, some discussion of the overall findings of the uniaxial and biaxial experiments, as well as the macro and meso-scale modeling effort, is necessary. Presented here is a brief summary of the findings of the experimental and numerical characterization results, and a discussion of conclusions that can be drawn from this work. Also, the short-comings of this work are discussed, and recommendations for future work are made.

7.1 Concluding Statements

Three distinct experimental test sequences, discussed in great detail in Chapters 3 and 4 of this thesis, have been completed in this work, each intended to classify various aspects of the mechanical behavior of the SS316L twill dutch woven wire mesh material. The first experimental testing regimen, a series of uniaxial tensile tests on standard flat tensile specimens incised at various material orientations, provided much information on the general elasto-plastic mechanical behavior of the subject material. Next, the central experiments to this work, uniaxial tensile tests on notched specimens, were conducted to gage the effect of various notch aspect ratios and orientation on the mechanical behavior of the woven wire mesh. Finally, biaxial tensile tests were performed on both smooth and notched cruciform specimens using an in-house designed linkage-based load frame, providing data pertinent to the development of a modified yield-surface, and results pertinent to understanding the effects of notches on the subject material in service type conditions. Taking a panoramic view of these experimental results allows for some significant conclusions to be drawn regarding the mechanical behavior of the subject material.

The mechanics of materials view for the modeling of, and design with, the metallic woven structure treated in this thesis has focused around the simplifying assumption of continuity and homogeneity of the material, as shown in Fig. 7.1. Indeed, engineers are constantly searching for simple yet accurate models for design and analysis, and so the applicability of the homogenization assumption for this class of materials in central to the expansion of use of this material in various industries. Overall, review of the experimental and

analytic modeling efforts in this thesis show that the subject material can be treated as a homogenous continuum with reasonable accuracy in most cases.

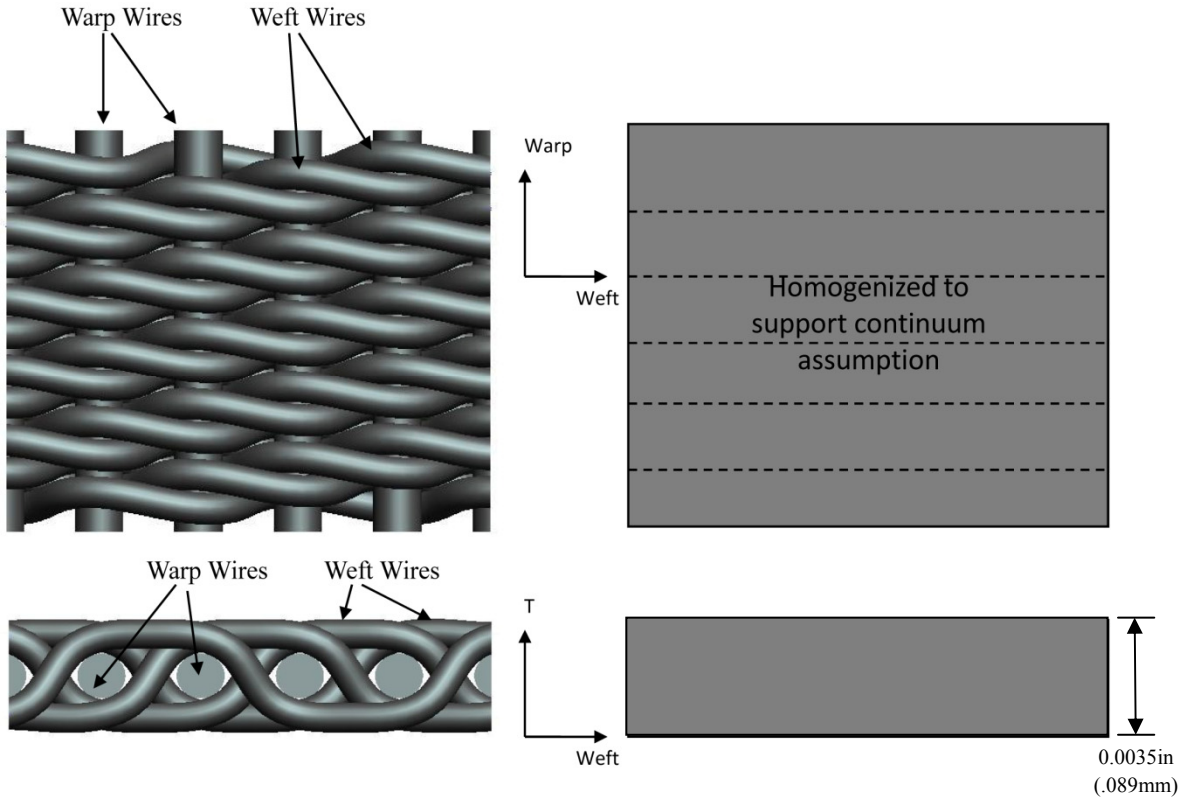

Figure 7.1: Illustration of the continuum assumption used in analytic and numerical modeling of the SS316L woven wire mesh material in this thesis.

The elastic constants are observed to follow trends associated with Hooke's Law, and in general it is found that an in-plane orthotropic constitutive relationship may be employed for the subject material with minimal error. In addition to the formulation of the orthotropic elastic constants, the smooth uniaxial testing results have been used to analyze the ability of the Hill yield criterion, which is fundamentally an orthotropic criterion based largely on the mechanical behavior observed in homogenous rolled plates, to predict the yield behavior of the SS316L woven wire mesh material. While the overall fit of the Hill criterion to the uniaxial experimental

results is reasonable, particularly in the principal material orientations and on the bias (45º), it has been found to be less acceptable in other off-axis orientations. Modifications to the Hill criterion to account for interaction between the shear and axial stress terms have been shown to improve the fit to the experimental data greatly, and so it is concluded that the interaction, or coupling, of the shear and axial stress terms is intrinsic to the yield behavior of the metallic woven wire mesh material.

The central work of this thesis is in the characterization of the mechanical behavior of this class of material when affected by a stress concentrator under both uniaxial and biaxial loads. For the case of uniaxially loaded notched geometries, the analytic solutions for the Stress Concentration Factor (SCF) are found to be directly applicable in only a few cases, namely cases of circular notches and medium aspect ratio elliptical notches aligned with the principle material axes. In general it has been observed that the analytical solutions tend to diverge from the experimental results as the notch aspect ratio approaches a slit or crack, and that the analytic solutions do not perform well, in terms of predicting magnitude and location of maximum stress, in the bias (45º) material orientation. It is possible that the divergence between the elasticity based analytic model and the experimental results is due in part the data analysis techniques employed in this thesis, and recommendations for improvement are made in the subsequent section. In general, it is concluded that the effective SCF is highly-dependent on the material and notch orientation, and that the inhomogeneous nature of this material reduces the effect of notch aspect ratio on the overall stress state in the mesh, particularly in orientations that exhibiting lower coupling between adjacent wires, such as the warp (0º) orientation. For the case of centrally located notches in the experimentally treated biaxially loaded cruciform specimen, the results clearly indicate that the orientation of the notch, the aspect ratio of the notch, as well as

the stretch ratio, are important parameters in accounting for the overall perturbation of the stress field. The results, however, are not conclusive with regards to the effect of these parameters on the exact SCF, and this is owed in part to the specimen geometry, and to the limitations of the data reduction methods used to analyze the DIC results. What is conclusive, however, is the trend of the SCF to be at a maximum when the notch is oriented with one of the principle material orientations, and at a minimum when the notch is at some inclination to the loading axes.

Another important conclusion which can be drawn from this thesis is that, in general, the finite element method is an acceptably accurate tool for modeling this class of materials. In nearly every case, the homogenized orthotropic FE model shows excellent agreement with the experimental DIC strain contours developed from uniaxial and biaxial tensile testing. Based on the simulation results and observations of model behavior, some suggestions can be made regarding the modeling of this class of materials: (1) a high-order in-plane quadrilateral element (such as PLANE82 in ANSYS) should be employed with a thickness option enabled [(0.0035in (0.089mm) in this case], (2) large lateral contractions (roughly equal to the axial extension) should be expected in off-axis material orientations, and care should be taken to assure the boundary conditions do not restrict these contractions, (3) the use of isotropic equivalent representations of the results, i.e., the Von Mises stress, should be avoided, as they generally do not predict maximum locations or values well, and (4) while in smooth cases element size is not observed to affect the results, element size must be strictly controlled (minimized and consistent) in notched regions. Again, deviation is observed for the case of slit type notches, which serves to reinforce the conclusion that this class of materials is not impacted a crack or slit to the same degree as a homogenous plate with equivalent elastic properties. Additionally, the multi-scale FE

modeling effort has shown that the yielding behavior observed on the macro-scale is driven by meso-scale wire plasticity and individual wire failure, it is has been demonstrated that a failure model can be successfully designed around this phenomenon to predict mesh failure.

This principal goal of this thesis is to formulate an approach for characterization of metallic woven wire mesh materials. Based on the results of this work, conclusions regarding the application of this approach to other specifications of this material class can be drawn, and recommendations for experiments and analysis can be made. In order of decreasing importance, the most effective characterization procedures are: (1) uniaxial tensile tests in the principal material orientations, and on the bias, (2) leverage uniaxial tensile test results to formulate material compliance, and plastic behavior, (3) intermediate off-axis tensile tests to confirm orthotropy, (4) Biaxial tensile tests to analyze material yield behavior under in-service conditions, (5) meso-scale FE modeling to analyze wire-level deformation and failure mechanisms, (6) macro-scale FE modeling to exercise material models and expand the test matrix.

7.2 Recommendations for Future Work

While the work presented in this thesis represents a significant contribution to the understanding of the mechanical behavior of metallic micronic woven structures, the overall lack of attention paid to this subject in the literature demands that this work be extended in the future. Based on the progress made in conducting the research presented in this thesis, and considering the challenges encountered, recommendations for the future study of micronic woven wire mesh materials can be made. In general, the following recommendations can be classified as either suggestions for improvement of data acquisition through better load frame and specimen design,

or as areas that have been identified as lacking sufficient development in this thesis for immediate employment by engineers in industry.

Recommendations for Improvement of Experimental Design and Data Analysis

Data Analysis

It is generally observed that the DIC method fails to perform well in regions of singularity at the root of a notch. For this reason, the SCFs produced in this work have been termed near notch SCF values, and are thus not indicative of the maximum values that should be expected at the root of the notch. An alternative data reduction technique is possible, however, that would allow for improved measurement of the SCF associated with a notched geometry using DIC measurements. The proposed method, which has been employed previously to measure fracture mechanics parameters [Mogadpalli and Parameswaran, 2008], involves the semi-empirical derivation of the stress fields in the notched body by using the DIC results to fit the governing equations to the observed data via regression analyis. Thus, DIC data taken from an area away from the notch edge, where this thesis has shown the results to be valid, could be used to extrapolate the state of stress at the notch edge. This method holds similarities to the Hutchinson-Rice-Rosengren (HRR) fields used to predict the state of stress near a plastic crack tip, in that it would involve the numeric solution of known field equations to predict stress values at the notch tip. Future work required to develop this method includes:

- The identification of potential functions which satisfy the boundary conditions of the various problems, thorough analysis and optimization of the correlation procedures, i.e., how many data points are necessary to obtain accurate results.

- Development of software code to perform the two-dimensional regression optimization of the field equations, and development of software code to solve the fourth order differential field equations that would result from such an analysis. The result of these developments would be a robust method for characterizing stress concentrations in this class of materials using DIC strain field data taken away from the notch tip, as well as providing for a mechanism to support quantitative comparison of FEM contours to experimental DIC contours.

Experimental Design Changes

- Modification to the biaxial test frame is necessary to improve the ability for alignment of the test specimen and linkage arms, and to increase the number of potential stretch ratios. Both of these problems can be solved by adding a track mechanism to the biaxial frame, rather than the using the predetermined stretch ratio adjustment holes in the main load plates as shown in Fig. 2.11. Such a tack mechanism would force the alignment of the apposing linkage arms, and allow for increased flexibility in adjustment of the stretch ratio.
- The grip assemblies must be improved such that unwanted lateral constraint at the fixed grips, which causes specimen buckling and out-of-plane deformations, is avoided in off-axis cases. Basset [Bassett and Postle, 1999] has suggested several remedies for this situation, including modifications to the test specimens and modified grips. The outcome of such a modification will be improved off-axis tensile test results, particular in the bias (45º) orientation, where accurate results are critical to the calibration of the Hill yield criterion, and for shear modulus determination.

- Given the desirable simplicity of the uniaxial test specimens employed in this study, as shown in Fig. 2.1, it is more attractive in this case to alter the grip mechanism. Thus, it is recommended that future work be carried out to design roller grips, i.e., grips that will allow for the large transverse contraction of the subject material associated with the bias (45º) material orientation, for use in off-axis tensile tests. This modification will help prevent buckling of the test specimen, and increase the accuracy of the off-axis DIC test results.

Recommendations for Improvement of the Proposed Models

- Future work is needed to develop definitions for the modified Hill criterion parameter terms, I and K, proposed in this thesis, such that experiments capable of defining these terms can be identified. Due to the shear stress and normal stress interaction implied by the addition of these terms, it is theorized that a biaxial tension plus shear test, along with the classical uniaxial and pure shear tests necessary to define the Hill constants, could be used for this purpose. Further development of the modified Hill yield criterion will require rigorous analysis to ensure its stability and convexity in all quadrants, as well as to provide a form that can easily be plotted as a failure envelope for comparison to other well-defined quadratic interaction yield theories such as Tsai-Hill or Tsai-Wu.
- Future work is required to improve the multi-scale failure model based on meso-scale equivalent plastic strain as presented in Section 6.2.3. Primary areas for improvement are in the addition of physical observations, such as wire strain hardening behavior, observed mesh failure modes from SEM fractography, and the effects of crimp interchange, to the model. The proposed constants, which must be defined based on physical observations

such as these, should be globally fit using periodic and symmetric functions of material orientation to reflect the orthotropy of the SS316L woven wire mesh.

- The numerical implementation of this failure theory must be improved via the addition of an adaptive time stepping routine that will enable the numerical solver to automatically bisect load steps that cause the failure theory to be exceeded by too large a margin. This addition will improve crack growth predictions, and lead to improved load drop prediction.
- Future work is needed to investigate the slit notch geometry from a fracture mechanics perspective. It is conceivable that a near field approach similar to the one employed by Mogadpalli and colleague [Mogadpalli and Parameswaran, 2008] could be employed to experimentally determine the stress intensity factors associated with the slit notches in both uniaxial and biaxial cases for the SS316L woven wire mesh material. This would be particularly useful in the weft (90º) material orientation, where the material is observed to fracture in a brittle manner.

REFERENCES

Amer, M.S., and Schadler, L.S., "Stress Concentration Phenomenon in Graphite/Epoxy Composites: Tension/Compression Effects," *Composites Science and Technology*. Vol. 57, pp. 1129-1137, 1997.

ANSYS Academic Research, Release 14.5, Help System, Command Reference Guide, 2012.

ASM International, 2000. *ASM Handbook Vol. 8: Mechanical Testing and Evaluation*, ASM International, Materials Park, OH.

ASTM Standard E8, 2004, "Standard Test Methods for Tension Testing of Metallic Materials," ASTM International, West Conshohocken, PA.

ASTM Standard E2016, 2006, "Standard Specification for Industrial Woven Wire Cloth," ASTM International, West Conshohocken, PA.

Bassett, R.J., and Postle, R., "Experimental Methods for Measuring Fabric Mechanical Properties: A Review and Analysis," *Textile Research Journal.* Vol.11, No. 69, pp. 866-875, 1999.

Bhatnagar, N., Bhardwaj, R., Selvakumar, P., and Brieu., M., "Development of a Biaxial Test Fixture for Reinforced Thermoplastic Composites," *Polymer Testing.* Vol. 26, pp. 154-161, 2007.

Blandford, R.K., Morton, D.K., Snow, S.D., and Rahl, T.E., "Tensile Stress-Strain Results for 304L and 316L Stainless Steel Plate at Temperature," *The Proceedings of the 2007 ASME Pressure Vessels and Piping Conference*. San Antonio, Texas, July 20-26, 2007.

Boubaker, B.B., Assidi, M., and Ganghoffer, J.F., "Evaluation of Poisson's Ratio of Textiles from Mesoscopic Models," *International Journal of Material Forming*. Vol. 3, Suppl. 1, pp. 81-84, 2010.

Carter, B., and Brown, T.R., "Handbook of Operational Amplifier Applications," *Texas Instruments Application Report SBOA092A*. 2001.

Cavallaro, P., Sadegh, A., and Quigley, C., "Decrimping Behavior of Uncoated Plain-woven Fabrics Subjected to Combined Biaxial Tension and Shear Stresses," *Textile Research Journal.* Vol. 77, No. 6, pp. 404-416, 2007.

Chen, S., Ding, X., and Yi, H., "On the Anisotropic Tensile Behaviors of Flexible Polyvinyl Chloride-coated Fabrics," *Textile Research Journal,* Vol. 77, No. 6, pp. 369-374, 2007.

Chiang, C., "On Stress Concentration Factors in Orthotropic Materials," *Journal of the Chinese Institute of Engineers*. Vol. 22, No. 3, pp. 301-305, 1999.

Choi, H.J., "The Problem for Bonded Half-Planes Containing a Crack at an Arbitrary Angle to the Graded Interfacial Zone," *International Journal of Solids and Structures*. Vol. 38, pp. 6559-6588, 2001.

Chu, T.C., Ranson, W.F., Sutton, M.A., and Peters, W.H., "Applications of Digital Image Correlation Techniques to Experimental Mechanics," *Experimental Mechanics*. Vol. 25, No. 3, pp. 232-244, 1985.

Gibson, R. F., 2007. *Principles of Composite Material Mechanics*, CRC Press, Boca Raton. pp. 47-81.

Hannon, A., and Tieran, P., "A Review of Planar Biaxial Test Systems for Sheet Metal," *Journal of Material Processing Technology.* Vol. 198, pp. 1 - 13, 2008.

Hill, R., 1956. *The Mathematical Theory of Plasticity*, Oxford University Press, London. pp. 318-325.

Hursa, A., Rolich, T., and Ercegović Razić, S., "Determining Pseudo Poisson's Ratio of Woven Fabric with a Digital Image Correlation Method," *Textile Research Journal*. Vol. 79, No. 17, pp. 1588-1598, 2009.

Juan, L., Shi, Y., and Wang, R., "Effect of Working Temperature on the Resistance Characteristics of a Pleated Stainless Steel Woven Filter," *Chinese Journal of Chemical Engineering*. Vol. 17, No. 6, pp. 949-954, 2009.

Kawabata, S., Niwa, M., and Kawai, H., "The Finite Deformation Theories of Plain Weave Fabric, Part 1: The Biaxial-deformation Theory," *Journal of the Textile Institute.* Vol. 64, pp. 21-46, 1964.

King, M., Jearanaisilawong, P., and Socrate, S., "A Continuum Constitutive Model for the Mechanical Behavior of Woven Fabrics," *International Journal of Solids and Structures.* Vol. 42, pp. 3867-3896, 2005.

Kraft, S., and Gordon, A.P., "Yield Characteristics of a Twill Dutch Woven Wire Mesh via Experiments and Modeling," *Journal of Applied Mechanics.* In Press.

Kraft, S., and Gordon, A.P., "Characterization of the Mechanical Behavior of a Metallic Fiber Woven Structure." *Textile Research Journal*. Vol. 81, No. 12, pp. 1249-1272, 2011.

Kraft, S., Bai, Y., Moslehy, F., and Gordon, A.P., "Characterization of the Orthotropic Elastic Constants of a Micronic Woven Wire Mesh via Digital Image Correlation," *Experimental Mechanics.* Pending.

Lekhnitskii, S.G., 1968, *Anisotropic Plates*, Routledge, London.

Lomov, S.V., Willems, A., Verpoest, I., and Zhu, Y., "Picture Frame Test of Woven Composite Reinforcements with a Full-Field Strain Registration," *Textile Research Journal*. Vol. 76, No. 3, pp. 243-252, 2006.

Makinde, A., Thibodeau, L., Neale, K.W., "Development of an Apparatus for Biaxial Testing Using Cruciform Specimens." *Experimental Mechanics*. Vol. 32, No. 2, pp. 138-144, 1992.

Meuwissen, M.H.H., "Yield Criteria for Anisotropic Elasto-Plastic Materials," *Internal Report WFW 95.152.* 1995.

Mogadpalli, G.P., and Parameswaran, V., "Determination of Stress Intensity Factor for Cracks in Orthotropic Composite Materials using Digital Image Correlation," *Strain*. Vol. 44, pp. 446-452, 2008.

Peters, W.H., and Ranson, W.F., "Digital Imaging Techniques in Experimental Stress Analysis," *Optical Engineering*. Vol. 21, No. 3, pp. 427-432, 1982.

Pierce, F.T., "The Geometry of Cloth Structure," *Journal of the Textile Institute.* Vol. 28, pp. 45-96, 1936.

Pilkey, W.D., 1997, *Peterson's Stress Concentration Factors 2nd Edition*, John Wiley and Sons, Inc, New York.

Probedrya, B.E., and Gorbachev, V.I., "Stress and Strain Concentration in Composite Materials," *The proceedings of the Fifth All-Union Conference on the Mechanics of Polymer and Composite Materials.* Riga, October, 1983.

Reddy, J.N., 2008. *An Introduction to Continuum Mechanics*, Cambridge University Press, New York, NY.

Saliklis, E.P., and Falk, R.H., "Correlating Off-Axis Tension Tests to Shear Modulus of Wood-Based Panels," *Journal of Structural Engineering*. Vol. 126, No. 5, pp. 621-625, 2000.

Shukla, A., and Dally, J.W., 2010. *Experimental Solid Mechanics*, College House Enterprises, Knoxville, TN.

Sih, G.C., Paris, P.C., and Erdogan, F., "Crack-Tip Stress Intensity Factors for Plane Extension and Plate Bending Problems," *Journal of Applied Mechanics*. Vol. 29, pp. 306-312, 1962.

Smits, A., Van Hemelrijck, D.V., Philippidis, T.P., and Cardon, A., "Design of a Cruciform Specimen for Biaxial Testing of Fiber Reinforced Composite Structures." *Composite Science and Technology.* Vol. 66, pp. 964-975, 2006.

Sun, H., Pan, N., and Postle, R., "On the Poisson's Ratios of a Woven Fabric." *Composite Structures*, Vol. 68, pp. 505-510, 2004.

Tan, S.C., "Finite-Width Correction Factors for Anisotropic Plate Containing a Central Opening," *Journal of Composite Materials.* Vol. 22, No. 11, pp. 1080-1018, 1988.

Tarfaoui, M., and Drean, J. Y., "Predicting the Stress-Strain Behavior of Woven Fabrics Using the Finite Element Method," *Textile Research Journal.* Vol. 71, No. 9, pp. 790-795, 2001.

Timoshenko, S.P., and Goodier, J.N., 1969, *Theory of Elasticity*, McGraw-Hill, New York.

Whitney, J.M., and Nuismer, R.J., "Stress Fracture Criteria for Laminated Composites Containing Stress Concentrations," *Journal of Composite Materials.* Vol. 8, No. 3, pp. 253-265, 1974.

Zhang, Y., Merrill, M.D., and Logan, B.E., "The Use and Optimization of Stainless Steel Mesh Cathodes in Microbial Electrolysis Cells," *International Journal of Hydrogen Energy*. Vol. 35, pp. 12020 - 12028, 2010.

APPENDIX A
DERIVATION OF THE STRESS STATE IN A UNIAXIALLY LOADED INFINITE ORTHOTROPIC PLATE WITH A CENTRAL ELLIPTICAL NOTCH

As the stress state is dependent on the material properties, we define them here:

$E_w := 3.0910^6 psi$ $E_s := 2.8810^6 psi$ $\nu_{ws} := 0.398$ $\nu_{sw} := 0.312$ $G_{ws} := 3.110^4 psi$

To allow calculation of the local material properties, we define them using the transformation equations:

$\varphi := \frac{\pi}{2}$ where φ is the material orientation

$$E_a := \left[\frac{1}{E_w}\cdot(\cos(\varphi))^4 + \left(\frac{1}{G_{ws}} - \frac{2\cdot\nu_{ws}}{E_w}\right)\cdot(\sin(\varphi))^2\cdot(\cos(\varphi))^2 + \frac{1}{E_s}\cdot(\sin(\varphi))^4\right]^{-1}$$

$$E_t := \left[\frac{1}{E_w}\cdot(\sin(\varphi))^4 + \left(\frac{1}{G_{ws}} - \frac{2\cdot\nu_{ws}}{E_w}\right)\cdot(\sin(\varphi))^2\cdot(\cos(\varphi))^2 + \frac{1}{E_s}\cdot(\cos(\varphi))^4\right]^{-1}$$

$$G_{at} := \left[\frac{1}{G_{ws}}\cdot\left[(\sin(\varphi))^4 + (\cos(\varphi))^4\right] + 4\cdot\left(\frac{1}{E_w} + \frac{1}{E_s} + \frac{2\nu_{ws}}{E_w} - \frac{1}{2\cdot G_{ws}}\right)\cdot(\sin(\varphi))^2\cdot(\cos(\varphi))^2\right]^{-1}$$

$$\nu_{at} := E_a\cdot\left[\frac{\nu_{ws}}{E_w}\cdot\left[(\sin(\varphi))^4 + (\cos(\varphi))^4\right] - \left(\frac{1}{E_s} + \frac{1}{E_w} - \frac{1}{G_{ws}}\right)\cdot(\sin(\varphi))^2\cdot(\cos(\varphi))^2\right]$$

Now, we can use the local material properties to solve the characteristic equation for μ , which is a measure of the anisotropy of the material:

$$f(\mu) = \frac{\mu^4}{E_1} + \left(\frac{1}{G} - \frac{2\nu_{12}}{E_1}\right)\mu^2 + \frac{1}{E_2}$$

we place the coefficients into a vector to allow mathcad to find the roots using the LaGuerre method

$$C := \begin{bmatrix} \frac{1}{E_a} \\ 0 \\ \left(\frac{1}{G_{at}} - \frac{2\nu_{at}}{E_a}\right) \\ 0 \\ \frac{1}{E_t} \end{bmatrix}$$

$$\text{polyroots}(C) = \begin{pmatrix} -9.943i \\ 9.943i \\ -0.104i \\ 0.104i \end{pmatrix}$$

The positive roots are taken for analysis

$\mu_1 := 9.943$ $\mu_2 := 0.104$

Now, apply the boundary conditions and define the geometry of the notch

$P := 228psi$ Where *P* is a remotely applied stress

$a := .125in$ *a* is the major axis of the elliptical notch

$b := \frac{a}{2}$ *b* is the minor axis of the elliptical notch

$\phi := 0$ ϕ is the notch orientation

Next, we define a function that defines the notch edge for all angles along the open contour:

$$l(\theta) := \sqrt{a^2(\sin(\theta))^2 + b^2(\cos(\theta))^2}$$

Now, we consider the terms proposed by Lekhnitskii that help form the potential functions that solve this problem:

$$\zeta_1(z_1) := \frac{z_1 + \sqrt{z_1^2 - a^2 - \mu_1^2 b^2}}{a - i\cdot\mu_1\cdot b} \qquad \zeta_2(z_2) := \frac{z_2 + \sqrt{z_2^2 - a^2 - \mu_2^2 b^2}}{a - i\cdot\mu_2\cdot b}$$

$$\alpha_1 := \frac{-P\cdot\sin(\phi)}{2}\cdot(a\cdot\sin(\phi) - i\cdot b\cdot\cos(\phi)) \qquad \beta_1 := \frac{P\cdot\cos(\phi)}{2}\cdot(a\cdot\sin(\phi) - i\cdot b\cdot\cos(\phi))$$

Where the ζ terms are part of the first term of an infinite series solution that forms the potential function, and the α and β terms are related to the boundary conditions of the problem

Finally, we can define the approximate complex potential functions as:

$$\Phi_1(z_1) := \frac{\beta_1 - \mu_2 \cdot \alpha_1}{\mu_1 - \mu_2} \cdot \frac{1}{\zeta_1(z_1)} \qquad \Phi_2(z_2) := \frac{-\beta_1 - \mu_1 \cdot \alpha_1}{\mu_1 - \mu_2} \cdot \frac{1}{\zeta_2(z_2)}$$

Taking the derivative of the complex potentials we get:

$$\frac{d}{dz_1}(\Phi_1(z_1)) \rightarrow \frac{0.5405394031405630653\text{in}^2 \cdot \text{psi} \cdot \left(\frac{z_1}{\sqrt{z_1^2 + 0.37055956640625\text{in}^2}} + 1 \right)}{\left(z_1 + \sqrt{z_1^2 + 0.37055956640625\text{in}^2} \right)^2}$$

$$\frac{d}{dz_2}(\Phi_2(z_2)) \rightarrow -\frac{0.0952269031405630653\text{in}^2 \cdot \text{psi} \cdot \left(\frac{z_2}{\sqrt{z_2^2 + -0.01558275\text{in}^2}} + 1 \right)}{\left(z_2 + \sqrt{z_2^2 + -0.01558275\text{in}^2} \right)^2}$$

To facilitate plotting of the stress distribution, and to allow calculation of the Cartesian stress terms, we define the following vectors:

$$i := 0, 1 .. 99$$

$$\theta_i := 0 + \frac{.0314}{2} \cdot i$$

$$x := a \cdot \cos(\theta) \qquad y := b \cdot \sin(\theta)$$

$$z_1 := x + \mu_1 \cdot y \qquad z_2 := x + \mu_2 \cdot y$$

We rewrite the potential function derivatives as the following variables:

$$\Phi_{1prime} := \frac{0.5405394031405630653\text{in}^2 \cdot \text{psi} \cdot \left(\frac{z_1}{\sqrt{z_1^2 + 0.3705595664062\text{in}^2}} + 1 \right)}{\left(z_1 + \sqrt{z_1^2 + 0.3705595664062\text{in}^2} \right)^2}$$

$$\Phi_{2prime} := -\frac{0.0952269031405630653\text{in}^2 \cdot \text{psi} \cdot \left(\frac{z_2}{\sqrt{z_2^2 + -0.0155827\text{in}^2}} + 1 \right)}{\left(z_2 + \sqrt{z_2^2 + -0.0155827\text{in}^2} \right)^2}$$

And finally we can write the Cartesian stress terms from their well known relation to the complex potential functions:

$$\sigma_{y_i} := 2 \cdot \text{Re}\left(\Phi_{1prime_i} + \Phi_{2prime_i} \right)$$

$$\sigma_{x_i} := 2 \cdot \text{Re}\left(\mu_1^2 \cdot \Phi_{1prime_i} + \mu_2^2 \cdot \Phi_{2prime_i} \right)$$

$$\tau_{xy_i} := -2 \cdot \text{Re}\left(\mu_1 \cdot \Phi_{1prime_i} + \mu_2 \cdot \Phi_{2prime_i} \right)$$

And conversion to the polar coordinate system allows for plotting of the theta component of stress:

$$\sigma_{\theta_i} := \sigma_{y_i} \cdot \cos\left(\theta_i\right)^2 + \sigma_{x_i} \cdot \sin\left(\theta_i\right)^2 - 2 \cdot \tau_{xy_i} \cdot \sin\left(\theta_i\right) \cdot \cos\left(\theta_i\right)$$

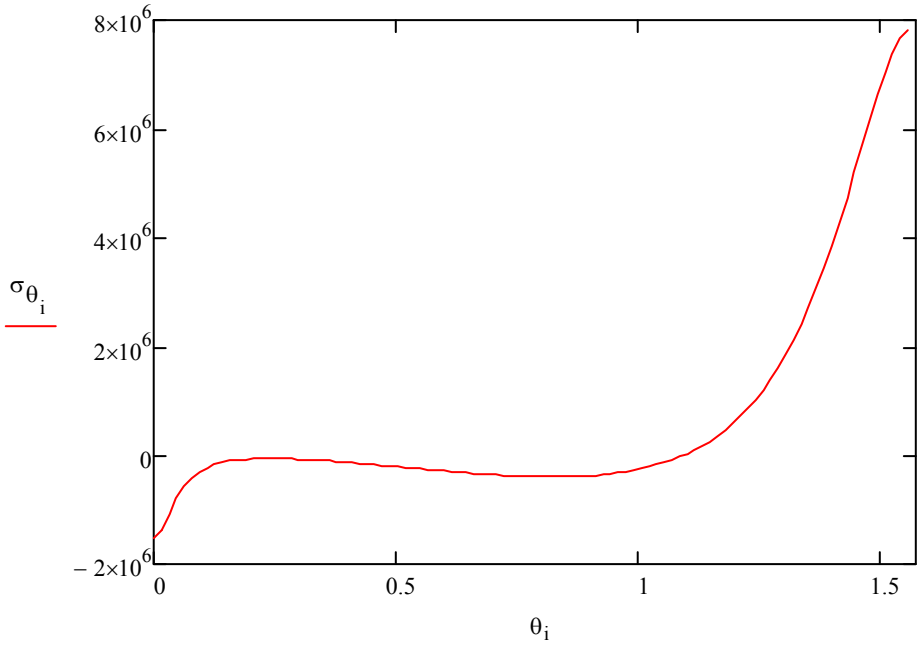
8×10^6
6×10^6
4×10^6
2×10^6
0
− 2×10^6
σθi
0
0.5
1
1.5
θi

APPENDIX B
ANSYS APDL CODES

List of ANSYS APDL Codes

The Uniaxial Macro-Scale FE Model:

```
!=============================================================5:07 PM 12/13/2012
!
!MOMRG-UCF-MAE
!ANSYS INPUT DECK - ORTHOTROPIC MODEL NOTCHED SPECIMEN
!STEVEN M. KRAFT
!
!VERSION 3.0
!!!!!!!!!!!!!!!!!!!!!!!!!!!!!!!!!!!!!!!!!!!!!!!!!!!!!!!!!!!!!!!!!!!!!!!!!!!!!!!!!!!!!!!!!!!!!!!!!!!!!!!!!!!!!!!!!!!!!!!!!!!!!!!!!!!!


finish
/clear
/PREP7

!=====define the parameters for the geometry and material orientation=====================

theta=45           !material orientation  with respect to the weft axis
ALPHA=0         !Notch orientation with respect to the loading axis
w=.75              !width of a standard specimen
l=1.25            !length of a standard specimen
r=.125            !circle notch radius
a=.125/2          !major radius of ellipse
b=.125            !minor radius of ellipse

!=======define Hill parameter values================================================

F=0.25
G=3.17
H=0.75
N=38.5
sy_max=22.8e3

!====set initial, final, and increment values for the parameters to be varied==================

theta_ini=0
theta_inc=15.0
theta_fin=90

!r_ini=.0625
!r_inc=.0625
!r_fin=.25

!a_ini=.0625
```

```
!a_inc=.0625
!a_fin=.5

!b_ini=.625
!b_inc=.0625
!b_fin=.25

j=1

!====Do Loop on the parameter of interest=======================================

*DO,theta,theta_ini,theta_fin,theta_inc
PARSAV,,parameters,txt                    !Save all parameters to database
*IF,j,GT,1,THEN
FINISH
/CLEAR
/PREP7
PARRESS,,parameters,txt                   !Read the paramters from the database
*ENDIF
FINISH

!=====File Naming Information================
/filename, uniaxial_EllipseNotch_ortho_param
/title, uniaxial_EllipseNotch_ortho_param

/PREP7

!define the geometry=================================================

BLC4,0,0,w,l,0                            !generates a rectangular area
CYL4,w/2,l/2,r                            !generates a circle for the notch
ARSCALE,2,2,1,(a/r),(b/r),1,0,1           !generates an ellipse if a and b are not equal to r
AGEN,2,3,,,(r+(r/2)),,,,1
ASEL,S,,,2,2,1,
ADELE,ALL
Local,22,1,w/2,l/2,0,0,0,0,,              !Create a local polar coordinate system to rotate ellipse
csys,22
ASEL,ALL
APLOT
AGEN,2,4, , , ,-ALPHA , , ,1              !Rotate ellipse by alpha
ASEL,S,,,3,4,1,
ADELE,ALL
ASEL,ALL
ASBA,1,2                          !generate notched geometry with symmetry - dimensions match
                                  !single wide specimen quadrant
```

```
!=========================================================================

!define a local system to transform material properties into desired orientation

local,11,0,0,0,0,0,theta,0,0,,        !the material is rotated into the theta orientation

!**NOTE**
!**the 0 orientation is considered the weft material direction in this code**

!=========================================================================

!Element definition

ET, 1, plane82
Keyopt,1,3,3
Keyopt,1,5,0
Keypot,1,6,0
R,1,.0035,

ESYS,11                              ! the local system is selected for all defined elements

!=========================================================================

!define the material model

MPTEMP,,,,,,,,
MPTEMP,1,0
MPDATA,EX,1,,3.09e6
MPDATA,EY,1,,2.88e6
MPDATA,PRXY,1,,.398
MPDATA,GXY,1,,.031e6

!define plasticity model - ANISO for now

!****NOTE*********************************************
!Material plasticity should be commented out for SCF determination*
!************************************************** *
!TB,ANISO                            !Anisotropic plasticity is employed
!TBTEMP,0

TSyx=10.29e3
TSyy=1.93*10.29e3
TSyxy=0.7*0.81*(10.29e3/sqrt(2))
CSyx=TSyx
```

```
CSyy=TSyy
CSyxy=TSyxy
TMx=2.8e5
TMy=7.0e5
TMps=.015e6

!TBDATA,1,TSyx,TSyy,TSyy,TMx,TMy,TMy
!TBDATA,7,CSyx,CSyy,CSyy,TMx,TMy,TMy
!TBDATA,13,TSyxy,TSyxy,TSyxy,TMps,TMps,TMps      !yield strengths and tangent moduli
are defined in data table


!=====================================================================

!Mesh the geometry using automatic meshing

ASEL,ALL

!Set the automatic meshing parameters

MSHAPE,0,2D
MSHKEY,0
smrtsize, 3
AMESH,ALL

!refine the mesh at the notch location

lrefine, 17,20,1,2

!=====================================================================

!switch back to the global system to define boundary conditions

csys,0

!====Define Fixed Condition on Bottom Edge=======

lsel,s,line,,1
nsll,s,1
D,all,all,0
nsel,all

!====Define Force Condition on Top Edge==========

lsel,s,line,,3
```

```
nsll,s,1
*get,bnum2,node,,count
F,all,fy,(.554/bnum2),,

nsel,all

FINISH

!=========================================================================

!Enter the solver

/solu

!we will apply a time step to ramp the mechanical load

antype,0                        !select static analysis type
nropt,auto                      !newton rhapson solver is set to automatic
lnsrch,auto                     !line search options are set to automatic
time, 1                         !time at end of load step
deltime,.1,.01,1                !set time increment
autots,on                       !toggle on/off auto time stepping
outres,esol,all                 !save element solutions for all time steps in the database
outres,rsol,all                 !save force reactions for all time steps in the database

solve                           !solve the problem

FINISH

!=========================================================================

!enter post-processing module

/post1


!!!!!!!!!!!!!!!!!!!!!!!!!!!!!!!!
!HILL CRITERION CALCS!
!!!!!!!!!!!!!!!!!!!!!!!!!!!!!!!!

etable,stress_x,s,x
etable,stress_y,s,y             !put the Cartesian stress values in element tables
etable,shear_xy,s,xy
```

```
!generate a dummy element table to be filled  with the hill values later
etable,HILL,s,1

!get the total number of elements in the model
*get,numelem,ELEM,,COUNT

!dimension arrays to be filled with the element table values
*dim,stressx,array,numelem,1,,,,
*dim,stressy,array,numelem,1,,,,
*dim,stressxy,array,numelem,1,,,,

!fill arrays with the stress components for future operations
 *vget,stressx,elem,1,etab,stress_x
*vget,stressy,elem,1,etab,stress_y
*vget,stressxy,elem,1,etab,shear_xy

!normalize the stress components by the maximum yield stress
*voper,sx_norm,stressx,div,sy_max,,
*voper,sy_norm,stressy,div,sy_max,,
*voper,sxy_norm,stressxy,div,sy_max,,

!square the stress components
*voper,stress_x_2,sx_norm,mult,sx_norm,,
*voper,stress_x_y,sx_norm,mult,sy_norm,,
*voper,stressxy_2,sxy_norm,mult,sxy_norm,,
*voper,stress_y_2,sy_norm,mult,sy_norm,,

!calculate the terms in hill criterion
*voper,hill_1,stress_x_2,mult,(G+H),,
*Voper,hill_2,stress_x_y,mult,(2*H),,
*voper,hill_3,stress_y_2,mult,(F+H),,
*voper,hill_4,stressxy_2,mult,(2*N),,

!hill_tot is the hill criterion value
*voper,hill_5,hill_1,sub,hill_2,,
*voper,hill_6,hill_3,add,hill_4,,
*voper,hill_tot,hill_5,add,hill_6,,

!place the hill criterion value into an element table
*do,k,1,(numelem),1
detab,k,HILL,hill_tot(k,1,1)
*enddo

 !plot the hill criterion values, averaged over the element and save an image
pletab,HILL,avg
```

```
/CONT,1,8,AUTO
/replot

/SHOW,TIFF,,0
TIFF,COMP,1
TIFF,ORIENT,HORIZ
TIFF,COLOR,2
TIFF,TMOD,1
/GFILE,800,
/CMAP,_TEMPCMAP_,CMP,,SAVE
/RGB,INDEX,100,100,100,0
/RGB,INDEX,0,0,0,15
/REPLOT
/CMAP,_TEMPCMAP_,CMP
/DELETE,_TEMPCMAP_,CMP
/SHOW,CLOSE
/DEVICE,VECTOR,0

!!!!!!!!!!!!!!!!!!!!!!!!!!!!!!!!!!!!!!!!!!!!!!!!!!!!!!!!!
!Sigma Theta around Opening Contour Results!
!!!!!!!!!!!!!!!!!!!!!!!!!!!!!!!!!!!!!!!!!!!!!!!!!!!!!!!!!

!Change the results coordinate system to polar
rsys,1

LSEL,S,LINE,,17,20,1
NSLL,S,1

*GET,numberOfNodes,NODE,,COUNT                  !Get the number of nodes
*GET,nodeNumber,NODE,,NUM,MIN                   !Get the minimum node number
PATH,CONTOUR,numberofnodes-1,6,1

!Generate the path along the opening contour
*DO,jj,1,(numberofnodes-1),1
nodenumber=NDNEXT(nodenumber)
PPATH,jj,nodenumber,,,,
*ENDDO

 !Plot the Theta Component of stress onto the path
PDEF,STRESSTH,S,Y,AVG

/output,stressth_%theta%_%alpha%_,txt           !Output the path to a text file
PRPATH,XG,YG,STRESSTH
/output
```

```
j=j+1
FINISH
*ENDDO
!Exit the routine
```

The Cruciform Biaxial Macro-Scale FE Model

```
!=====================================================10:48 AM 3/9/2013
!MOMRG-UCF-MAE
!ANSYS INPUT DECK - BIAXIAL CRUCIFORM ORTHOTROPIC MODEL NOTCHED
SPECIMEN
!STEVEN M. KRAFT
!
!VERSION 2.0
!!!!!!!!!!!!!!!!!!!!!!!!!!!!!!!!!!!!!!!!!!!!!!!!!!!!!!!!!!!!!!!!!!!!!!!!!!!!!!!!!!!!!!!!!!!!!!!!!!!!

FINISH
/CLEAR
/Prep7

!Define the model Parameters==========================================
*SET,d,.8
*SET,l1,1.5
*SET,l2,1.5
*SET,r,0.18
*SET,pi,3.14159265
*AFUN, RAD
*SET,rr,.125
*SET,aa,.125
*SET,bb,.125/18
theta=0

!Set parameters and increments for do loops=================================
ALPHA_INI=0
ALPHA_FIN=90
ALPHA_INC=15

a_ini=1
a_fin=1.2
a_inc=.2

!==========================================================================

!define Hill parameter values
F=0.25
G=3.17
H=-0.75
N=38.5
sy_max=22.8e3
!==========================================================================
```

```
!Nested Do loops simulate the various biaxial loading ratios and notch orientations
j=1
*DO,a,a_ini,a_fin,a_inc
*DO,ALPHA,ALPHA_INI,ALPHA_FIN,ALPHA_INC
PARSAV,,parameters,txt
*IF,j,GT,1,THEN
FINISH
/CLEAR
/PREP7
PARRESS,,parameters,txt
*ENDIF
finish

!=====File Naming Information==================
/filename, Cruciform_Specimen_notched
/title, Cruciform_Specimen_notched

/prep7

!define the geometry=========================================================
K,1,-L1,0,0,
K,2,-L1,d/2,0,
K,3,-((d/2)+r),d/2,0,
K,4,-(d/2),(d/2)+r,0,
K,5,-(d/2),l2,0,
K,6,0,l2,0,
k,7,-(d/2),(d/2),0,
k,8,0,0,0

CIRCLE,7,r,,3,270,

!generate lines connecting key points

LSTR,      1,      2
LSTR,      2,      9
LSTR,      12,      5
LSTR,      5,      6
LSTR,      6,      8
LSTR,      8,      1

!define the area to be meshed

AL, all
```

```
!generate a circle for the notch
CYL4,0,0,rr

!generate an ellipse if a and b are not equal to r
ARSCALE,2,2,1,(aa/rr),(bb/rr),1,0,1,1

!Define Local polar coordinate system for notch rotation
Local,22,1,w/2,l/2,0,0,0,0,,
csys,22
ASEL,ALL

!Rotate the notch by alpha
AGEN,2,2, , , ,-ALPHA , , ,1,1
ASEL,S,AREA,,2
LSEL,S,EXT,
LSEL,ALL
ASEL,ALL
ASBA,1,2,SEPO

!generate notched geometry with symmetry - dimensions match single wide specimen quadrant


!=====================================================================

!define a local system to transform material properties into desired orientation

local,11,0,0,0,0,theta,0,0,,        ! the material is rotated into the theta orientation

!**NOTE**
!**the 0 orientation is considered the weft material direction in this code**

!=====================================================================

!Mesh Parameters=====================================================

ET,1,plane82
KEYOPT,1,3,0
KEYOPT,1,5,0
KEYOPT,1,6,0

ESYS,11                             ! the local system is selected for all defined elements

!define material model==============================================

MPTEMP,,,,,,,,
```

```
MPTEMP,1,0
MPDATA,EX,1,,3.09e6
MPDATA,EY,1,,2.88e6
MPDATA,PRXY,1,,.398
MPDATA,GXY,1,,.031e6

!define plasticity model - ANISO for now

!****NOTE*********************************************
!Material plasticity should be commented out for SCF determination*
!*****************************************************

!TB,ANISO                        !Anisotropic plasticity is employed
!TBTEMP,0

TSyx=10.29e3
TSyy=1.93*10.29e3
TSyxy=0.7*0.81*(10.29e3/sqrt(2))
CSyx=TSyx
CSyy=TSyy
CSyxy=TSyxy
TMx=2.8e5
TMy=7.0e5
TMps=.015e6

!yield strengths and tangent moduli are defined in data table
!TBDATA,1,TSyx,TSyy,TSyy,TMx,TMy,TMy
!TBDATA,7,CSyx,CSyy,CSyy,TMx,TMy,TMy
!TBDATA,13,TSyxy,TSyxy,TSyxy,TMps,TMps,TMps

!mesh the geometry and boundary conditions==================================

ASEL,ALL
MSHAPE,1,2D
MSHKEY,0
smrtsize, 2

!If the notch is rotated, the geometry lables will change. This is handled with IF, THEN logic:

*IF,ALPHA,EQ,0,OR,ALPHA,EQ,90,THEN

lesize,21,0,0,750
AMESH,ALL
LSEL,S,LINE,,21
CM,NOTCH,LINE
```

```
LSEL,ALL
LREFINE, 14,14,1,1                          ! mesh is refined near the Fillet

!apply the boundary conditions

csys,0

lsel,s,line,,20
nsll,s,1
D,all,uy,0
nsel,all

lsel,s,line,,19
nsll,s,1
D,all,ux,0
nsel,all

lsel,s,line,,15
nsll,s,1
*get,bnum,node,,count
f,all,fX,-(10/(4*bnum)),,
nsel,all

lsel,s,line,,18
nsll,s,1
*get,bnum,node,,count
f,all,fY,(a*10/(4*bnum)),,
nsel,all

!apply component names to the boundary condition lines for later use

lsel,s,line,,15
cm,boundryx,line
lsel,s,line,,18
cm,boundryy,line

*ELSEIF,ALPHA,NE,0,OR,ALPHA,NE,90,THEN

lesize,15,0,0,700
amesh,all
lsel,s,line,,15
cm,notch,line
lsel,all
lrefine, 14,14,1,1                          ! mesh is refined near the Fillet
```

```
!apply the boundry conditions

csys,0
lsel,s,line,,21
nsll,s,1
D,all,uy,0
nsel,all

lsel,s,line,,20
nsll,s,1
D,all,ux,0
nsel,all

lsel,s,line,,16
nsll,s,1
*get,bnum,node,,count
f,all,fX,-(10/(4*bnum)),,
nsel,all

lsel,s,line,,19
nsll,s,1
*get,bnum,node,,count
f,all,fY,(a*10/(4*bnum)),,
nsel,all

!apply component names to the boundary conditions for later reference

lsel,s,line,,16
cm,boundryx,line
lsel,s,line,,19
cm,boundryy,line

*ENDIF

lsel,all

finish

!=====================================================================

!Enter the solver

/solu

!we will apply a time step to ramp the mechanical load
```

```
antype,0                        !select static analysis type
nropt,auto                      !newton rhapson solver is set to automatic
lnsrch,auto                     !line search options are set to automatic
time, 1                         !time at end of load step
deltime,.1,.01,1                !set time increment
autots,on                       !toggle on/off auto time stepping
outres,esol,all                 !save element solutions for all time steps in the database
outres,rsol,all                 !save force reactions for all time steps in the database

solve                           !solve the problem

FINISH

!=====================================================================

!enter the general post processor

/post1

!!!!!!!!!!!!!!!!!!!!!!!!!!!!!!!!
!HILL CRITERION CALCS!
!!!!!!!!!!!!!!!!!!!!!!!!!!!!!!!!

etable,stress_x,s,x
etable,stress_y,s,y             !put the Cartesian stress values in element tables
etable,shear_xy,s,xy


!generate a dummy element table to be filled  with the hill values later
etable,HILL,s,1

!get the total number of elements in the model
*get,numelem,ELEM,,COUNT

!dimension arrays to be filled with the element table values
*dim,stressx,array,numelem,1,,,,
*dim,stressy,array,numelem,1,,,,
*dim,stressxy,array,numelem,1,,,,

!fill arrays with the stress components for future operations
 *vget,stressx,elem,1,etab,stress_x
*vget,stressy,elem,1,etab,stress_y
*vget,stressxy,elem,1,etab,shear_xy
```

```
!normalize the stress components by the maximum yield stress
*voper,sx_norm,stressx,div,sy_max,,
*voper,sy_norm,stressy,div,sy_max,,
*voper,sxy_norm,stressxy,div,sy_max,,

!square the stress components
*voper,stress_x_2,sx_norm,mult,sx_norm,,
*voper,stress_x_y,sx_norm,mult,sy_norm,,
*voper,stressxy_2,sxy_norm,mult,sxy_norm,,
*voper,stress_y_2,sy_norm,mult,sy_norm,,

!calculate the terms in hill criterion
*voper,hill_1,stress_x_2,mult,(G+H),,
*Voper,hill_2,stress_x_y,mult,(2*H),,
*voper,hill_3,stress_y_2,mult,(F+H),,
*voper,hill_4,stressxy_2,mult,(2*N),,

!hill_tot is the hill criterion value
*voper,hill_5,hill_1,sub,hill_2,,
*voper,hill_6,hill_3,add,hill_4,,
*voper,hill_tot,hill_5,add,hill_6,,

!place the hill criterion value into an element table
*do,k,1,(numelem),1
detab,k,HILL,hill_tot(k,1,1)
*enddo

 !plot the hill criterion values, averaged over the element and save an image
pletab,HILL,avg
/CONT,1,8,AUTO
/replot
/SHOW,TIFF,,0
TIFF,COMP,1
TIFF,ORIENT,HORIZ
TIFF,COLOR,2
TIFF,TMOD,1
/GFILE,800,
/CMAP,_TEMPCMAP_,CMP,,SAVE
/RGB,INDEX,100,100,100,0
/RGB,INDEX,0,0,0,15
/REPLOT
/CMAP,_TEMPCMAP_,CMP
/DELETE,_TEMPCMAP_,CMP
/SHOW,CLOSE
/DEVICE,VECTOR,0
```

```
!!!!!!!!!!!!!!!!!!!!!!!!!!!!!!!!!!!!!!!!!!!!!!!!!!!!!!!!
!Sigma Theta around Opening Contour Results!
!!!!!!!!!!!!!!!!!!!!!!!!!!!!!!!!!!!!!!!!!!!!!!!!!!!!!!!!

!The results coordinate system is Cartesian
rsys,0

cmsel,s,notch,line                                  !select the notch line component

nsll,s,1

*GET,numberOfNodes,NODE,,COUNT                      !Get the number of nodes
*GET,nodeNumber,NODE,,NUM,MIN                       !Get the minimum node number

!Generate the path along the opening contour
PATH,CONTOUR,numberofnodes-1,10,3
*DO,jj,1,(numberofnodes-1),1
nodenumber=NDNEXT(nodenumber)
PPATH,jj,nodenumber,,,,
*ENDDO

!Plot the Cartesian stress components onto the path
PDEF,STRESSY,S,Y,AVG
PDEF,STRESSX,S,X,AVG
PDEF,STRESSXY,S,XY,AVG

!output the results to a text file
/output,stressth_%CARTESIAN%_%a%_%ALPHA%_,txt
PRPATH,XG,YG,STRESSX,STRESSY,STRESSXY
/output

finish

!Enter the time history post processor=========================================

/post26

!!!!!!!!!!!!!!!!!!!!!!!!!!!!!!!!!!
!Load-Displacement Curve!
!!!!!!!!!!!!!!!!!!!!!!!!!!!!!!!!!!

!NOTE: This series of commands is useful if displacement boundary conditions are applied
!         otherwise, ignore

!Select the Y  boundary component and all of the nodes on that line
```

```
cmsel,s,boundryy,line
nsll,s,1
*GET,numberOfNodes,NODE,,COUNT                  !Get the number of nodes
*GET,nodeNumber,NODE,,NUM,MIN                   !Get the minimum node number

!extract the reaction force in the y-direction
RFORCE,2,nodeNumber,F,Y
*DO,ii,1,(numberOfNodes-1),1                    !do this over all selected nodes
nodeNumber = NDNEXT(nodeNumber)
RFORCE,3,nodeNumber,F,Y

!sum the reaction force of all nodes on the boundary
ADD,2,2,3
*ENDDO
PLVAR,2                                         !Plot the result with respect to time

!output results to a text file
/output,Biaxial_notch_load_time_Y_%A%_%ALPHA%_,txt
PRVAR,2
/output

!Do the same for the X component
lsel,all
cmsel,s,boundryx,line
nsll,s,1
*GET,numberOfNodes2,NODE,,COUNT                 !Get the number of nodes
*GET,nodeNumber2,NODE,,NUM,MIN                  !Get the minimum node number

!extract the reaction force in the x-direction
RFORCE,4,nodeNumber2,F,X
*DO,iii,1,(numberOfNodes2-1),1                  !do this over all selected nodes
nodeNumber2 = NDNEXT(nodeNumber2)
RFORCE,5,nodeNumber2,F,X

 !sum the reaction force of all nodes on the boundary
ADD,4,4,5
*ENDDO
PLVAR,4                                         !Plot the result with respect to time

!output the results to a text file
/output,Biaxial_notch_load_time_X_%A%_%ALPHA%_,txt
PRVAR,4
/output
finish
```

```
j=j+1
FINISH
*ENDDO
*ENDDO
!Exit the routine
```

Macro-Scale Uniaxial Failure Simulation - Element Death

```
!=====================================================!12:46 PM 3/17/2013
!MOMRG-UCF-MAE
!ANSYS INPUT DECK - CRACK GROWTH SIMULATION IN THIN ORTHOTROPIC
!PLATE WITH CIRCULAR NOTCH
!STEVEN M. KRAFT
!
!VERSION 7.0
!!!!!!!!!!!!!!!!!!!!!!!!!!!!!!!!!!!!!!!!!!!!!!!!!!!!!!!!!!!!!!!!!!!!!!!!!!!!!!!!!!!!!!!!!!!!!!!!!!!!!!!!!!!!!!!!!!!!!!!!!!!!!!!!!
finish
/clear
/PREP7
!
!define the parameters for the geometry and material orientation
!
theta=0                 !material orientation  with respect to the WEFT axis
w=.75                   !width of a standard specimen
l=1.25                  !length of a standard specimen
r=.125                  !circle notch radius
a=.125                  !major radius of ellipse
bb=.125                 !minor radius of ellipse
!set the time increment for the do loop to perform the load steps
TM_BEGIN=2
TM_INCR=1
TM_END=15
!
!
!define meso-scale strain parameters for each orientation to aid in element death criterion
!
!maximum plastic strain for ss316l wires used as failure criterion
UTEPw=0.43
UTEPs=0.05
!
*IF,THETA,EQ,90,THEN
aw=1.00e-4
as=0
bw=120.0
bs=0
cw=1.23
cs=0
eyw=0
eys=0
*ELSEIF,THETA,EQ,75
aw=2e-4
```

```
as=0
bw=120.0
bs=0
cw=0.40
cs=0
eyw=.002
eys=0
*ELSEIF,THETA,EQ,60                    !**NOTE: 90 degrees is WARP in this code**!
aw=1.25e-5
as=0
bw=130
bs=0
cw=0
cs=0
eyw=.025
eys=0
*ELSEIF,THETA,EQ,45
aw=3.5e-4
as=0
bw=150.0
bs=0
cw=0
cs=0
eyw=0.018
eys=0
*ELSEIF,THETA,EQ,30
aw=8.00e-4
as=5.40e-4
bw=180
bs=80
cw=0
cs=0
eyw=0.0384
eys=0.018
*ELSEIF,THETA,EQ,15
aw=1.95e-3
as=3.3e-3
bw=205
bs=150
cw=-0.085
cs=-0.200
eyw=0.0075
eys=0.011
*ELSEIF,THETA,EQ,0
aw=.0035
```

```
as=8.00e-3
bw=215
bs=200
cw=-.275
cs=-.350
eyw=0.0027
eys=0.018
*ENDIF
!
FINISH
!
/PREP7
!
!define the geometry============================================================
!
BLC4,0,0,w,l,0                                  !generates a rectangular area
CYL4,w/2,l/2,r                                  !generates a circle for the notch
ARSCALE,2,2,1,(a/r),(bb/r),1,0,1                !generates an ellipse if a and b are not equal to r
AGEN,2,3,,,((0*w/1)-(0*w/40)),,,,1
ASEL,S,,,2,2,1,
ADELE,ALL
!
!create local coordinate system to rotate the ellipse by
LOCAL,22,1,W/2,L/2,0,0,0,0,,
CSYS,22
ASEL,ALL
APLOT
AGEN,2,4, , , ,-ALPHA , , ,1                    !rotate the ellipse by alpha
ASEL,S,,,3,4,1,
ADELE,ALL                    !
ASEL,ALL
ASBA,1,2                                        !generate notched geometry without symmetry
!
!================================================================================
!
!define a local system to transform material properties into desired orientation
!
local,11,0,0,0,0,theta,0,0,,       ! the material is rotated into the theta orientation
!
!***NOTE***
!THETA IS DEFINED WITH RESPECT TO THE WEFT DIRECTION IN THIS CODE, I.E.,
!THETA=0 IS WEFT
!
!================================================================================
!
```

```
!Element definition
!
ET, 1, plane82
Keyopt,1,3,3
Keyopt,1,5,0
Keypot,1,6,0
R,1,.0035,
!
ESYS,11                    ! the local system is selected for all defined elements
!
!=====================================================================
!
!define the material model
!
MPTEMP,,,,,,,,
MPTEMP,1,0
MPDATA,EX,1,,3.09e6                    !orthotropic elastic model employed
MPDATA,EY,1,,2.88e6
MPDATA,PRXY,1,,0.398
MPDATA,GXY,1,,.031e6
!
!define plasticity model - ANISO for now
!
TB,ANISO                               !Anisotropic plasticity is employed
!
TSyx=14.29e3
TSyy=28.0e3
TSyxy=0.7*0.81*(10.29e3/sqrt(2))
CSyx=TSyx
CSyy=TSyy
CSyxy=TSyxy
TMx=2.8e5
TMy=7.0e5
TMps=.015e6
!
!yield strengths and tangent moduli are defined in data table
TBDATA,1,TSyx,TSyy,TSyy,TMx,TMy,TMy
TBDATA,7,CSyx,CSyy,CSyy,TMx,TMy,TMy
TBDATA,13,TSyxy,TSyxy,TSyxy,TMps,TMps,TMps
!=====================================================================
!
!Mesh the geometry using automatic meshing
!
ASEL,ALL
!
```

```
!Set the automatic meshing parameters
!
MSHAPE,0,2D
MSHKEY,0
SMRTSIZE, 1
AMESH,ALL
AREFINE,3,,,2
!
!refine the mesh at the notch location
LREFINE, 17,20,1,2
!
!=====================================================================
!
!switch back to the global system to define boundary conditions
!
CSYS,0
!
!Fix the bottom edge
!
LSEL,S,LINE,,1
NSLL,S,1
D,ALL,ALL,0
NSEL,ALL
!Dimension the table of time-displacement values
*DIM,DISP_TIME,TABLE,16
!Displacement values
DISP_TIME(1)=0,.002,.004,.006,.008,.009,.01,.011,.012,.013,.014,0.015,0.016,0.017,0.018,0.01
9
!Time values
DISP_TIME(1,0)=0,1,2,3,4,5,6,7,8,9,10,11,12,13,14,15
!
FINISH
!
!=====================================================================
!
!Enter the solver
!
/solu
!
!we will apply a time step to ramp the mechanical load
!
!LS 1
!
LSEL,S,LINE,,3
NSLL,S,1
```

```
D,ALL,UY,%DISP_TIME%
NSEL,ALL
!DL,3,,UY,%DISP_TIME%
!
antype,0                        !select static analysis type
nropt,auto                      !newton rhapson solver is set to automatic
lnsrch,auto                     !line search options are set to automatic
NLGEOM,Off                      !Nonlinear geometry option turned off
solcontrol,on                   !optimized non-linear
KBC,0                           !loads are ramped
time, 1                         !time at end of load step
nsub,5,5000,1                   !set number of substeps
autots,ON                       !toggle on/off auto time stepping
outres,esol,all                 !save element solutions for all time steps in the database
outres,rsol,all                 !save force reactions for all time steps in the database
!
solve                           !solve the problem
!
FINISH
!
!=================================================================
!Enter the general post-processor
/POST1
!
SET,LAST
!
ESEL,ALL                                        !Select all elements
!
!Generate element tables of total Y-COMPONENT mechanical strain components in the plane
ETABLE,E_EQV_TOT,EPTO,Y
!
!Generate a dummy element table to be re-filled with WARP damage values later
ETABLE,DAMAGEW,S,1
!Generate a dummy element table to be re-filled with WEFT damage values later
ETABLE,DAMAGES,S,1
!
!Get the total number of elements in the model
*GET,NumElem,ELEM,,COUNT
!
!Dimension the strain array to the number of elements in the model
*DIM,STA_EQV,ARRAY,NumElem,1,,,,                !
!
!Put Element table strain values into the array for manipulation
*VGET,STA_EQV,ELEM,1,ETAB,E_EQV_TOT
!
```

```
! evaluate the meso-scale plasticity model for warp wires
*VOPER,TGW,STA_EQV,SUB,EYW
*VOPER,EW_1,TGW,MULT,BW
*VFUN,EW_2,EXP,EW_1
*VOPER,EW_3,AW,MULT,EW_2
*VOPER,EW_4,CW,MULT,STA_EQV
*VOPER,EW_T,EW_4,ADD,EW_3
!
!evaluate the meso-scale plasticity model for weft wires
*VOPER,TGS,STA_EQV,SUB,EYS
*VOPER,ES_1,TGS,MULT,BS
*VFUN,ES_2,EXP,ES_1
*VOPER,ES_3,AS,MULT,ES_2
*VOPER,ES_4,CS,MULT,STA_EQV
*VOPER,ES_T,ES_4,ADD,ES_3
!
! damage defined as the ratio of meso-scale plastic strain to ultimate plastic strain of ss316l wires
*VOPER,DAMW,EW_T,DIV,UTEPw
*VOPER,DAMS,ES_T,DIV,UTEPs
!
!Do loop places WARP damage values into dummy element table defined earlier
*GET,NumElem,ELEM,,COUNT
*DO,k,1,(NumElem),1
DETAB,k,DAMAGEW,DAMW(k,1,1)
*ENDDO                                    !
!
!Do loop places WEFT damage values into dummy element table defined earlier
*GET,NumElem,ELEM,,COUNT
*DO,k,1,(NumElem),1
DETAB,k,DAMAGES,DAMS(k,1,1)
*ENDDO
!
!
!Select all elements with a damage value greater than or equal to 1.00
ESEL,S,ETAB,DAMAGEW,1.00,,,0
ESEL,A,ETAB,DAMAGES,1.00,,,0
!
!Get the number of elements selected
*GET,NUMSEL,ELEM,,COUNT
!If - Then logic determines if CM file is to be written
*IF,NUMSEL,EQ,0,THEN
ESEL,ALL
COUNT=0
*ELSEIF,NUMSEL,GT,0
```

```
!Select all elements with a damage value greater than or equal to 1.00
ESEL,S,ETAB,DAMAGEW,1.00
ESEL,A,ETAB,DAMAGES,1.00
      CM,TOKILL,ELEM                    ! Create Kill Element Component
         CMWRITE,KILL_LIST,CM           ! Write Component to Disk
count=1
*ENDIF
!
parsav,all
!
!Plot contour map of accumulated WARP damage, redirect plot to tiff file
ESEL,S,LIVE
PLETAB,DAMAGEW,AVG
/SHOW,TIFF,,0
TIFF,COMP,1
TIFF,ORIENT,HORIZ
TIFF,COLOR,2
TIFF,TMOD,1
/GFILE,800,
/CMAP,_TEMPCMAP_,CMP,,SAVE
/RGB,INDEX,100,100,100,0
/RGB,INDEX,0,0,0,15
/REPLOT
/CMAP,_TEMPCMAP_,CMP
/DELETE,_TEMPCMAP_,CMP
/SHOW,CLOSE
/DEVICE,VECTOR,0
!
 !Plot contour map of accumulated WEFT damage, redirect plot to tiff file
ESEL,S,LIVE
PLETAB,DAMAGES,AVG
/SHOW,TIFF,,0
TIFF,COMP,1
TIFF,ORIENT,HORIZ
TIFF,COLOR,2
TIFF,TMOD,1
/GFILE,800,
/CMAP,_TEMPCMAP_,CMP,,SAVE
/RGB,INDEX,100,100,100,0
/RGB,INDEX,0,0,0,15
/REPLOT
/CMAP,_TEMPCMAP_,CMP
/DELETE,_TEMPCMAP_,CMP
/SHOW,CLOSE
/DEVICE,VECTOR,0
```

```
!
ESEL,ALL
PARSAV,ALL
FINISH                                  !Exit the post-processor
!=====================================================================
!
!LS2 AND THE REMAINING STEPS.
!
!Do loop runs the remaining time steps
*DO,TM,TM_BEGIN,TM_END,TM_INCR
!
!Save all parameters before entering the solver
parsav,all
!
/SOLU
antype,,rest                            !Restart the solution and continue with remaining load
steps
parres                                  !Read parameter file into the database
!
!
!If - then logic decides whether to execute element kill or to proceed to next load step
*IF,COUNT,EQ,0,THEN
      ESEL,ALL
*ELSEIF,COUNT,GT,0,AND,COMPEXIST,GT,0,THEN
      /INPUT,KILL_LIST,CM                   ! Read in Component from Disk
         CMSEL,S,TOKILL                     ! Select Current Component
      /INPUT,KILL_LIST_2,CM                 ! Read in Component from Disk
      CMSEL,A,TOKILL_2                      ! Select Previous Component
      EKILL,ALL                             ! Kill selected elements
      CM,TOKILL_2,ELEM                      ! Create secondary Kill Element Component
         CMWRITE,KILL_LIST_2,CM             ! Write Component to Disk
*ELSEIF,COUNT,GT,0,AND,COMPEXIST,EQ,0,THEN
      /INPUT,KILL_LIST,CM
      CMSEL,S,TOKILL
      EKILL,ALL
      CM,TOKILL_2,ELEM                      ! Create secondary Kill Element Component
         CMWRITE,KILL_LIST_2,CM             ! Write Component to Disk
*ENDIF
!
ESEL,ALL
!
nropt,auto                              !newton rhapson solver is set to automatic
lnsrch,auto                             !line search options are set to automatic
solcontrol,on                           !optimized nonlinear
nlgeom,off                              !Nonlinear geometry option turned off
```

```
kbc,0                                   !loads are ramped
time, TM                                !time at end of load step
nsub,5,1000,1                           !number of sub-steps
autots,on                               !toggle on/off auto time stepping
outres,esol,all                         !save element solutions for all time steps
outres,rsol,all                         !save force reactions for all time steps
esel,all
solve
FINISH
!
!=========================================================================
!
/POST1                                  !Enter the general post-processor
!
SET,LAST
!
ESEL,ALL                                !Select all elements
!
!Generate element tables of total Y-COMPONENT mechanical strain components in the plane
ETABLE,E_EQV_TOT,EPTO,Y
!
!Generate a dummy element table to be re-filled with WARP damage values later
ETABLE,DAMAGEW,S,1
!Generate a dummy element table to be re-filled with WEFT damage values later
ETABLE,DAMAGES,S,1
!
*GET,NumElem,ELEM,,COUNT          !Get the total number of elements in the model
!
!Dimension the strain array to the number of elements in the model
*DIM,STA_EQV,ARRAY,NumElem,1,,,,
!
!Put Element table strain values into the array for manipulation
*VGET,STA_EQV,ELEM,1,ETAB,E_EQV_TOT
!
! evaluate the meso-scale plasticity model for warp wires
*VOPER,TGW,STA_EQV,SUB,EYW
*VOPER,EW_1,TGW,MULT,BW
*VFUN,EW_2,EXP,EW_1
*VOPER,EW_3,AW,MULT,EW_2
*VOPER,EW_4,CW,MULT,STA_EQV
*VOPER,EW_T,EW_4,ADD,EW_3
!
! evaluate the meso-scale plasticity model for weft wires
*VOPER,TGS,STA_EQV,SUB,EYs
*VOPER,ES_1,TGS,MULT,BS
```

```
*VFUN,ES_2,EXP,ES_1
*VOPER,ES_3,AW,MULT,ES_2
*VOPER,ES_4,CW,MULT,STA_EQV
*VOPER,ES_T,ES_4,ADD,ES_3
!
!damage defined as the ratio of meso-scale plastic strain to ultimate plastic strain of ss316l wires
*VOPER,DAMW,EW_T,DIV,UTEPW
*VOPER,DAMS,ES_T,DIV,UTEPS
!
!Do loop places WARP damage values into dummy element table defined earlier
*GET,NumElem,ELEM,,COUNT
*DO,k,1,(NumElem),1
DETAB,k,DAMAGEW,DAMW(k,1,1)
*ENDDO                                    !
!
!Do loop places WEFT damage values into dummy element table defined earlier
*GET,NumElem,ELEM,,COUNT
*DO,k,1,(NumElem),1
DETAB,k,DAMAGES,DAMS(k,1,1)
*ENDDO
!
!Select all elements with a damage value greater than or equal to 1.00
ESEL,S,ETAB,DAMAGEW,1.00,,,0
ESEL,A,ETAB,DAMAGES,1.00,,,0
!
*GET,NUMSEL,ELEM,,COUNT                   !Get the number of elements selected
!If - Then logic determines if CM file is to be written
*IF,NUMSEL,EQ,0,THEN
      ESEL,ALL
      count=0
*ELSEIF,NUMSEL,GT,0
      ESEL,S,ETAB,DAMAGE,1.00
      CM,TOKILL,ELEM                      ! Create Kill Element Component
         CMWRITE,KILL_LIST,CM             ! Write Component to Disk
      count=1
*ENDIF
!
!Determine status of previous to kill component
*GET,COMPEXIST,COMP,TOKILL_2,TYPE
!
parsav,all
!
!Plot contour map of accumulated WARP damage, redirect plot to tiff file
ESEL,S,LIVE
PLETAB,DAMAGEW,AVG
```

```
/SHOW,TIFF,,0
TIFF,COMP,1
TIFF,ORIENT,HORIZ
TIFF,COLOR,2
TIFF,TMOD,1
/GFILE,800,
/CMAP,_TEMPCMAP_,CMP,,SAVE
/RGB,INDEX,100,100,100,0
/RGB,INDEX,0,0,0,15
/REPLOT
/CMAP,_TEMPCMAP_,CMP
/DELETE,_TEMPCMAP_,CMP
/SHOW,CLOSE
/DEVICE,VECTOR,0
!
!Plot contour map of accumulated WEFT damage, redirect plot to tiff file
PLETAB,DAMAGES,AVG
/SHOW,TIFF,,0
TIFF,COMP,1
TIFF,ORIENT,HORIZ
TIFF,COLOR,2
TIFF,TMOD,1
/GFILE,800,
/CMAP,_TEMPCMAP_,CMP,,SAVE
/RGB,INDEX,100,100,100,0
/RGB,INDEX,0,0,0,15
/REPLOT
/CMAP,_TEMPCMAP_,CMP
/DELETE,_TEMPCMAP_,CMP
/SHOW,CLOSE
/DEVICE,VECTOR,0
!
!
ESEL,ALL
PARSAV,ALL
FINISH                                  !Exit the post-processor
*ENDDO
!
!
!ENTER TIME-HISTORY POST PROCESSOR
!
/post26
!
!Create job names for each run for each output file
!
```

```
!**NOTE: The output files are referenced as 90-theta, such that the
!          standard orientation convention is maintained in the results

LOAD_DISP_JOB='LOAD_DISP_notched%90-theta%_.txt'
!
!Create index files for each output file set
!
*CFOPEN, INDEX_LOAD_DISP,txt,,append
*VWRITE, LOAD_DISP_JOB
%C
!
!select line containing DIS BC for force reaction
LSEL,S,,,3
!Select all of the nodes on that line
NSLL,S,1
!extract the reaction force in the y-direction
*GET,numberOfNodes,NODE,,COUNT                  !Get the number of nodes
*GET,nodeNumber,NODE,,NUM,MIN                   !Get the minimum node number
RFORCE,2,nodeNumber,F,Y
*DO,i,1,(numberOfNodes-1),1                     !do this over all selected nodes
nodeNumber = NDNEXT(nodeNumber)
RFORCE,3,nodeNumber,F,Y
!sum the reaction force of all nodes on the boundary
ADD,2,2,3
*ENDDO
!Plot the result with respect to time
PLVAR,2
!
!output is redirected from the screen to a text file
/output,LOAD_DISP%90-theta%_,txt
PRVAR,2
/output
!
FINISH
```

APPENDIX C
DATA ACQUISITION CIRCUIT DESIGN REFERENCE

List of Parts

1. Futek load cell model #LCM300
2. Omega LVDT sensor model #LD621-15
3. CUI, Inc. AC/DC power supplies model #ESTA 12W
4. Lego NXT Mindstorm analog to digital converter and controller
5. Burr Brown INA-125 instrumentation amplifier
6. Burr Brown INA-118 instrumentation amplifier
7. 1μF capacitors (4)
8. 10kΩ resistors (8)
9. RS-232 breakouts (4)
10. Voltage supply terminals (4)
11. Electrical enclosure
12. Vernier NXT sensor adapters (4)

Data Acquisition Sensors and Components

Load Cell

Futek Model # LCM300

Rated Output: 2mV/V nom.

Excitation: 15VDC maximum

Maximum Load: 250lb (1112N)

LVDT Sensor

Omega Model # LD621-15

Excitation: 10 - 30VDC @ 25mA

Output: 0 - 10VDC

Maximum Deflection: 0.6in (15.0mm)

DC Power Supplies

CUI, Inc. Model # ESTA 12W

Maximum Power: 12 Watts

Output Voltage: 12VDC

Maximum Output Current: 1.0A

Input Voltage: 90 - 264 VAC

NXT Mindstorm Analog to Digital Converter and Controller

Lego Product # 8547 - NXT2.0

Maximum Input Voltage: 5VDC

Analog Signal Processing Board

Burr Brown INA 125 Instrumentation Amplifier:

- Precision Voltage References at 1.24V, 2.5V, 5.0V, and 10.0V
- Dual Supply Range: +/- 1.35V to +/- 18.0V
- Input Range +/- 40V
- 16 PIN DIP Packaging
- Variable Amplification

Burr Brown INA 118 Instrumentation Amplifier:

- 8 PIN DIP Packaging
- Dual Supply Range: +/- 1.35V to +/- 18.0 V
- Input Range: +/- 40V
- Variable Amplification

Other Components:

1µF Capacitor (4)
10kΩ Resistors (8)
RS-232 Breakouts (4)
Voltage Supply Terminals (4)

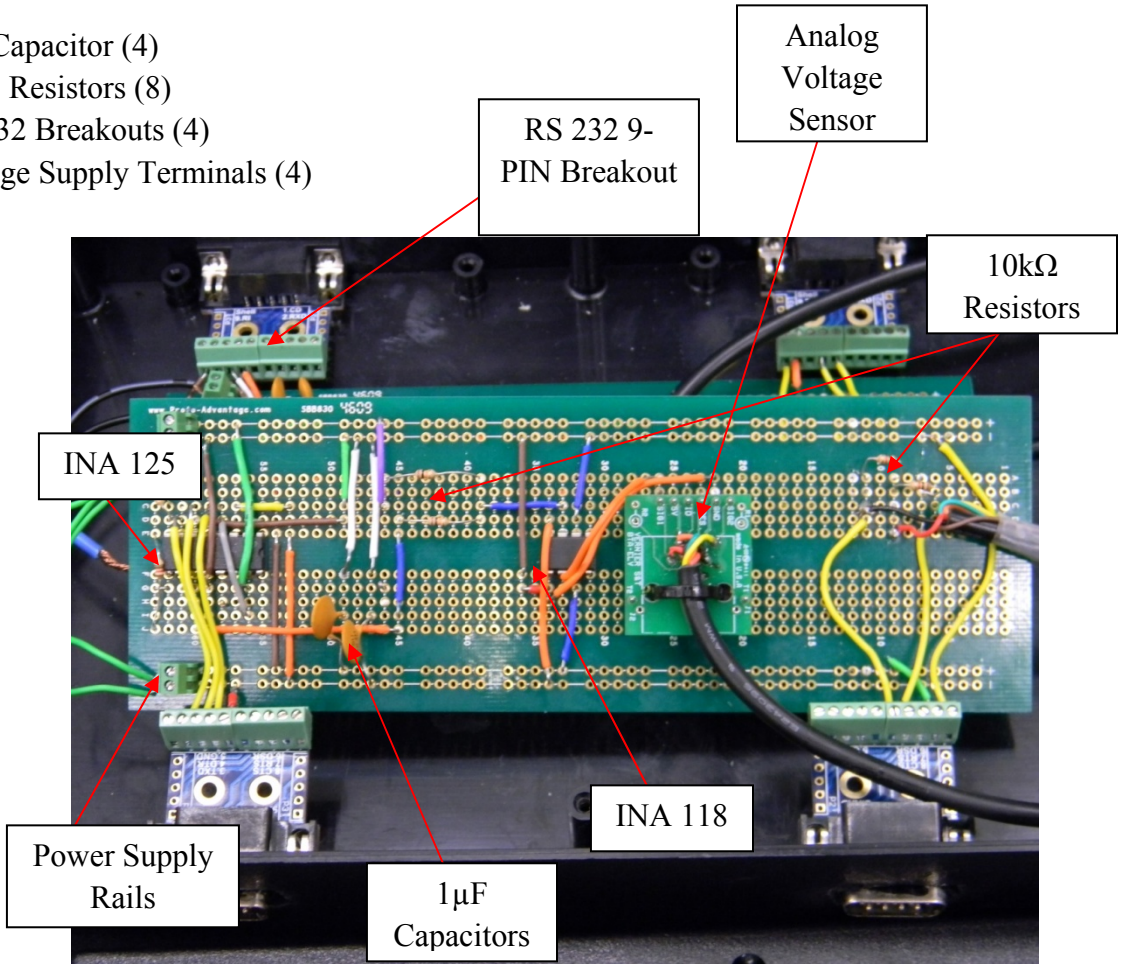

Complete Data Acquisition System

Schematic of Basic Circuits Used

The Non-Inverting Summing Amplifier (INA-118)

$$E_o = E_1 + E_2$$

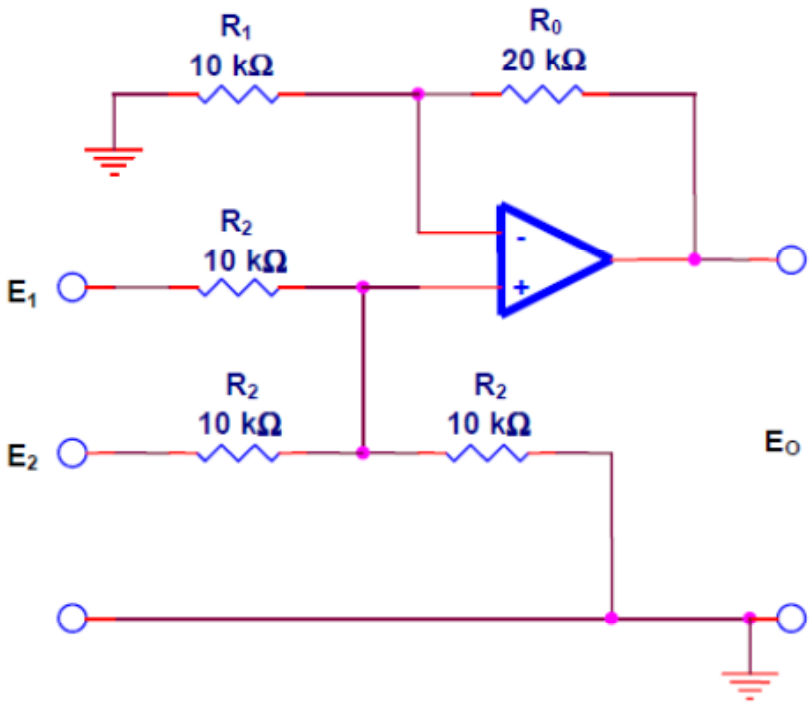

The Resistive Voltage Divider (LVDTs)

$$E_o = E_1 \frac{R_2}{R_1 + R_2}$$

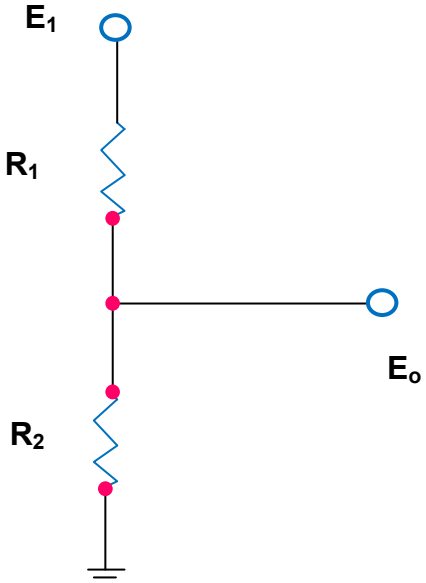

APPENDIX D
BIAXIAL LOAD FRAME COMPONENTS

The Assembled Biaxial Load Frame in Equibiaxial Tension

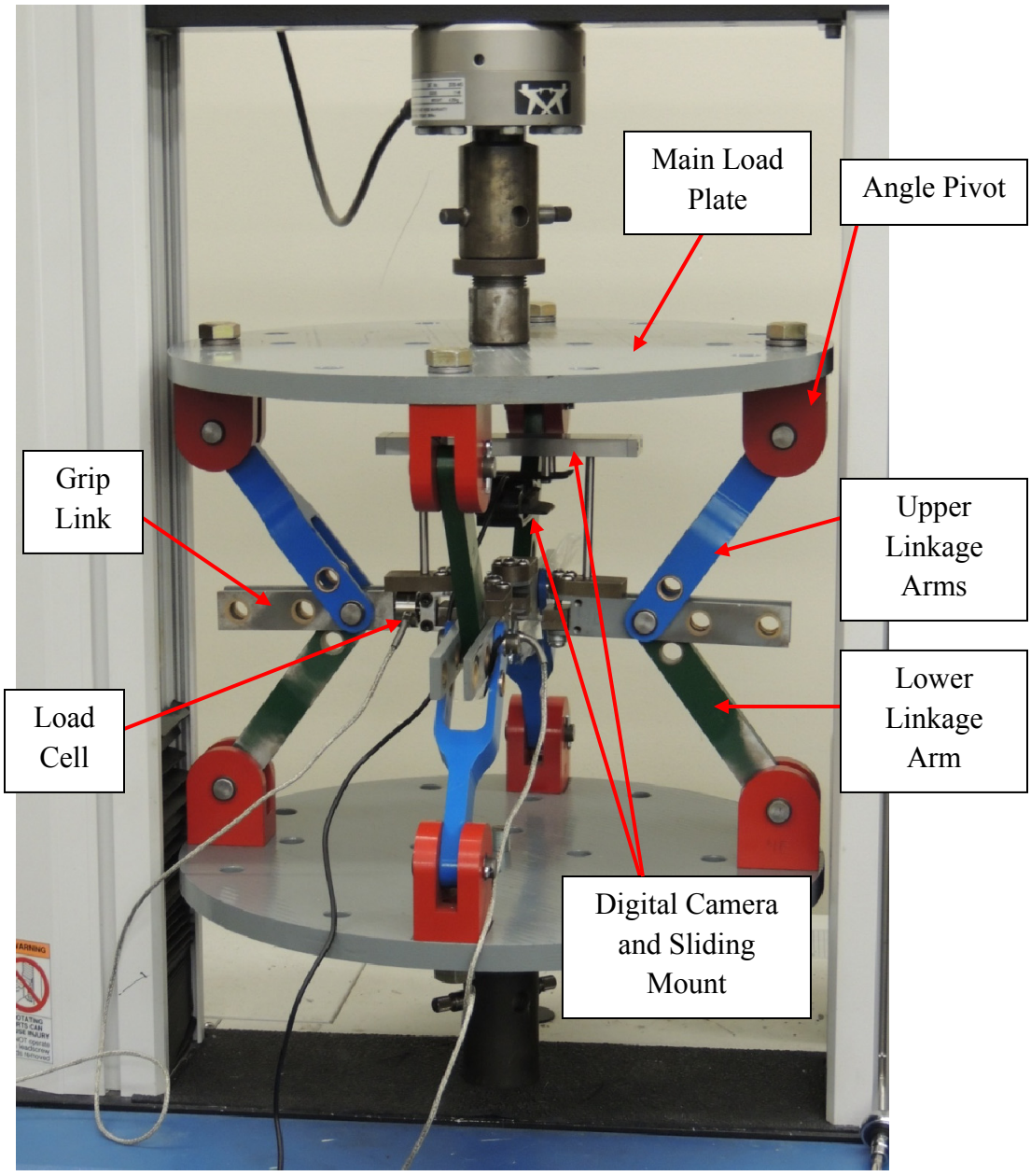

Main Load Plate

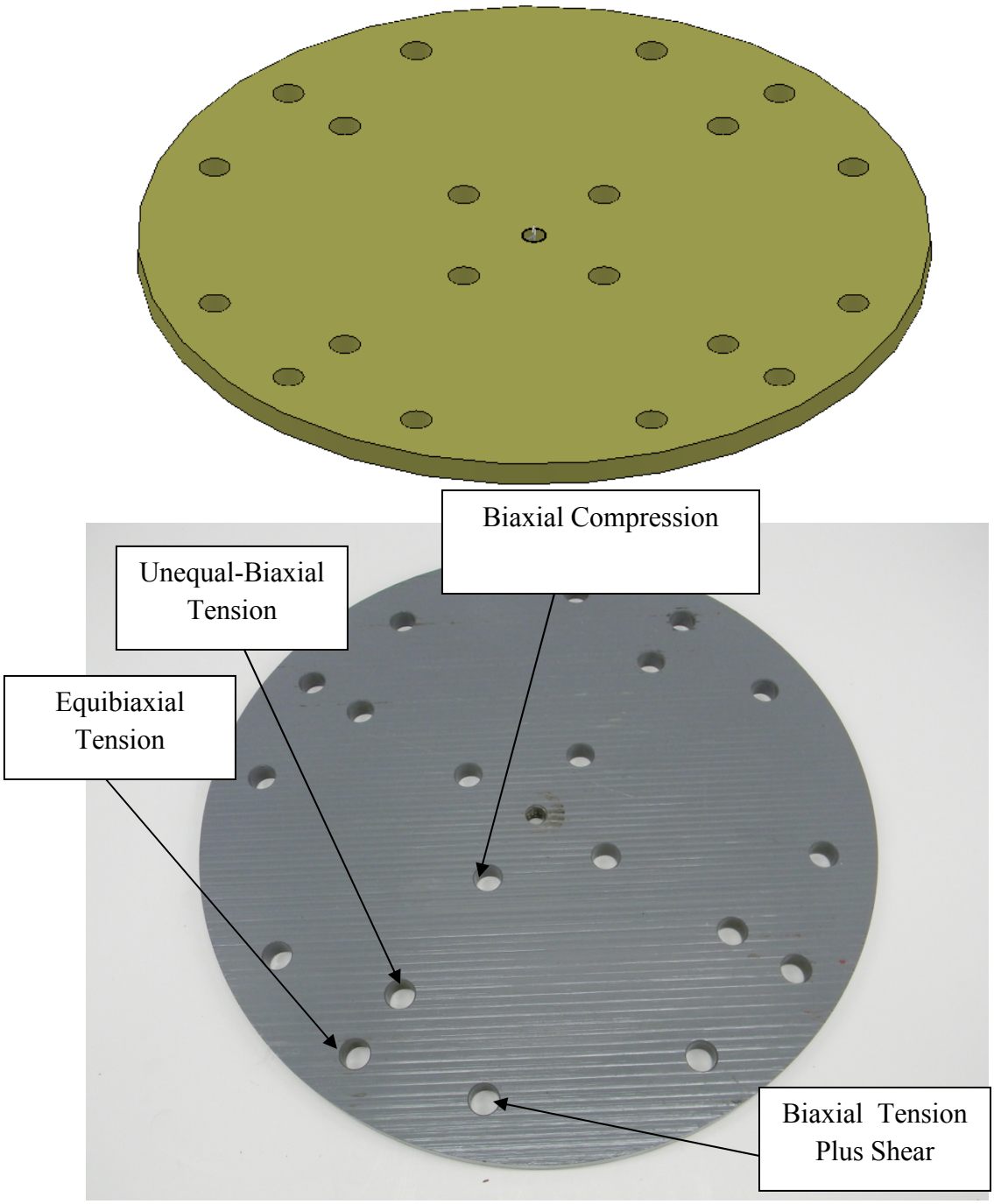

Angle Pivot

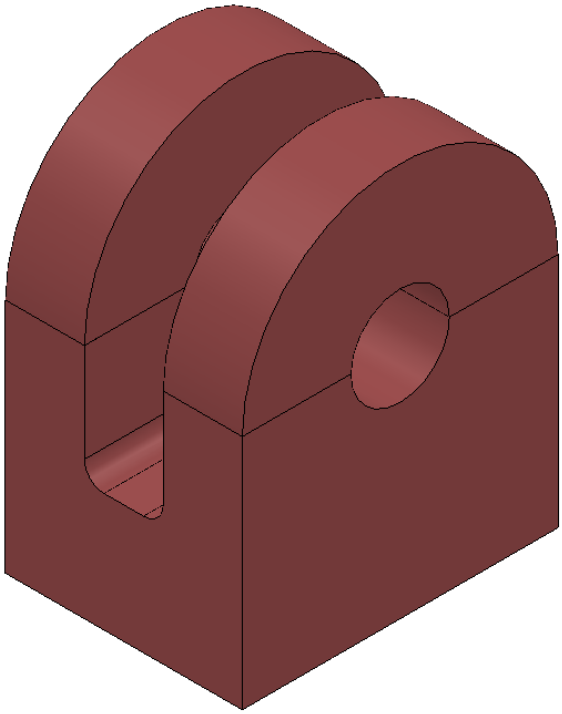

Upper Linkage Arm

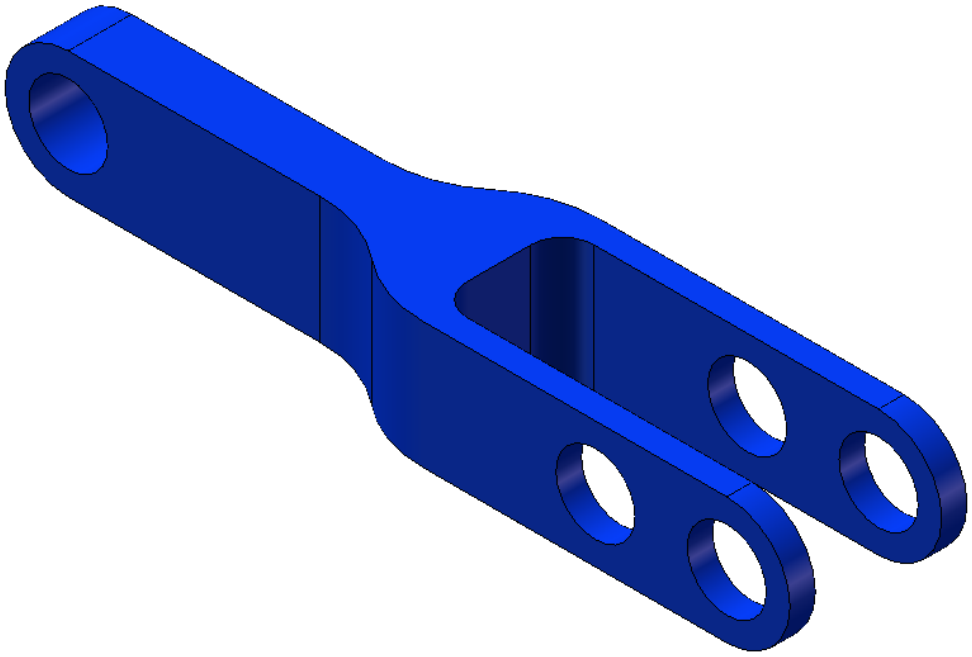

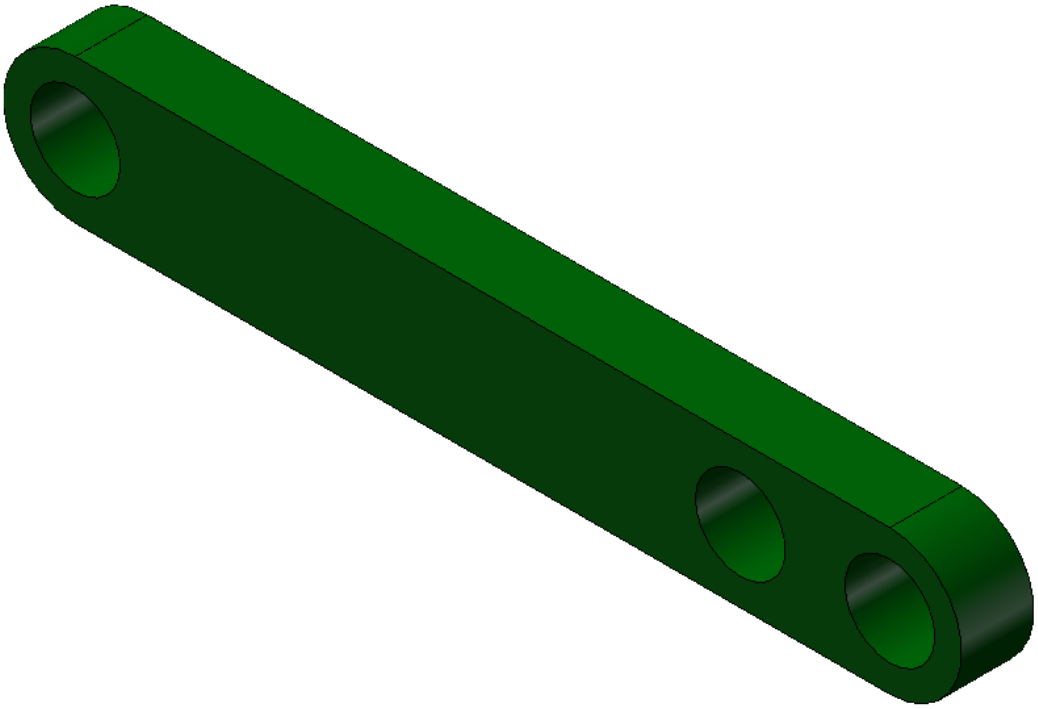


3A

Grip Assembly

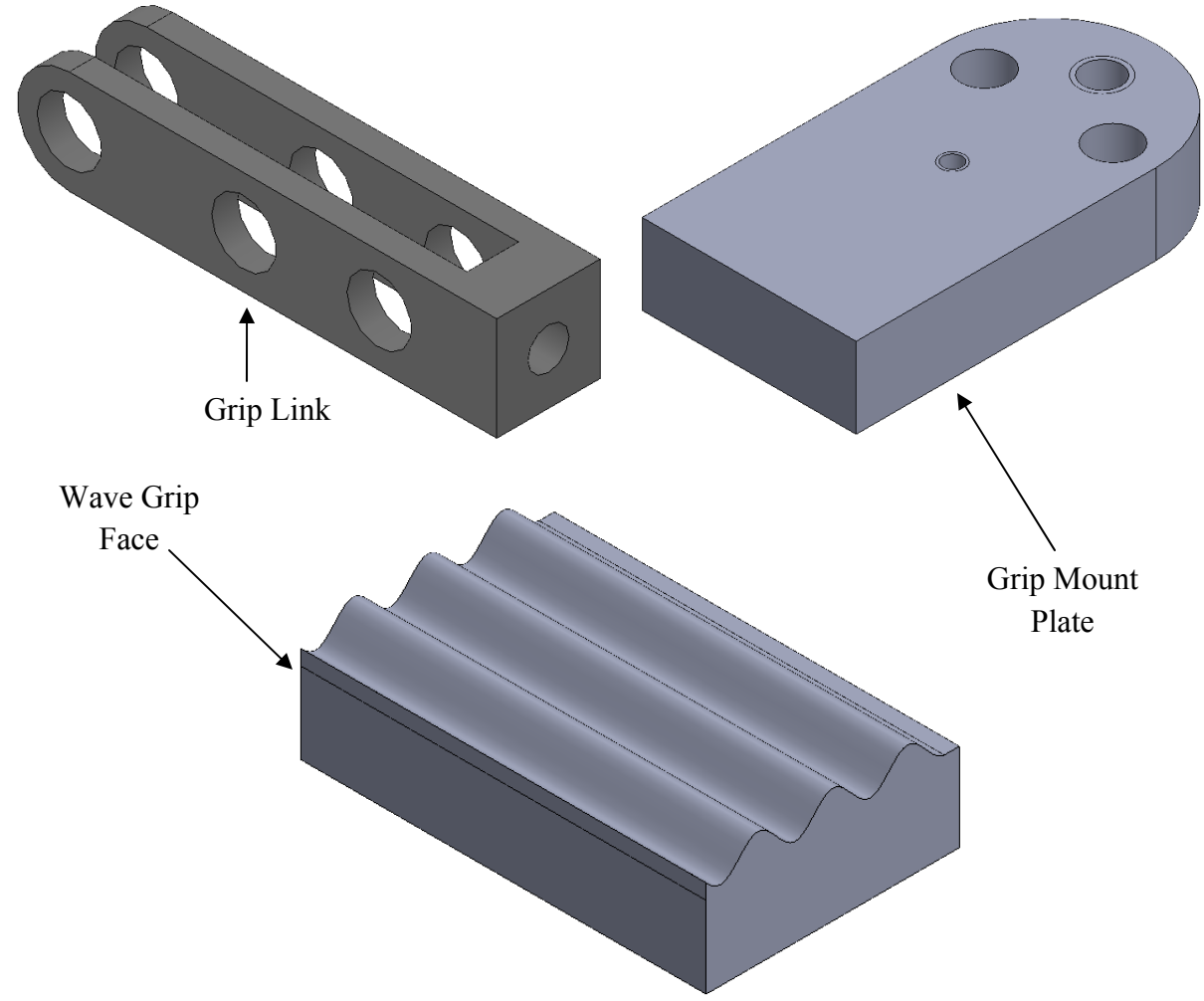

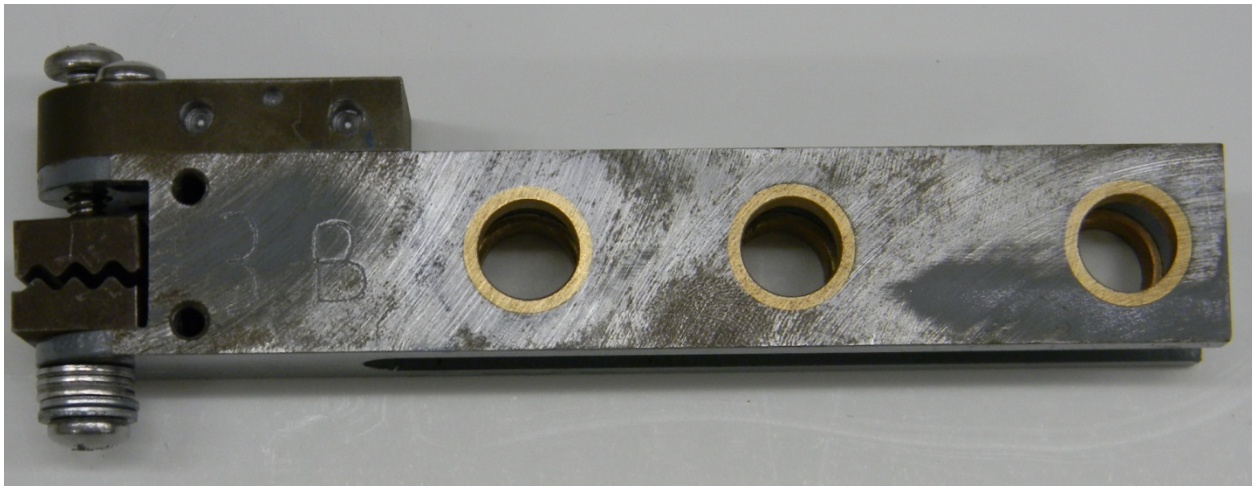

Camera Mount Assembly

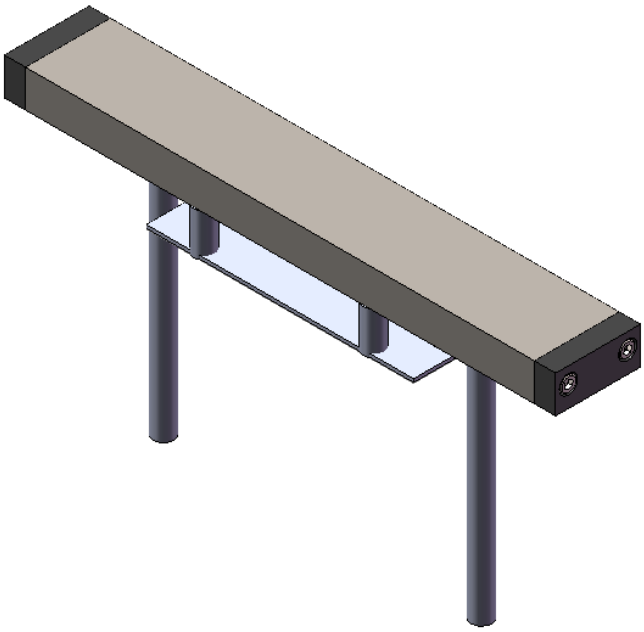

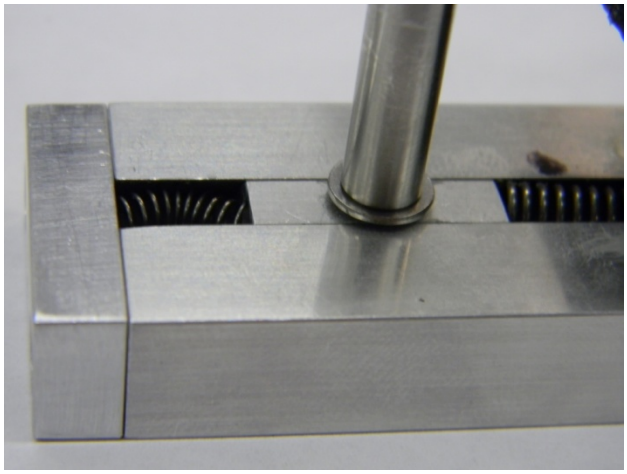

Part Drawings

Angle Pivot

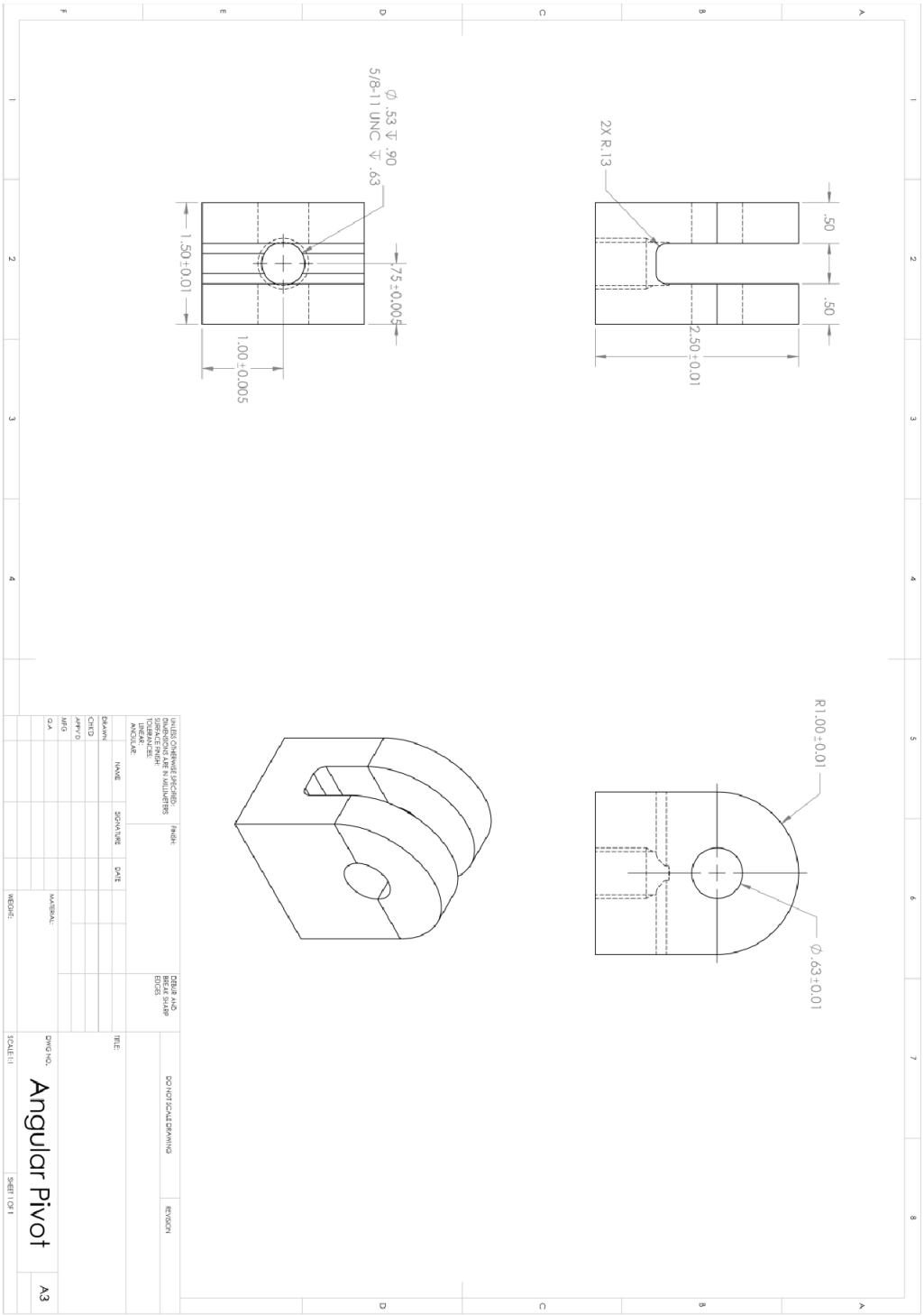

Grip Link A

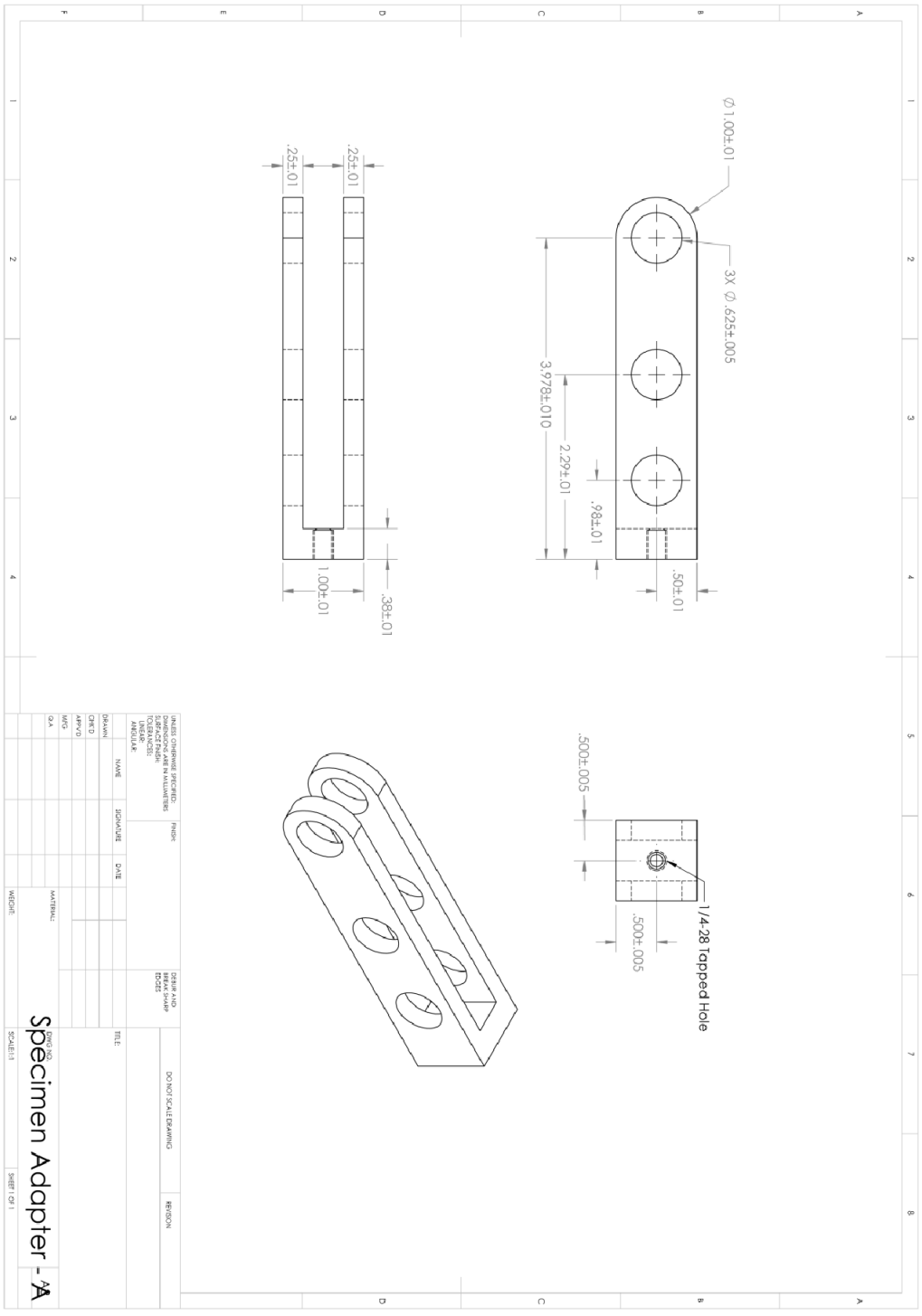
Ø1.00±.01
3X Ø .625±.005
3.978±.010
2.29±.01
.98±.01
.50±.01
.25±.01
.25±.01
1.00±.01
.38±.01
.500±.005
.500±.005
1/4-28 Tapped Hole
Specimen Adapter - A

Grip Link B

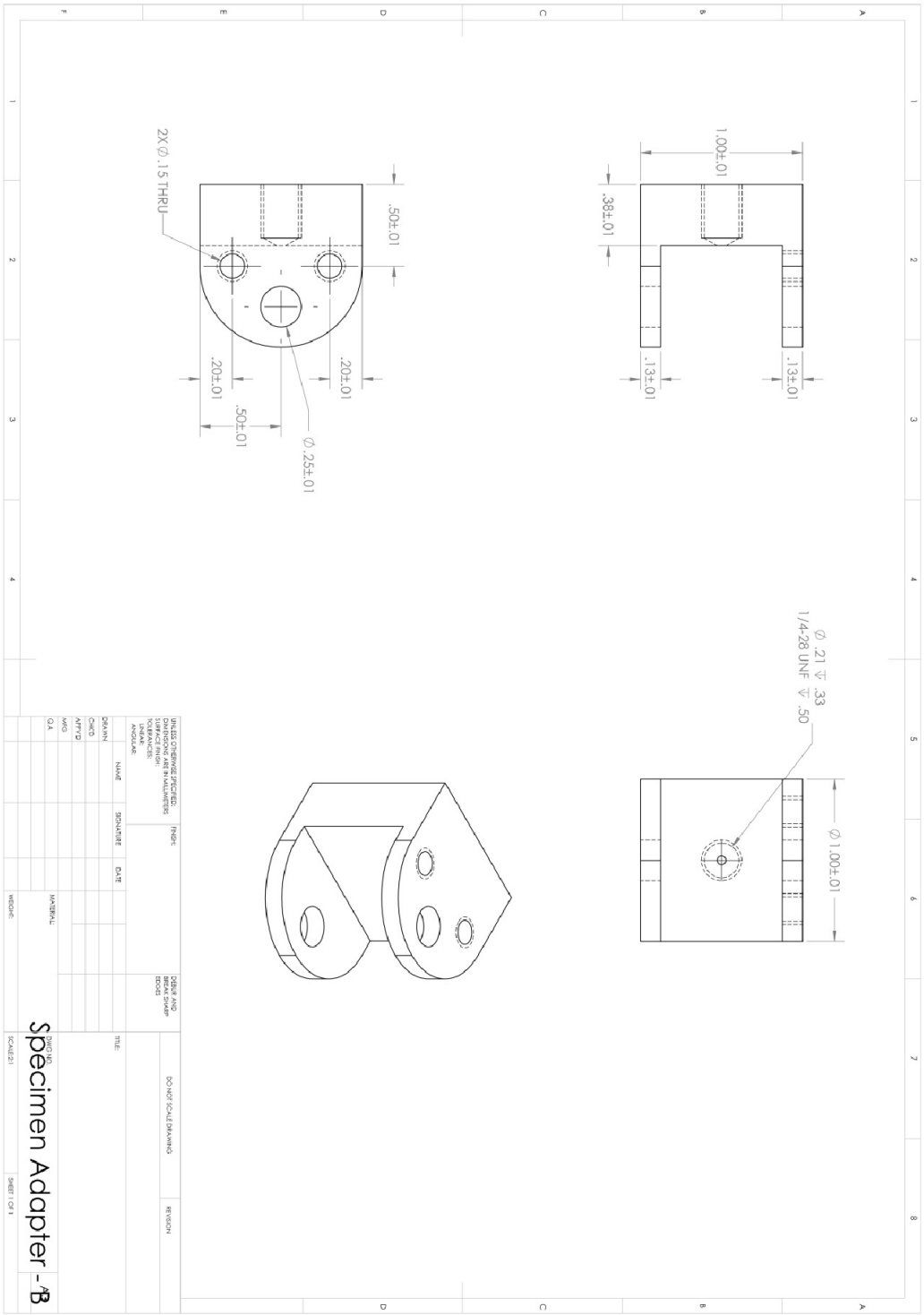
1.00±.01
.38±.01
.13±.01
.13±.01
2X Ø.15 THRU
.50±.01
.20±.01
.20±.01
.50±.01
Ø.25±.01
Ø.21 ⩛ .33
1/4-28 UNF ⩛ .50
Ø1.00±.01
UNLESS OTHERWISE SPECIFIED:
DIMENSIONS ARE IN MILLIMETERS
SURFACE FINISH:
TOLERANCES:
LINEAR:
ANGULAR:
FINISH:
DEBUR AND BREAK SHARP EDGES
NAME
SIGNATURE
DATE
DRAWN
CHK'D
APP'D
MFG
Q.A
MATERIAL:
WEIGHT:
TITLE:
Specimen Adapter - B
DWG NO.
SCALE:2/1
SHEET 1 OF 1
DO NOT SCALE DRAWING
REVISION

Lower Linkage Arm

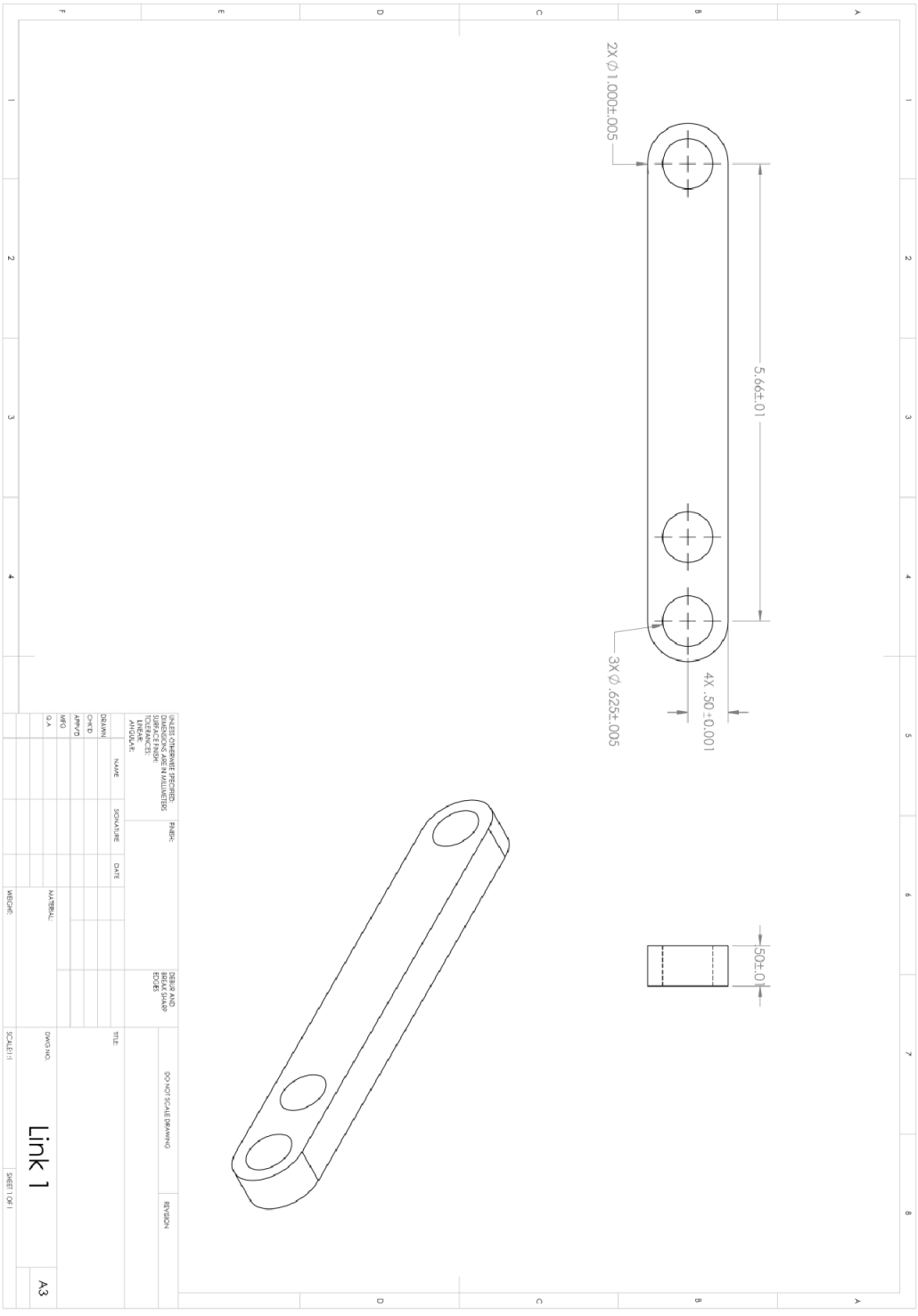

Upper Linkage Arm

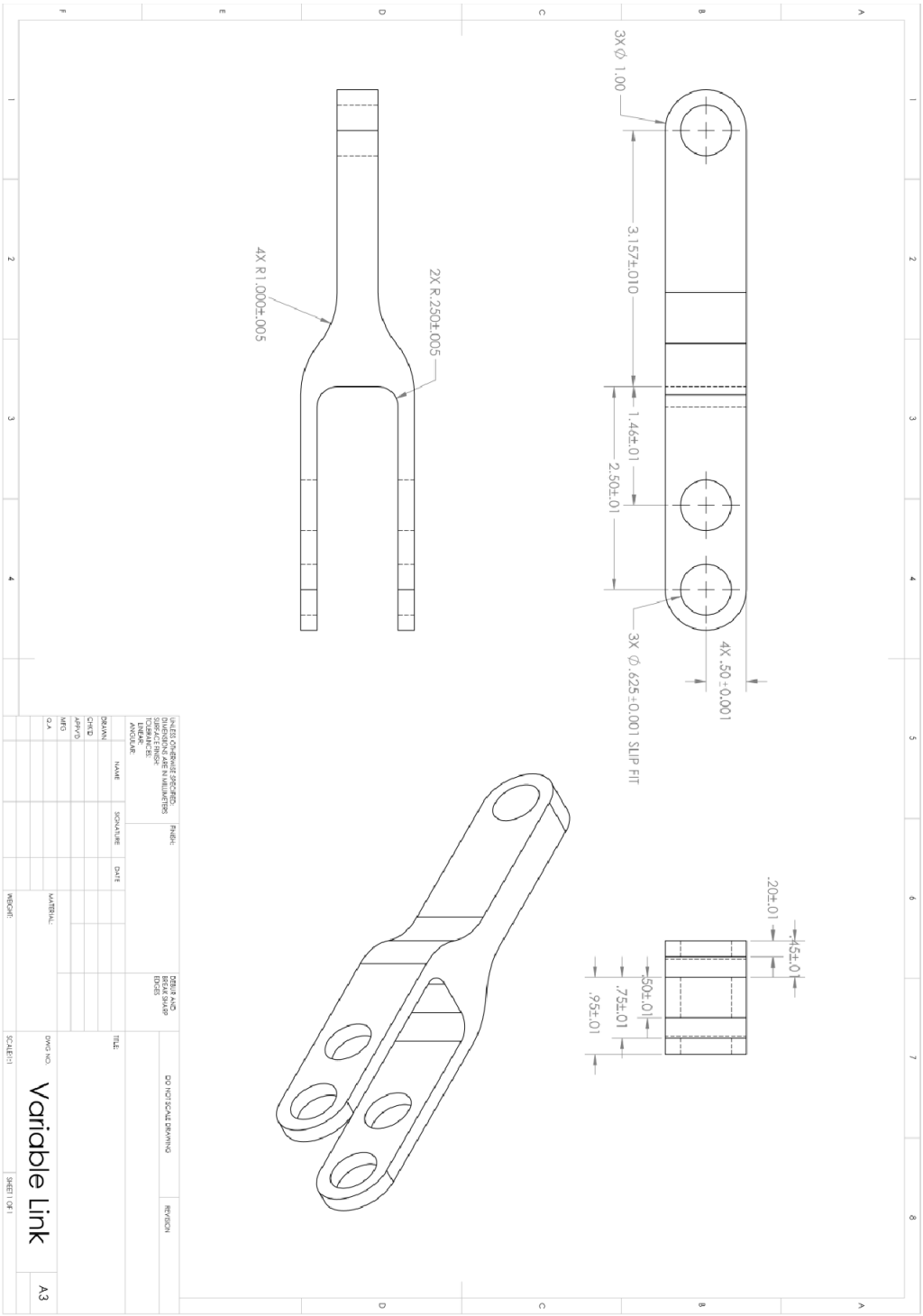

Main Load Plate

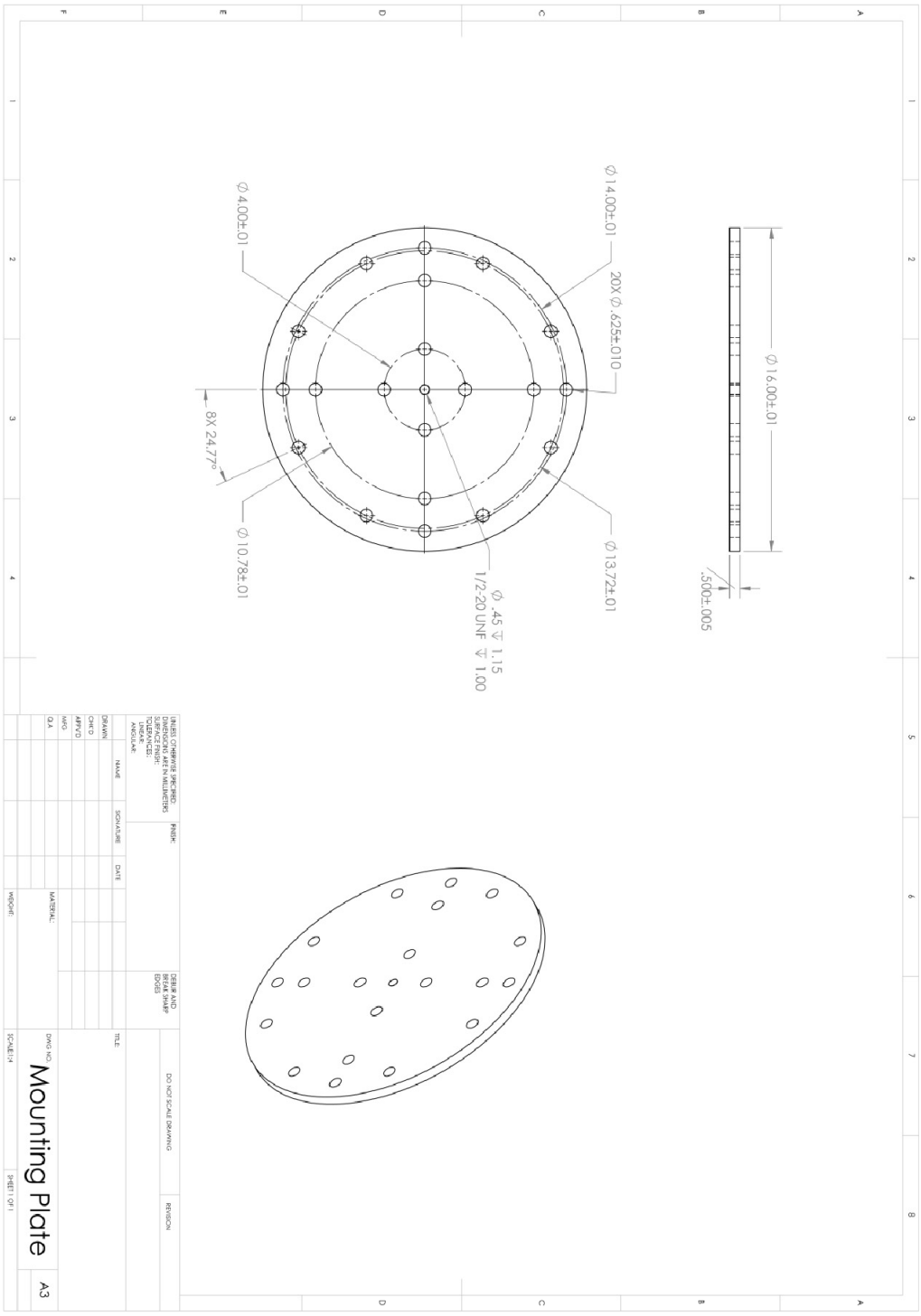

Slider

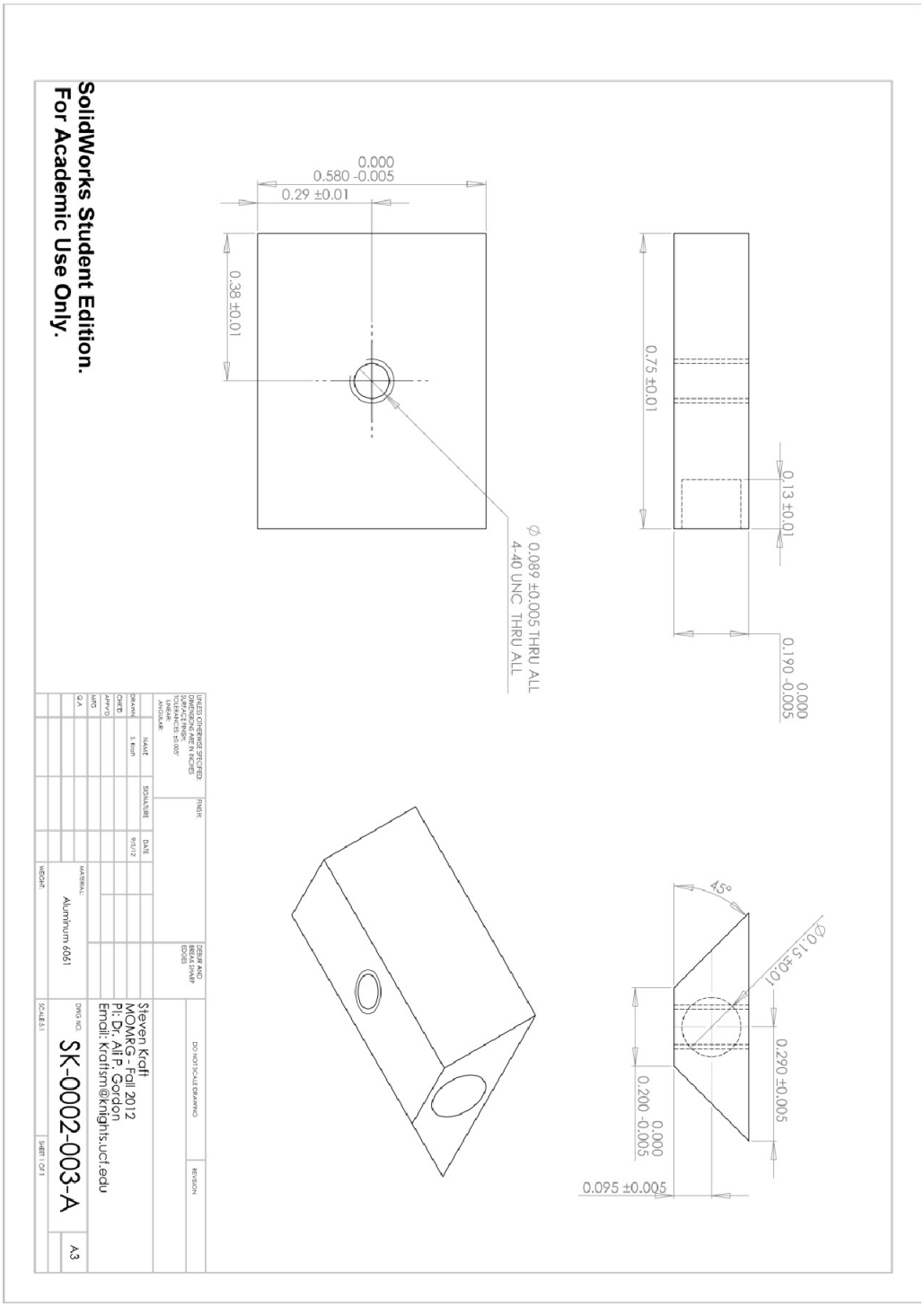
SolidWorks Student Edition.
For Academic Use Only.
0.000
0.580 -0.005
0.29 ±0.01
0.38 ±0.01
Ø 0.089 ±0.005 THRU ALL
4-40 UNC THRU ALL
0.75 ±0.01
0.13 ±0.01
0.000
0.190 -0.005
45°
Ø0.15 ±0.01
0.290 ±0.005
0.200 -0.005
0.000
0.095 ±0.005
Steven Kraft
MOMRG - Fall 2012
PI: Dr. Alf P. Gordon
Email: Kraftsm@knights.ucf.edu
Aluminum 6061
SK-0002-003-A
A3

Slider Track

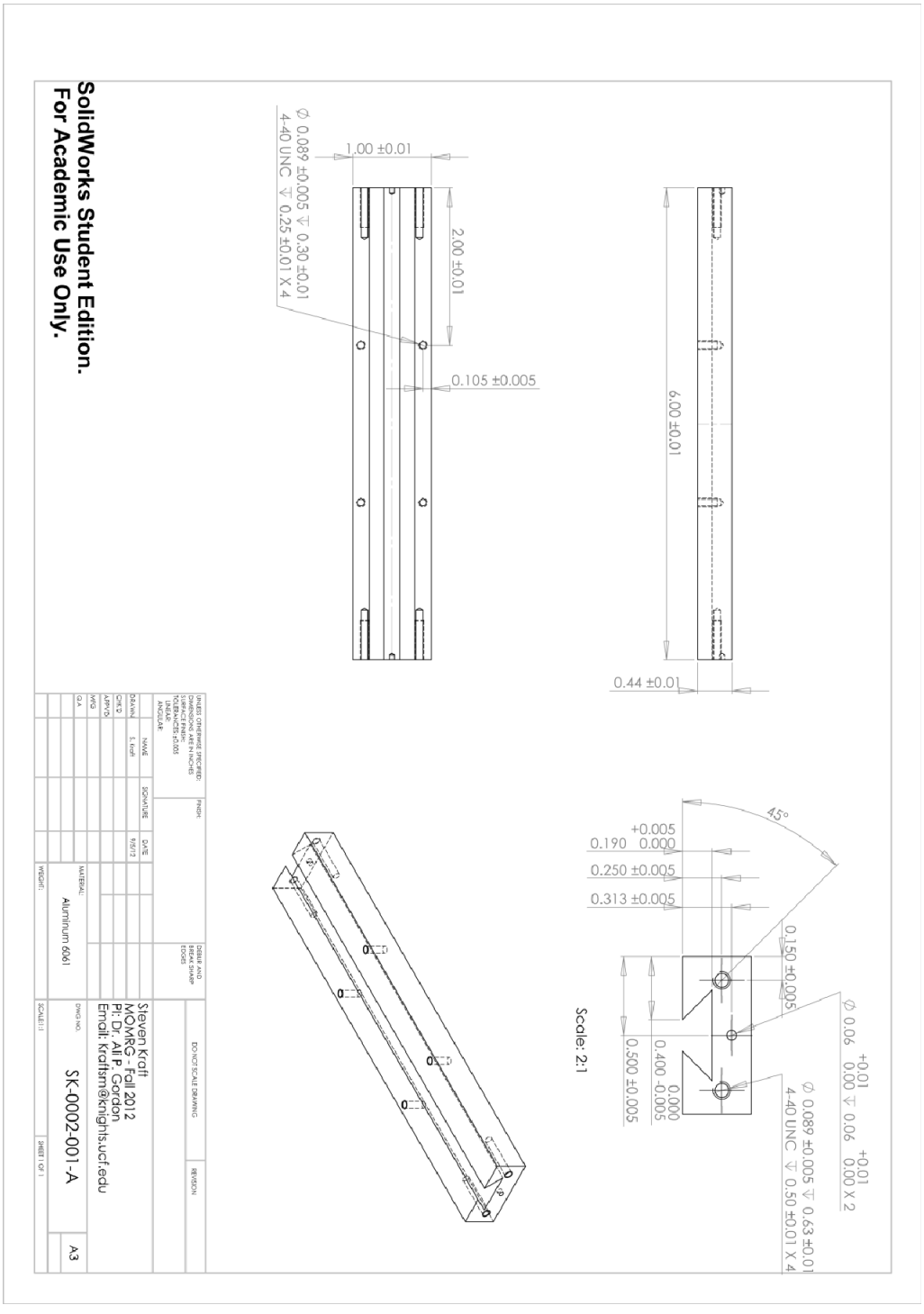

Wave Grip Top

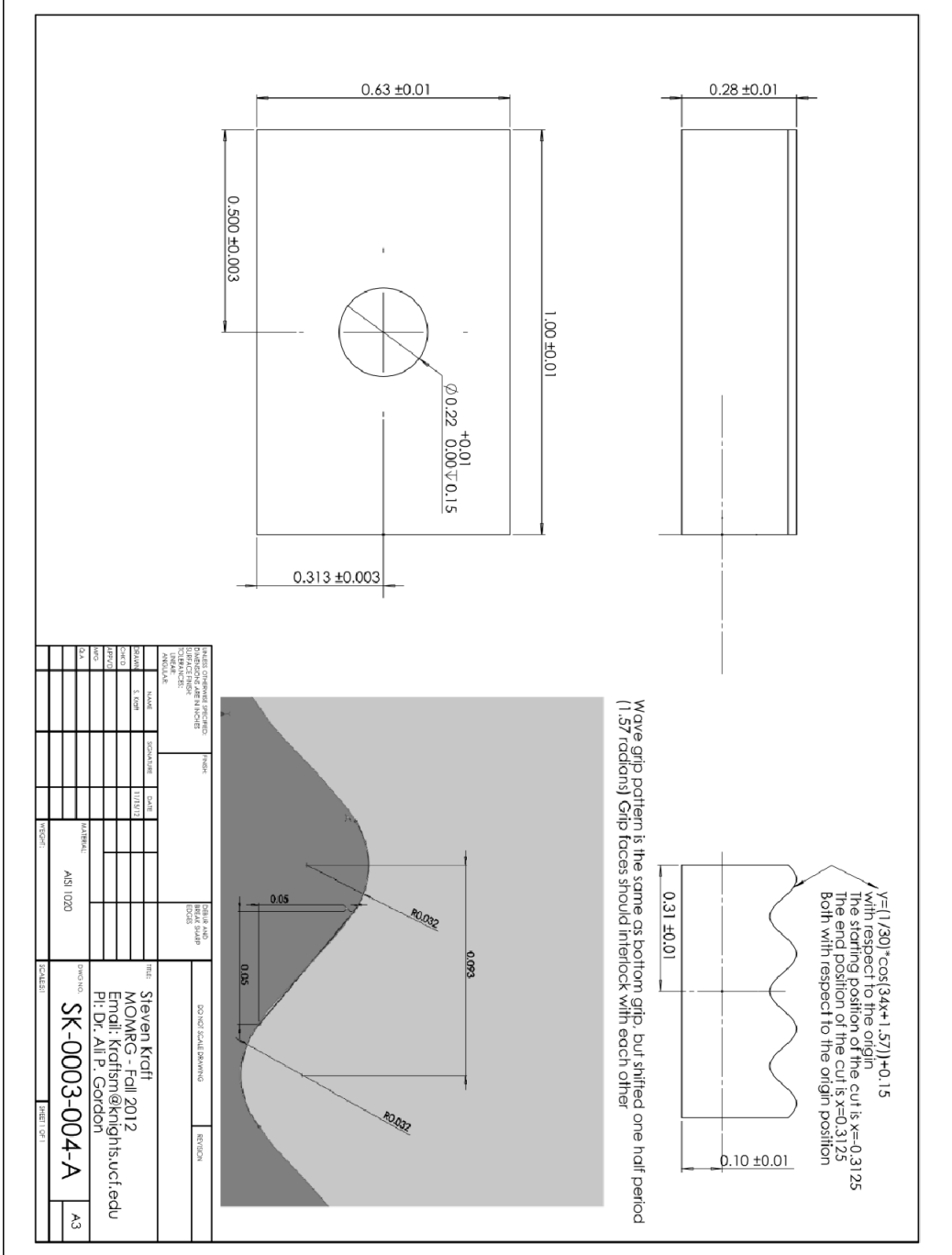

Wave Grip Bottom

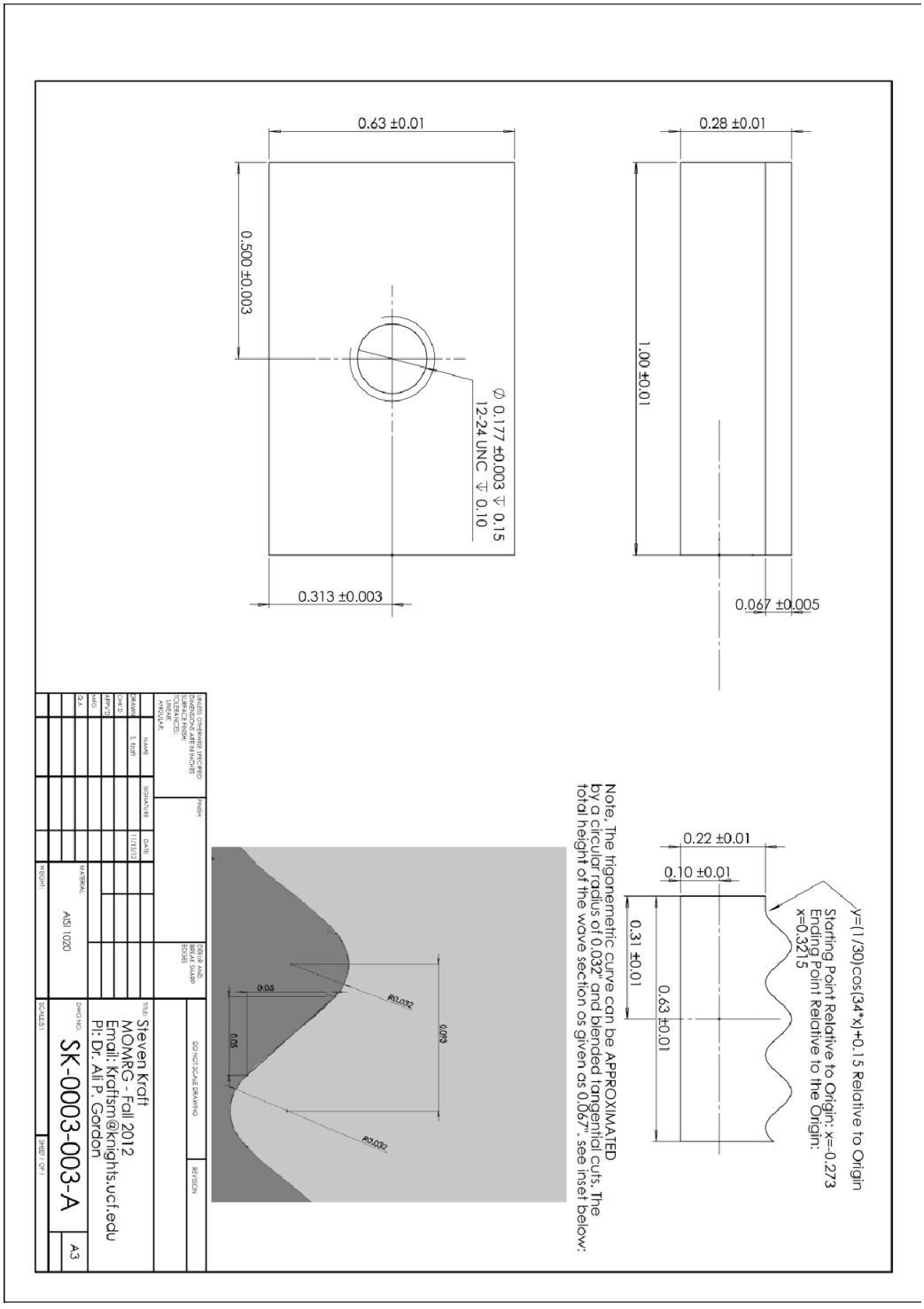

Grip Plate

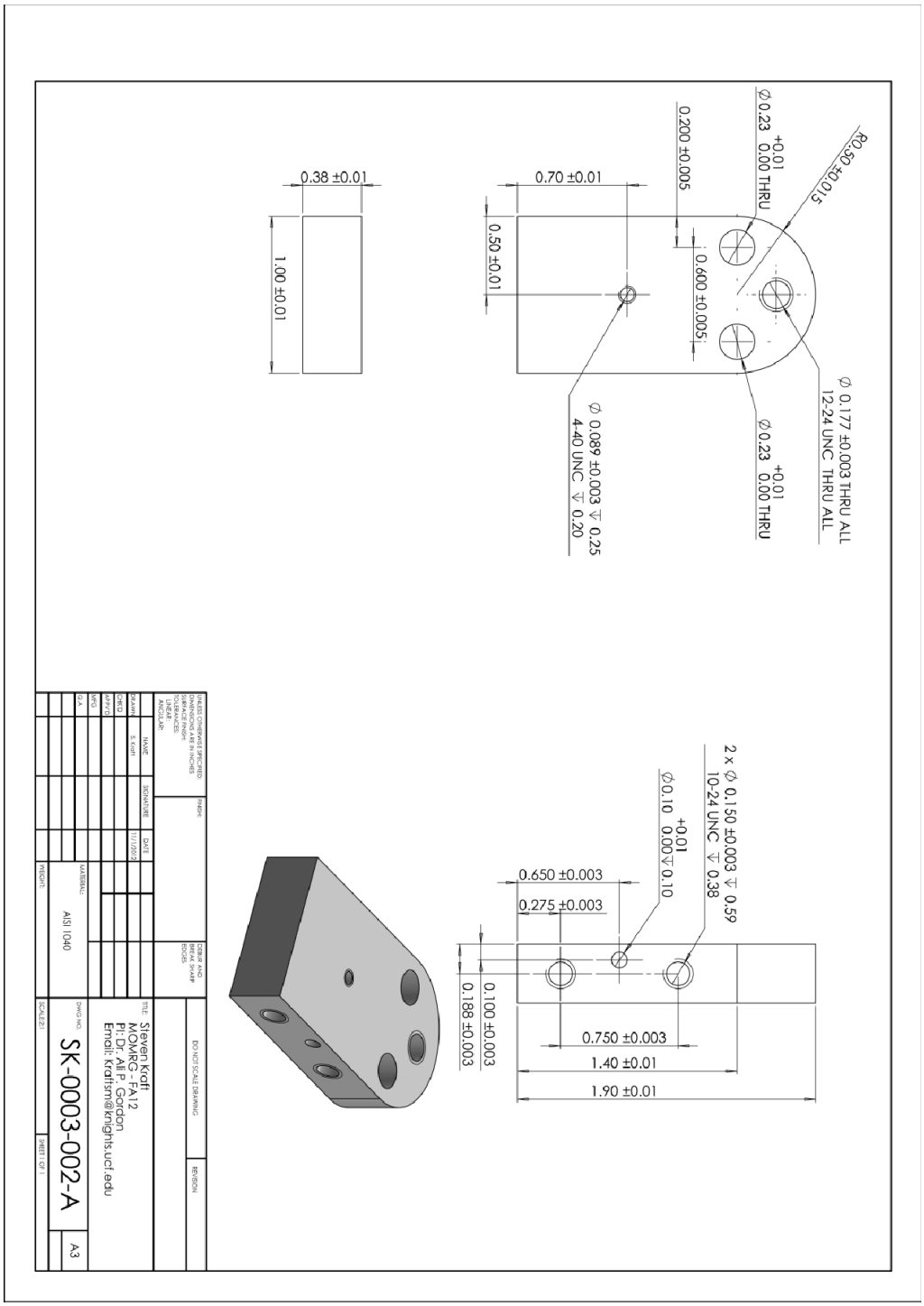
R0.50±0.01
Ø0.23 +0.01 0.00 THRU
0.200 ±0.005
0.70 ±0.01
0.50 ±0.01
0.600 ±0.005
0.38 ±0.01
1.00 ±0.01
Ø 0.177 ±0.003 THRU ALL
12-24 UNC THRU ALL
Ø0.23 +0.01 0.00 THRU
Ø 0.089 ±0.003 ↧ 0.25
4-40 UNC ↧ 0.20
2 x Ø 0.150 ±0.003 ↧ 0.59
10-24 UNC ↧ 0.38
Ø0.10 +0.01 0.00 ↧ 0.10
0.650 ±0.003
0.275 ±0.003
0.100 ±0.003
0.188 ±0.003
0.750 ±0.003
1.40 ±0.01
1.90 ±0.01
UNLESS OTHERWISE SPECIFIED:
DIMENSIONS ARE IN INCHES
TOLERANCES:
FRACTIONAL
ANGULAR:
NAME
SIGNATURE
DATE
DRAWN
K.Kraft
12/7/2018
CHECKED
ENG APPR.
MFG APPR.
Q.A.
COMMENTS:
MATERIAL:
AISI 1040
FINISH
DO NOT SCALE DRAWING
REVISION
DWG NO.
SK-0003-002-A
SCALE:2/1
SHEET 1 OF 1
A3
Steven Kraft
NSWARG / FTA 12
PI: Dr. Ali P. Gordon
Email: kraftsm@knights.ucf.edu